GeRoFan : une architecture et un plan de contrôle basés sur la radio-sur-fibre pour la mutualisation des réseaux d'accès mobile de nouvelle génération

Ahmed Haddad

Doctorat ParisTech

T H È S E

pour obtenir le grade de docteur délivré par

Télécom ParisTech
Spécialité "Informatique & Réseaux"

présentée et soutenue publiquement par

Ahmed HADDAD

le 26 avril 2013

GeRoFAN: Une architecture et un plan de controle basés sur la radio-sur-fibre pour la mutualisation des réseaux d'accès mobile de nouvelle génération.

Directeur de thèse: Maurice GAGNAIRE

T
H
È
S
E

Jury:

M. Leonid G. KAZOVSKY, Professeur, Stanford University, Stanford, CA	Rapporteur
M. Josep PRAT, Professeur, Universitat Politècnica de Catalunya (UPC), Barcelona	Rapporteur
M. Gérard POGOREL, Professeur, Télécom ParisTech, Paris	Examinateur
M. Christophe KAZMIERSKI, Ingénieur, Alcatel-Lucent/Thales III-V Lab, Paris	Examinateur
M. Joel MAU, Ingénieur, Institut-Mines Telecom, Paris	Examinateur
M. Richard TOPER, Ingénieur, PDG de SETICS, Paris	Invité
M. Edouard DOLLEY, Chargé de prospectives, ARCEP, Paris	Invité
M. Maurice GAGNAIRE, Professeur, Télécom ParisTech, Paris	Directeur de thèse

GeRoFAN: Une architecture et un plan de controle basés sur la radio-sur-fibre pour la mutualisation des réseaux d'accès mobile de nouvelle génération.

Résumé: L'architecture actuelle des réseaux d'accès radio n'est pas adaptée en terme de capacité à supporter l'accroissement continu du trafic dans les systèmes cellulaires *4G* et au-delà. L'objectif de cette thèse est de proposer une architecture réseau générique, GeRoFAN (Generic Radio over Fiber Access Network) pour la fédération des stations de base des systèmes cellulaires de nouvelle génération (*WiMAX, 4G LTE*). Deux innovations technologiques majeures sont utilisées pour l'implémentation de l'architecture GeRoFAN: la radio-sur-fibre (RoF) et les modulateurs réflexifs éléctro-absorbants.

La thèse vise aussi à concevoir pour l'architecture GeRoFAN un plan contrôle et un canal de signalisation adapté permettant le basculement des ressources radio, selon la fluctuation du trafic, entre un grand nombre de cellules réparties à l'échelle métropolitaine. Cependant, il a été bien avéré que la transmission optique de plusieurs canaux radios en utilisant la RoF analogique est assujettie à des multiples facteurs de dégradation physique altérant la qualité du signal de ces canaux et induisant une perte dans leur capacité de Shannon. L'originalité du plan de contrôle de GeRoFAN est de réaliser une affectation optimisée des canaux radios sur les porteuses optiques, grace au multiplexage par sous-porteuse (SCM), afin d'ajuster la capacité de Shannon dans chaque cellule radio à la charge de trafic à laquelle elle est soumise. A cet effet, une connaissance fine des contraintes physiques de la transmission RoF est requise pour le plan de contrôle. Cette connaissance est acquise par l'élaboration d'un modèle analytique des divers bruits de transmission du système GeRoFAN. Contrairement à des propositions comparables, le plan contrôle de GeRoFAN se doit d'être le plus transparent que possible à la technologie des systèmes radio concernés. Sa nature " MAC radio agnostique " vise à permettre, grâce au multiplexage en longueur d'onde et au routage optique WDM, la fédération de plusieurs opérateurs utilisant différentes technologies radio sur la même infrastructure. Plus généralement, avec la mutualisation de l'architecture GeRoFAN, le plan de contrôle permet de virtualiser les ressources radiofréquences et de promouvoir de nouveaux modèles économiques pour les opérateurs Télécoms.

Le dernier volet de la thèse se focalise sur la valeur "business" du paradigme GeRoFAN. Les contours du nouveau éco-system d'affaire promu par GeRoFAN sont définis. Les motivations/attentes des différentes parties prenantes dans cet éco-system sont esquissées, les contraintes réglementaires et organisationnelles soulevées sont adressées afin d'assurer un déploiement sans heurts de GeRoFAN. Bien qu'exigeant un nouveau modèle réglementaire, il s'agit de mettre en évidence l'intérêt économique de la solution GeRoFAN, tout particulièrement en comparaison à la RoF digitale, à travers des études technico-économiques chiffrant les couts d'investissement (CapEx), les couts opérationnels (OpEx) et les possibles retours sur investissement. A cet effet, deux modèles économiques sont proposés mettant en évidence la valeur ajoutée de GeRoFAN tout au long de la chaine de valeur.

Mots clefs: Féderation des Réseaux d'Accès, Radio-sur-Fibre Analogique, Virtualisation des Radio-Fréquences, Etude Technico-Economique.

GeRoFAN: An Architecture and a Control Plane based on Radio-over-Fiber for the Mutualization of Next-Generation Radio Mobile Backhaul.

Abstract:

Current radio access networks architectures are not suited in terms of capacity and backhauling capabilities to fit the continuing traffic increase of *4G* cellular systems. The objective of the thesis is to propose an innovative and generic mobile backhauling network architecture, called GeRoFAN (Generic Radio-over-Fiber Access Network), for next generation mobile systems (*WiMAX, 4G LTE*). Two major technological innovations are used to implement GeRoFAN: analog Radio-over-Fiber (RoF) and reflective amplified absorption modulators.

The aim of this thesis is to design for such an architecture an original Control Plane (CP) and a signaling channel enabling to balance radio resources between a set of neighboring cells at the access/metropolitan scale according to traffic fluctuations. The transmission of several radio frequencies by means of an analog RoF link suffers from several impairments that may degrade the capacity of the radio system. The originality of the GeRoFAN-CP consists in mapping radio frequencies with optical carriers by means of Sub-Carrier Multiplexing (SCM) in order to optimize the Shannon's capacity within the various cells covered by the system according to the current traffic load. For that purpose, a deep analysis and modeling of the various physical layer impairments impacting the quality of the radio signal is carried out. Unlike comparable approaches, the GeRoFAN-CP is as independent as possible from the radio layer protocols. Thus, the "radio MAC-agnostic" nature of the GeRoFAN-CP enables to federate multiple operators using different radio technologies onto the same backhauling optical infrastructure. Subcarrier and wavelength division multiplexing (SCM/WDM) as well as WDM optical routing capabilities are exploited onto the GeRoFAN transparent architecture. More globally, the GeRoFAN-CP enables a form of "radio frequency virtualization" while promoting new business models for Telecom service providers.

The last part of the thesis focuses on the business value of the GeRoFAN paradigm. The expectations of the different stake-holders and main regulatory/organizational entities that could be involved in the deployment of GeRoFAN infrastructures should be addressed in order to achieve a smooth deployment of this new type of mobile backhauling. Economics of the GeRoFAN architecture are investigated in terms of OpEx/CapEx valuation and investment profitability, especially in reference to digitized RoF. Two business models are then proposed to study how GeRoFAN contributes to enriching the cellular backhauling service value chain.

Keywords: *Mobile Backhauling, Analog Radio-over-Fiber, Radio-Frequency Virtualization, Backhaul Techno-Economics.*

Contents

List of Figures

List of Tables

Version courte de la thèse en Français

1.1 Introduction

La convergence fixe-mobile et l'ubiquité des services large-bande constituent deux défis majeurs pour les opérateurs télécoms. L'émergence de nouvelles applications trés consommatrices de débits et accessibles via les terminaux mobiles de nouvelle génération met d'ores et déjà en

évidence les limites de capacité des réseaux radio-mobiles actuels (UMTS). Le développement des réseaux alternatifs 4G confirme cette insuffisance. Une telle technique impose l'utilisation de fréquences porteuses plus élevées, supérieures, voire très supérieures à 3 GHz pour des réseaux UWB (autour de 60 GHz) et/ou une réduction drastique de la taille des cellules (désignées par Node-B en UMTS) pour offrir un plus grand débit par unité géographique. L'architecture actuelle des réseaux d'accès radio (Radio Access Network ou RAN) fédérant plusieurs Node-Bs sur un même contrôleur central (ou RNC) n'est pas adaptée à une telle évolution, et ce pour deux raisons. La première, de type CAPEX, a trait au coût intrinsèque de l'infrastructure à mettre en place. La montée en débit du trafic transporté dans les futurs réseaux cellulaires ne pourra pas être satisfaite par les paires de cuivre actuellement utilisés dans le RAN. La multiplication des équipements radio inhérente à l'accroissement de la densité de Node-Bs pose le problème de l'investissement à réaliser par les opérateurs pour la mise en place de leur infrastructure. La seconde, de type OPEX, a trait aux coûts d'exploitation et de maintenance élevés en raison du grand nombre et de la dispersion géographique des équipements radio à superviser. La gestion du soft-handover, la minimisation des interférences ou le contrôle dynamique de gain des antennes dans le cas de pico-cellules d'une centaine de mètres demande une réactivité beaucoup plus grande du RAN.

Nous proposons dans cette thèse deux approches complémentaires pour répondre à ce challenge. La première consiste à atteindre la réactivité requise au moyen d'une topologie RAN simplifiée, faisant appel à des technologies optiques transparentes avancées telles que le multiplexage en longueurs d'onde (WDM), la modulation par sous-porteuse (SCM), le routage optique, la transmission par la technologie radio-sur-fibre (RoF) et les modulateurs optiques réflexifs. La seconde approche consiste en une gestion centralisée de l'intelligence nécessaire pour l'allocation dynamique des ressources radio, cette centralisation ayant lieu plus en amont que dans les réseaux actuels. L'originalité de ces deux approches est de viser une mutualisation multi-opérateurs, multi-technologies de l'infrastructure RAN à une échelle métropolitaine. L'architecture RAN proposée et le plan contrôle qui sera développé doivent permettre une transition sans rupture dans le développement des différentes technologies envisagées pour les réseaux de 4ème génération (4G).

Il y a une quinzaine d'années, la faisabilité du transport point-à-point de fréquences radio par le biais de porteuses laser a été démontrée. Une telle technique connue sous le nom de radio-sur-fibre (RoF) permet de déporter les équipements de traitement du signal radio traditionnellement situés au pied de chaque antenne vers l'autre extrémité de la fibre. L'insensibilité de la fibre optique aux perturbations électromagnétiques extérieures, sa faible atténuation et sa très grande bande passante autorisent un déport de plusieurs dizaines de kilomètres entre les équipements radio et l'antenne elle-même. Des études récentes ont démontré les avantages tirés des technologies RoF lorsque celle-ci est appliquée à des réseaux radio organisés sous forme

de bus, par exemple le long d'une ligne de TGV. Cette approche linéaire a été généralisée au milieu des années 2000 au cas d'architectures maillées point-à-multipoint incluant une fonction de routage optique. Très vite, l'intérêt de pouvoir mutualiser les équipements radio, hormis les antennes, en un point unique est apparu comme un avantage majeur de la RoF pour les opérateurs. Le fait que tous les équipements de traitement du signal radio puissent être co-localisés chez l'opérateur autorise la mutualisation d'un certains nombre d'équipements tels que les oscillateurs radio à la fréquence intermédiaire ou/et à la fréquence radio. Aujourd'hui, deux usages de la technique RoF doivent être distingués : indoor et outdoor. Le RoF indoor consiste en une nouvelle génération de réseaux locaux sans fil à très haut débit, par exemple utilisant l'Ultra Wideband (UWB) opérant à des fréquences de plusieurs dizaines de GHZ pour du Gbps par usager. Le RoF outdoor vise quant à lui à fédérer des antennes de type de celles utilisées dans les réseaux radio-cellulaires. En matière de RoF outdoor, plusieurs projets (USA, Hollande, UK, Portugal, Espagne etc.) ont été réalisés ou sont en cours, souvent avec la réalisation de maquettes opérationnelles. Toutefois ces investigations restent très focalisées sur la faisabilité de ces architectures au niveau de la couche physique. Pour beaucoup de ces projets, la façon de distribuer les ressources radio aux stations de base fait l'hypothèse a priori de la conception d'une nouvelle technique d'accès multiple à l'intérieur des cellules. En ce cens, ces propositions se substituent aux techniques d'accès radio développées pour les systèmes cellulaires. L'une des originalités de la démarche retenue dans cette thèse pour la conception du plan contrôle et du canal de signalisation est de ne pas remettre en cause les standards d'accès radio existants. Pour cela, le plan contrôle ne prend en compte que l'allocation de ressources à l'échelle de la durée de vie des connexions d'usager vis-à-vis de la capacité globale d'une cellule, voire à l'échelle des fluctuations macroscopiques de la charge offerte à des cellules géographiquement proches. L'accès au niveau paquet qui est l'apanage du protocole MAC ne fait pas partie du plan contrôle et est supposé rester inchangé.

Suivant le type de modulation RoF retenue, soit l'oscillateur à la fréquence intermédiaire (IF) seul, soit cet oscillateur et l'oscillateur à la fréquence radio (RF) peuvent être déportés du site où se trouvent les antennes vers le nIJud où est centralisée l'intelligence du plan contrôle. Selon la modulation adoptée, le niveau de mutualisation des équipements peut varier. Dans les deux cas, la nouvelle architecture RAN retenue conduit à des économies en matière d'investissement matériel (CapEx) comme en matière d'exploitation et maintenance (OpEx), les Node-B ne requérant pratiquement plus d'équipements sensibles sur le terrain.

En résumé, la motivation d'origine de cette thèse part d'un constat simple. La fourniture de services mobiles large-bande ubiquistes est un objectif clé des réseaux cellulaires de nouvelle génération. A l'évidence, les usagers ne sont pas ubiquistes dans la mesure où ils se trouvent à un seul endroit à la fois. Ainsi, plutôt que de dupliquer les ressources radio (les Node-B) dans leur totalité pour couvrir le territoire comme cela est fait dans les réseaux actuels, il nous parait

plus judicieux de ne garder que la partie strictement indispensable de ces Node-B sur le terrain, à savoir les antennes et les démodulateurs RoF. Toute la portion " noble " du Node-B, à savoir les équipements de traitement du signal radio, les multiplexeurs/démultiplexeurs et les modems nécessaires à la conception du multiplex à la fréquence intermédiaire et à sa transposition dans le domaine radio-fréquence sont déportés à la tête du réseau où ils peuvent être mutualisés.

1.2 Etat de l'art et evolution des architectures pour l'accès cellulaire

1.2.1 Technologies de réseaux d'accès-métro pour la féderation des RANs

La federation des stations de base (BS) des réseaux d'accès radio mobile peut se faire par l'intermédiaire de plusieurs technologies illustrées à travers le panorama dans la Figure 3.2. Aux Etats-Unis par exemple et selon une étude réalisée par Yankee Group [110], la féderation des BS par la paire de cuivre (T1/E1) en mode TDM et en utilisant la technologie PDH représente pres de 90% de l'ensemble du panorama des solutions techniques, suivi par les faisceaux hertziens (FH) point à point ou point à multi-point avec 6% et enfin la fibre optique. Cependant, d'autres technologies peuvent etre utilisées pour la féderation des BS incluant des solutions filaires comme les liaisons louées T1/E1 ou la fibre optique, ou des solutions sans-fil comme les faisceaux hertziens, la communication satellitaire, la technologie FSO (transmission par des ondes millimétriques à haute capacité avec des lasers directifs), les technologies WiFi et WiMAX.

Le tableau 3.1 dresse un comparatif des differentes technologies utilisées pour la féderation des BS. La comparaison est réalisée selon cinq axes differents: la capacité, la distance/la couverture, Prise en compte des obligations de qualité de service QoS (délai de bout en bout, gigue, fiabilité de la transmission etc.), synchronisation, cout (déploiement et opérationnel) et les strategies possibles des operateurs telecoms pour mieux capitaliser du projet du déploiement de la technologie en question.

Il est evident qu'aucune technologie ne prétend à elle toute seule satisfaire les exigences que requiert la federation d'un large nombre de BS pour les systemes cellulaires de nouvelle géneration. Plusieurs publications et études de benchmark ont montré que la solution dominante pour le court terme serait maintenue autour des liens louées (T1/E1) cependant les opérateurs telecoms sont convaincus de la nécessité de repenser leur architecture de féderation autour d'un mix-technolgique où des technologies à haute capacité supportant nativement la QoS comme la fibre s'imposerait progressivement sur le long terme. Dès lors, nous avons réalisé une comparaison sous forme de benchmark des differentes technologies decrites avant par rapport à la solution de réference: la paire de cuivre pour des liaisons louées de type T1/E1. La comparaison

Table 1.1: Comparatif des technologies de féderation des BS.

		Capacité	Couverture	QoS	Synchronisation	Cout	Strategies pour l'opérateur
Technologies Filaires	**Liens cuivre loués**	faible (∼ 2 Mbps)	Suffisante	Garantie	native	faible CapEx (dejà existant), mais haut OpEx (cout de location du lien augmente linéairement avec la distance et la capacité)	Multiplexer plusieurs liens T1/E1 pour une plus grande capacité. Exploiter la technologie xDSL sur la meme infrastructure dejà installée.
	Fibre	"illimitée"	Suffisante	Garantie	Temps d'horloge fourni	Cout pénalisant de déploiement, et frais de maintenance augmentant avec la distance	Capitaliser sur les réseaux optiques à tres haut débit de type FFTx. Cloud RAN basés sur la RoF. Promouvoir la convergence et l'intégration fixe-mobile autour d'un réseau unifié.
Technologies Sans-fil	**Faisceaux Hertziens (FH)**	Grande mais dépendante de la modulation et les protocoles adoptés	LoS requis	Garantie	Supportée	Cout de déploiement pouvant etre pénalisant. OpEx: Frais d'utilisation de spectre dépendants de la reglementation en vigueur.	Diminuer l'OpEx en utilisant des frequences non-reglementées. Partage et mutualisation du site FH par plusieurs opérateurs.
	Satellite	Moyenne	Couverture flexible	Fort délai de propagation	Supportée	Plus couteux qu'une solution à base de liens louées et à capacité equivalente	Diminuer le cout d'investissement en utilisant une politique de facturation du service en fonction de son usage. La solutions ultime pour les endroits generallement difficilement caccessibles (territoires éloignées, archipèles isolés etc.)
	FSO	Assez grande mais dépendante des conditions de propagation	LoS préviligiée	Garantie	Supportée	Pas d'investissement lourd spécialement requis (*vs.* fibre). Garantir des bandes reglementées avec des faisceaux directifs (*vs.* FH dans des bandes reglementées et sans intérférence ou transmission sur bandes non reglementées mais sujet à intérférence *WiFi*), mais haut OpEx (necessité du stabilité du systeme)	Promouvoir des solutions hybrides en utilisant les FHs ne requerant par la condition LoS comme issue contre les obstroctions à travers des configurations topologiques [42] en boucle ou en bus. FMC: convergence fixe/mobile, FSO utilisé comme extension de l'Ethernet optique dejà deployé dans les regions métropolitaines. [128].
	WiFi	Grande	LoS requis	Sauf *802.11e*, la QoS est supportée	Pas assez élaborée pour son usage pour la federation des BSs	Faible CapEx grace à sa maturité technologique et à la production de masse. OpEx faible: usage des bandes non-reglementées.	Offload du trafic packet haut-débit sur les points de présence WiFi (mechanismes d'offload avancés à travers: *Hot-spot 2.0* [42]). Capitaliser sur les points de présence *WiFi* sous la propriété d'une partie tierce dans les espaces privés [117].
	WiMAX	Grande	LoS ou non-LoS	Garantie	Synchronisation précise par GPS	Cout de deploiement du réseau (CapEx), OpEx: Frais de licence du spectre	Le processus de standarisation devrait abaisser les couts. Solution de choix pour les régions rurales et à faible pénetration.
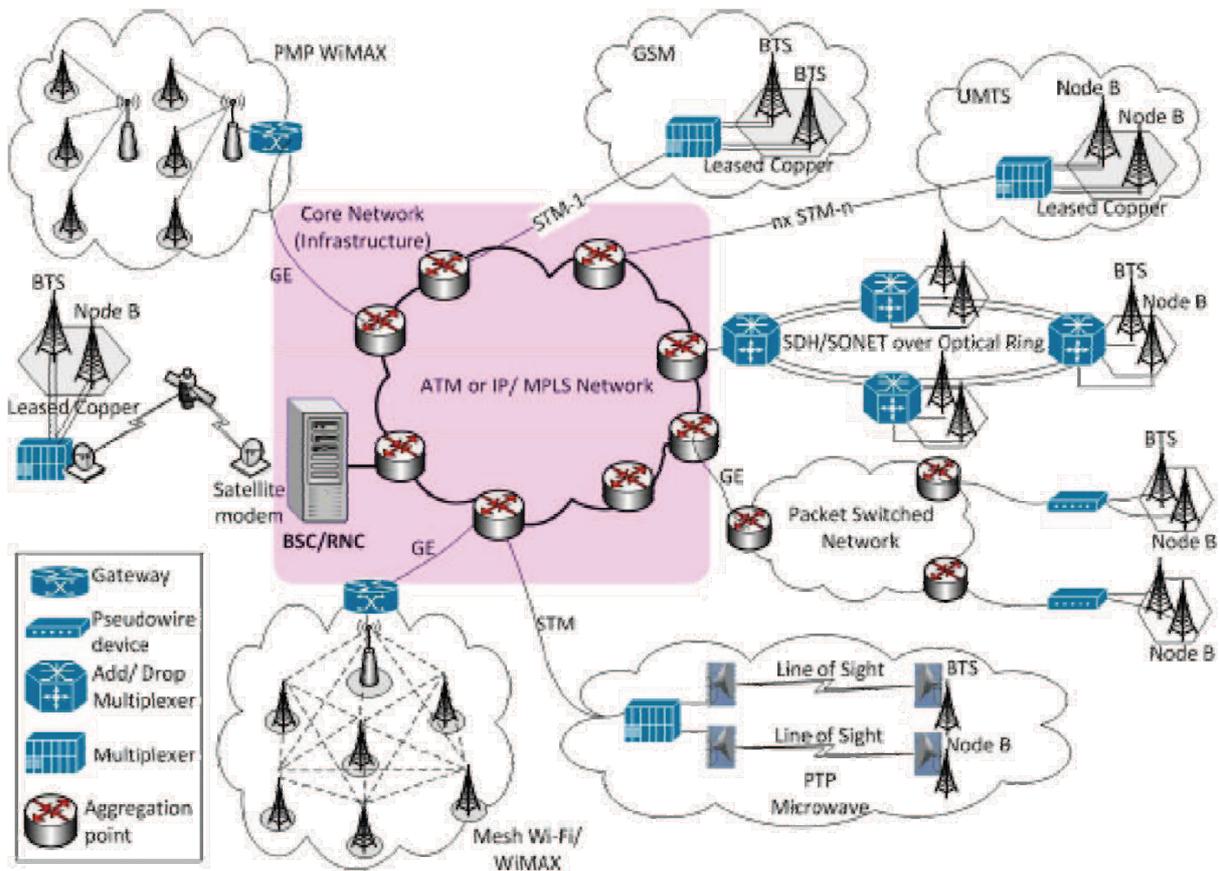
Figure 1.1: Technologies traditionnelles et émergentes de federations des BS [102].

est réalisée selon deux aspects: un aspect technique (produit de la capacité et de la portée) et un aspect financier/economique calculé par le cout cumulatif du lancement de la technologie et son exploitation (TCO: Total Cost of Ownership). Les données et les hypothèses utilisées pour ce calcul sont tirées des divers rapports et publications suivants: [38], [107], [118], [45] et [122].

La Figure 3.4 présente le positionnement des différentes technologies ainsi que les possibles directions strategiques que pourraient suivre un opérateur telecom pour faire évoluer son réseau jusqu'à converger vers la féderation des BSs par la fibre optique comme solution à long terme.

1.2.2 Modulation Radio-sur-Fibre (RoF)

La modulation RoF est considérée comme le moyen le plus adéquat pour fédérer un grand nombre d'antennes et déplacer les équipements de traitement radio et l'intelligence de la périphérie vers la tête de l'infrastructure. Suivant le type de modulation choisi, l'emplacement des oscillateurs locaux (LO IF, LO RF) devrait favoriser plus de mutualisation et un design plus minimaliste des sites radio. En somme, trois formats de modulation sont identifiés:
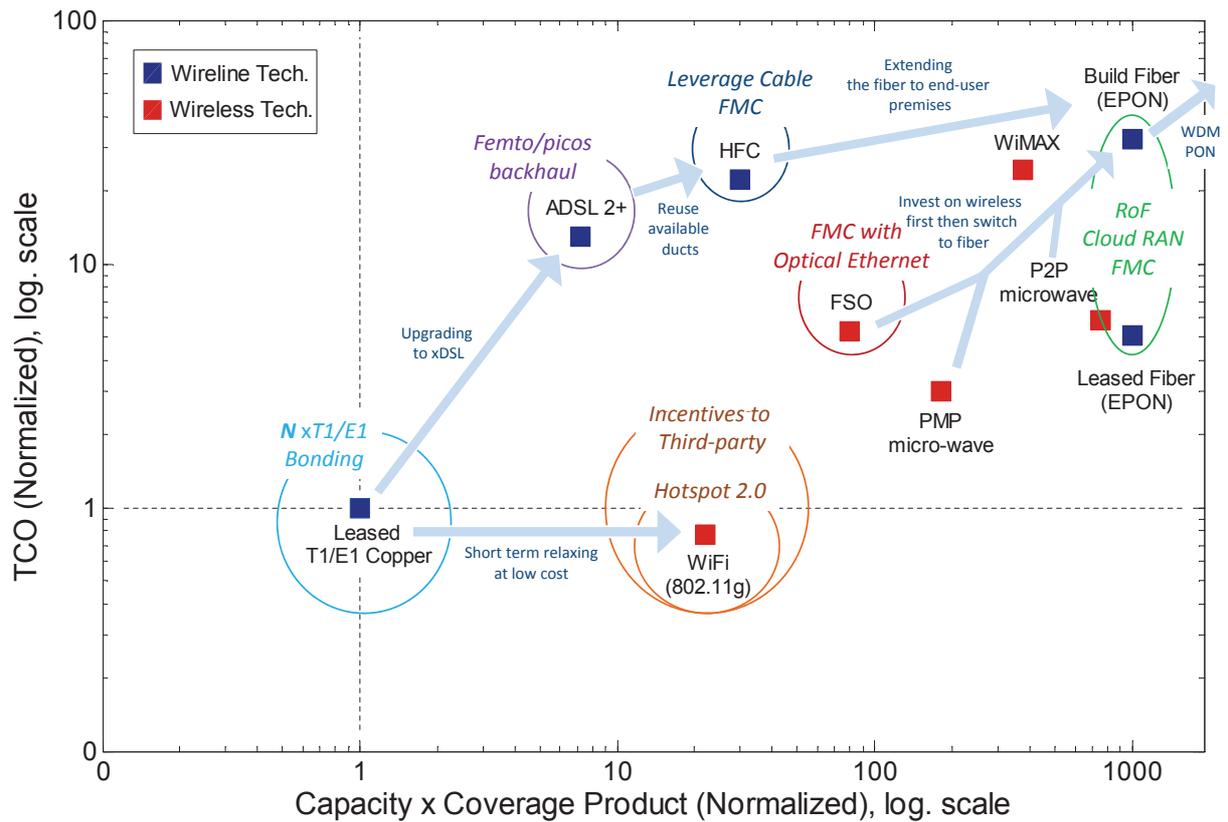
Figure 1.2: Benchmark des solutions technologiques de féderations des BSs et directions strategiques possibles d'évolution pour un opérateur Télécom.

- Bande de Base sur fibre (BB-o-F):les oscillateurs LO IF et LO RF sont localisés à chaque BS.

- Multiplex de fréquence intermédiaire sur fibre (IF-o-F): Seul un LO RF est nécessaire à chaque BS

- Radiofréquence sur fibre (RF-o-F): Toute la complexité (LO IF, LO RF) est déplacée vers les sites centraux. Le rôle de la station de base se limite à l'amplification du signal et la conversion optique/electrique.

Depuis plus d'une décennie, les deux premiers formats de modulation sont bien maitrisés pour des fréquences allant jusqu'au GHz. La modulation RF-o-F est la solution la plus attrayante en terme de coût. Par contre, c'est elle qui présente la plus grande complexité de mise en IJuvre surtout si l'on considère des systèmes radio dont les fréquences porteuse sont élevées (fréquences millimétriques).

Contrairement aux trois variantes de la RoF citées précedémments et qui supposent une transmission analogique du signal radio, une autre variante de la transmission RoF appelée

(a) Analog RoF transmission link

(b) Digitized RoF transmission link
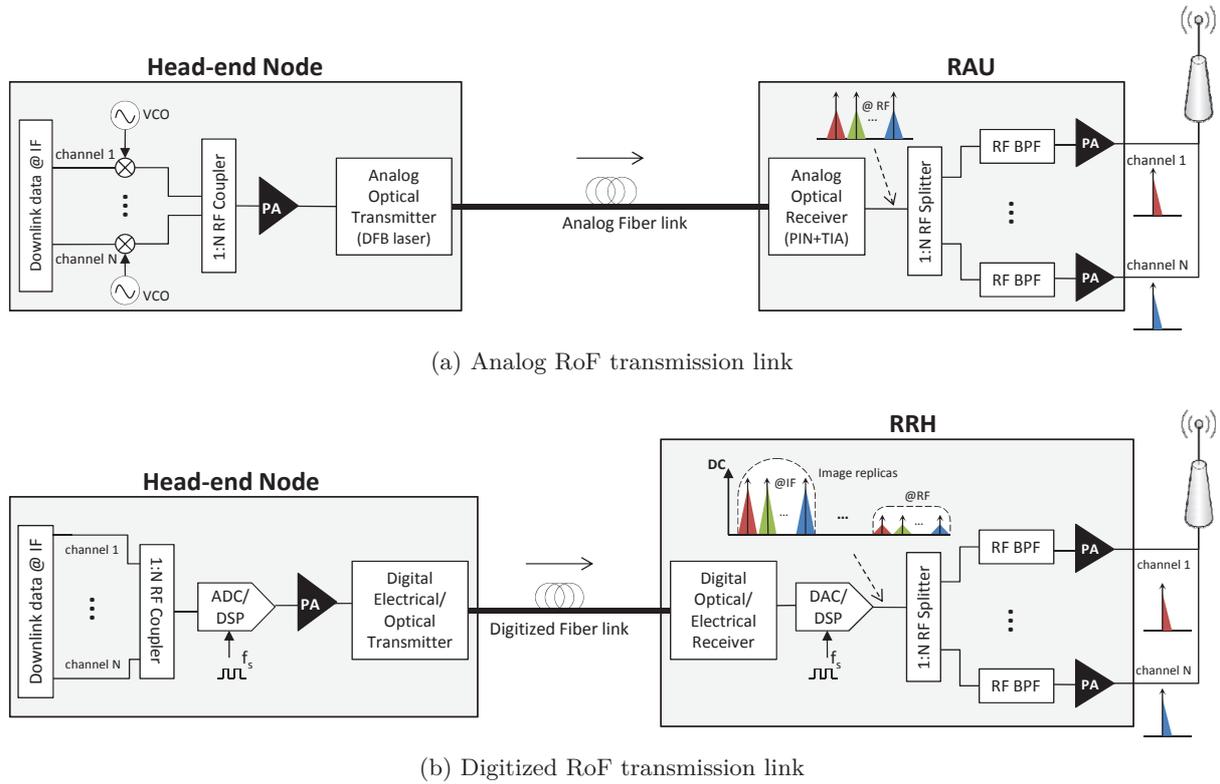
Figure 1.3: Multi-channel radio signal distribution using Radio-over-Fiber (RoF).

Table 1.2: Modèle de trafic adopté pour les 3 scenarios.

	Vocal	BE Web	Multimedia on Web	VoD	Débit/connexion
Mix$_1$	65%	30%	5%	0%	$\simeq 38.5\ kbps$
Mix$_2$	50%	35%	10%	5%	$\simeq 157\ kbps$
Mix$_3$	30%	40%	20%	10%	$\simeq 294\ kbps$

RoF digitale (D-RoF) se base sur la transmission du flux numerisé des sous porteuses radio analogiques. En comparaison à la A-RoF, la RoF digitale nécessite toute la chaine de circuit chargée de la numerisation du signal notamment l'échantillonnage et la quantification dans les stations de bases. Connue pour etre plus resistante aux effects de degradations physiques relatives à la transmission analogique, la D-RoF nécessite par contre un cout supplémentaire de déploiement (cout des numeriseurs) et d'exploitation (l'électronique des numériseurs et les cartes de traitement associées à base de FPGA ou DSP sont penalisants en terme de consommation energitique surtout à tres haut-débit). A cet effet, nous avons réalisé une comparaison entre les deux variantes de la RoF (digitale et analogique) dont la chaine de transmission typique est illustrée dans la Figure 3.10.

La comparaison entre la A-RoF et la D-RoF se base sur 2 critères de couts: le cout CapEx (cout d'équipements et d'infrastructure) et le cout OpEx (cout opérationel relatif à la con-

sommation energitique). La comparaison est réalisée selon 3 scenarios de traffic, chacun est construit comme un mix de 4 services offert par un operateur télécom. Il s'agit du service de communication vocale (symétrique, temps réel à 16 kbps), du service Best Effort (BE) du navigation web (non temps réel, asymétrique à 30.5 kbps), service multimedia interactif sur le web (384 kbps utilisant un codec video de type MPEG-4) et enfin le service de la video à la demande (VoD) (flux continue en temps réel, hautement asymatrique à 2 Mbps). Les 3 scenarios de traffic sont une pondération des 4 services cités comme le montre le tableau 3.2. Le premier scenario (Mix_1) correspond à un trafic à forte dominante du service vocale. Le second scenario (Mix_2) décrit un profil de trafic du passé proche, c'est à dire un traffic equilibré entre les données paquets et les connections vocales, enfin le troisième scénario (Mix_3) décrit la tendance qui commence à se profiler actuellement et qui s'accentura prochainement où le trafic generé par les utilisteurs mobiles est essentiellement de type paquet. Enfin il est à noter que dans le soucie de ne pas penaliser le lien D-RoF lors du dimensionnement des équipements requis, la fréquence d'échantillonage est calculée sur la base de la theorie d'échantillonage passe-bande (Band-Pass Sampling Theory) qui permet d'échantilloner à des signaux haute-fréquences mais passe-bande à une fréquence moins elevée ce qui relaxe largement la contrainte sur les numeriseurs requis pour le lien D-RoF.

Grace à un benchmark sur les couts unitaires des équipments nécessaires pour chacune des deux variantes RoF ainsi que les données sur leur consommation moyenne energitique, nous dressons la comparaison entre les deux technologies A-RoF et D-RoF en calculant le rapport CapEx et OpEx de la D-RoF relativement à la A-RoF pour les 3 scenarios cités en fonction des nombres de connections dans la cellule. Les résultats de la comparaison sont illustrés dans la Figure 3.12 . Nous remarquons essentiellement qu'à faible charge (faible nombre de connections), la A-RoF est plus couteuse que la D-RoF, alors que la tendance s'inverse entre les deux technologies au fur et à mésure que la charge augmente. En effet, à forte charge, une grande capacité est requise pour supporter le flux à tres haut débit generé par l'ensemble des connections. Avec la D-RoF, le transport d'un si grand débit nécessite des modulateurs digitaux plus couteux (des transpondeurs optiques à tres haut débit Ethernet 10Gbps voire meme 40Gbps), des numeriseurs (convertisseurs analogiques/numeriques ADC/DAC) plus rapides et plus précis (travaillant à des bandes plus larges et avec des fréquences d'échantillonage plus élévées). Par ailleurs, ces equipements sont de plus en plus consommateurs d'énergie meme si dans l'absolue l'efficité energitique (c-à-d la consommation energitique par bit par seconde) est plus elevée à mésure qu'on monte en débit, le bilan de la facture energitique augmente sensiblement avec l'accroissement du trafic. Ainsi, la technique A-RoF tire avantage de sa transparence optique pour afficher un OpEx et un CapEx plus faible que la D-RoF surtout à forte charge de trafic.
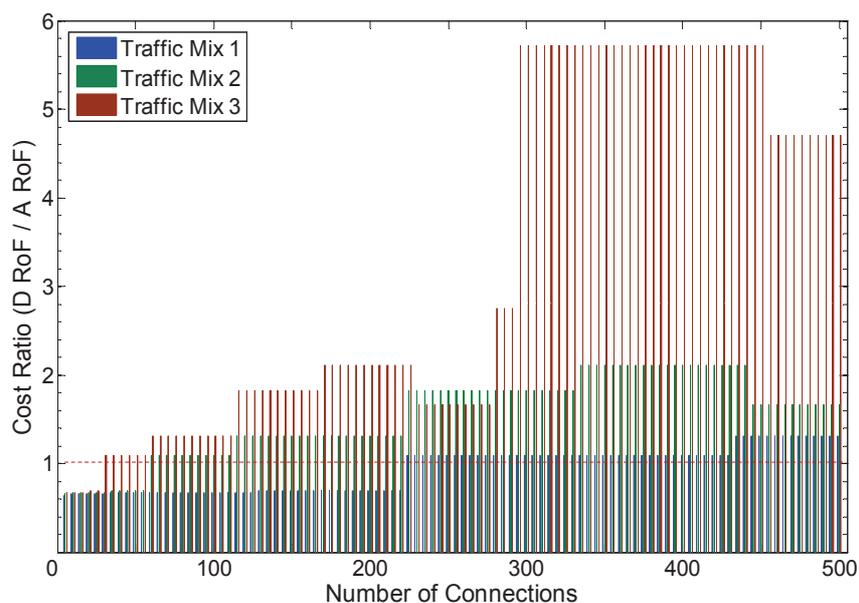
(a) Evolution du ratio du CapEx D-RoF/A-RoF avec la charge de trafic.
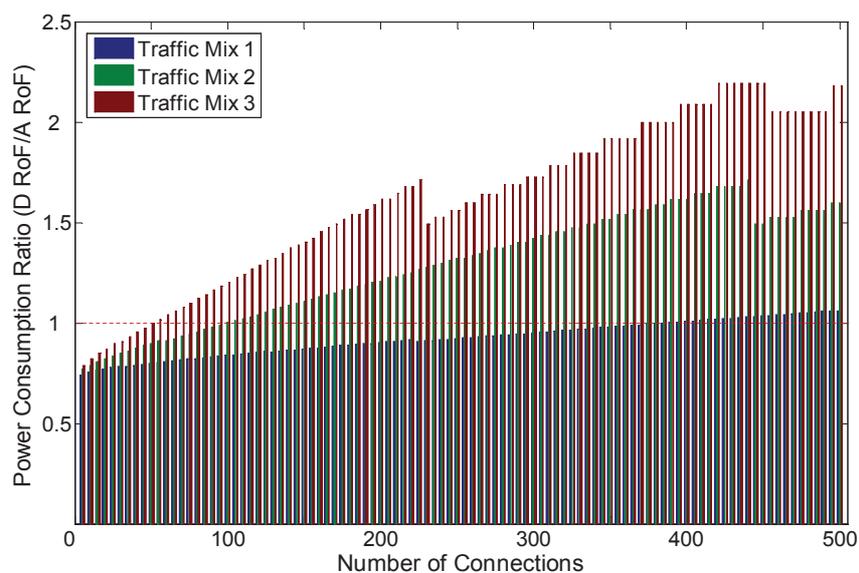
(b) Evolution du ratio de la consommation energitique ratio avec la charge de trafic.

Figure 1.4: Evaluation du CapEx et de la consommation energitique pour les 3 differents scenarios de trafic.

1.2.3   Des modèles avancés d'architecture réseau d'accès-métro

Depuis les progrès réalisés par les techniques RoF, un intérêt croissant s'est porté vers la définition d'architecture de réseaux RoF en usage indoor et outdoor. Les conditions difficiles de propagation du signal (surtout à des fréquences plus élevées) dans un environnement outdoor orientent principalement les investigations entreprises vers la faisabilité de ces architectures au

niveau de la couche physique. Ces études ont négligé jusqu'ici le design d'un plan de contrôle pour optimiser l'allocation des ressources radio/optiques sur la base de considération physiques. Parmi les travaux réalisés dans le conception d'architecture métro outdoor, nous mentionnons 4 approches qui ont retenu notre attention et qui pourraient constituer des entrées utiles pour la définition de notre architecture générique:

- Dans [11], une architecture optique est proposée à base de A-RoF pour la féderation des stations de base installées le long d'un train à grande vitesse et destinée à fournir une connection haut débit aux passagers. Cette solution permet d'exploiter la centralisation apportée par la A-RoF pour concevoir des BSs à simples configurations et permettre de gérer depuis la tete du réseau tous les mecanismes liés au handover et aux basculement de resources en fonction de l'itinéraire du train.

- Dans RoFnet [88], les auteurs proposent l'utilisation de modulateurs réflexifs à chaque station de base. Ces dernières reçoivent deux longueurs d'onde, la première module le trafic descendant et la seconde une longueur d'onde continue qui grâce au modulateur réflexif module le trafic montant de la cellule. Les auteurs de décrivent pas par contre la topologie adoptée pour leur réseau métropolitain de type RoF. L'apport des modulateurs réflexifs comme spécifié dans l'architecture de RoFnet pourra inspirer le rôle que devront jouer ces composants dans notre architecture.

- Dans [146], les auteurs proposent une architecture robuste RoF en anneau pour desservir différentes stations de base regroupées en sous-anneaux dupliqués. L'architecture proposée implémente des mécanismes d'autoprotection et d'auto-restoration grâce à la structure d'anneau et la duplication des stations de base dans les sous-anneaux. L'utilisation de réseaux de Bragg fixes et accordables (T-FBG) permet de jouer sur une relative dynamicité dans l'allocation des porteuses optiques. Par contre, aucune logique de contrôle n'est formalisée pour commander le partage des ressources. D'autre part, l'absence de modulateurs réflexifs, rend l'architecture plus couteuse et moins transparente que celle proposée dans cette thèse.

- Dans [132], une architecture à base de A-RoF appelée FUTON permet de féder plusieurs technologies sur la meme infrastructure optique et grace à la centralisation de la A-RoF réaliser un traitement de signal et de calcul partagé entre les differents systemes. Le but étant de tirer le meilleur de chaque systeme tout en mutualisant l'architecture réseau les supportant. Cependant, contrairement à notre approche, FUTON n'est pas MAC-radio agnostique et travaille à l'échelle paquet (la connexion individuelle) ce qui réduit l'intéret d'une architecture génerique visant à etre transparente par rapport au systeme radio servi.

1.2.4 Architecture GeRoFAN

La Figure 3.16 illustre le type d'architecture hybride radio/fibre que nous proposons dans cette thèse. Cette architecture se compose de trois éléments principaux:

- le HOLT (Hybrid Optical Line Termination) constitué du noeud final centralisant les opérations de génération et de maintenance de la porteuse optique et implémentant la logique de contrôle de basculement dynamique des ressources à travers un porteuse optique de signalisation $\lambda^{\star}$. Au sein du HOLT, ce noeud est raccordé au routeur AWG chargé d'exécuter cette allocation dynamique.

- la partie métropolitaine (Feeder Section- FS) composée de sous réseaux tout optiques connectés aux ports du routeur AWG et déployés chacun sur une zone spécifique de la métropole. La topologie des sous réseaux pouvant etre une boucle optique, un arbre ou un bus optique.

- Les RAUs (Radio Access Unit) servant des cellules de type LTE ou WiMAX. Les RAUs sont équipés de R-OADM pour l'extraction et l'injection des porteuses optiques et de modulateurs amplifiés à électro-absorption (RAM). La figure ... illustre l'architecture d'une RAU dans le cas où GeRoFAN sert un seul opérateur/systeme radio. Cependant l'architecture est aussi adaptée à un service multi-opérateur/multi-technologies radios. En effet ceci est possible en empilant plusieurs pairs de ROADM/RAM et en utilisant un commutateur à radio frequence (RF switch) pour distribuer chaque radio frequence vers son ROADM/RAM associé. De ce fait, plusieurs opérateurs coéxistent dans le meme réseau GeRoFAN, servant la meme cellule et mutualisant les equipments radio "front-ends" comme l'antenne et l'amplificateur à faible bruit (LNA) placé avant le commutateur radio. L'architecture de la RAU multi-service/multi-opérateur (MS-RAU) ainsi que la HOLT correspondante (M-HOLT) sont montrées dans la Figure 3.18.

Plan de controle: Le plan de controle de GeRoFAN (GeRoFAN-CP) est en charge de gérer l'allocation des resources radio entre cellules à une echelle temporelle de plusieurs dizaines de minutes (ce qui correspond à la variation de la charge de trafic agrégée dans la cellule) et/ou la gestion des resources à la fois radio et optiques entre sous-réseaux à l'échelle multi-horaire. De ce fait, l'innovation majeure du plan de controle de GeRoFAN est d'etre MAC-radio agnostique c'est à dire transparent par rapport au système radio servi. Cette transparence permet à GeRoFAN d'etre utilisé dans un contexte multi-technologique et multi-opérateur. La Figure 3.20 représente la gestion optimisée de la ressource radio et optique entre differents districts servis par les sous réseaux de GeRoFAN tout au long d'un profile journalier typique du trafic radio mobile.
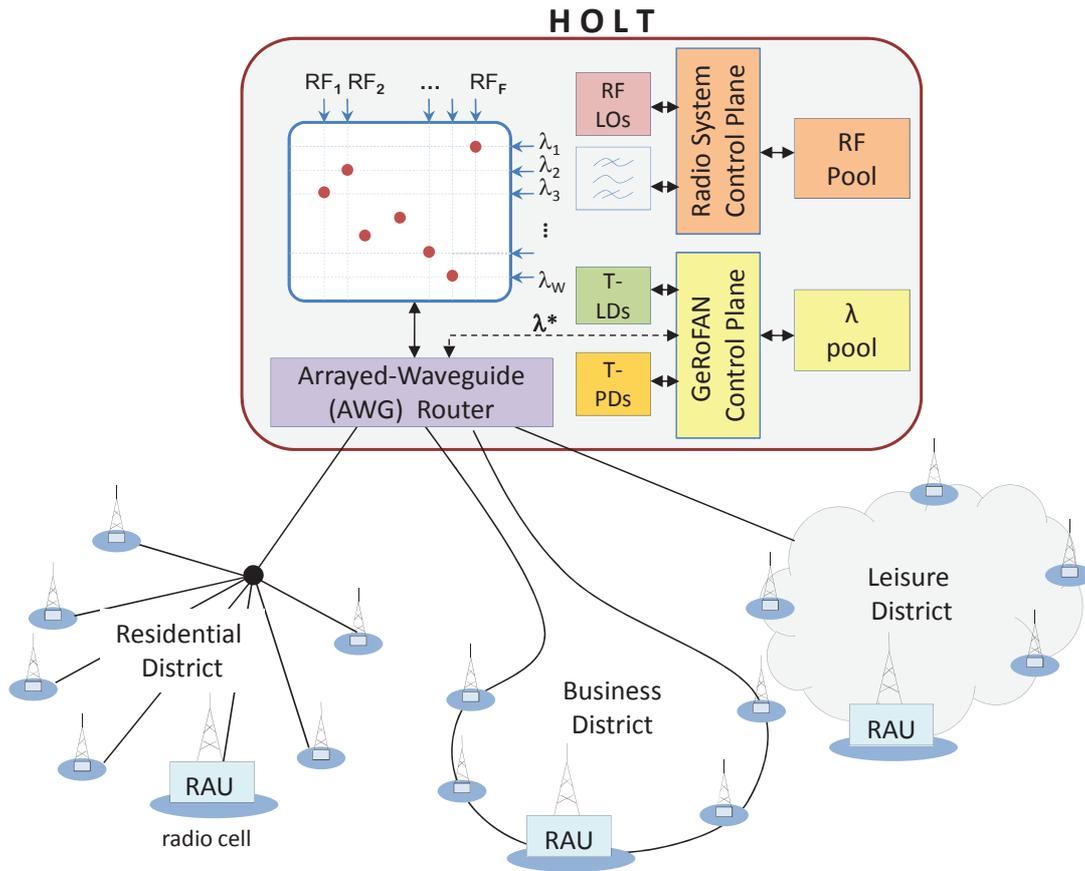
Figure 1.5: Architecture de GeRoFAN.

Par ailleurs, le plan de controle de GeRoFAN est en charge de gérer la matrice de placement des Radio Frequences (RFs) sur les porteuses optiques OCs. L'affectation des ressources radio sur les porteuses optiques est réalisée d'une manière à consommer le moins que possible des canaux optiques nécessaires pour le transport tout en gérant les bruits de transmission de la couche optique ce qui permettra de préserver la capacité de Shannons de ces canaux radio. On parle ainsi d'un plan de controle intégrant les limitations de la transmission par la RoF anaogique (QoT-aware Control Plane).

1.3 Limitations physiques de la transmission Radio-sur-Fibre

Comme il a été indiqué dans les sections précedentes, la transmission des signaux radios par la RoF analogique est soumise à des contraintes de bruit de la couche physique optique qui risquent de dégrader la qualité de transmission (QoT) du canal radio et de ce fait réduire sa capacité de Shannon. Le but de cette section est de formaliser mathématiquement les differents bruits inclus dans la transmission RoF analogique de GeRoFAN.
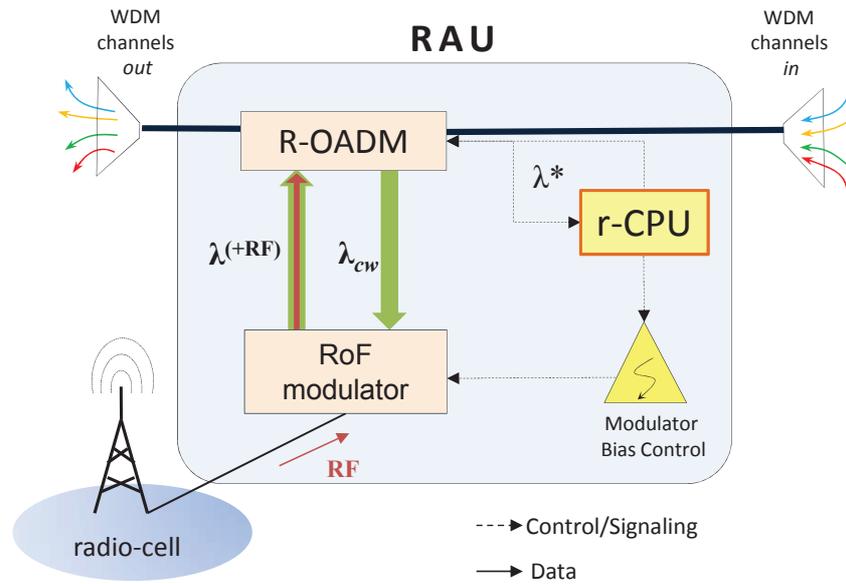
Figure 1.6: Architecture de la RAU pour un trafic sens montant.

A travers la modélisation analytique des différents bruits, le GeRoFAN-CP détermine la stratégie optimale de placement des RFs sur les canaux optiques apte à préserver la capacité radio du système cellulaire et satisfaire la charge dans la cellule. Dans un contexte de trafic dynamique, où les différentes cellules radio ne sont pas soumises à la meme charge de trafic, il s'agit de déterminer le rapport Signal sur Bruit (SNR) optimal à chaque cellule qui permettra d'ajuster la capacité de Shannon dans la cellule à la charge de trafic à laquelle elle est soumise. Ainsi un SNR trop fort dans une cellule où la charge de trafic est faible conduit à une situation de gachis de capacité dans la cellule alors qu'un SNR faible dans une cellule soumise à une forte activité radio conduit à des taux de rejet importants pénalisant la qualité de service fourni aux utilisateurs mobiles dans cette cellule. Afin d'évaluer l'impact de chaque bruit de la couche physique sur le SNR final du canal radio nous développons un modèle géneral appelé QoT-tool (outil de qualité de transmission) analysant les principaux bruits de transmission de l'archictecture GeRoFAN. Afin de faciliter l'analyse des différents bruits en question nous les classons en 4 grandes categories:

Categorie I (Cat.I) désigne la penalité de modulation (MP) calculée par la figure de bruit du modulateur (reflexif) amplifié à electro-absorption (RAM).

Catégorie II (Cat. II) désigne les bruits de distortions dues aux intermodulations entre sous porteuses portées par le meme canal optique. Symbolisée par IMDs, cette catégorie re-grouppe 3 sous bruits d'intermodulation principaux: les intermodulations dues au RAM (IMD-RAM), les intermodulations due à la modulation OFDM des sous-porteuses (IMD-OFDM) et les intermodulations due aux battements entre canaux optiques (OBI).
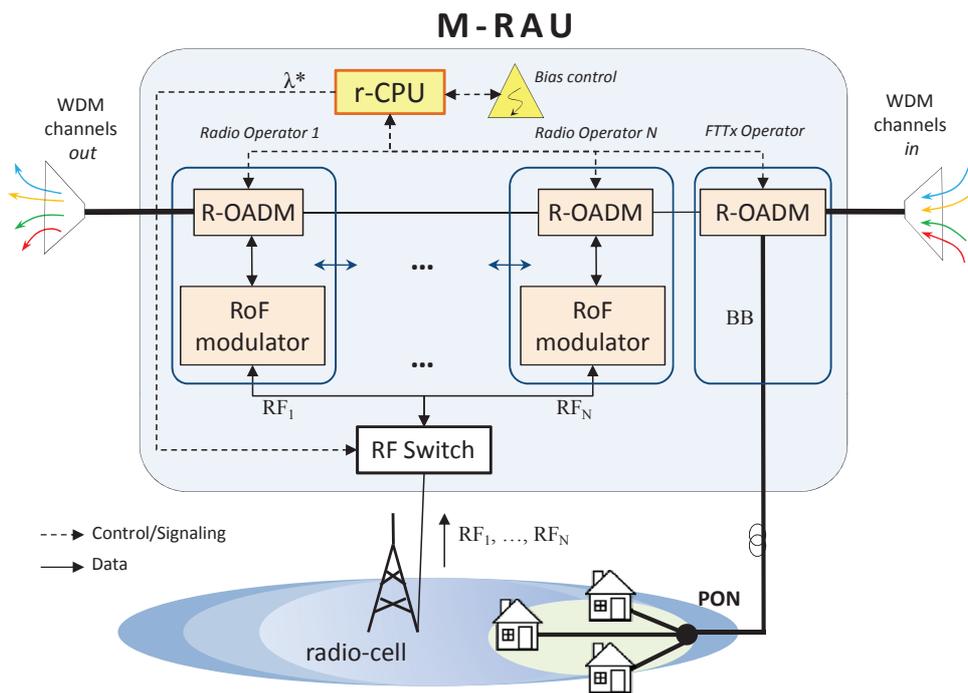
(a) M-RAU pour le trafic sens montant.
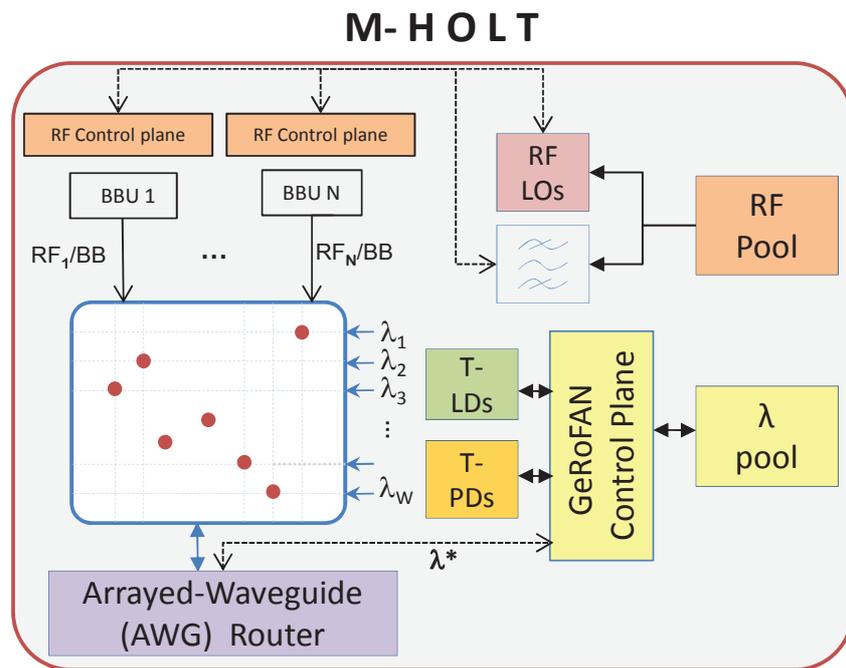
(b) M-HOLT

Figure 1.7: GeRoFAN pour une féderation multi-opérateur/multi-technologique.

Catégorie III (Cat. III) désigne les bruits due à la propagation par la fibre optique. Ces bruits sont distribués selon trois sous catégories: Cat. III-A pour le bruit de dispersion de mode de polarization (PMD) et le bruit RBS. Cat. III-B pour le bruit des effets
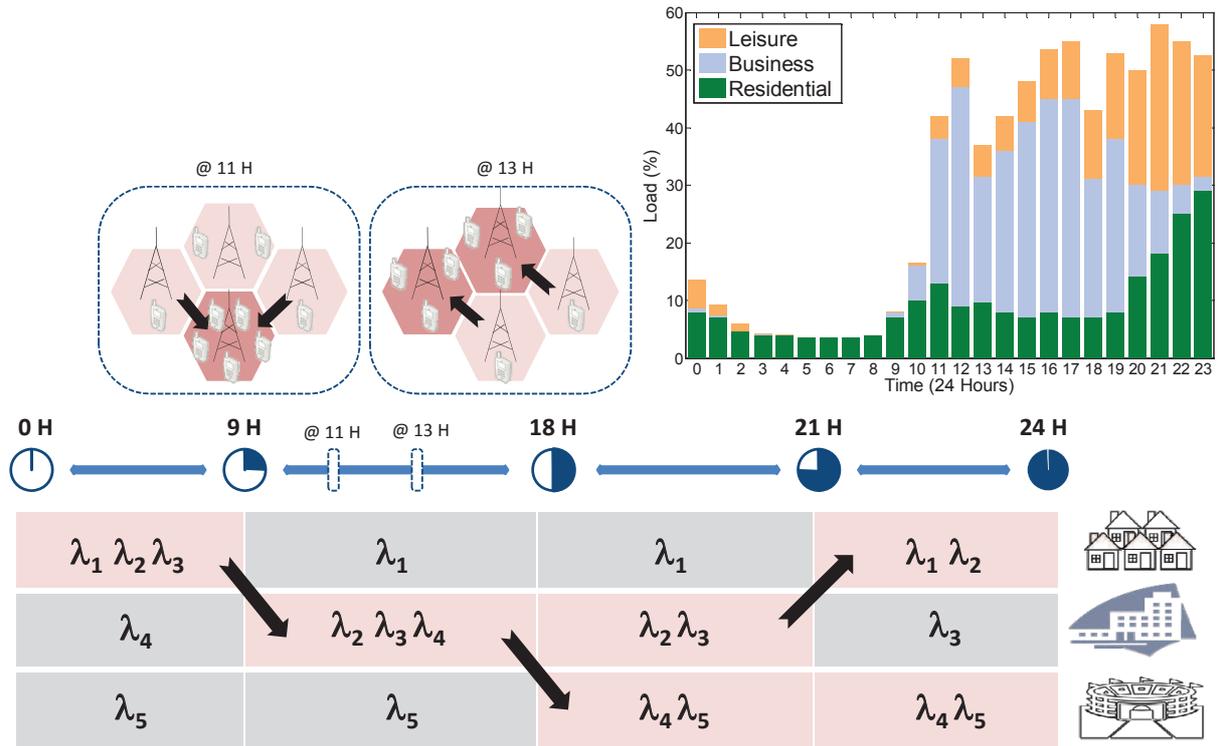
Figure 1.8: Gestion de la resource radio/optique à court et à moyen terme par le GeRoFAN-CP.

non-linéaires de la fibre due à la transmission WDM (WDM NLEs). Cat. III-C pour la dispersion chromatique (CD) de la fibre.

Catérogie IV (Cat. IV) Regrouppe tous les autres bruits du systeme GeRoFAN. Il s'agit essentiellement du bruit d'intéference (Crosstalk XT) entre canaux optiques dues aux imperfections du ROADM et des multiplexeurs WDM dans les AWGs, mais aussi les autres pénalités du systeme comme: la pénalité du splitter, le bruit des emissions spontannées des amplificateurs intégrés au modulateur RAM (ASE SOA), bruit des récepteurs et circulateurs etc. Dans la suite, nous détaillons analytiquement l'expression de chacun de ces bruits.

1.3.1   Catégorie I

La pénalité de modulation (MP) est calculée par la Figure de Bruit (NF) du modulateur qui dépend aussi du gain RF du lien RoF. Meme si le RAM réalise une fonction d'amplification du signal optique (par l'amplificateur SOA intégrée à l'EAM), l'efficacité de modulation dépend du SNR du signal radio modulant et du SNR de la porteuse optique modulée. La pénalité de modulation est explicitée selon l'équation ci-dessous:
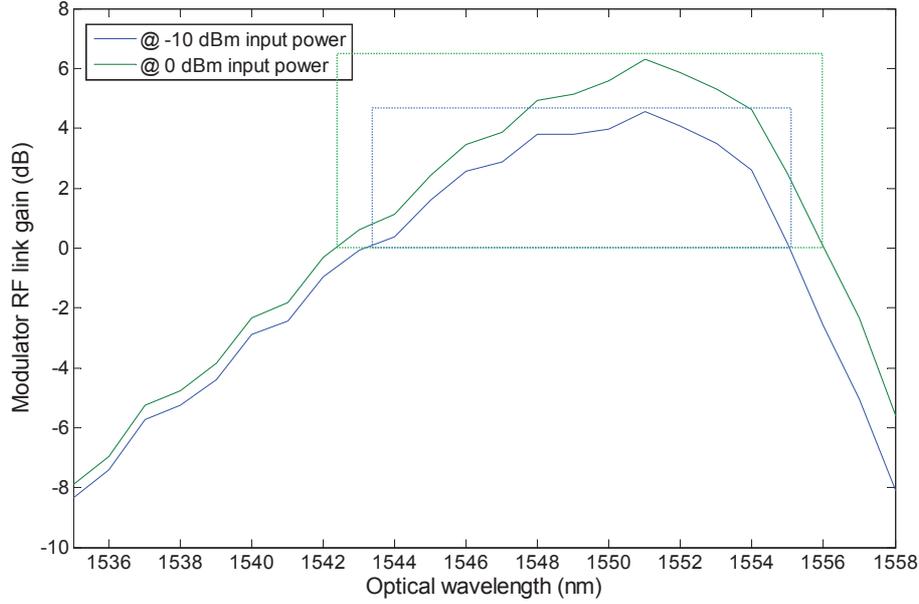
Figure 1.9: Gain RF de lu modulateur reflexif EAM en fonction de la longueur d'onde du canal optique.

$$NF = \frac{N_{out}}{k \cdot T^K \cdot B \cdot G} \tag{1.1}$$

Given: N_{out} Le bruit à la sortie du RAM, k La constante de Boltzmann, T^K la température ambiante du systeme en Kélvin and B la largeur de bande de bruit.

La figure 4.4 illustre l'évolution du gain G du lien RoF en fonction de la longueur d'onde du canal optique à 0 dBm et -10 dBm de puissance optique à l'entrée du modulateur.

1.3.2 Catégorie II

- IMD-RAM: Les intermodulations du modulateur sont dues à la non-linéarité intrinsèque de la fonction de transfert du modulateur electro-absorbant. On calcule l'amplitude des intermodulations causées par deux tones ou trois tones en faisant un développement en série de Taylor de la fonction de transfert f du RAM jusqu'à l'ordre 4, en effet les coefficients d'intermodulation deviennent negligeables au delà de cet ordre.

$$N_{2i\pm j} = \frac{3}{4} \cdot \frac{K_3}{3!} \cdot V_b^3 \cdot m_i^2 m_j \cdot P_o \tag{1.2a}$$

$$N_{i\pm j\mp k} = \frac{3}{2} \cdot \frac{K_3}{3!} \cdot V_b^3 \cdot m_i m_j m_k \cdot P_o \tag{1.2b}$$

Avec: m_i: l'indice de modulation optique (OMI) du canal radio i; V_b: Tension de bias de l'EAM; $K_3 = \frac{d^3 f}{dV^3}\big|_{V_b}$: 3rd Coefficient de 3eme ordre de la fonction de transfert f calculé à

la tension de bias et P_o: Puissance moyenne reçue par le modulateur RAM.

- IMD-OFDM: Due à la modulation OFDM des sous porteuses radio comme le stipule le standard LTE ou WiMAX, les canaux radio essuient des intermodulations dues aux battements entre les sous porteuses OFDM qui les composent. De ce fait, ces intermodulations dites IMD-OFDM sont calculées suivant l'équation ci-dessous:

$$I(\ell) = \frac{1}{6}d_{\ell-1}^2 + \frac{2}{3}d_\ell^2 + \frac{1}{6}d_{\ell+1}^2 \qquad (1.3)$$

Ayant: $d_i^2 = \frac{(P_o K_3 m_o^2 V_b^3)^2}{2} \cdot \mathcal{M}(N_{sc})$: L'amplitude du bruit relativement crée par les sous porteuses OFDM composant le canal radio i; m_o: OMI d'une seule sous porteuse OFDM; $\mathcal{M}(N_{sc})$: Nombre total des produits composites IMD3 produits par le battement des sous porteuses OFDM également espacées et au nombre de N_{sc} calculé selon: [101].

- OBI: Dans les arbres optiques ou architectures en étoile comme les réseaux optiques passifs PONs, les différents canaux optiques à la meme longueur d'onde et modulés par leurs sous proteuses se rejoignent au niveau de récepteur et sont couplés génerant des interférences entre les différents canaux. Ces intérferences appelées OBI se manifestent sous forme d'intermodulations touchant les sous porteuses de la meme manière que les autres formes d'intermodulation (IMD-RAM, IMD-OFDM).

1.3.3 Catégorie III

- RBS: Le bruit RBS est un bruit observé dans les architectures réseaux reflexifs où le signal montant et le signal descendant empreintent la meme fibre optique. Due aux micro-heterogeneités du verre de la fibre optique, une partie du signal est refléchi vers l'arrière du signal en fonction de sa propagation, ce signal refléchi interfére avec le signal utile circulant dans le meme sens diminuant le rapport signal à bruit SNR du signal utile. La pénalité RBS dépend de la longueur d'onde et croit avec la distance parcourue.

- PMD: La dispersion de mode de polarisation est due au décalage entre les deux champs de polarisation composant le signal optique au fur et à mésure de sa propagation. Ce décalage de la PMD induit un affaiblissement de l'amplitude de la sous porteuse une fois détectée par le récepteur et par la suite diminuant son SNR. Cette pénalité est décrite par l'équation ci-dessous:

$$\delta = \cos(\pi \cdot f \cdot \tau) \qquad (1.4)$$

Avec: $\tau = \beta_{pmd} \cdot \sqrt{L}$: Le délai différentiel de groupe dans la fibre; β_{pmd}: Le coefficient PMD de la fibre monomode calculé à la longueur d'onde du signal optique.

- CD: La dispersion chromatique est le phénemoène le plus connu dans un systeme WDM optique. Physiquement, il est du à la différence de délai de propagation entre les différents canaux optiques due à la différence de leurs vélocités respectives. Ce phénomène est plus accentué avec une modulation Double Bande Latérale (DSB) adoptée dans l'architecture GeRoFAN. La modulation DSB est assez courante dans les systemes de transmission à fréquences faibles ou modérées grace à sa simplicité et son faible cout d'implémentation. Cependant sur des grandes distances, les deux bandes du spectre du signal DSB ne parcourent pas la fibre avec la meme vélocité génerant un décalage entre les sous porteuses des deux bandes, ce décalage se manifeste par un affaiblissement d'amplitude et un déphasage pouvant induire l'extinction du signal au moment de la détection dans les cas extrèmes. La penalité de la dispersion chromatique CD est calculée en terme de EVM (error vector magnitude) qui mésure le décalage entre la position du symbole reçu par rapport à sa position supposée dans le cas d'une transmission idéale. La pénalité SNR due à la dispersion étant l'inverse du carrée de l'EVM, celui est exprimée par l'équation ci-dessous:

$$\langle EVM^2 \rangle \simeq \frac{1}{N_{sc}} \cdot \left[(N_{sc}+1) + \sum_{n=-N_{sc}/2}^{N_{sc}/2} \eta^2 \cos(\frac{\omega_n^2}{2} - \frac{\lambda^2 DL}{2\pi c})^2 - 2\eta \exp(\frac{-\sigma_\varphi^2}{2}) \sum_{n=-N_{sc}/2}^{N_{sc}/2} \cos(\frac{\omega_n^2}{2} - \frac{\lambda^2 DL}{2\pi c}) \right]$$
(1.5)

Avec: $\eta = |\frac{J_1(m)}{J_o(m)}|$: L'amplitude relative de la porteuse par rapport à ces deux bandes latérales dans le cas d'une modulation DSB; J_i: La fonction de Bessel d'ordre i; m: L'OMI total du signal multiplex transporté par la porteuse optique et exprimé en fonction des OMIs m_i des différents canaux radio; N_{sc}: Le nombre de sous porteuses OFDM par canal radio; ω_n: la fréquence angulaire de la n^{eme} sous porteuse OFDM et σ_φ: La puissance de bruit de phase moyenne d'un canal radio.

1.3.4 Catégorie IV

Cette catégorie inclut essentiellement les bruits d'intérférence WDM qui se manifestent dans les ROADMs et les multiplexeurs optiques dans les routeurs AWG au niveau du HOLT. Ces intérférences optiques peuvent etre soit entre canaux optiques de meme longueur d'onde (homodyne crosstalk) ou bien entre canaux optiques à des longueurs d'onde différentes (intérference héterodyne).

Dans cette catégorie, nous incluons aussi la pénalité due au splitter optique, les bruits du récepteur, le bruit des émissions spontannées de l'amplificateur intégré SOA au modulateur electro-absorbant.

Le tableau 4.5 identifie 7 paramètres dont dépendent les différents bruits decrits ci-haut. Ces paramètres constituent des leviers d'action pour le plan de controle pour pouvoir maitriser

Table 1.3: Les limitations de transmission physique de GeRoFAN.

	Bruit	W	$[\lambda]$	$\lambda_{i|1\cdots W}$	$N_{RF/\lambda}$	$[f]$	$f_{i|1\cdots F}$	L_{opt}
Cat.I	MP		•		•	•		•
Cat.II	IMD-RAM		•		•	•	•	
	IMD-OFDM		•		•	•	•	
	OBI		•		•	•	•	•
Cat.III	RBS		•		•			•
	CD		•		•	•		•
	PMD		•			•		•
	WDM NLEs	•	•	•	•			•
Cat.IV	ROADM/AWG XT	•		•	•	•		
	SOA ASE		•					•
	Penalité du splitter				•			

la magnitude des bruits correspondants et maximiser par la suite la capacité de Shannon dans la cellule. Ces paramètres incluent:

- **Le canal optique:** Representé par la valeur de la longueur d'onde du canal $[\lambda]$ et le rang du canal au milieu du multiplex WDM se propageant dans la fibre $\lambda_{i|1\cdots W}$.

- W**:** Le nombre total des canaux optiques dans la fibre.

- $N_{RF/\lambda}$**:** Le nombre de canaux radio RF par canal optique.

- **La sous porteuse radio** f**:** Représentée par la valeur de sa fréquence radio $[f]$ et le rang relatif de la sous porteuse dans le multiplex SCM transporté par la meme porteuse optique $f_{i|1\cdots F}$.

- L_{opt}**:** La longueur du lien optique reliant la RAU et la HOLT supposée constante une fois le déploiement est réalisé.

Ces différents bruits intéragissent ensemble pour décider de la pénalité finale au niveau de chaque canal radio. L'intéraction des différents bruits varie d'une architecture à une autre en fonction de la topologie du réseau. Nous considérons deux topologies possibles pour GeRoFAN: une boule optique ou un arbre à l'image des PONs. Certains bruits vont etre associés exlusivement à l'architecture en boucle alors que d'autres bruits sont associés uniquement à la topologie en arbre (comme la pénalité du splitter). Nous illustrons à travers les deux Figures 4.13 et
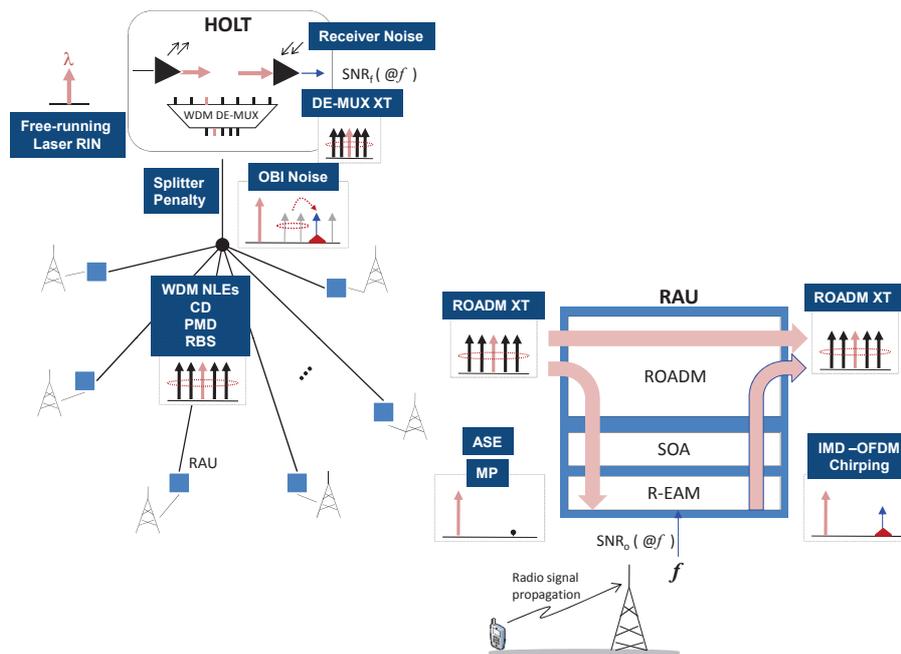
Figure 1.11: Illustration des différents bruits dans le cas d'une architecture GeRoFAN en arbre.

4.14, comment les différents bruits décrits ci-haut intéragissent dans le cas d'une architecture en boucle et une architecture en arbre.
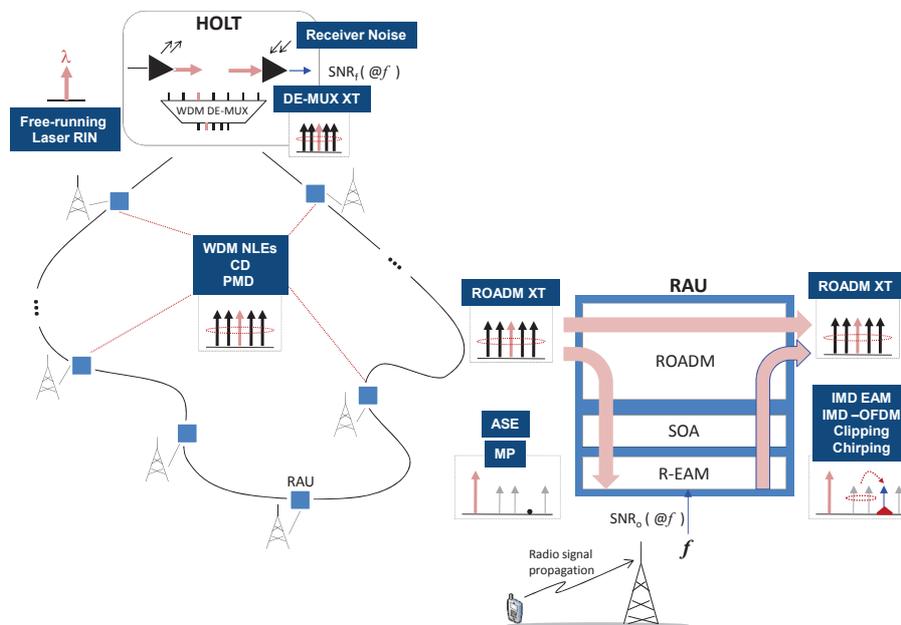
Figure 1.10: Illustration des différents bruits dans le cas d'une architecture GeRoFAN en boucle.

1.4   Conception du plan de controle pour GeRoFAN

La stratégie optimisée pour le transport des canaux radio fréquence RF par la RoF analogique peut etre formulée comme un problème d'optimisation résolu par une méta-heuristic multi-objectifs, appelée PaGeO (Pareto-based Genetic Optimization).

PaGeO est un algorithme d'optimisation multi-objectif utilisant le concept d'algorithme genetique et l'optimisation par l'approche Pareto. En alliant ces deux concepts, PaGeO tire avantage de la robustesse des algorithmes genetiques et le compromis réalisé par le front de Pareto.

1.4.1   l'algorithme PaGeO

Le schema algorithmique de PaGeO et ses paramètres sont fournis dans la Figure 5.9 et le tableau 5.3. Nous décrivons dans la suite les principales étaps consitutant l'algorithme.

La première étape consiste à classifier les individus d'une population (chromosomes) en deux groupes: chromosomes faisables et chromosomes non-faisables. Des chromosomes sont non-faisables quand certaines contraintes sont violées notamment: le nombre maximum de RFs que peut transporter une porteuse optique, altérer la planification cellulaire, duplication de la meme fréquence associé à la meme cellule ...

Certains chromosomes seront corrigés afin que le nombre des individus faisables soit largement supérieur aux chromosomes non-faisables. Les deux groupes de chromosomes suivent ensuite deux processus en parellèle. Pour les chromosomes faisables on evalue leur fonction objectif en utilisant l'outil QoT (QoT-tool). La fonction objectif est un vecteur de taux de rejet dans chaque cellule ainsi que le nombre de canaux optiques OC utilisés. Les différents chromsomes faisables sont classés en front de dominance F_i, le premier front étant le front de Pareto est utilisé pour vérifier si les critères de convergence de l'algorithme sont atteintes. Ces critères incluent le nombre maximum de génerations atteints ou la deviation δ entre la fonction objectif atteinte et une représentation de la fonction idéale comme indiqué dans l'Equation 5.24. Si les critères d'arret ne sont pas encore atteintes, un partage de la "fitness" réprésente la qualité de la solution en utilisant la distance Euclidienne est exploité. Parallèlement, les chromosomes non-faisables sont aussi classés par analogie en fronts infaisables de dominance.

$$\delta = min_{x \in \mathcal{B}} \frac{|f(x) - f^\star|}{|f^\star|} \tag{1.6}$$

La population de la nouvelle géneration est construite en utilisant des procédés d'évolution des algorithmes génetiques. L'élitisme consiste à sélectionner une proportion des meilleurs chromosomes pour intégrer la nouvelle population. Des techniques d'évolution permettent de produire la descendance constituant la nouvelle géneration à partir de la géneration précedente, notamment: le reproduction entre chromosomes (cross-over), et la mutation génetique

Table 1.4: Paramètres d'initialisation de PaGeO

Taille de la population ($\wp$)	100
Selection des parents	Strategie de tourniquet [78]
Taille du pool des parents ($\mathcal{M}$)	50% of $\wp$
Taux de mutation p_m	0.001 [78]
Taux de combinaison (reproduction) p_X	0.6 [78]
Proportion des immigrants ($\Im$)	25% of $\wp$
Proportion des élites (ξ)	5% of $\wp$
Nombre maximum de géneration	1000
(Classification Euclidenne) $nc_E(x)$	$\displaystyle\sum_{\substack{y \in P \\ r(y)=r(x)}} max\left\{\frac{\sigma_{sh} - d_E(x,y)}{\sigma_{sh}}, 0\right\}$ [23]
(Classification de Hamming) $nc_H(x)$	$\displaystyle\sum_{\substack{y \in \overline{P} \\ r(y)=r(x)}} max\left\{1 - \frac{d_H(x,y)}{\overline{\sigma_{sh}}}, 0\right\}$
Distance Euclidenne $d_E(x,y)$	$\displaystyle\sqrt{\sum_{i=1}^{|\Psi|+1} \left(\frac{f_i(x)-f_i(y)}{f_i^{max}-f_i^{min}}\right)^2}$ [23]
Distance de Hamming $d_H(x,y)$	$\displaystyle\sqrt{\sum_{i=1}^{|\Psi|}\sum_{j=1}^{|\Lambda|}\sum_{k=1}^{|F|} \left(x_{i,j,k} - y_{i,j,k}\right)^2}$
Rayon de la niche σ_{sh}	≈ 0.44 [78]
Rayon de la niche $\overline{\sigma_{sh}}$	2
Seuil de déviation $\delta^\star$	1%

des chromosomes (mutation) en changeant aléatoirement la représentation matricielle des chromosomes. La population est enrichie par des individus complétement étrangers au processus ci-dessus, ce procédé s'appelle enrichissement par immigration avec une proportion spécifiée dans les paramètres de l'algorithme.

Enfin la population est complétée par une sélection aléatoire de la population de la géneration précedente. Une fois la nouvelle géneration formée, on reprend le meme processus de façon itérative.

La Figure 5.10 représente une illustation des étapes clefs composant l'algorithme PaGeO.

1.4.2 Stratégies alternatives de transport des RFs

Afin d'évaluer les performances de PaGeO, nous comparons notre algorithme par rapport à d'autres politiques de transport de RFs sur les OCs par la RoF analogique. Quatres politiques sont retenues:

- FCA: le canal radio est placé sur le premier canal optique pouvant l'accueillir.

- RCA: le canal radio est placé sur un canal optique pouvant l'accueillir aléatoirement.

- FFCA: Le canal radio est placé sur le premier canal optique pouvant l'accueillir moyennant un taux de rejet inférieur à un seuil fixé. Si aucun canal optique ne respecte le seuil en

(1) Ranking & Fitness sharing

Classify the $\wp$ individuals of (**P$_o$**) into feasible (**P**) and infeasible ($\overline{\textbf{P}}$) individuals

Correct infeasible individuals such that $|\textbf{P}| > \textbf{4}|\overline{\overline{\textbf{P}}}|$

infeasible   *feasible*

(1.b)   **(1.a)**

Evaluate infeasibility measure   Evaluate objective value ←→ *QoT-tool*

unfeasible fronts $\overline{\textbf{F}i}$ feasible fronts **Fi**

Dominance-based ranking   Dominance-based ranking

Fitness sharing (Hamming distance)

Select $\mathcal{F}$: the Pareto set of **P**

$\mathcal{B}$: the Pareto set of ($\mathcal{F} \cup \mathcal{B}$)

Stopping criteria reached **?**

No   *Yes*

Exit

Fitness sharing (Euclidian distance)

P$_o$ ← Q

(2) The new population for the next generation

Elitism: Select ξ elits (i.e., with the best fitness)

Selecting the mating pool ($\mathcal{M}$) via binary tournament procedure

Offspring generation (**Q**) via cross-over operation

Mutation of **Q**

Random Immigrants ($\mathcal{I}$)

$\textbf{Q} \leftarrow \textbf{Q} \cup \xi \cup \mathcal{I}$

Complete **Q** with the remaining individuals randomly from $\textbf{P}_o \backslash \{\mathcal{M} \cup \xi\}$

Figure 1.12: Etapes de l'algorithme PaGeO.
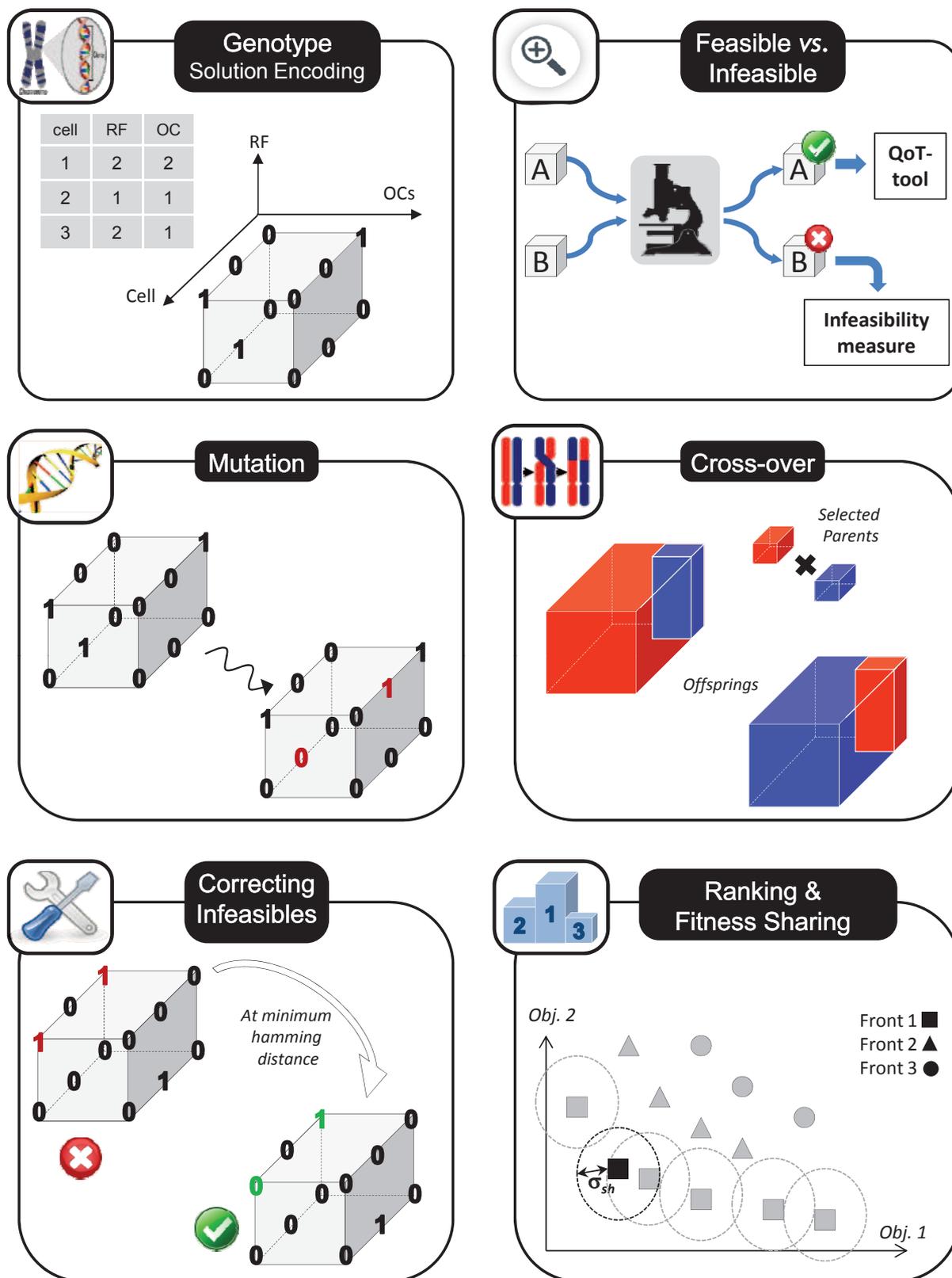
Figure 1.13: Illustration des étapes clefs de PaGeO.

Algorithm 1: Pseudo-code de l'algorithme FFCA.

    input : $\mathcal{N}$: Set of radio-cells. W: OCs Pool.

    output: $\Lambda^{\star}$: Selected OCs for backhauling. $(\rho_n)_{n=1..N}$: Rejection ratio at each cell.

    // Routine initialization ...

1 $\rho_{max} \leftarrow 0\%$;

2 $\Lambda^{\star} \leftarrow \emptyset$;

3 $n \leftarrow 1$;

4 **while** $n \leq \mathcal{N}$ **do**

5 $\Omega \leftarrow$ Set of candidate OCs from W able to carry the RFs of cell n;

6   Select *the first listed* OC $\lambda^{\star} \in \Omega$ such that: $\forall i = 1..n, \rho_i \leq \rho_{max}$;

7   **if** $\lambda^{\star} \neq \emptyset$ **then**   // OC $\lambda^{\star}$ is selected to backhaul RFs of cell n

8 $n \leftarrow n + 1$;

9 $\Lambda^{\star} \leftarrow \lambda^{\star}$;

10   **else**   // OC $\lambda^{\star}$ does not exist

11 $n \leftarrow 1$;

12 $\Lambda^{\star} \leftarrow \emptyset$;

13 $\rho_{max} = \rho_{max} + 0.1\%$;   // Relaxing the constraint on ρ_{max}

14   **end**

15 **end**

---

question, ce dernier est augmenté afin de relaxer les contraintes sur le placement et le processus est réitéré de nouveau. Le pseudo code de l'algorithme FFCA est fourni ci-dessus.

- IM-free CA: Le placement des RFs sur les OCs est réalisé d'une manière à éviter complètement les bruits d'intermodulation IMD3. Le choix du placement, bien que requérant beaucoup de canaux optiques, est fait selon la regle de Golomb qui assure une assignation ne génerant aucune combinaison d'intermodulation.

1.5 Performance numérique

Nous conduisons une série de simulations nuémriques afin d'évaluer la performance de PaGeO. Le scénario consiste à déployer GeRoFAN pour la féderation d'une vingtaine de cellules de type LTE. Les paramètres du systeme radio utilisé sont résumés dans le tableau 5.1.

1.5.1 Quelle topologie pour GeRoFAN: boucle ou arbre ?

La figure 5.12 montre le taux de rejet par cellule ainsi que le nombre de porteuses optiques OC requises pour le transport des canaux radio. Les résultats sont évalués à différentes charges de trafic par cellule. Les résultats numériques indiquent la supériorité des l'architecture GeRoFAN

Table 1.5: Radio parameters of the simulation.

Fréquence centrale des canaux radios	2.5 GHz
Largeur de bande du canal radio [133]	5 MHz
Puissance radio transmise	+10 dBm
Distance inter-RAU	$\sqrt{3} \cdot 500 \ m$
Position de l'utilisateur mobile	@250 m
Exposant d'affaiblissement	3.65
(Distribution log.) Variance de l'effet de masque	3 dB
Affaiblissement du à la propagation libre	25.5 dB
Gain RF de l'antenne isotropique	15 dBi
Gain RF de l'amplificateur LNA	15 dB
Figure de bruit du LNA	5 dB
Puissance de bruit par sous porteuse OFDM	−140 dBm

en arbre sur la topologie en boucle. En termes de taux de rejet, l'architecture arbre atteint un gain de l'ordre de 25% à forte charge de trafic et jusqu'à 90% de gain à charge modéré. Des gains significatifs en terme de OCs sont aussi reportés jusqu'à 57% avec la borne inférieure (3 OCs) atteinte à charge modérée. En effet, le bruit cumulatif dans la boucle penalise le rapport signal à bruit SNR induisant une perte de la capacité radio du système. Afin de combattre l'impact des intermodulations IMD et les intérférences optiques, une topologie optique en boucle utilise plus de porteuses optiques OCs que l'architecture en arbre.

Due à l'accumulation des bruits le long de la boucle optique, on note à travers la figure 5.13, une augmentation significative de la part de la pénalité de modulation MP et les IMDs dans le profil de pénalité totale pour une boucle plutot qu'un arbre. Par ailleurs, on peut noter l'abaissement de la part des bruits de la 4eme catégorie (Cat.IV) (16% pour l'arbre et 11% pour la boucle) alors qu'un splitter n'est requis pour une architecture en boucle, en outre, on note la contribution marginale ($< 1\%$) des bruits de Cat.III-A (PMD et RBS) pour une boucle optique due à l'absence du RBS dans le calcul des bruits de transmission.

1.5.2 PaGeO *vs.* les stratégies alternatives

En démontrant la supériorité de la topologie arbre sur la boucle optique, nous considérons par la suite uniquement le cas d'une architecture arbre pour le déploiement de GeRoFAN. Nous comparons les performances de notre algorithme PaGeO avec les stratégies alternatives de transport RFs FCA, RCA, FFCA et IM-free CA en termes de taux de rejet et de capacité optique requise pour assurer le transport. Les résultats de cette comparaison sont illustrés dans la figure 5.15.
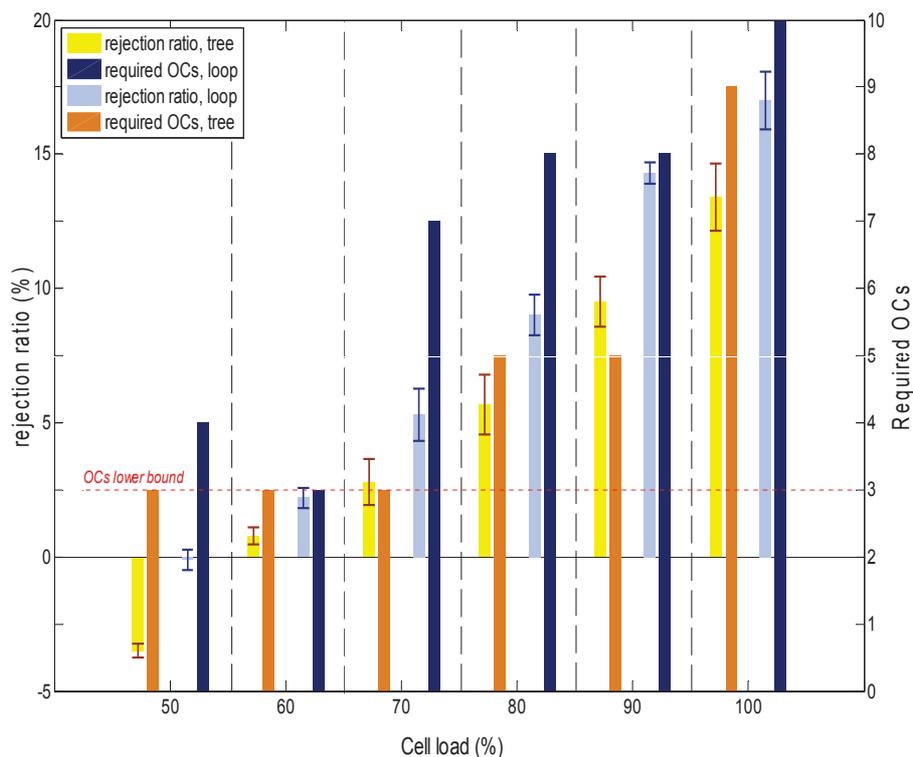
Figure 1.14: Comparaison entre l'architecture en boucle et celle en arbre pour GeRoFAN en terme de taux de rejet (axe à gauche) et de nombre de porteuses optiques requises (axe à droite). Les valeurs négative de taux de rejet indiquent un excès de capacité par rapport à la charge de trafic. Les valeurs de taux de rejet indiquées sont des des moyennes, les STD bars donnent la variance entre les différentes cellules.
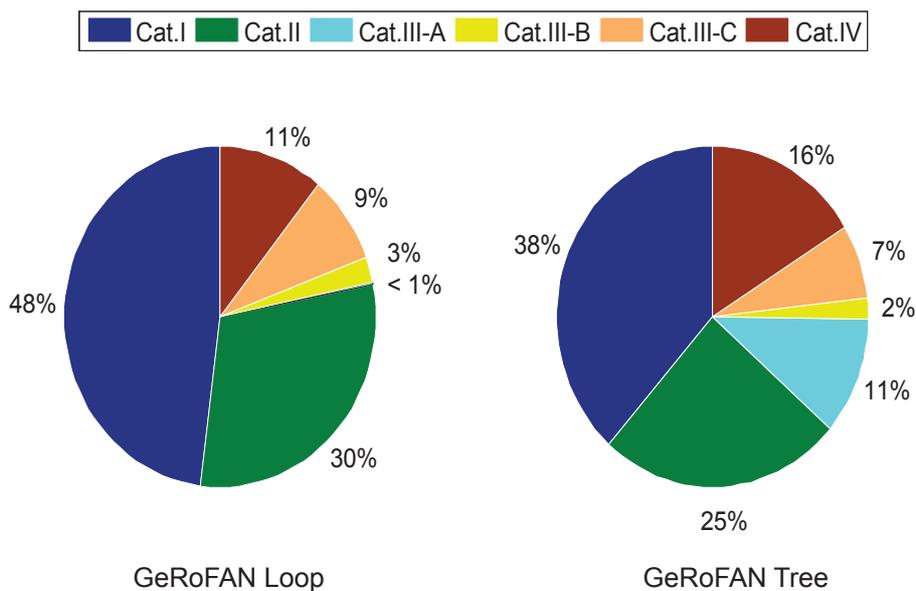
Figure 1.15: "Profiling" de la QoT: Part de chaque catégorie de bruit dans la penalité globale.
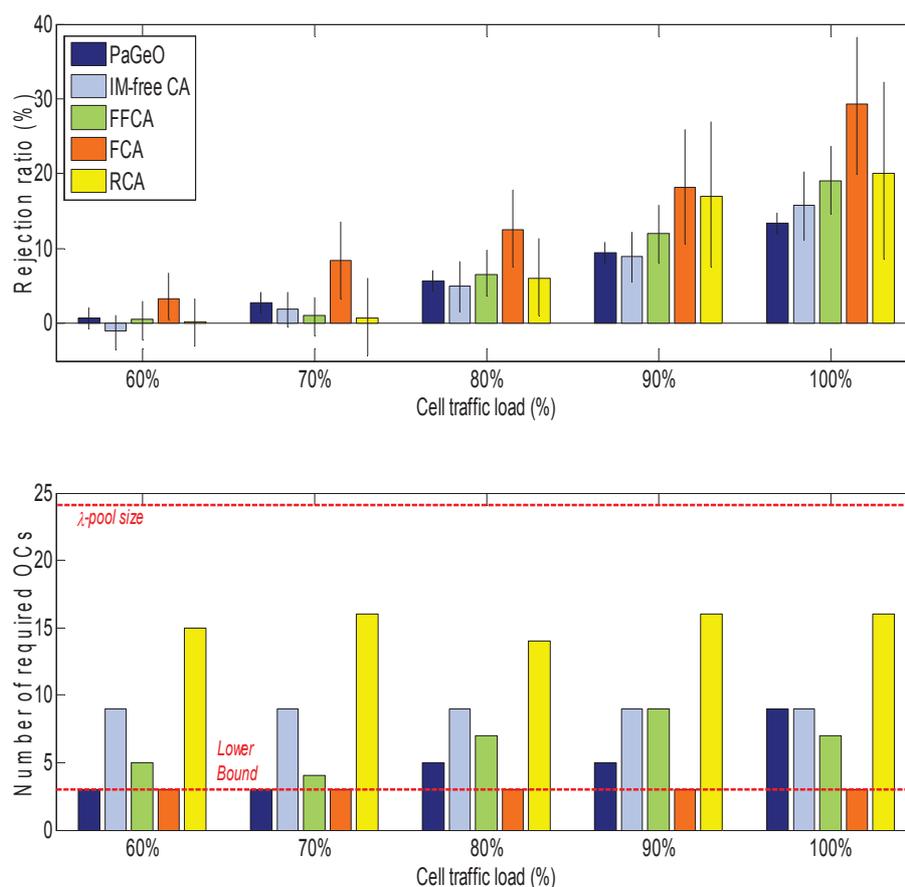
Figure 1.16: PaGeO vs. les stratégies de transport alternatives (RCA, FCA, FFCA et IM-free CA) en terme de taux de rejet et de nombre de porteuses optiques requises.

En adossant les canaux radio sur le premier canal optique disponible, la politique FCA atteint nécessairement le nombre minimum de porteuses optiques par contre cette politique est réalisée au détriment du taux de rejet dans les cellules. Bien que QoT-agnostique, la politique RCA combat les contraintes de transmission RoF due à la sélection aléatoire des canaux optiques, cependant ceci est réalisé au prix d'un nombre de porteuses optiques assez élevé (70% de l'ensemble du pool optique). FFCA peut etre considéré comme la version QoT-intégré du FCA, FFCA consomme 3 OCs de plus en moyenne par rapport à FCA mais atteint des taux de rejet plus faibles que FCA (en moyenne 85% plus faible). Les résultats montrent que on aura besoin de 7 OCs en plus que la borne inférieure pour implémenter la politique IM-free CA. Cette dernière annule les intermodulations et réduit ainsi le taux de rejet dans les cellules. Cependant, le taux de rejet résiduel pour la politique IM-free CA spécialement à forte charge montre qu'en consommant beaucoup de OCs pour annuler les intermodulations n'arrange pas l'impact d'autres bruits (WDM-NLEs, OADM XT...) dont la pénalité augmente avec le nombre de porteuses optiques utilisées.

Enfin pour notre algorithme, PaGeO atteint un compromis excellent par rapport aux autres politiques de transport entre les deux objectifs: le taux de rejet cellulaire et le nombre de porteuses optiques requises. En effet, PaGeO consomme en moyenne 2 OCs moins que FFCA, tout en atteignant à deux reprises la borne inférieure at charge modérée. Par ailleurs, les taux de rejet atteints par PaGeO sont assez proches de l'algorithme IM-free CA. En effet, les taux de rejet de l'IM-free CA montrent qu'en se focalisant exclusivement sur les intermodulations IMDs ne réussit pas seul à diminuer substentiellement les taux de rejet dans les cellules, car de ce fait la politique IM-free CA ignore les autres bruits qui peuvent se manifester surtout quand un nombre élevé de OCs est utilisé. Ceci donc premeut plutot une politique de gestion globale des contraintes de la qualité de transmission RoF plutot qu'une focalisation ciblée sur un seul bruit plutot qu'un autre.

Enfin, grace à son optimisation multi-objectifs resolu via le front de Pareto, l'algorithme PaGeO atteint uniformément ses résultats de taux de rejet entre les différentes cellules mieux que les autres politiques. Ceci peut etre remarqué grace à la longueur des STD bars représentant la variance des résultats de taux de rejet entre les cellules.

1.6 Conclusion

La montée en débit inhérente à l'utilisation des nouveaux terminaux mobiles (smart-phones) pose le problème de la capacité inadaptée des réseaux d'accès radio (RAN) actuels. La téléphonie mobile de 4ème génération (LTE, LTE-advanced) va nécessiter de fait une forte densification des antennes. Dans ce contexte, l'architecture actuelle des réseaux d'accès radio présente plusieurs défauts. Elle est très hiérarchique. Elle n'exploite pas la souplesse du multiplexage statistique. Elle ignore les fonctions de protection et de restauration. Elle n'est pas économiquement adaptable à l'échelle à une densification des stations de base.

Nous avons proposé dans cette thèse une nouvelle architecture appelée GeRoFAN de réseaux d'accès radio basée sur l'exploitation de réseaux tout-optiques WDM permettant de desservir des stations de base pouvant être exploitées par différents opérateurs et reposer sur des technologies distinctes. L'originalité de l'approche proposée consiste en la possibilité d'allouer dynamiquement de la ressource radio-fréquence, et donc de la bande passante, au prorata de la charge de trafic dans des zones géographiques d'activités différentes. Nous exploitons pour cela les potentialités de la radio-sur fibre (RoF) analogique et de la modulation par sous-porteuse (SCM). Nous avons introduit les concepts de HOLT (Hybrid Optial Line Termination) et de RAU (Radio Access Unit). Pour chaque sous réseau optique, une HOLT est située à la tête du réseau dans les locaux de l'organisme censé gérer dynamiquement l'allocation des ressources radio (typiquement une collectivité locale). Les RAUs sont quant à elles réparties le long de chaque sous réseau optique. Typiquement, les têtes de réseau HOLT sont situées au niveau des

actuels commutateur d'accès. Une seule station de base appartenant à un unique opérateur est connectée à chaque RAU. Par contre, les stations de base raccordées sur les différentes RAUs d'une même boucle peuvent être opérées par différents opérateurs radio-mobiles. En d'autres termes, les HOLTs et les infrastructures optiques sont mutualisées entre différents opérateurs exploitant éventuellement des réseaux radio-mobile de type différents (GSM, WiMAX, LTE, LTE-advanced etc.). Nous avons proposé en outre la conception d'un plan contrôle permettant grâce à l'utilisation d'un canal de signalisation, de faire glisser des ressources radio-fréquence d'une station de base vers une autre, au gré de la dynamique spatio-temporelle du trafic. Ce plan de controle opère une stratégie de transport des canaux radio par les porteuses optiques permettant de minimiser les taux de rejet dans chaque cellule tout en consommant moins de porteuses optiques que possible. Cette politique optimisée de transport est le fruit d'une stratégie dérivée par un algorithme génetique basé sur l'optimisation par front de Pareto, appelée PaGeO. Contrairement aux autres politiques de transport qu'elles intégrent ou ignorent les contraintes de la qualité de transmission de la RoF analogique, PaGeO assure un excellent compromis entre l'optimisation de la capacité radio par cellule et la capacité optique requise pour implémenter la stratégie de transport.

Notre approche est en cohérence avec les concepts de CRAN (Collaborative RAN) et de Cloud RAN tels qu'ils ont été présentés par des équipementiers et les organismes de standarisation. Ces concepts visent tous à favoriser une gestion agnostique du spectre radio. Ils préconisent tous l'utilisation de la technique RoF pour mutualiser à la tête du réseau les équipements de traitement du signal radio.

General Introduction

Contents

2.1 Motivation, Objectives and Thesis Outline

T_{HE} rapid growth of the smart-phones market is at the origin of a strong increase in the traffic within radio-mobile access systems. Deploying smaller radio cells and/or operating at higher radio frequencies (greater than 5 GHz) are envisioned to fulfill the increasing need of capacity per unit area. This advocates for a higher densification of radio cells. Existing Radio Access Network (RAN) architectures are not economically suited to cope with such an evolution. In fact, while an unprecedent technological improvement has been made in the radio section and the core section of the mobile network, the cellular backhaul is left as the weak part threatening the efficiency of the overall system. More generally, the metro-access area is considered as the most costly part of public networks because of its low level of mutualization. Today, the biggest cost challenge facing wireless service providers is the backhaul network– the part of the network ranging from the base station to the radio network controller. Current backhaul infrastructure relies mainly on narrow-band Time Division Multiplexing (TDM) systems consisting in leased copper lines or point-to-point/point-to-multi-point microwave links. As a result, the deployed network architecture is not optimized to handle the increasing traffic volumes propelled by packet voice and bandwidth hungry packet data services. Since the last decade, many mobile operator executives have approved a raising of nearly 15% to 20% in the annual expenditures [38] dedicated to the backhaul in order to get enough capacity to their cell sites for a high-quality *3G+* and very soon *4G* end-user experience. At the mean time, the flat-pricing model adopted by the mainstream of mobile carriers coupled with an inefficient strategy for the backhaul consisting in simply leasing additional TDM lines as the capacity grows have generated a gap
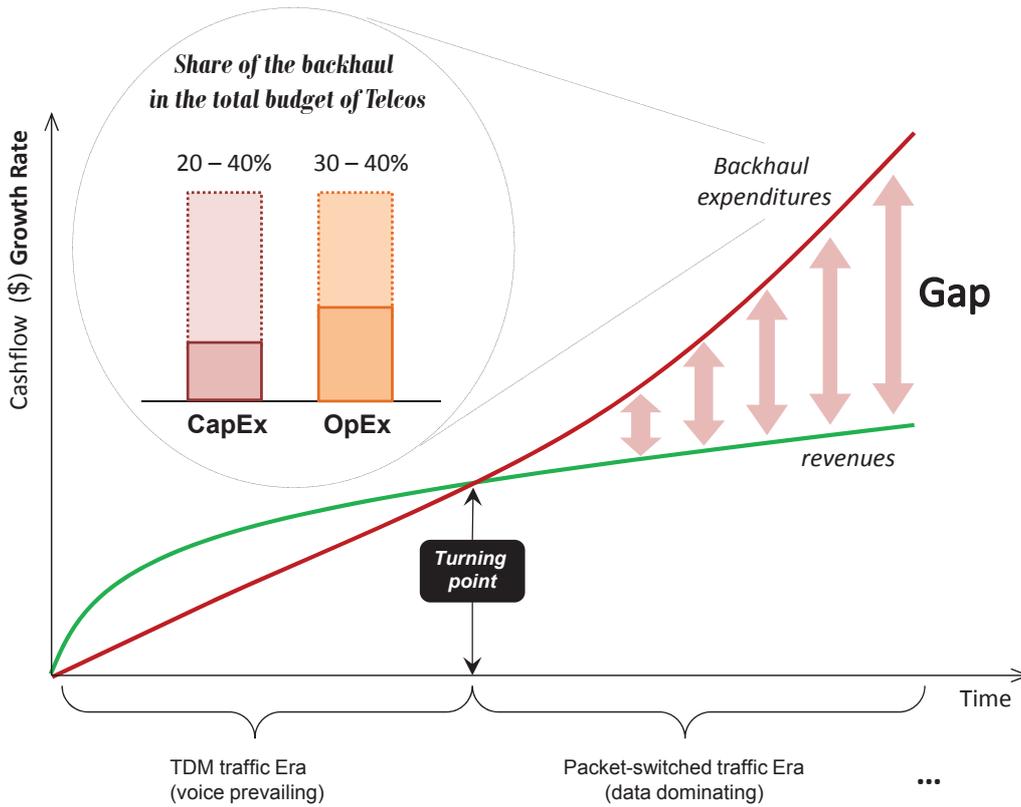
Figure 2.1: The current challenge of mobile carriers: Revenues growth rate flatting while expenditures growth rate are taking off propelled by the traffic increase. How carriers can bridge the gap and reverse the trend ?

in the operating margin of the mobile operator which increases with the traffic growth as shown in Figure 2.1.

Considering the heavy weight of backhaul expenditures on mobile carriers total budget[1], it is necessary to rethink current mobile backhauling towards alternative solutions offering a sustainable high capacity. Fiber optics with its "unlimited" bandwidth and the advances in opto-electonic/photonic devices are well positioned to contribute in shaping the new cellular backhaul. To make full benefit of the huge bandwidth and connectivity offered by optical networks and the mobile features provided by next generation wireless systems, the integration of wireless and optics by means of Radio-over-Fiber (RoF) technology is an attractive solution for decreasing the costs and clearing the path for fixed/mobile infrastructure convergence.

The objective of this thesis is to propose an innovative all-optical network infrastructure called GeRoFAN (Generic Radio-over-Fiber Access Network) and to investigate its potentialities. The GeRoFAN architecture aims to backhaul *4G* radio access systems (based either on *WiMAX* or *LTE*) by means of analog RoF. Situated at mid-range between optics and wireless,

---

[1]According to IDATE [118], mobile operators spend $20 - 40\%$ of their annual CapEx and $30 - 40\%$ of their annual OpEx on cellular backhauling.

the main research question in the thesis revolves around the technical and economic require-
ments that have to be addressed to make the GeRoFAN architecture an enabler for a harmonious
wireless-optics integration.

The research conducted in this thesis is structured into four main parts:

- Chapter **2** carries out a comprehensive state of the art on the evolution of the cellular
  backhauling and its main future trends. In this chapter, we position the GeRoFAN archi-
  tecture within the backhaul solutions constellation and we highlight its main innovative
  features.

- The second part of the research is provided by Chapter **3** which focuses on physical layer
  impairments modeling of analog RoF transmission. The outcome of this work constitutes
  a valuable input for an optimized exploitation of the GeRoFAN system.

- The third part of the research is focused on how the GeRoFAN system intelligence (its
  Control Plane) should be designed to achieve an efficient cellular backhauling. More
  algorithmic oriented, the third part of the thesis considers successively a static (Chapter
  4) and a dynamic traffic context (Chapter **5**).

- The last part of the research addresses the economics of the GeRoFAN paradigm and
  investigates its business relevance (its added value) through different economic models.

The diagram in Figure 2.2 represents how the different parts of the research are linked
together.

2.2   Contributions and Statement of Originality

The contributions highlighted by this doctoral research are multi-fold and can be itemized as
the following:

- A RoF-based all-optical network architecture (GeRoFAN) is proposed for cellular back-
  hauling and the mutualization of next generation radio systems. The originality of GeRo-
  FAN is to make use of advanced amplified reflective optical modulators, optical WDM
  technologies combined with analog RoF to achieve an elegant integration between optics
  and wireless within a unified network infrastructure. At the network design stage, a major
  innovation is pointed out by the GeRoFAN solution: its radio MAC-agnostic and analog
  RoF impairment-aware control plane (*c.f* Part I) .

- Thus, unlike the mainstream literature which points out the limitations of analog RoF,
  this research offers the opportunity to capitalize on the benefits of analog RoF while
  mitigating its Quality-of-Transmission (QoT) limitations; the ultimate aim being to show
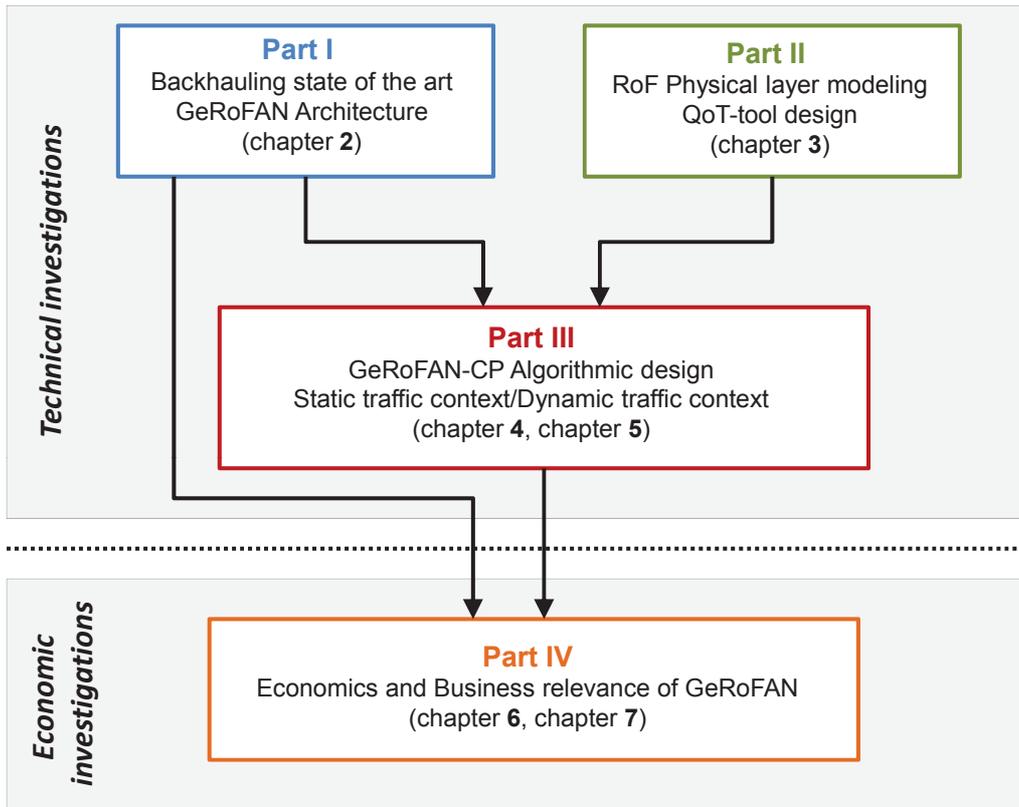
Figure 2.2: The four main work-packages structuring the thesis.

that analog RoF is still an attractive solution to backhaul next generation cellular systems. At this stage, the main originality of our study consists in providing a deep knowledge of all physical layer impairments involved in the GeRoFAN network. A comprehensive analytical modeling of RoF transmission limitations is realized as an essential step to make the cellular backhauling by GeRoFAN as transparent as possible to the radio system (*c.f* Part II).

- The optimization models designed to achieve such a QoT-aware cellular backhauling by the GeRoFAN-CP constitute the third main originality of this PhD thesis (*c.f* Part III). Indeed, a wide range of optimization approaches (exact methods through integer linear programming, evolutionary algorithms, multi-objective Pareto optimization, greedy algorithms, iterative tabu-search meta-heuristics) are exploited to best-fit the GeRoFAN-CP requirements. In particular, we show how the GeRoFAN-CP, supported by the knowledge of the physical layer impairments along with an adapted optimization tool, achieves an adjusted fine-grained management of the radio system capacity. Such a matching between the cellular system and GeRoFAN interests gives rise to what is commonly called *backhaul service provisioning*.

- The economic assessment of the GeRoFAN architecture and the business value of its cellular backhaul service constitute the fourth main contribution of the research (*c.f* part IV). The key originality highlighted at this stage is to show how the value chain orchestrating the cellular backhauling business market could be enriched by the GeRoFAN solution without shadowing the challenges raised by such a new assumed commercial and regulatory context.

2.3 Publications

This dissertation consists of an overview and of the following conference and journal publications:

- "Impairment-aware Control Plane for Next Generation Radio-over-Fiber Access Networks", <u>A. Haddad</u>, M. Gagnaire and E.A. Doumith, in *IEEE/Proc. of the 2nd Int. Conf. Network of the Future*, Nov. 2011, Paris.

- "Impairment-aware Radio-over-Fiber Control Plane for LTE Antenna Backhauling", <u>A. Haddad</u>, E.A. Doumith and M. Gagnaire, in *IEEE/ Proc. of Int. Conf. on Communications (ICC)*, June 2012, Ottawa.

- "Next Generation Access Systems Backhauling using Radio-over-Fiber: a Prospective Approach", <u>A. Haddad</u> and M. Gagnaire, in *IEEE/Proc. of Summer Topicals*, July 2012, Seattle, WA.

- "Pareto Optimization for Radio-over-Fiber 4G Base Stations Backhauling", <u>A. Haddad</u> and M. Gagnaire, in *Proc. of the 15th Int. Telecommunications Network Strategy and Planning Symposium (Networks'12)*, Oct. 2012, Rome.

- "PaGeO: Pareto-based Genetic Optimization for LTE Radio-over-Fiber Cellular Backhauling", <u>A. Haddad</u> and M. Gagnaire, in *IEEE/Proc. of the 8th Int. Conf. on Wireless and Mobile Computing, Networking and Communications (WiMob'12)*, Oct. 2012, Barcelona.

- "Differentiated Radio-over-Fiber-based Backhauling for Dynamic LTE Capacity Provisioning", <u>A. Haddad</u> and M. Gagnaire, To appear in *IEEE/ACM Transactions on Networking (ToN) journal*, Q1-2013.

- "Optimized Radio-over-Fiber-based Cellular Backhauling Strategy using Genetic Algorithms and Pareto Fronts", <u>A. Haddad</u> and M. Gagnaire, To appear in *Special issue of Telecommunication Systems Journal (TSJ)– Business and Economics Collection, Springer Ed.*, 2013.

Publications and a European patent dealing with research not related directly to the work of this thesis are also enlisted:

- "A Meta-heuristic Approach for Monitoring Trail Assignment in WDM Optical Networks", <u>A. Haddad</u>, E. A. Doumith and M. Gagnaire, in *IEEE/IFIP Proc. of the Int. Congress on Ultra-modern Telecommunications and Control Systems and Workshops (ICUMT'10)*, Oct. 2010, Moscow.

- "A fast and Accurate Meta-heuristic for Failure Localization Based on the Monitoring Trail Concept", <u>A. Haddad</u>, E. A. Doumith and M. Gagnaire, in *Telecommunication Systems Journal (TSJ)– Business and Economics Collection, Springer Ed.*, 2011.

- MeMoTA 2.0 Software European Patent (2010), *"Meta-heuristic for Monitoring Trail Assignment: [un algorithme de deploiement de circuits optiques (m-trail) pour la localisation non-ambigue de pannes dans les reseaux WDM translucides]"*.

Part I

GeRoFAN Backhauling Architecture

RoF-based Mobile Backhauling

Contents

3.1 Introduction

RECENTLY, mobile backhauling has received considerable attention from operators, seeking to upgrade and even to rethink their existing backhaul infrastructure to meet in a cost-effective way the increasing demand of bandwidth. This chapter focuses on the salient features and issues of cellular backhaul with a focus on optical fiber as a promising answer to rising mobile data traffic.

Chapter 3 is structured as follows. A survey of the various technologies used for backhaul is carried out in Section 3.2. We spotlight current and upcoming trends of the backhaul network together with telcos' strategies. Section 3.3 investigates the opportunities of leveraging the optical fiber for mobile backhaul through Radio-over-Fiber (RoF) technology. A comparison between the two main techniques of RoF, analog or digitized, is realized to show the economic benefit of employing Analog RoF (A-RoF) for broadband mobile backhaul. In Section 3.4, we describe GeRoFAN (Generic RoF Access Network), an all-optical network architecture relying

on A-RoF, for cellular backhauling. The key features of the GeRoFAN Control Plane (CP) are
introduced at the end of this chapter.

3.2   Cellular backhaul: Current and future trends

3.2.1   The mobile backhaul section

The mobile backhaul section designates the portion of the network that connects the Base
Station (BS) (*a.k.a* Base Station Transceiver (BTS) in *2G* or Node-B in *3G* systems) which
communicates with the mobile equipment through the air interface and the radio network con-
troller at the central office (*a.k.a* Mobile Switching Center (MSC) and Radio Network Controller
(RNC) for *2G* and *3G* respectively). More generally, the backhaul consists of a group of radio
cell sites aggregated into a hub sites being connected to the edge node of the core network.
Figure 3.1 illustrates the generic model of the backhaul section spanning from the cell site
("Wireless Last Mile" domain) to the core transport network. Three subcomponents constitute
the mobile backhaul: the cell site, the aggregation site, and the Metro network [113].
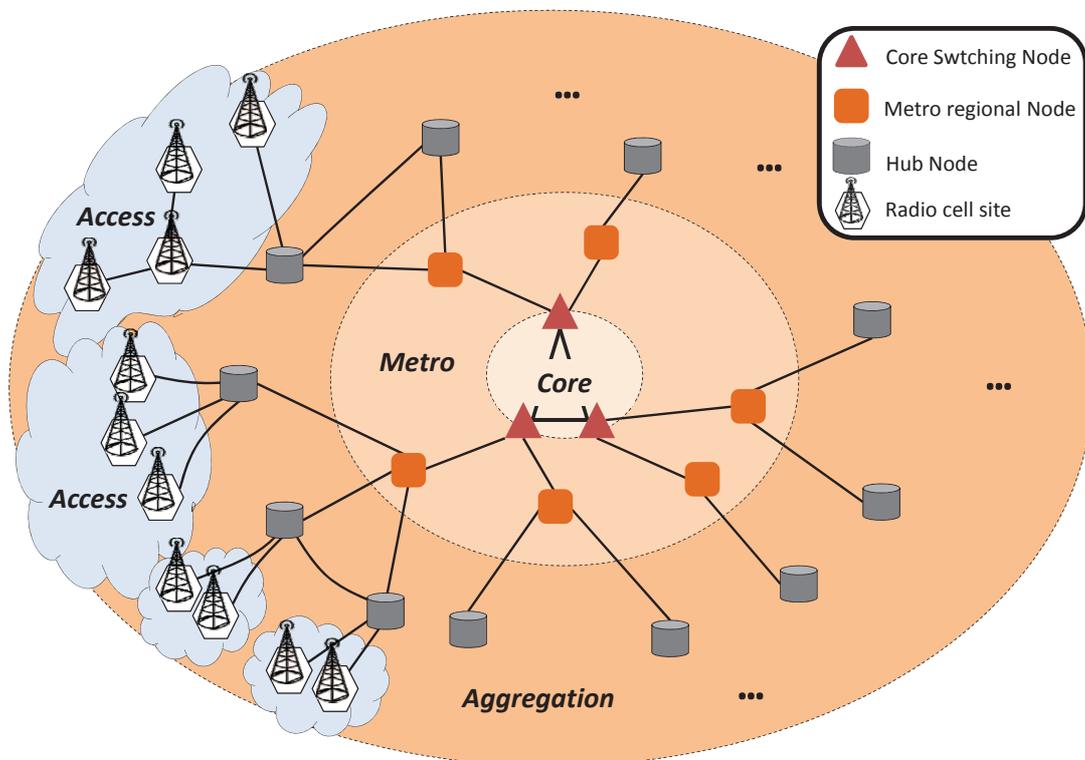
Figure 3.1: Generic model and subcomponents of the mobile backhaul.
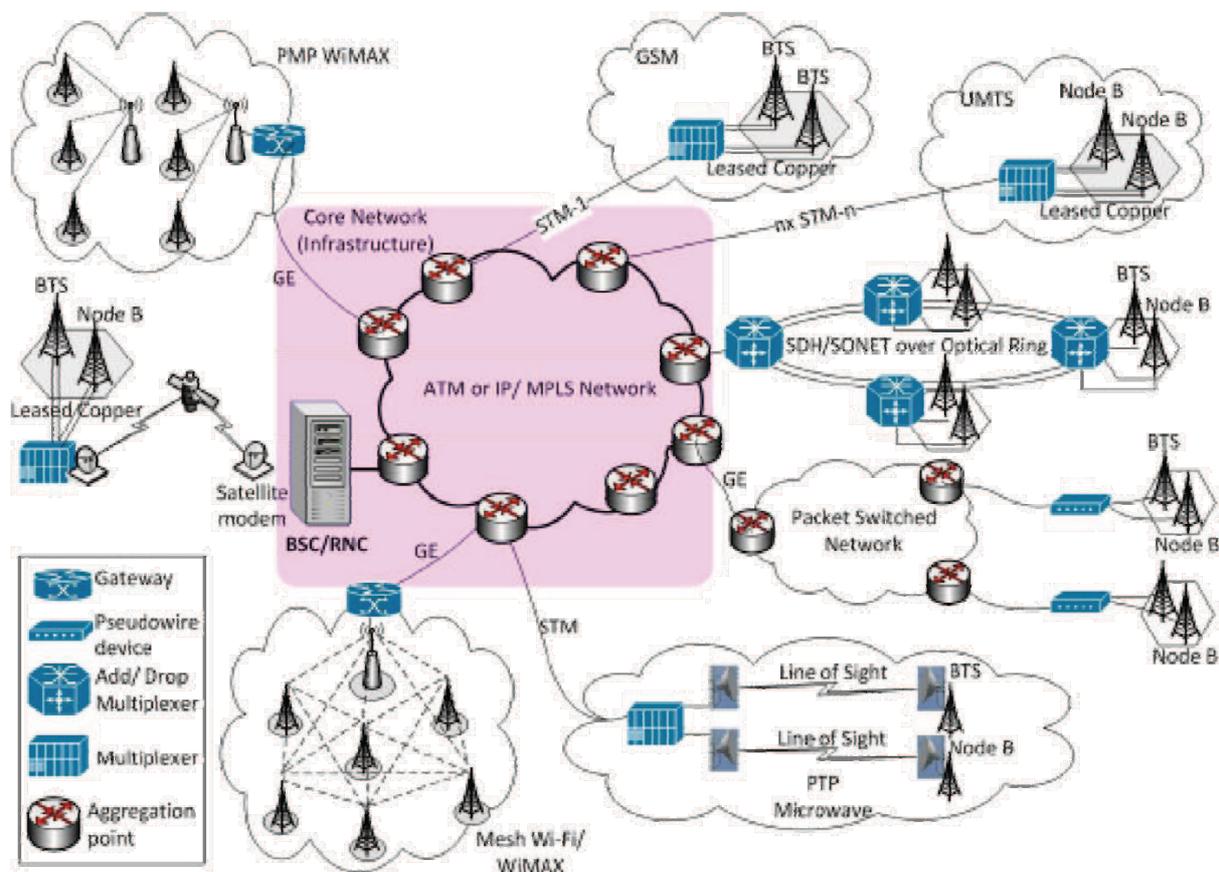
Figure 3.2: Traditional/emerging backhaul technologies: A big picture view [102].

3.2.1.1 Backhaul technologies at the access/agregation segments

The current backhaul network relies on various technologies to aggregate the radio traffic and transport it to the network controller. Figure 3.2 shows a big picture of the different technologies used for current and emerging cellular backhaul.

As it can be noticed, three physical mediums dominate today's backhaul: copper, optical fiber and microwave radio links. In the US for instance, leased T1/E1 copper lines reaches up to 90% of backhaul infrastructure followed by microwave radio links (about 6%) and optical fibers (about 4%)[110]. In the following, we describe the main characteristics of these technologies and alternative solutions for backhauling either prospective (*WiFi, WiMAX*) or emerging (circuit emulation using pseudo-wire).

• **Copper:** Copper cables constitute the traditional backhaul medium originally used in *GSM* system between the BTS and the Base Station Controller (BSC). The traffic between BTS and BSC is TDM multiplexed and transported in predefined time slots using the Plesiochronous Digital Hierarchy (PDH). Two PDH standards are used to transport TDM circuits over copper cables: the T-carriers and the E-carriers delivering data-rates ranging from 2.048

Mbps to 565, 148 Mbps in Europe. When traffic grows and TDM does not suffice then Ethernet and xDSL technologies (*e.g.* G.SHDSL, VDSL2) are often used on copper to deliver the required bandwidth. T1/E1 copper lines dominate the backhaul solutions as they provide suitable support for legacy voice traffic, with deterministic Quality of Service (QoS). In addition, timing and synchronization are inherent to leased T-/E-circuits. However, the significant growth in the number of deployed base stations[1] and thus associated leased copper connections makes T1/E1 copper lines no longer a cost-efficient choice for backhaul.

- **Fiber:** Fiber-based backhauling solutions range from point-to-point (P2P) optical links, Synchronous Digital Hierarchy (SDH)/Synchronous Optical NETworking (SONET) rings to reusing existing Passive Optical Networks (PONs) as detailed in Section 3.3. Unlike PDH-based circuit copper lines, optical fibers are deployed in dense urban and suburban locations, considered as high traffic areas. Existing leased T-/E-circuit copper lines are merged and multiplexed into higher rate optical fiber connections STM-x. Despite the high bandwidth of optical connections which enables them to accommodate high capacity backhaul, the deployment cost of optical fiber at the backhaul may be prohibitive. Results reported by [102] indicate that an optical ring should a least serve 4 cell sites to achieve 27% or more cost savings compared to P2P copper connections.

- **Microwave and Satellite wireless backhaul:** Microwave and satellite links are utilized in geographically challenging sites where wired connections are infeasible or difficult to deploy. Microwave technology in particular has become an efficient complement to fiber and copper. Microwave radio links use either licensed (6 − 38 GHz) or unlicensed (2.4 − 5.8 GHz) spectrum bands. The latter enables to reduce Capital Expenditures (CapEx) but raises radio interference issues. While the capacity of a microwave link depends on the coverage and the exploited spectrum band, Line of Sight (LoS) between cell sites and aggregation nodes is often required. When LoS is satisfied, microwave link can be quickly installed to cover long distances, implemented either through P2P, Point-to-Multi-Point (PMP) or multi-hop configurations. The digital transmission over microwave links can be realized over PDH, SDH/SONET or Ethernet standard. Apart the LoS requirement, backhaul performance of microwave links are still sensitive to weather conditions. In this matter, weather conditions-aware techniques, employing adaptive modulation schemes [92], are designed to mitigate microwave signal fading due to change in propagation conditions. On the other hand, operators may resort at last to satellite communications for locations where no other backhauling technologies are feasible. In some scenarios when sites spread over several distant islands have to be connected, cellular backhauling via satellite links is more cost-effective than deploying costly submarine cables. Transmission

---

[1]Fueled mainly by the increasing number of mobile subscribers. According to a Yankee Group 2010 research study [110], the number of cell sites went up in the US from 30.045 in 1996 to 245.000 in 2009, it is expected to reach 300.000 in 2012. The number of leased T1/E1 circuits increases as the cellular system technology evolves as as well. The implementation of *GPRS/EDGE* (*2.5 G*) requires four times the number of leased lines used in *GSM*, the factor increases to 8 with *HSPA* (*3.5G*) and expected to be 16 when *LTE* (*4G*) will be fully deployed.

over satellite links are mostly based on PDH circuits. Their short installation times, flexible coverage and exploitation (using DAMA[2] technique for instance) should not mask their major drawbacks namely their high cost and long propagation delay[3].

- **Free-Space Optics:** Free-Space Optics (FSO) are another means of high bandwidth backhauling technology capable of 1 Gbps data rate transmission that can be mapped over SONET/SDH standard (STM-4). FSO is a LoS transmission technology using directive laser beams to provide optical bandwidth connections. FSO does not require fiber-optic cable or the securing of spectrum licences for radio-frequency solutions. However, the requirement of hight stability mounting for FSO and the susceptibility to obstructions and fog attenuation make them less attractive for large-scale mobile backhaul deployment [128].

- **Prospective wireless technologies for backhaul:** *WiFi* **and** *WiMAX*

Wireless Fidelity (*WiFi*) was originally designed for indoor usage based on the *IEEE 802.11* standards operating in the 2.4 and 5 GHz unlicensed bands. Recent advances in industry and academia demonstrated the feasibility to extend the usage scope of *WiFi*: recently as small cell-localized *WiFi* point of presence to offload traffic in *3G* radio systems, and prospectively as an attractive low-cost solution for backhaul which can substitute microwave links. However, the deployment of *WiFi* as a backhaul technology poses design challenges relevant to the achieved throughput, distance, coverage, packet efficiency, timing and synchronization. Several solutions are proposed to tackle these different issues. For example, the *802.11n* standard exploits MIMO techniques together with frequency reuse to improve the throughput up to 600 Mbps. In addition, to provide long distance outdoor coverage, proprietary modifications of the MAC protocol are introduced[4], while packet overhead is reduced through header compression techniques. Lastly, as QoS including timing and synchronization is an essential requirement for mobile backhaul, the *802.11e* amendment was introduced to support QoS on *WiFi* networks.

Wireless interoperability for Microwave Access (*WiMAX*) was originally designed for outdoor usage and defined through the *802.16* standards. Based on OFDM modulation with higher spectral efficiency than *WiFi*, *WiMAX* provides higher throughput (75 Mbps per single channel and up to 350 Mbps with channel aggregation) and longer coverage range (up to 50 Km for a single hop). It operates in both licensed and unlicensed spectrum bands with LoS and non-LoS connectivity, although data-rate is reduced for a non-LoS transmission. Compared to *WiFi*, *WiMAX* is already used for backhaul thanks to the *802.16-2004* standard designed for fixed connectivity applications in P2P, PMP, and complex mesh topologies. Unlike standard *WiFi*, *WiMAX* PMP mode supports guaranteed QoS through centralized scheduling mechanisms and the support of different service classes.

---

[2]Demand Assigned Multiple Access (DAMA) dynamically allocates bandwidth resources based on actual requests from the users. DAMA enables usage-based billing mechanisms which helps reduce the incurred expenses of building a Satellite communication site.

[3]As an illustration, the cost of a transponder for an equivalent bandwidth of full T1-circuit used on a full time basis is 5000\$ - 12000\$ per month, that is as much as 16 to 40 times the average cost of a single T1 leased link in US as reported by Yankee Group [110].

[4]Involving MAC layer parameters such as: contention window, round-trip time delay and acknowledgment time-out.

• **The Pseudo-Wire (PW) framework:** The pseudo-wire framework was introduced as a backhaul technology to transport traditional services (TDM, ATM) over Packet-Switched Networks (PSN), *e.g.* Ethernet, IP or MPLS. Such a circuit emulation mechanism is referred to as "TDM/ATM Pseudo-wire" transport. Compared to legacy circuit switched backhaul based on T-/E-carriers, pseudo-wire techniques let capitalize on the lower cost per megabit provided by packet-switched networks which enables to achieve a cost-efficient backhaul and paves the way for a convergent "all-packet" transport. Several standards have been published by the IETF[5] to address circuit emulation for *GSM* backhaul and the transport of ATM services used in *UMTS* backhaul over packet-switched networks. Figure 3.3 shows the pseudo-wire protocol architecture activated between two provider edge devices tunneling a TDM or ATM payload into a PSN. The protocol stack highlights four different layers. The Encapsulation layer composed of three sub-layers: first the TDM or ATM payload is encapsulated using the payload convergence sub-layer. The Timing sub-layer provides timing and synchronization within PSN [102] and the Sequencing sub-layer handles out-of-order packet arrival and packet loss issues. Depending on the payload (T1/E1 bit streams or ATM cells), the Encapsulation layer decides the type of processing and the required added headers to form the "pseudo-wire frame". Prior to packet transport layer, multiple pseudo-wire connections are managed using the Pseudo-wire mux/demux layer and finally the PSN convergence layer allows pseudo-wires to be independent of the underlaying PSN type while meeting the service requirements. Although the design of a PSN-based cellular backhauling poses technical issues relevant to time synchronization, QoS and packet efficiency, specifications of the Pseudo-wire framework address some of these issues. Combined with MPLS RSVP-TE, as a connection-oriented switching paradigm, the pseudo-wire framework enables the provision of an end-to-end QoS with fast packet delivery.

The diversity of aforementioned solutions used for backhaul shows that there is no clear unique answer to think what is the technology that drives the evolution of backhaul networks. In fact, although copper T1/E1 leased lines are still today predominant in the backhaul big picture [110], their incapacity to accommodate cost-efficiently traffic growth makes alternative solutions worth to consider by telcos. Partially inspired from [102], Table 3.1 synthesizes a comparison between the different backhaul technologies through five criteria: Capacity, Distance/Coverage, QoS support (end-to-end delay, jitter, reliability etc.), Timing/Synchronisation, Cost and possible telcos' strategies to leverage the backhaul investment.

Telcos' strategies for selecting the right backhaul technology or/and upgrading their existing backhaul network are driven by two time-horizon objectives. At the short term, an operator seeks the immediate benefit of the backhaul technology particularly for coping with the traffic increase at the cell site, the reference scenario for risk/benefit assessment being the existing backhaul infrastructure (leased T1/E1 copper). At the medium/long term, the oper-

---

[5]Internet Engineering Task Force: RFC 3985, RFC 4385, RFC 5086, RFC 5087 etc.

Table 3.1: Backhaul technologies comparison.

		Capacity	Coverage	QoS	Synchronization	Cost	Leverage Strategies for Operators
Wireline Technologies	Leased Copper	Low (∼ 2 Mbps)	No additional requirement	Guaranteed	Natively provided	low CapEx (already exists), but high Operational Expenditures (OpEx) (leasing cost increases linearly with capacity and distance)	Bonding multiple T1/E1 lines. Running xDSL technologies, that can be reused for femto/pico-cell backhaul.
	Fiber	Very High	No additional requirement	Guaranteed	Provides timing reference	High roll-out, CapEx and maintenance fees increasing with distance	Leveraging existing fiber using fixed broadband xPON technologies (*c.f.* Section 3.3). RoF-based "Cloud RAN" (*c.f.* Section 3.2.2). Fixed Mobile Convergence (FMC): Promoting fiber-wireless convergence.
Wireless Technologies	Microwave	High but depending on the framing protocol and the modulation techniques	LoS requirement	Guaranteed	Provided	High upfront CapEx. Licence spectrum fees with high maintenance cost.	Lower the OpEx through unlicensed bands with care to interference. Multi-carrier site sharing.
	Satellite	Medium	Flexible coverage	High propagation delay	Provided	More expensive at an equivalent T1/E1 link.	Usage-based billing to alleviate high investment cost (Sharing). The ultimate solution for challenging areas (islands, remote locations).
	FSO	Very High but still dependent on the propagation conditions	LoS privileged	Guaranteed	Provided	No heavy investment infrastructure (*vs.* fiber). Securing spectrum license with narrow beam (*vs.* interference-free licensed microwaves or interference-subject unlicensed *WiFi*), but high OpEx (mounting stability, susceptibility to beam obstruction)	Promoting hybrid solutions by bridging with non-LoS microwave links to overcome obstructions through ring and daisy-chained configurations [42]. FMC: FSO as an extension of optical Ethernet (already deployed in metropolitan areas) to mobile backhaul [128].
	WiFi	High	LoS	Excepting *802.11e*, QoS is originally not supported	Not enough accurate for backhaul applications	Low CapEx due to mass production. Low OpEx: Unlicensed spectrum.	Offloading high-bandwidth best-effort traffic through public hot-spots (Evolved offloading mechanisms through *Hotspot 2.0* [42]). Leverage widespread private/in-building *WiFi* owned by third party through incentive micro-payment technology-based methods [117].
	WiMAX	High	Both LoS and non-LoS with multi-hop for higher coverage	Guaranteed	Accurate through GPS as a reference clock	CapEx network building, OpEx: Licensed spectrum fee	Standardization drives the total cost down. Strong candidate for rural and metro areas deployment.
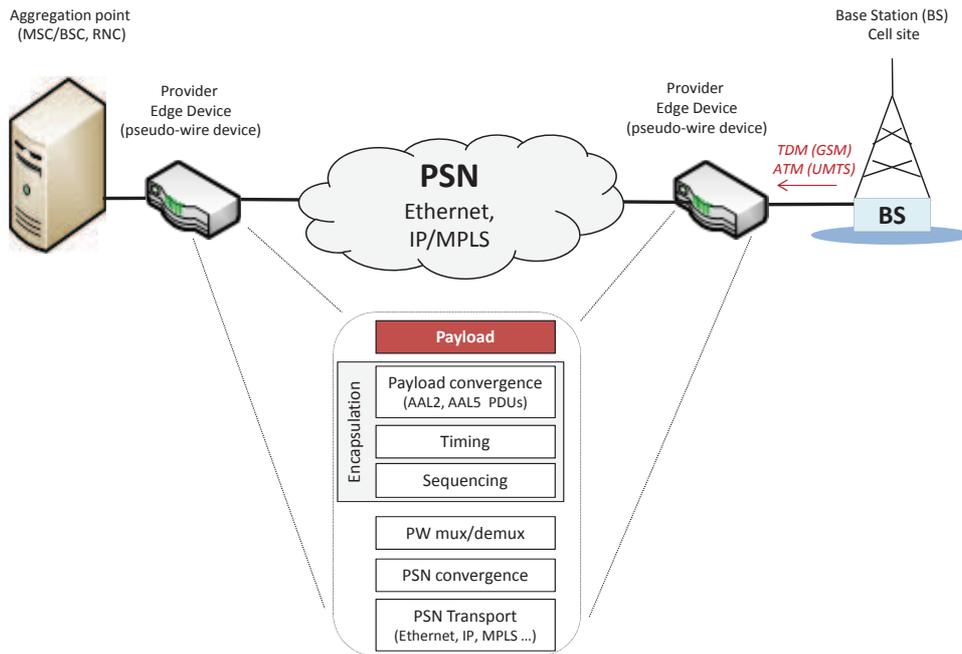
Figure 3.3: Pseudo-Wire Protocol Stack.

The Pseudo-wire protocol stack is implemented at both provider edge devices. The encapsulation layer provides any information needed by the edge devices to forward packets from the PSN frontier to the TDM/ATM network frontier, and to reconstruct the original TDM/ATM payload from the received packets. The encapsulation of TDM bit streams is not a mere packetization process since lost packets can cause service interruption. In fact, usually multiple T1/E1 frames are grouped together into one big frame before encapsulation and only the time slots in use within each T1/E1 circuit are sent. The encapsulation techniques used by Pseudo-wire rely on AAL (ATM Adaptation Layer) to provide QoS-compliant transfer of voice-grade channels, data and telephony signaling. Specifically, AAL1 PDUs (Packet Data Unit) for Constant Bit Rate applications (voice call), AAL2 PDUs for Variable Bit Rate applications (time slots are dynamically assigned, *e.g. 2.5G/3G*), AAL5 to handle signaling exchanged between Node-Bs and RNC over the Iub interface in *3G* [102].

ator investigates the foreseen Return on Investment (RoI) of the strategy. At this stage, the operator estimates the potential business value featured by prospective applications that lay on the upgraded/new backhaul network. Both time-horizon objectives are synthesized through the schematics in Figure 3.4. We have positioned several backhaul technologies in the diagram according to two dimensions: the capacity-coverage product and the required Total Cost of Ownership (TCO), both normalized to the reference scenario of a single leased T1/E1 copper line. The diagram shows also examples of possible attractive investment strategy paths for an operator. The techno-economic framework to assess the TCO for the different technologies is inspired from the economic modeling in [141]. Data and background assumptions used for the schematics are applied to developed markets and based on recent research consulting/watch service reports from: [38], [107], [118], [45] and [122].

TCO is evaluated by computing cumulative CapEx (deployment expenses) and OpEx (including: maintenance, ongoing leasing cost, licensed spectrum fees) cashflow per cell site over 5 years. The reference scenario of T1/E1-leased copper backhauling assumes a monthly leasing fee of 300 €per link [110].
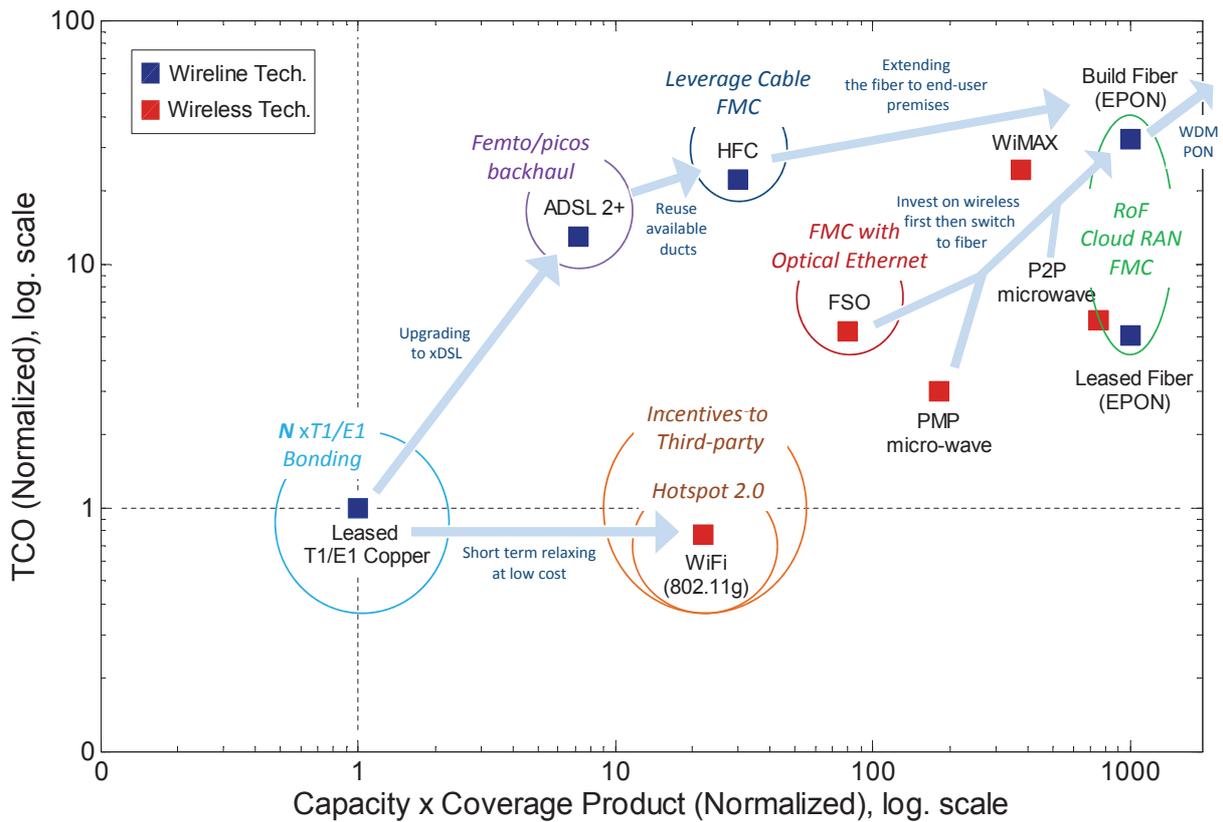
Figure 3.4: Backhaul benchmark and telcos' leverage strategies.

Several leverage strategy paths are highlighted for Telcos aiming at upgrading their backhaul network with attractive RoI. The first reachable strategy consists in reusing the already deployed copper infrastructure to run xDSL, ADSL2+ is a cost-effective strategy to backhaul pico-cells and femtos installed in the subscriber premises. Other operators privileged the low-cost *WiFi* solution to relax, at short term, the requirement on backhaul. In general, wireless solutions are considered being more cost-efficient to address short/medium term requirement for backhaul. Indeed, an analysis carried out by Telecom business consulting companies [107] shows that deploying wireless backhaul (microwave, Enhanced *WiFi*, FSO) first then building a fiber network later provides operators with up to 27% of savings, and up to 31% when leasing fiber. More prospective strategies such as building a high-capacity backhaul network using WDM-PONs are definitely long-term. In fact, the investment payback of WDM-PON is higher than other strategies and the technology is not yet standardized.

3.2.1.2 Design considerations for evolved packet backhaul

Several studies have pointed out the limitations of the current backhaul especially at the last mile and the aggregation part to absorb the increasing amount of traffic generated in each radio cell [110][118]. While the connectivity type offered by the backhaul network is influenced by the technology used in the RAN and factors such as geographical locations of the cell site, bandwidth requirements, sustainable investment and local regulations, there is a wide consensus to rethink the evolved backhaul around the pure packet IP-based switching network. The design considerations for an all-IP-based mobile backhaul are summarized below [113]:

- **VLAN Models:** Implementing a Virtual Local Access Network (VLAN) model in the back-haul enables to separate the traffic either based on services or/and locations through tagged and untagged frames (original standard defined in *IEEE 802.1Q*). Overlaying

VLANs on the backhaul enables more efficient management of the traffic in terms of capacity and QoS. Originally defined as a LAN-based solution for flexible networking of entreprise business divisions, the model of VLAN is undergoing standards extension efforts (*IEEE 802.1ad* and *802.1ah*) to meet operators needs for backhaul.

- **Class of Services (CoS):** The evolved packet-based mobile backhaul network needs to be capable of recognizing the CoS settings of the different traffic streams, doing any re-marking of packets if required, prioritizing, classifying and scheduling packets. The back-haul has to be able to support within a unified transport infrastructure the main traffic streams including voice, video, network signaling/management, and best-effort data while providing low packet loss.

- **Transport and Services:** MPLS and pseudo-wire technologies are used as the transport mechanism in both pure packet and hybrid types of mobile backaul architectures (*c.f.* see Subsection 3.2.2). The advantage of using MPLS for transporting pseudo-wires connections is that it is agnostic to the transport media and more scalable than a traditional Layer 2 networks. The new extension of the MPLS standard (MPLS-TP) enables to capitalize on the maturity of the original protocol and to benefit from its advantages in terms of protection schemes, faster convergence times and connection-oriented transport. On the other hand, the PBB-TE (Provider Backbone Bridge-Traffic Engineering) initiative aims at extending the legacy widespread Ethernet protocol to meet the "carrier-grade" re-quirements. Both MPLS-TP and PBB-TE rely on the establishment of predefined virtual connections through the packet transport network by appending labels, computing and provisioning the required resources.

- **Synchronization:** Synchronization is a challenging requirement for all-packet backhaul, in-deed unlike TDM, packet transport does not inherently support network synchronization. In mobile radio systems, synchronization is used to support cellular handoff, interference management, mobile localization, and the delivery of real-time services like voice and video streaming. Two major standards namely the *IEEE 1588* and the ITU Synchronous Ethernet (*Sync-E*) are developed to support clock synchronization for packet-switched mobile backhaul. *Sync-E* operates at Layer 1 of the communication stack and thus runs independently from upper layer transmission protocols.

  In *Sync-E*, each node recovers the clock information from upstream nodes and then dis-tributes it to downstream nodes after filtering jitter. However, to get implemented, *Sync-E* requires hardware support in all devices in the network. The *IEEE 1588* protocol runs in parallel with data traffic. Unlike *Sync-E*, *IEEE 1588* requires only the installation of a grand master clock at the RNC to get implemented. However, *IEEE 1588* is sensitive to

network congestion, jitter and delay, and in some cases, it complicates traffic engineering and planning. While much focus has been done on timing and frequency synchronization, phase synchronization is an additional requirement in *4G* systems that has to be addressed[6]. Looking for comprehensive standard, the IETF proposed the TICTOC architecture –a unified framework for frequency and timing distribution over packet switched networks, based on existing standards or extensions like the Network Timing Protocol (NTP) or the *IEEE 1588 v2* [102].

- **Reliability and Fault Detection:** Fault detection mechanisms need to be implemented at different levels of the backhaul network. Failure detection has to be implemented both at the Ethernet physical and link layers. MPLS offers for instance protection schemes at the link and node level with fast failure detection and convergence times.

3.2.2 Evolution of the backhaul protocol stack: Migration paths

Several survey studies conducted with operators [38][118] pointed out the evolution towards an all-packet backhaul network as a cost-effective investment able to meet in a sustainable way the traffic increase. Related backhaul evolution steps will be common and the difference will lie in whether all operators will experience all the transformation stages or whether some can accelerate or side step one or two of the stages. The challenge of the evolution lies in the complexity to manage the transition to packet backhaul whilst maintaining existing high quality of legacy (circuit-switched) services. A smooth transition to pure packet backhaul architecture involves intermediate steps to set up hybrid approaches where TDM and packet traffic coexist together within the same backhaul network with different levels of integration. In that matter, the Pseudo-wire framework combined with MPLS for instance constitutes an attractive and a mature technology for operators looking for implementing pseudo-wires at the BS to enable an IP RAN before the IP capability is supported in the BS themselves. The gradual transition from legacy circuit-switched to prospective pure packet backhaul network is illustrated in Figure 3.5. Hybrid architectures lay at intermediate stages with legacy circuit traffic is increasingly integrated within packet transport.

The evolution of the backhaul can also be achieved by starting the mutation from the access part. As detailed in subsection 3.2.1.1, the evolution of the access/aggregation section of the backhaul consists in making the different underlaying physical technologies as "agnostic" as possible to handle different transport standards. Meanwhile, the access/last mile section evolves in-line with the planned mutation of the backhaul depicted in Figure 3.5. A flat architecture of the RAN highlights such an evolution of the access. Indeed, from *2G/3G* to *4G* systems, more

---

[6]In *LTE* and *WiMAX*, the same wireless frequency can be reused in different phases, a capability that enables *4G* service providers to serve more customers on the same frequency range. Hence, a synchronization method supporting phase synchronization is needed. The *IEEE 1588* protocol supports phase synchronization which is not the case of *Sync-E*.
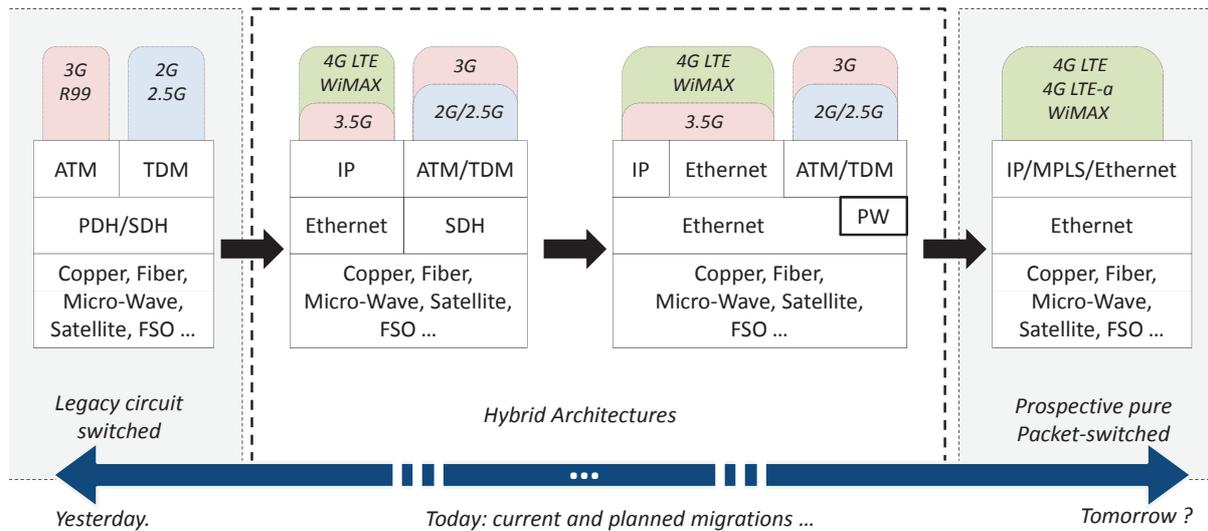
Figure 3.5: From legacy to prospective backhaul: Evolution of the protocol stack.

The figure illustrates the main stages describing the evolution of the transport protocols used for backhaul. The migration steps from legacy circuit switched backhaul towards pure packet transport are achieved along with maintaining backward compatibility to achieve a smooth transition. Yesterday, legacy circuit transport based on PDH/SDH (SONET) were sufficient to accommodate voice-grade traffic from *2G/2.5G* cellular systems. With the first release of *3G*, ATM has been used to handle data traffic requiring higher and variable bandwidth, still the backhaul remains globally managed through a circuit rationale. Today, it is widely admitted that legacy backhaul could not cope with the new traffic pattern (bursty, non-deterministic, requiring differentiated QoS). Hybrid architectures describes how backhaul mutates towards a coexistance between circuit and packet transport. Currently, such a co-existence is achieved by overlaying the ATM/TDM backhaul with the IP/Ethernet backhaul. Similarly to access where *WiFi* hot-spots, Distributed antennas and small cells are deployed to offload traffic of the macro-cell, running both TDM/ATM and IP/Ethernet backhaul networks in parallel could leverage telcos' investments and achieve scalability. In that scenario, low-priority high bandwidth traffic can be offloaded from the legacy TDM/ATM network to the new packet backhaul. Planned hybrid architectures put an emphasis on higher integration of native TDM/ATM traffic into the emerging packet switching network. The pseudo-wire (PW) technology gains more maturity among backhaul platform vendors and adoption from telcos looking to upgrade their backhaul network. The hybrid packet/circuit backhaul is implemented either by using an interworking gateway between the BS node and the BS controller node or running a dual stack TDM/Ethernet on both nodes. Tomorrow, *2G* networks will be turned off allowing for the pure packet transport for mobile broadband (*4G, WiMax*). The prospective pure packet approach will not become reality until technical challenges summarized in subsection 3.2.1.2 inherent to packet transport are addressed. Actually, the current "telecom backhaul bubble" promotes two transport technologies leading the competition for the unified all-packet backhaul: Carrier Grade Ethernet (CGE) and MPLS-TP [118]. CGE could be the ultimate convergence transport technology but its widespread adoption will depend on the real advantage offered over the more mature MPLS-based technologies.

efforts have been done in removing intermediate components in the RAN architectural model, thus reducing signalling and concentrating system intelligence. The BSC used in *2G* to middle the backhaul connection between the cell site (BTS) and the MSC has been removed in *4G* clearing the path for a direct backhaul link between the node-B and the RNC. Meanwhile, more pico/small cells spring up around the node-B to enhance coverage and bring capacity where it is actually needed, still control functionalities remain mainly located at the node-B. The leitmotiv behind such an evolution is dematerializing the access by separating progressively processing/control functionalities at the cell site from execution functionalities that can be remotely controlled. An IDATE survey [118] describes the roadmap of the evolution of the access through three key steps as depicted in Figure 3.6.
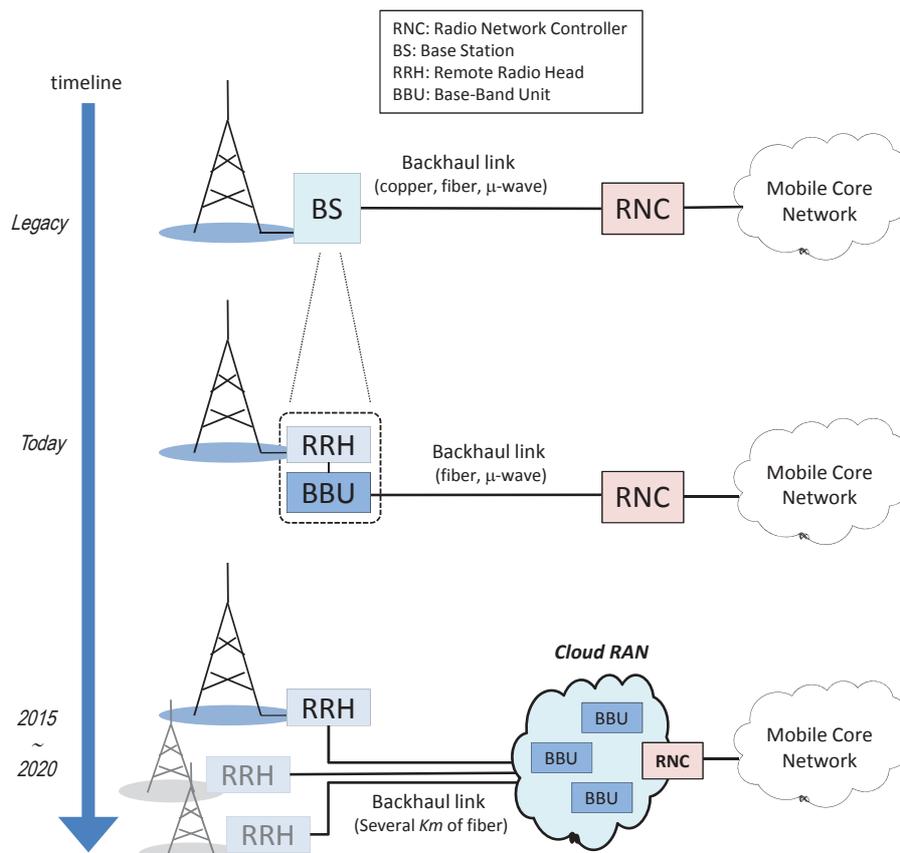
Figure 3.6: Evolution of the Access-Backhaul towards the "Cloud RAN".

The access section is evolving to meet the new backhaul network requirements. At the BS, signal processing and control functionalities *a.k.a* BaseBand Unit (BBU) module are decoupled from "passive" radio functionalities called Remote Radio Head (RRH). Today such a splitting enables to implement cost-efficiently cell sectorization and MIMO techniques by mutualizing the same BBU between several radio heads. However, the major gain expected by operators from this evolution comes when the BBU is deported more deeply in the backhaul network leaving only the RRH at the access. Indeed, the closer the radio access point from the end-user, the lower the number of users per unit area and the radio link performance increases multi-fold. The next stage of the access evolution should focus on the most cost-effective way to apply the RRH/BBU decoupling at a multi-radio cell site scale. In fact, adding more RRHs or increasing cell densification increases the throughput per user and most of the times such an approach enables the differentiation between operators. The evolved access architecture backhauls several distributed RRHs to a pool of BBUs which could be mutualized and used on a job demand basis as envisioned through "Telecom Cloud"[a]. Today, several mobile backhaul equipment vendors are launching into the market proven solutions featuring such an evolution. Alcatel-Lucent's LightRadio BS model or the collaboration between the chip manufacturer Intel and the Chinese operator ZTE to merge telecoms and IT cloud expertise highlight the opportunities for operators and equipment vendors alike [145]. Actually, a recent watch report released by IDATE [118], foresees the "Cloud RAN" as the near future for the access backhaul with an approximate time-line set at $2015 - 2020$ for first field deployed solutions.

---

[a]"Telecom Cloud" is a generic concept aiming at applying the Cloud paradigm for wireless networks.

3.3 Leveraging the fiber at the access: Radio-over-Fiber

With the dramatic increase of throughput at each BS driven by intensive bandwidth mobile applications and the advances in metro-access optical networks, the use of fiber optics to provide the required bandwidth for cellular backhauling has been largely investigated [72]. Such an integration between optics and wireless offers significant advantages while supporting both optical wire-line and mobile wireless connectivity. To leverage optical fiber investment at the

access, Radio-over-Fiber (RoF) is considered as a key driver technology.
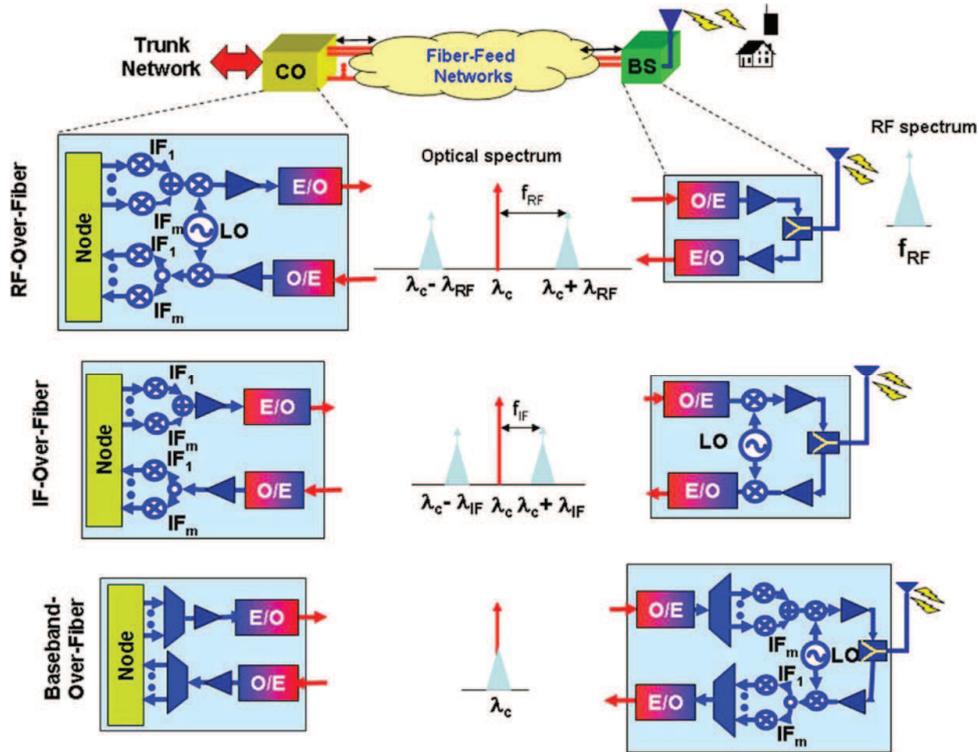
Figure 3.7: Analog RoF transport schemes (from [22]).

3.3.1 Radio-over-Fiber technology

RoF techniques are considered today as very promising to facilitate the backhauling of a large number of remote antennas. RoF find its application both in indoor and outdoor environments [22]. RoF consists in transporting the radio signals by means of an optical carrier from the remote site to the head-end node of the cellular network where it will be processed. The first investigations dedicated to RoF are dating from the years 90s. These preliminary studies demonstrated the point-to-point feasibility of RoF transmission.

3.3.1.1 RoF: Transport options

Depending on the frequency of the radio-signal being transported on the optical link, RoF backhauling prevents the usage of costly IF and/or RF oscillators at the antenna's site. Two variants of RoF have been investigated in the literature either the radio channel is transported as an analog or as a digital signal.

• **Analog RoF Transport:** The oldest variant known as Analog RoF (A-RoF) has been devel-
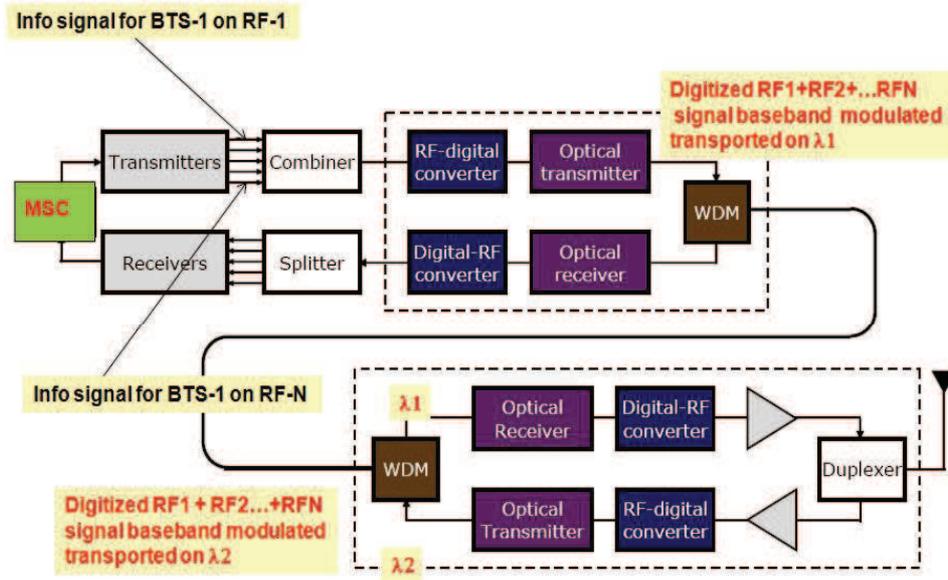
Figure 3.8: Digitized RoF transport scheme.

This Figure shows a bi-directional multi-wireless signal transmission using digitized RoF. Several Radio Frequencies (RF-1...RF-N) from the MSC (Mobile Switching Center, the head-end switching node in *2G* system) and destined to the BTS are first combined, then digitized and optically transported over the D-RoF link. At the BTS and upon optical/electrical conversion, the analog multi-wireless signal is recovered from the digitized stream using an Digital-to-RF converter before power amplification and radiation at the antenna. Note that in TDD wireless systems (like *2G* for instance), where uplink and downlink transmissions are performed at the same radio frequency alternatively, the D-RoF link requires two wavelengths per BTS to carry the bidirectional traffic. As shown in the figure, WDM mux/demux are also needed at the edges of the optical link.

oped these last fifteen years. A-RoF features analog optical signal transmission techniques[7] like Intensity Modulation Direct Detection (IMDD) for frequencies up to ~ 30 GHz while optical heterodyning is privileged for *mm*-wave signals [70] to mitigate the transmission limitations due to fiber dispersion at these high frequencies. In general, there are three possible methods for transporting RF signals over an A-RoF link as depicted in Figure 3.7 namely: RF-over-Fiber, IF-over-Fiber and Baseband-over-Fiber [22].

1. The first approach, RF-over-Fiber, provides a maximum simplification of the BS configuration, where the RF signal generation and processing is centralized at the CO. This reduces the network cost and increases its flexibility by including switching and routing functionality at the CO. In RF-over-Fiber, the RF signal at the BS intensity-modulates (either directly or externally) an optical channel. It is then transported through the optical link to the CO (Central Office) where the RF signal is recovered via direct detection using a photo-detector. Despite its advantages, there are several drawbacks with RF-over-Fiber transmission; especially for *mm*-wave frequencies limited by the performance of transceivers (high speed optical modulation

---

[7]Apart IMDD (assumed for our modeling in Chapter 4) and optical heterodyning, alternative modulation techniques based on harmonics generation (optical frequency multiplication) are also reported in [98].

and photo-detection schemes) and the effect of fiber chromatic dispersion on the detected signal.

2. To tackle the effect of fiber chromatic dispersion and to use low-speed optoelectronic devices, the wireless signal is down-converted to a lower intermediate radio frequency (IF) at the BS before optical transmission. IF-over-Fiber transmission may constitute an attractive solution to achieve low cost deployment when combined with multi-mode optical fibers. However, with IF-over-Fiber, the complexity of the BS architecture is increased requiring at least a Local Oscillator (LO) and a mixer to perform signal frequency translation. Such a complexity presents some limitations when it comes to upgrade/reconfigure the system in order to include additional radio channels or to modify the wireless frequency.

3. Baseband-over-Fiber modulation refers to the situation where the the radio frequency is down-converted to Baseband before transmission through the optical link. In addition of requiring low speed optoelectronic devices, this scheme has the advantage of using mature and already on-the-shelve electronics for signal processing at the BS. Furthermore, Baseband-over-fiber transport is independent of the air-interface which means that the BS must have the intelligence to process the signal before transporting the baseband information back to the CO.

- **Digitized RoF Transport:** A more recent version of RoF known as digitized RoF (D-RoF) has been proposed during these last ten years thanks to the increasing speed of electronics [2]. Compared to A-RoF, D-RoF produces from the original analog radio signal a sampled digital serial stream that can be used to modulate an optical channel and detected like any other digital information. In comparison to A-RoF, D-RoF requires a relocation of the analog-to-digital (ADC) and digital-to-analog (DAC) functions at the BS and the implementation of Digital Signal Processing (DSP) functionalities within the transmitter and the receiver modules. Similarly to A-RoF, it is possible to rebuild directly at destination the pre-modulated RF signal without the usage of costly RF/IF oscillators. Meanwhile, in the case of broadband RF signals or applications in the *mm*-wave frequency bands, the speed of electronics needed for the design of ADC/DAC may become restrictive. In that case, it is possible to digitize only the pre-modulated IF signal instead of the RF signal, an RF oscillator being needed at destination to up-convert the IF signal to the radio carrier frequency. Figure 3.8 illustrates the basic principle of a P2P D-RoF link.

The main advantage of A-RoF is transparency along the transmission between the CO and remote BSs. Such a transparency makes the capacity held by A-RoF systems more flexible to manage, however, as it will be underlined in this thesis A-RoF is more sensitive to physical layer impairments than D-RoF. Cellular backhauling using A-RoF is particularly simple, cost-effective

and easy to upgrade. The major drawback of A-RoF is the addition of noise and distortions which limits the dynamic range resulting in a reduced coverage. In fact, unlike D-RoF whose dynamic range is dependant on receiver sensitivity, the dynamic range of A-RoF decreases linearly with the fiber length and the number of radio channels [154]. With D-RoF, the signal distribution inherits the advantages of optical fibre digital transport. With the performance improvement and cost reduction of ADCs and DACs, it is possible to achieve radio digitization and reconstruction at the BS. Today available circuitry on the shelves enables narrow-band radio digitization. The limitation of D-RoF arises when digitizing multiple radio channels or a wide-band signal such as *UWB* or *mm*-wave applications. For instance, a single channel at the upper band of the *LTE* FDD system, say 3600 MHz[8], would require a sampling rate of at least 7200 MHz according to Shannon's sampling theorem. Assuming a 9-bit ADC/DAC resolution, this yields to 64.8 Gbps bit stream, which would not be practical. The line bit-rate reduction can only be achieved by means of a lower resolution of the ADC/DAC and/or a decrease of the sampling rate (by frequency shifting or using Band Pass Sampling (BPS) technique as it will be detailed later) to be massively implementable on remote BS.

3.3.1.2   RoF: Networking options

● **Hybrid fiber-radio network architectures:**

There are plenty of proposals in the literature aiming at using RoF modulation to realize hybrid fiber-radio network architectures [89]. In the first level of the multiplexing hierarchy, several radio channels can be backhauled either using Sub-Carrier Multiplexing (SCM) in A-RoF, where multiple RFs modulate the same optical carrier, or through TDM in D-RoF to enable the transport of several digitized radio channels on the same optical carrier. In a second level of the multiplexing hierarchy, Wavelength-Division Multiplexing (WDM) provides an extra level of reconfiguration as wavelength can be used as an additional routing dimension. Equipping the CO with an optical cross-connect functionality would enable the dynamic reconfiguration of the optical distribution network connecting the different Radio Access Units (RAU) as shown in [76]. The maturity of wavelength selective optical components such as Optical Add Drop Multiplexers (OADM) and optical routers makes WDM networking a key factor to boost the development of advanced RoF network architectures. In addition, the traffic isolation benefit brought by WDM allows multi-service delivery and multi-operator deployment as recommended for next generation networks. As discussed later, the use of WDM provides the opportunity for seamless bridging with broadband fixed networks (FFTx) which speeds-up the realization of fixed-mobile network convergence.

In [88], a WDM/SCM A-RoF distribution network called *RoFnet* is proposed to connect several RAUs to the CO. In *RoFnet*, two wavelengths are assigned to each RAU: the first one

---

[8]Considering *LTE* FDD Band number 22: $3410 - 3500$ MHz (uplink)|$3510 - 3600$ MHz (downlink).

being modulated by the downstream traffic and the second one corresponds to a continuous wavelength which will be used to modulate upstream traffic coming from the radio-cell.

In [146], a hybrid star-ring architecture consisting of a star network on the upper level and many concatenated ring subnets on the lower level is proposed for SCM radio signals overlaying a PON. The upper level star network ensures high network capacity and its weakness in reliability is overcome by the concatenated ring subnets with self-healing capabilities.

Another networking solution has been proposed in [11] where RoF is used for feeding the RAUs installed along the rail tracks to provide broadband mobile services to train passengers. Thanks to the intelligence centralization provided by RoF, the system enables the *moving cell* concept, where instead of the train moving along a fixed repeated cell pattern, the RoF system considers a cell pattern that moves together with the train, so that the latter can communicate on the same frequency during the whole connection, also avoiding most cumbersome handovers.

The EU-Project *FUTON* [132] proposes an A-RoF-based flexible optical architecture for wireless systems to jointly process radio signals from different RAUs. A key originality of the *FUTON* architecture consists in taking advantage of the transparency of A-RoF to the modulation format and signal processing centralization at the CO to serve various kinds of overlaying technologies (*WiMAX/LTE, 3G, UWB, WiFi...*).

• **Integration with fixed broadband PONs:**

Given the massive deployment of FFTH networks, an operator can leverage the high capacity of PONs to achieve an integrated fixed-mobile metro-access optical backbone. The integration of RAUs through RoF links with fixed broadband PONs can be realized through various architectural configurations as the metro-access ring network exposed in [46]. Some PON-radio system integration schemes are depicted in Figure 3.9. A first intuitive solution consists in sharing blindly the same Optical Network Termination (ONT) between a customer Optical Network Unit (ONU) and an RAU. However despite its simplicity and unless designing suitable traffic prioritization techniques, the benefit of such a scheme may be lowered because of occasional congestion that causes QoS degradation when too numerous RAUs are connected. To manage efficiently both RAU and fixed broadband traffic, a single integrated ONU-RAU hybrid device may be required as shown in the proposal of [44] where EPON and WiMAX are merged together into a single network interface.

When the bandwidth offered by a standard PON network[9] is not large enough to meet the bandwidth requirements to backhaul both fixed broadband terminations and RAUs, a WDM overlay could be used to provide extra capacity. Such an integration scheme consists in using the optical capacity of the WDM-PON by separating a group of RAUs from other ONUs through coarse or dense WDM multiplexing [2].

• **Challenges and constraints at the MAC layer:**

---

[9]With a single upstream/downstream optical channel.
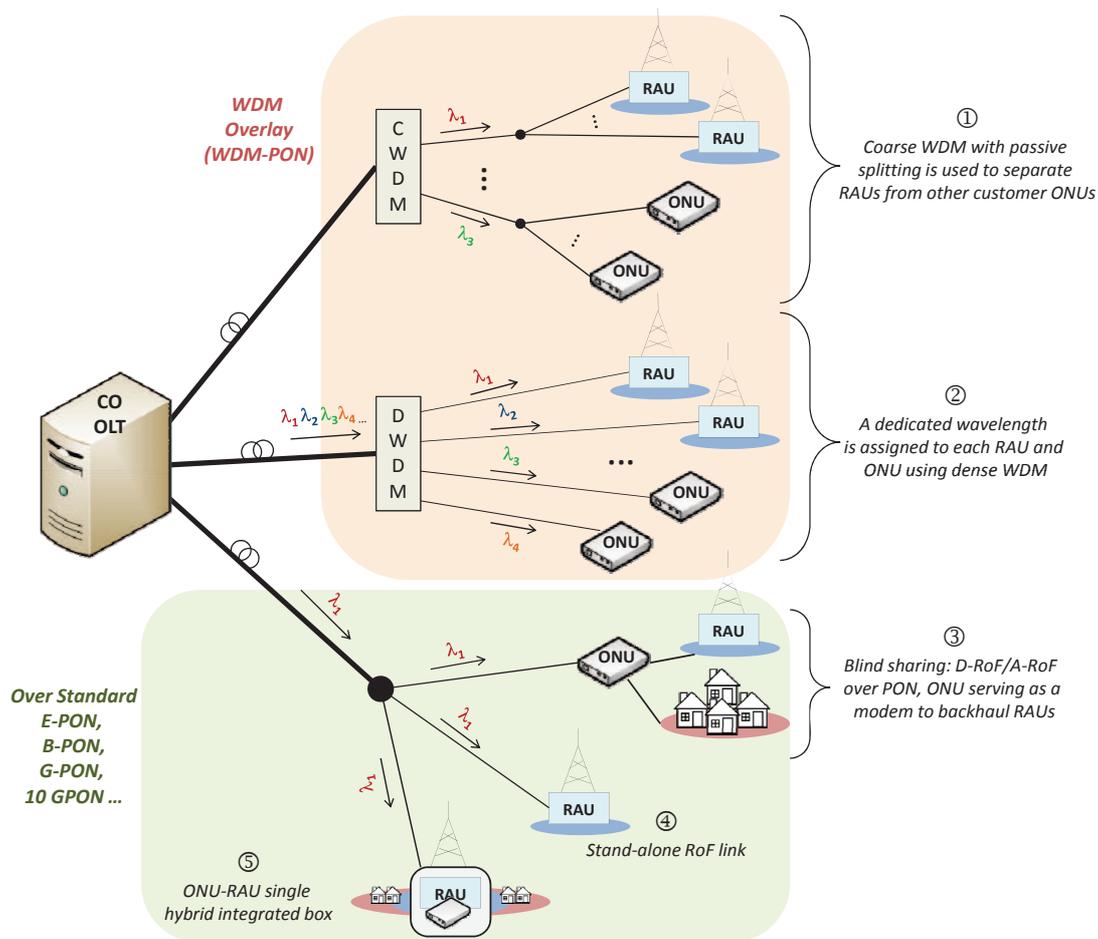
Figure 3.9: Different RoF-fixed optical broadband integration schemes.

For RoF-based PMP radio signal distribution systems, the constraints imposed by upper layers especially in terms of Round Trip Time (RTT) delays at the MAC level may limit the maximum RoF link length. By centralizing both signal processing and radio resource management at the CO, mobility management and mobile's medium access delays are also controlled remotely. As a consequence, to avoid poor performance (data throughput) or failure of the MAC mechanisms, a special care has to be dedicated to the network design in order to make the RoF layer not conflicting with the MAC protocol timing constraints [9]. Since RoF technology was thought initially to federate a high number of RAUs, it's likely that only short RoF links may be accommodated with systems where distributed MAC protocols are implemented (like *IEEE 802.11* standard). In contrast, centrally controlled MAC protocols such as those used in *Hyper-LAN* and *WiMAX* systems are more suitable for long RoF distribution links. Actually, it turns out to be difficult to work out a RoF deployment in a PMP configuration without constraining the link design by MAC considerations.

In indoor applications, where different MAC protocols are still competing to get standard-ized, there is a possibility to design as in [10] and [68] a RoF network together with its own MAC protocol. Liberty of choice in the design of the best-suited MAC protocol for the consid-ered configuration does not exist in public outdoor environment. Mobile *WiMAX* and *3GPP 3G/4G* mobile systems have their MAC protocols already standardized. Thus, unless designing a gateway to interface seamlessly with the radio system MAC layer as proposed in [60] and [69] which comes at an increased complexity of the system, RoF outdoor systems should be the most *MAC-agnostic* as possible. Furthermore, a RoF MAC-agnostic backhaul network constitutes a cost-effective solution to accommodate the reality envisioned by [48] and [83], where various radio mobile systems coexist seamlessly together.

(a) Analog RoF downlink transmission link.

(b) Digitized RoF downlink transmission link.
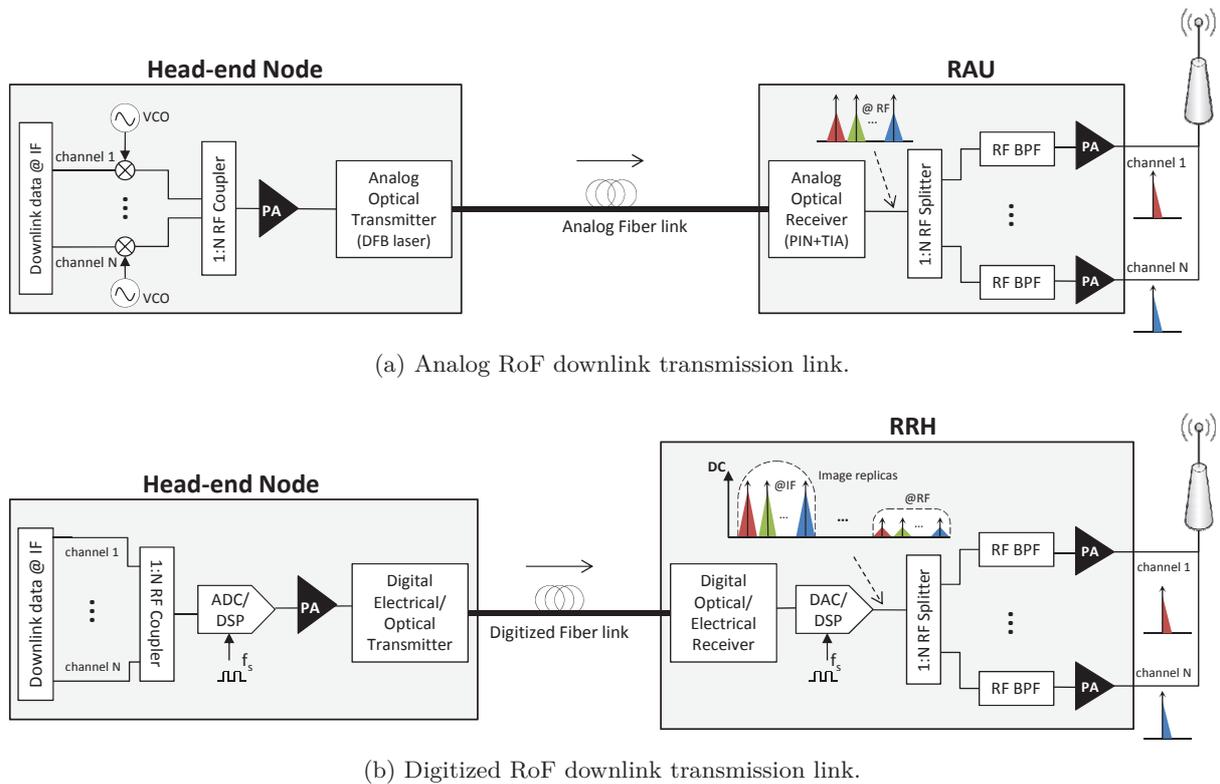
Figure 3.10: Multi-channel radio signal distribution using Radio-over-Fiber (RoF).

With a sufficient bandwidth of the laser and the Receiver Optical Sub-Assembly (ROSA) package of an A-RoF link, the multi-channel SCM radio signal is recovered and each radio channel is extracted using a Band-Pass Filter (BPF). For the case of D-RoF, we exploit the up-conversion feature of the bandpass sampling theory. At the output of the DAC, several images replicas of the digitized SCM signal spread through different Nyquist regions. Most of the power of the sampled signal falls within low order Nyquist regions (at Baseband and IF) leaving higher order Nyquist regions (at RF) with low spectral power distribution. Selecting the appropriate Nyquist region provides the bandpass original SCM signal at the desired wireless frequency, thus preventing the use of oscillators and mixers at the RRH. Note that depending on the sampling rate and the spacing between the radio sub-carriers of the original signal, the different channels may be located at the same Nyquist region or at different regions, the spacing between channels after bandpass sampling is reduced accordingly [111].

3.3.2 D-RoF *vs.* A-RoF: An economic analysis

In this section, we focus on the comparison between analog and digital optical transmission for RF distribution based on RoF technology. Figure 3.10 shows the block diagram (for downlink) of A-RoF and D-RoF transmission links respectively. Using A-RoF (subfigure 3.10a), several modulated radio signals generated at the head-end node at Intermediate Frequencies (IF) are up-converted to their radio-frequencies by means of mixers and Voltage Controlled Oscillators (VCOs), then power combined to form an SCM RF signal that directly modulates a DFB laser. Upon reception at the RAU, the analog modulated optical carrier is photo-detected using a PIN diode implemented with a Trans-Impedance Amplifier (TIA). The recovered SCM signal is power splitted, each RF is extracted from the multiplex using a stack of BPFs, then amplified and radiated into the cell. The schematic of multi-channel radio signal transmission using D-RoF (subfigure 3.10b) is similar to A-RoF but it highlights additional items required for signal digitization. In the downlink path, several wireless channels at different IFs are electrically combined at the head-end node before digitization using an ADC locked at a given sampling frequency (f_s). Considering OFDM modulated signals (*WiMAX*, *LTE*), the ADC is supported by a DSP to implement FFT(Fast Fourier Transform)/IFFT (Inverse FFT) processing blocks. The sampling rate of the ADC is selected based on the Band Pass Sampling theory. BPS under-samples a modulated signal to achieve frequency shifting by intentionally aliasing the information bandwidth of the signal. Hence, unlike classical Shannon's sampling, a significant reduction of the the sampling rate can be achieved, since BPS is no longer based on the frequency of the radio carrier but on the occupied bandwidth of the signal [116].

Upon digitization, the serial digital bit stream is processed and transmitted using an optical digital transmitter. The digital processing at the transmitter includes bit framing, appending a preamble sequence and additional fields for control and clock management, the details of these operations depends on the adopted digital transmission technology (PDH/SDH links, P2P Ethernet). Upon reception by the digital receiver at the RRH, the analog signals including the image replicas are reconstructed with a DAC. The output analog signal is amplified and power-splitted into several branches of BPFs. By focusing on the RF spectrum replicas in higher order Nyquist zones, each filter extracts the desired wireless channel at its radio frequency before the air-interface. By doing so, the wireless signals are up-converted to their air propagating microwave frequency without requiring any mixers or local oscillators, which simplifies the architecture of the RRH. The experimental feasibility of such a frequency relocation scheme using bandpass sampling theory has been addressed and discussed in [154].
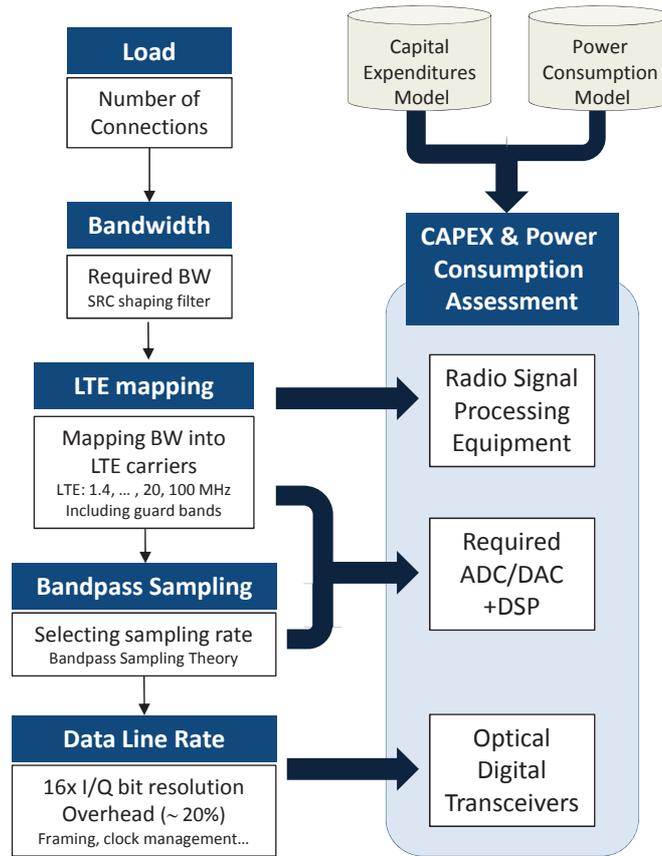
Figure 3.11: Methodology for A-RoF and D-RoF link modeling.

For each traffic load, the required Bandwidth (BW) is determined assuming a Square-Root Cosine (SRC) filter with a roll-off factor of 0.25 for pulse shaping. BW is mapped according to the standardized radio carrier spacings. Guard bands are also included on both sides of the RF channel according to the mobile system standard [133]. Using the bandpass sampling theory, the required sampling rate is computed which enables to target the suitable ADC/DAC for that purpose. In-phase (I) and Quadrature-phase (Q) samples are quantized with 16-bit resolution. Additional overhead bits are included for framing, control sequences and clock management. The proportion of such an overhead varies with the adopted transmission protocol. The sampling rate with the overhead bit rate gives the total line rate.

3.3.2.1   Traffic, Cost and Energy consumption models

The comparison scenario between A-RoF and D-RoF assumes four different types of services whether being symmetric/asymmetric or real-time/non real-time. Using service QoS attributes detailed in [153], we consider in the following four traffic types, namely: a conversational voice service (real-time symmetric, 16 *kbps*, using AMR speech Codec), a Best-Effort (BE) Web browsing (non real-time asymmetric, 30.5 *kbps*), an interactive multimedia service on Web (384 *kbps* with MPEG-4 video Codec) and Video on Demand (VoD) (real-time streaming and highly asymmetric, 2 *Mbps*). Then, three traffic-mixes are considered in our model and computed as a weighted composition of the four aforementioned traffic types. The data-rate of each traffic-mix and the corresponding service composition are given in Table 3.2. Mix$_1$ corresponds to a typical service composition when the voice traffic is dominant, Mix$_2$ may describe the recent past trend in traffic distribution (the overall traffic is equally splitted between voice and data)

Table 3.2: Traffic model based on services mix.

	Voice	BE Web	Multimedia on Web	VoD	Data-rate/connection
Mix$_1$	65%	30%	5%	0%	$\simeq 38.5$ *kbps*
Mix$_2$	50%	35%	10%	5%	$\simeq 157$ *kbps*
Mix$_3$	30%	40%	20%	10%	$\simeq 294$ *kbps*

Three traffic-mixes are considered to illustrate three key phases of the traffic evolution of mobile users. Mix$_1$: operators still deal with voice call service as the dominant transported traffic. Mix$_2$: More and more internet applications turns on mobile platforms, voice and data are equally distributed. Mix$_3$: Data overtook voice-grade traffic, heavy data-rate streaming services (like live or VoD stream) gain more popularity and challenge the capacity of the backhaul network to cope with.

while Mix$_3$ stands for the current trend observed by operators (with the rapid development of mobile smart-phones and the widespread of rich-content sharing applications, data overtook voice traffic) and expected to strengthen for the coming years.

The comparison between A-RoF and D-RoF RF distribution schemes addresses both the CapEx cost in terms of number and types of required equipment and OpEx cost in terms of energy consumption. Figure 3.11 depicts the methodology of the simulation scenario. Starting from a given cell load (number of connections according to traffic-mix Mix$_i$), the required bandwidth (BW) (including guard bands) is mapped into radio carriers as specified by the mobile radio system (*LTE* is assumed in our case) [133]. Then the minimum sampling rate is computed using bandpass sampling theory. Actually, the choice of the sampling frequency depends on the minimum f_{min} and maximum f_{max} frequencies of the signal. Equation system 3.1 expresses the relationships that must be satisfied to prevent spectral aliasing [62]

$$\begin{cases} 2\frac{f_{max}}{n_z} \le f_s \le 2\frac{f_{min}}{n_z-1} \\ 1 \le n_z \le \lfloor \frac{f_{max}}{B_s} \rfloor \end{cases} \tag{3.1}$$

where n_z is an integer, B_s stands for the bandwidth of the passband signal and $\lfloor \bullet \rfloor$ designates the integer floor function. According to the passband sampling theory, the digitized signal in the spectral domain is replicated at n_z multiples of the sampling frequency. On one hand, a higher n_z leads to a lower sampling frequency (which relaxes the requirements on the DAC/ADC) but produces in the same and narrower Nyquist region more signal images closer to each other. In fact, studying the performance of multi-channel transmission by D-RoF, it was shown in [154], that original RF signals that do not belong to the same Nyquist zone (because of a narrower Nyquist region), the spacing between their replicas falling in the same Nyquist region is drastically reduced which in turn increases the inter-channel interference and degrades the Signal to Noise Ratio (SNR) of the recovered RF signals. One the other hand, a lower n_z leads to a higher sampling rate which increases the cost of the required technology of the ADC/DAC. As in [62], a tradeoff between the aforementioned constraints is achieved by selecting n_z at mid-range and the sampling rate is calculated accordingly. The data-line rate of the digital bit stream is determined assuming a 16-bit quantization and including processing overhead.
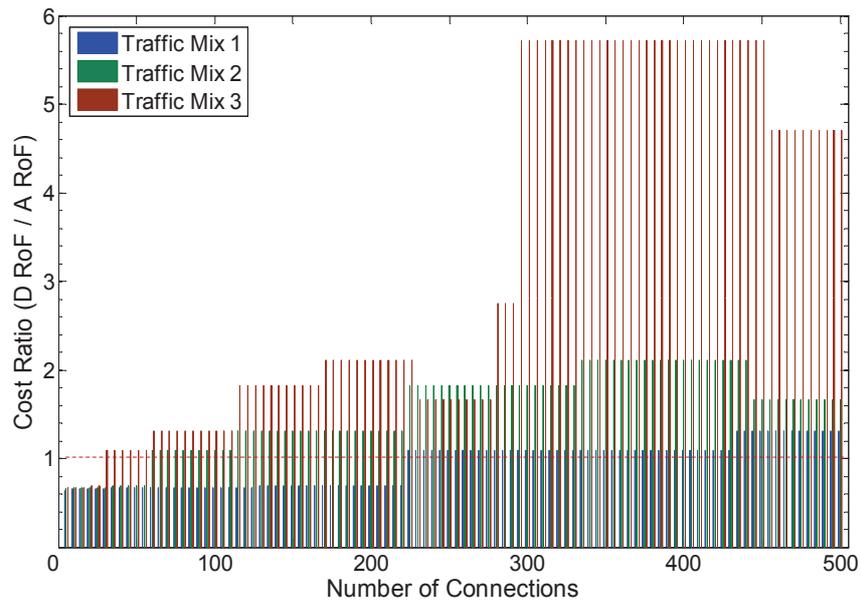
(a) Evolution of CapEx ratio D-RoF/A-RoF with traffic load.
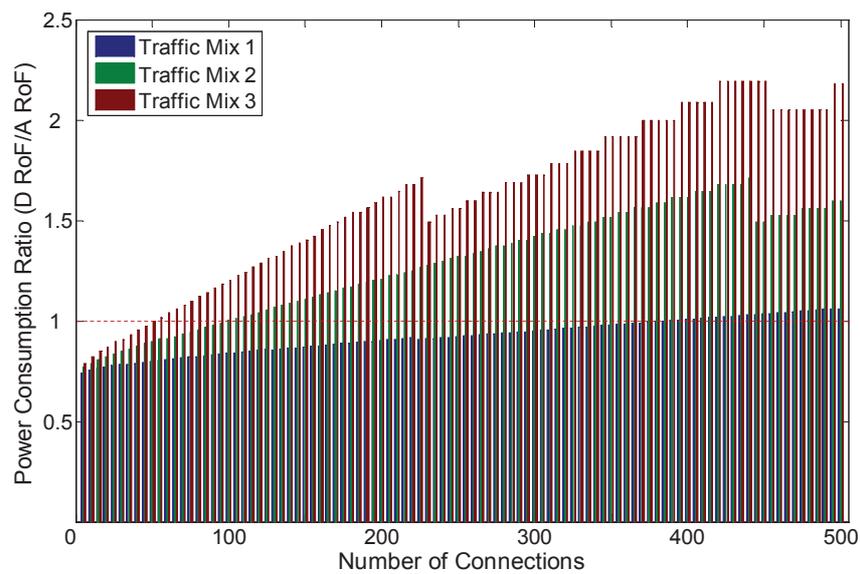
(b) Evolution of power consumption ratio with traffic load.

Figure 3.12: CapEx and power consumption assessment for 3 different traffic mixes.

The total cost of the RoF link is computed through an inventory of the different equipment involved in the transmission chain. As shown in Figure 3.11, they are deduced at different stages of the methodology process. RF signal processing equipments (amplifiers, VCO, filters etc.) are determined at the *LTE* RF carriers band. The calculated sampling rate determines the required ADC/DAC and the digital transmission line-rate enables to target the suitable digital transceiver. Our cost model database uses available price information from suppliers (for low volumes production). For the digital transmission, a typical T1/E1 LIU framer module[10]

for instance costs $\approx$ 400€, while a 1000Base-LX, 10GbE-LR and 40GbE-LR optical Ethernet transceivers costs $\approx$ 1000€, $\approx$ 2000€ and $\approx$ 6800€ respectively based on the estimations in [34]. The cost of digitizers increases with the resolution, the sampling rate and the processed bandwidth. In our evaluation, the considered ADC/DAC devices operate with 16-bit resolution and 50 MHz bandwidth. Typical reported costs[11] are for instance 850€ at 50 MSample/s and 4000€ at 250 MSample/s. For the analog case, a typical low noise DFB laser with 2.5 GHz bandwidth and a ROSA package can comfortably fulfill the required operation; a total cost of 2000€ is considered[12]. A $1:2$ Power splitter/combiner[13], an RF Bandpass cavity filter[14] and a wideband VCO with an up-converter frequency mixer[15] cost a total of around 60€. Both analog and digitized links use amplifiers to boost the signal at the transmitter driver (head-end node) and to fulfill the cell coverage (RAU, RRH). Based on the analysis in [115], a amplifier gain of 25 dB is typically required to cover a 100 m cell range. In our model, a wideband RF amplifier[16] with a cost of 50€ is assumed.

Both A-RoF and D-RoF transmission links are compared also in terms of power consumption. Data of power efficiency and energy consumption are provided in Table 3.3.

Figure 3.12 illustrates the evolution of the CapEx and power consumption ratios of Digitized to Analog RoF versus traffic load (expressed in number of connections according to the three traffic-mixes).

One notices that D-RoF enables lower CapEx than A-RoF only at low traffic loads. The CapEx advantage of A-RoF over D-RoF increases with traffic evolution which tends to be more packet-oriented than circuit-oriented. In terms of OpEx, the superiority of D-RoF on A-RoF is noticeable only under traditional predominant voice traffic. Note that the sawtooth shape of the OpEx (Figure 3.12b) and the stair-steps shape of the CapEx (Figure 3.12a) costs are justified by the fact that above a small increment in the number of connections, transmission equipment of a higher hierarchy (for instance T3/E3 instead of T1/E1 transceivers) are required for the D-RoF link. Similarly, in Figure 3.12, the cost ratio of D-RoF to A-RoF may decrease at specific values of traffic loads when the number of connections increases. This is the case for

---

[10]Line Interface Unit (LIU) reported from Dell-Sonic Wall Inc.

[11]Reported from National Instruments Inc.

[12]Reported from OZ510 datasheet at *opticalzonu.com* [34]. A total cost of 1600€ is also reported in [115]

[13]RPS-2-30+ wideband (10 − 3000 MHz) with 22 dB isolation. Reported from *mini-circuits.com*.

[14]SY-BP-2250+, wideband BPF with insertion loss < 1.5 dB at 2 GHz. Reported from *mini-circuits.com*.

[15]ROS-2500+, wideband VCO with 20 MHz 3-dB bandwidth, −16 dB 2nd harmonic. SIM-U432H+ for up-converter mixer. Both reported from *mini-circuits.com*.

[16]ZX60-2534M-S+ (38.5 dB gain at 2 GHz) reported from *mini-circuits.com*.

[17]With GMSK (*2G*) and 8-PSK (in *EDGE*) modulations, the PAPR is low regardless of the modulating signal which allows to work closer to the 1-dB compression point of the PA, thus increasing the power efficiency.

[18]Although not considered for the sake of simplicity in the assessment, a high back-off (due to a high PAPR) degrades the Signal-to-Quantization Noise Ratio as well, thus lowering the maximum resolution of the ADC/DAC.

[19]Figures of maximum power consumption are average values scaled to a single transmission port. They are based on CISCO Nexus7000/Juniper EX8216 GigaBit Ethernet transceivers and derived from [73] [147]. The E-circuit standards form part of the PDH/SDH transmission hierarchy where groups of E1 circuits are bundled onto higher capacity E3 and E5 circuits. Only commonly used E-circuits are considered in the model.

Table 3.3: Power consumption model for A-RoF and D-RoF links.

Laser	DFB laser biased at 40 mA with a drop modulation voltage of 2 V [31]	80 mW
	Laser dedicated cooling: Power required to cool the heat dissipated by 1 W [108]	$\simeq 0.36\ W$
	Laser bias driver	60 mW
PIN	PIN reverse biased at 3 V with a photocurrent of 1 mA [31]	3 mW
	Trans-Impedance Amplifier (TIA)	80 mW
LO	RF Voltage-Controlled Oscillator (VCO) delivering 12 V with 28 mA supply current.	336 mW
BPF	RF filter with DC power characteristics 5 V and 4 mA.	20 mW
PA	The energy consumption of an amplifier is mainly determined by its efficiency. Such a metric shows how efficiently the supply DC power is converted to RF power. Broadband electrical amplifiers suffer generally from a poor efficiency compared to narrow-band Class-A amplifiers. In the RoF link, Power Amplifiers (PA) are introduced at the transmission stage (transmitter drive amplifier) and at the reception stage (output PA prior to the antenna). For both stages, we consider a PA with an efficiency of $\eta_{max} = 22\%$ at the 1-dB compression point. Unlike *2G/2.5G* mobile system radio signals characterized by constant envelope amplitude over time[17], OFDM-modulated *LTE/WiMAX* radio signals suffer from high Peak-to-Average Power Ratio (PAPR) that leads to signal clipping. In *LTE* for instance, a maximum clipping probability of $p = 10^{-4}$ leads to a PAPR γ given by: $\gamma = -\frac{1}{2}\mathcal{W}\left[-6\frac{\ln(1-p)^2}{\pi \cdot N^2}\right]$, where N the number of OFDM subcarriers and $\mathcal{W}[\bullet]$ the Lambert's $\mathcal{W}$-function [121]. To meet achieve such a PAPR value, a back-off [18] from the 1-dB compression point is operated which further decreases the efficiency of the amplifier. After back-off, the efficiency of the amplifier is re-evaluated as: $\eta = \eta_{max}/\gamma$. To compute how much needed supply DC power, we estimate the transmit power at the output of the PA. For broadband operation, the optical transmitter is considered to have a lossy matching which requires +5 dBm at the output of the transmitter drive amplifier [31]. The transmit power at the output of the reception stage PA is determined by the wireless range required to fulfill the radio cell coverage. For instance, based on the propagation model specified in [97], a transmit power of 2 W is sufficient to cover a pico-cell size of $\sim 100\ m$	
Digital Transceivers	Each optical digital transceiver is equipped with an optical Small-form Factor Pluggable (SFP) interface (or XFP/SFP+ for bit-rates of 10 Gbps) to perform the optical transmission of the digital stream. Following the approach of [134], the total power consumption of a transceiver is split into two main parts. The first one is traffic independent and models the power consumption of the backplane of the transceiver. The second one is line-rate sensitive [124] and has to be related to the amount of traffic traversing the transceiver interface. The relative influence of these power quantities is regulated by a weighing parameter α [134]. Thus, given: P_{max} the maximum power consumption of the transceiver, B_{max} the transceiver nominal bit-rate and B the transmitted bit-rate, the power dissipated by the transceiver is: $P_{tr} = P_{max} \cdot \left(\alpha + (1-\alpha)\frac{B}{B_{max}}\right)$. Following are typical reported values of P_{max}[19] for different transceivers:	
	E1 line transceiver	$\simeq 225.28\ mW$
	E3 line transceiver	$\simeq 1.54\ W$
	E5 line transceiver	$\simeq 5.65\ W$
	1 Gbit Ethernet Transceiver	$\simeq 9.31\ W$
	10 Gbit Ethernet Transceiver	$\simeq 39.18\ W$
	40 Gbit Ethernet Transceiver	$\simeq 104\ W$
ADC/DAC	ADC/DAC power consumption P_c increases linearly with the sampler clock frequency f_s according to [12]. The energy required for an ADC/DAC to process a charge sample at a given SNR is: $P_c \simeq \frac{f_s \cdot kT \cdot SNR}{(\alpha \cdot V_{DD})^2}$ where: k the Boltzmann's constant; T the absolute temperature; α the fractional swing and V_{DD} the supply voltage. It was shown in [111] that for a high resolution ADC/DAC, the SNR is jitter noise limited. Thus, considering a 16-bit quantization, the SNR is taken to be ~ 40 dB. Power consumption of the DSP is estimated assuming a single-chip flexible-size FFT/IFFT processor fabricated in 0.25 μm CMOS technology [61]. With 1024-point FFT, the processor dissipates 400 mW at 200 MHz clock frequency, thus displaying a figure of merit of 2 mW/MHz. Note that the size of the FFT block scales with the radio channel bandwidth.	
Losses	Cooling loss: Additional cooling required for system equipment [8]	$\simeq 10\%$
	Loss within power supply system and battery backup [8]	$\simeq 5\%$
TDM	The power consumption efficiency of a $1:k$ TDM MUX evolves approximately as $\log_2(k)$ times the consumption efficiency of a $1:2$ TDM MUX [123].	$\simeq 0.04\ mW/Mbps$ for $k = 2$

instance at 220 connections of traffic Mix_3 when the new introduced equipment is very little mutualized by the traffic connections.

(a) Traffic Mix_1 (b) Traffic Mix_2 (c) Traffic Mix_3
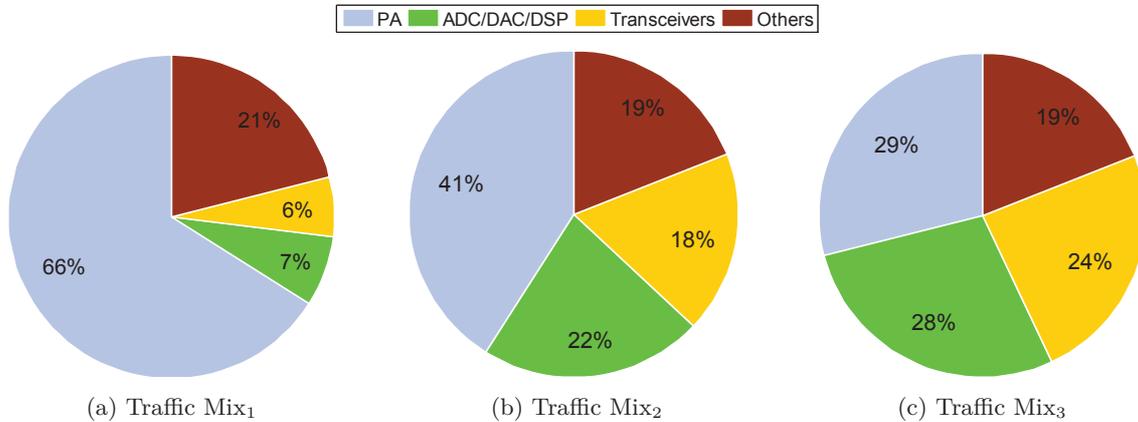
Figure 3.13: Power consumption profiling for 3 different traffic mixes.

At all traffic-mixes, the PA is the first major power-consuming, with a share of 66% at Mix_1 dropping to 29% at Mix_3. The power consumption of ADC/DAC/DSP evolves considerably as data traffic prevails over voice (Mix_2 and Mix_3). The power-consumption profiling shows also the increasing share of power consumption of digital transceivers, at Mix_3 the latter occupies 1/4 of the total power consumption. Finally, one notices the contrast between voice-prevailing traffic mix and data-dominating traffic mix. In fact, at Mix_1, the overall share of power consumption of electronics (34%) remains low compared to the PA consumption, while at Mix_3, ADC/DAC/DSP and digital transceivers taken together amount for nearly half of the total power needed by the D-RoF link.

We depict in Figure 3.13 a profiling of the power consumption of the D-RoF link at the three traffic-mixes. The profiling addresses the share of the main components of the D-RoF link (Power Amplifier, Optical Digital Transceivers, ADC/DAC/DSP and other system components) in the total power consumption.

3.3.2.2   Distributed radio sites using CPRI/OBSAI

Currently two protocols, namely Common Public Radio Interface (CPRI) [55] and the Open Base Station Architecture Initiative (OBSAI) [103], implement bandpass sampling-based I/Q digitization with standardized specifications on the sampling rate, the digital line-rate and a dedicated communication protocol for the transfer of the digitized signal. Both CPRI and OBSAI aims at making compatible radio equipments between the different vendors by proposing standardized and at some extent[20] open interfaces between radio equipments and between the radio equipment and radio controller.

• **CPRI:** In addition to the user plane (containing I/Q digitized data blocks), CPRI protocol specifies control/management and synchronization signals. Such overheads enable the digitized flow to be exchanged between the RRH and the radio equipment controller (head-end node) over a digital (either electrical or optical) serial link. In a distributed

---

[20]CPRI reserves a specific-vendor information field at its layer 2 protocol stack [55].
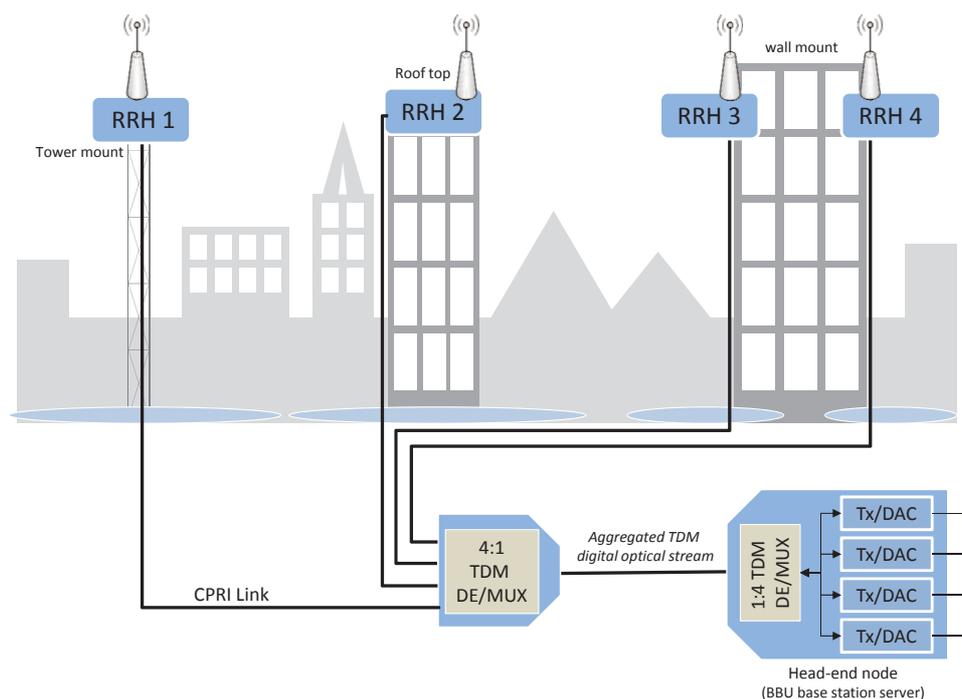
Figure 3.14: Distributed D-RoF architecture using CPRI.

Under heavy traffic loads, several CPRI links may be required to connect the RRHs to the radio network controller. The figure illustrates four RRHs connected to the Base-band Unit (head-end node) via a tree-topology using CPRI. A TDM MUX/DEMUX is used to aggregate the four CPRI links into a single TDM digital optical stream. The distributed D-RoF architecture follows the rationale of the Distributed Antenna System (DAS) concept. By splitting a macro-cell into smaller cells, it becomes possible to best manage bandwidth allocation by redirecting radio resources at the right traffic spot.

configuration, several RRHs can be linked to the head-end node using several network topologies: a tree, a star, a daisy-chain or a unidirectional ring. Originally indicated for P2P high capacity links, CPRI enables multiple digital flows to be connected to the radio controller in TDM mode. The type of the topology impacts the aggregated CPRI bit-rate; in a daisy-chained topology for instance, the closest RRH from the head-end node bears the accumulated digital flow from/towards the other cascaded RRHs.

- **OBSAI:** The OBSAI specification is supported both by equipment vendors and semi-conductor companies. The open group starts in 2002 and aims at defining an open standardized internal modular base station with specified interfaces. OBSAI sampling specifications are similar to CPRI, but the maximum line-rate (after control and management overhead) reaches 6144 Mbps.

- **CPRI *vs.* OBSAI:** Both CPRI and OBSAI are the most mature base station standardization initiatives. They share similar radio interfaces, but some differences are highlighted. By extending its specifications until the transport and application layers, OBSAI is better positioned towards multi-vendor interoperability, while by focusing on transport defini-
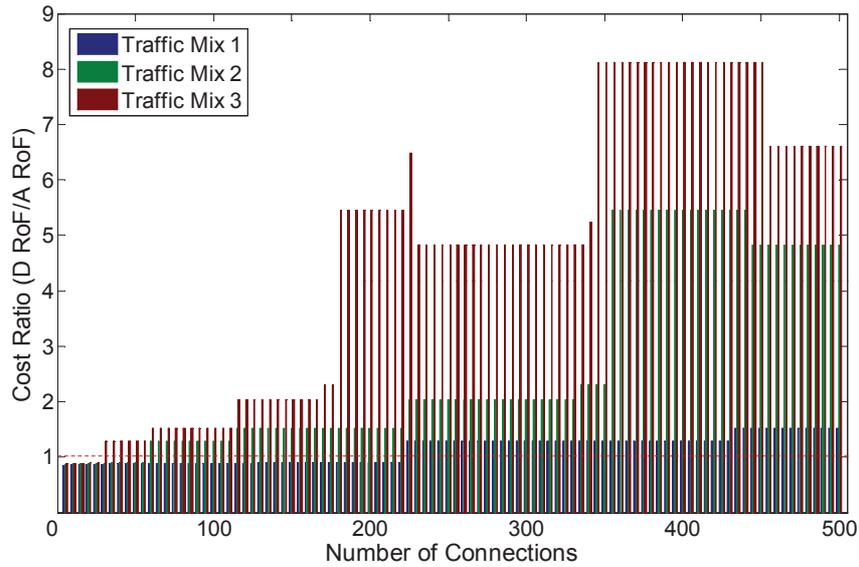
(a) CAPEX ratio *vs.* the number of connections.
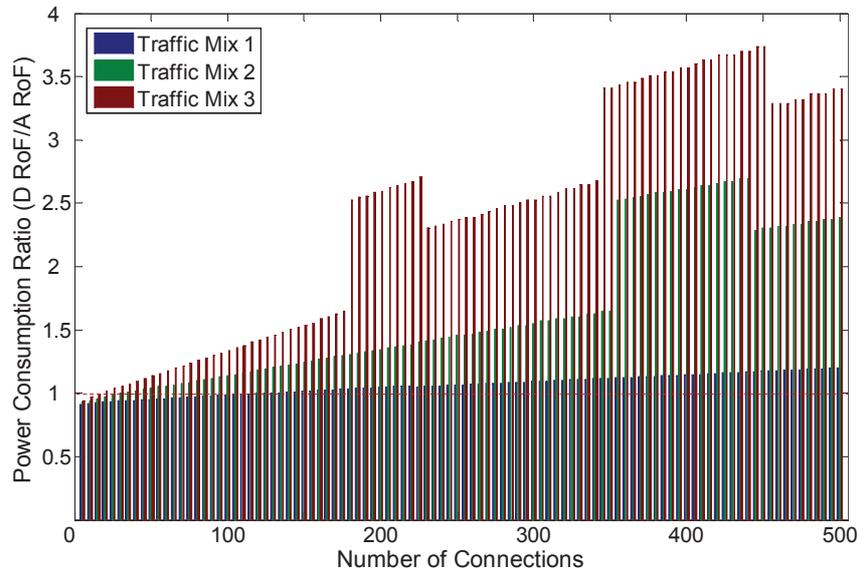
(b) Power consumption ratio *vs.* the number of connections.

Figure 3.15: Distributed D-RoF using CPRI: CAPEX and power consumption ratio.

tion, CPRI is more open transport oriented. Another main difference between CPRI and OBSAI lies in protocol implementation. CPRI leverages on higher carrier grade capacity thanks to air-interface programmable I/Q sample size, while OBSAI has a fixed message and sample envelope size. To enable flexibility, OBSAI trades with more overhead. For a 3072 Mbps link for instance, CPRI requires less than 7% of protocol overhead (measured in bytes) while 20% of overhead is necessary for OBSAI [21]. Finally, CPRI requires for the data-plane a bit-error rate (10^{-12})[21] less stringent than OBSAI (10^{-15})[55].

---

[21]According to CPRI specification 4.2 [*http://www.cpri.info*], it should be a design goal to avoid Forward Error Correction (FEC) at layer

- **Distributed D-RoF architecture using CPRI:** Since CPRI is more protocol efficient than OBSAI, we map the D-RoF link depicted in Figure 3.10b into a CPRI link. Indeed, the D-RoF link is mapped into several CPRI links when the line-rate exceeds the maximum line-rate specified by the protocol, *i.e* 3072 Mbps. The distributed D-RoF system architecture is illustrated in Figure 3.14. To backhaul several RRHs using a tree-based CPRI network, a TDM multiplexer and demultiplexer is used. Cost and power consumption assessments of the distributed CPRI architecture are carried out by following the same methodology described in Figure 3.11 but including the required CPRI overhead and selecting the sampling rates as specified by the CPRI standard to backhaul LTE channels [55]. A 1 : 4 TDM MUX/DEMUX (at 3.072 Gbps) costs 7000€ [34] and its power consumption is given in Table 3.3. Figure 3.15a depicts the evolution of the cost ratio of D-RoF/A-RoF in the distributed CPRI configuration and the power consumption ratio with the number of connections (traffic load) for the three traffic-mixes. Compared to results displayed in Figure 3.12, globally the cost of the distributed D-RoF link based on CPRI is higher than A-RoF link. The additional equipment needed to implement the distributed D-RoF network (TDM MUX/DEMUX, as well as more equipment are required by distributing the antennas[22]) explains the increase of the D-RoF link cost while the cost of A-RoF is kept unchanged. The trend is confirmed with the increase of the power consumption ratio between both RoF backhaul options as depicted in Figure 3.15b.

3.4 Generic RoF Access Network

Economic and power consumption advantages of A-RoF compared to D-RoF, motivate the proposal of an all-optical cellular backhaul architecture called GeRoFAN (Generic Radio-over-Fiber Access Network) featuring the transport of RF traffic from/to the RAUs to/from the head-end node network controller by means of A-RoF links. Figure 3.16 depicts the global architecture of the GeRoFAN network. Several RAUs, serving *4G* system radio cells and deployed across various geographical districts, are federated via an all-optical network to a head-end node also called Hybrid Optical Line Transmission (HOLT). The federating optical infrastructure between the HOLT and RAUs may be based on several optical loops, optical daisy-chains or optical trees. In this figure, a district refers to a set of neighboring cells corresponding typically to a leisure district, a residential district or a business district. By a rule of thumb, the number of cells within a given district is constrained by the power budget of the fiber link.

The usage of reflective optical modulators at the RAUs enables to mutualize all the optical transceivers at the HOLT and prevents from equipping each remote site with a dedicated costly

---

1 to reduce overhead and achieve cost-efficiency.

[22]Although the cost of a single equipment at the RRH is lower than the previous case since it works at lower digital rate, such cost saving is not sufficient enough to make the CapEx of the overall distributed architecture lower than the single D-RoF link considered previously.
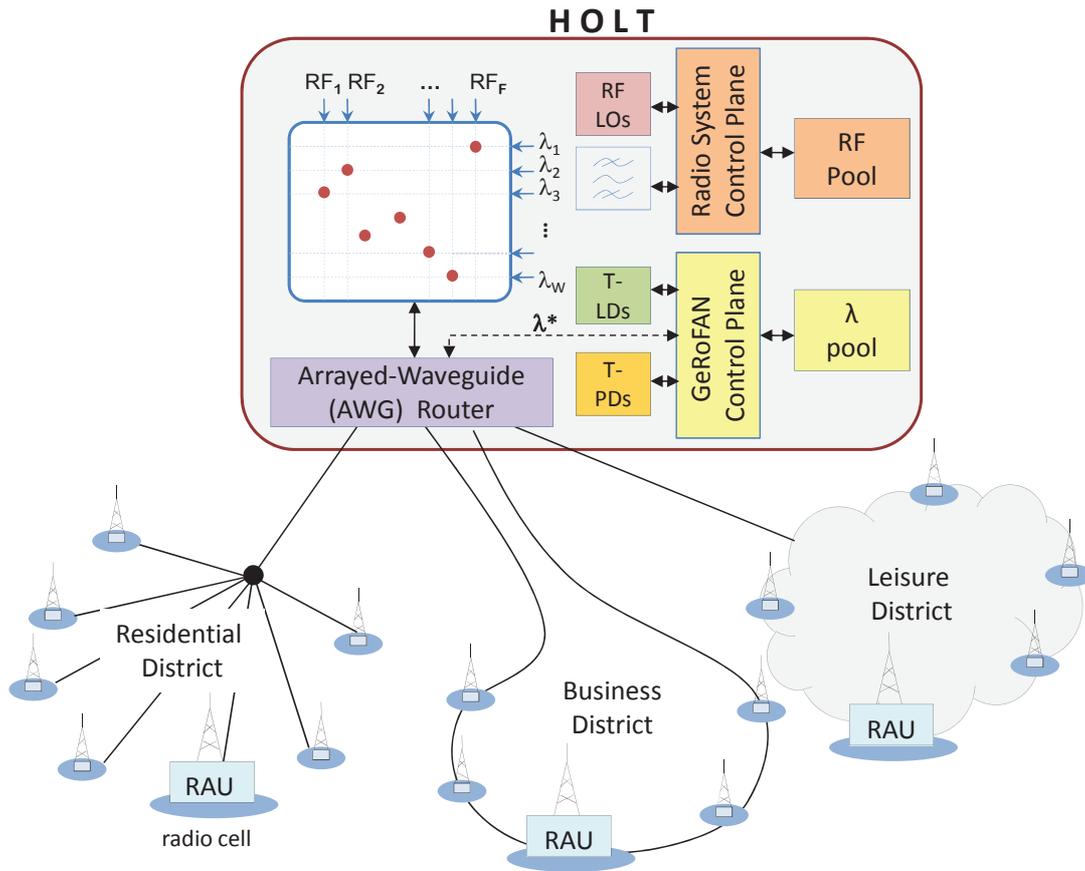
Figure 3.16: Generic Radio-over-Fiber Network Architecture.

tunable laser diodes and tunable photo-detectors. In addition, thanks to the transparency to the modulation format, A-RoF enables to co-localize at the HOLT all radio equipment (signals processors, RF LOs and mixers, ...) leaving the architecture of the RAU as simple as possible. The GeRoFAN system is supported by an innovative Control Plane (CP).

The CP exploits such a mutualization of radio and optical equipment at the HOLT, to allocate dynamically Optical Channels (OCs) and RFs according to the traffic fluctuation within each radio cell or more globally among districts. The GeRoFAN CP manages an RF-onto-λ switching matrix to control the placement of RFs onto OCs. Optical channels are then dynamically routed to each covered district by means of an Arrayed Wave-Guide (AWG) optical router located at the HOLT. AWG routers are cheap and cost-effective to implement in LiNbO3 or InP VLSI chips, however, their flexibility depends on the tunability of light sources [90]. An AWG router is a passive device made of a set of N monomode waveguides inserted between two passive optical stars $M \times N$ and $N \times M$ respectively. The switching mechanism of the AWG is based on the proprieties of optical interfometry. Assuming an AWG with P ports, if the AWG input/output ports are indexed by k ($k \in 0, \cdots, P$), the router is designed such that any
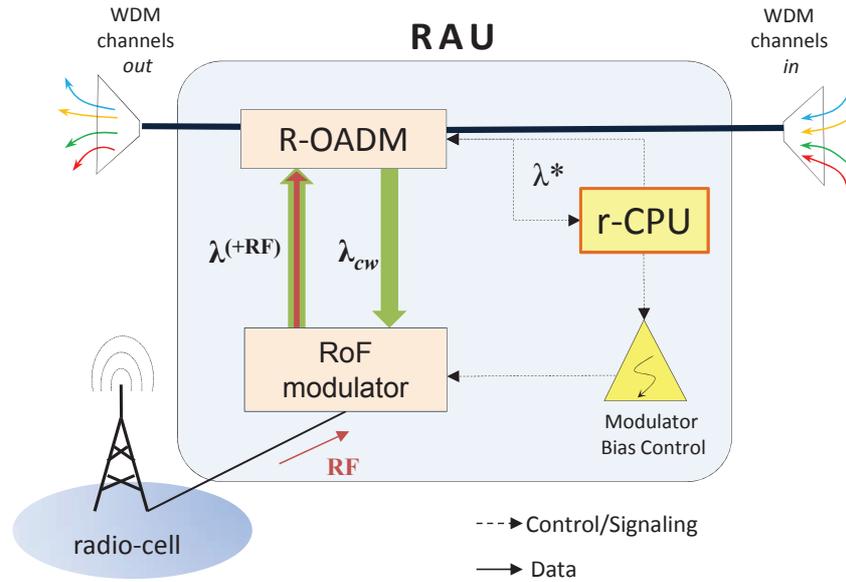
Figure 3.17: Radio-Access Unit (RAU) Architecture (for upstream radio traffic).

wavelength tuned at index k arriving on port p_i exits on output port p_o following the arithmetic rule $p_i + k \equiv p_o[P]$, where $x \equiv y[z]$ means x equals y *modulo z*.

3.4.1 The Radio Access Unit

The internal architecture of the RAU is depicted in Figure 3.17. We exploit the possibility to replace optical light sources at the RAU by a low-power consuming, easy-to-manage and remotely fed (from the HOLT) colorless RoF modulator[23]. At an RAU, the OC is dropped from the input WDM multiplex signal by a Reconfigurable Optical Drop and Add Multiplexer (ROADM). To distribute downstream traffic, the transported RFs are extracted from their OCs, amplified and radiated by the antenna into the cell. To backhaul upstream traffic generated within a given cell, an OC is extracted by the ROADM, modulated by its RFs in the analog RoF modulator and reinserted into the WDM multiplex. Some colorless RoF transceivers (Semi-conductor amplifier, Electro-absorption modulators ...) can perform both detection and modulation functions within the same device, assuming that the OCs' wavelengths used respectively for downstream and uplink traffic are widely separated to avoid interference. In addition, the RAU is equipped with a remote Control Plane Unit (r-CPU) whose role is depicted in subsection 3.4.3.

---

[23]Several options are envisioned based on electro-optic, electro-absorption modulators, injection-locked lasers. As developed in Chapter 4, the choice of the A-RoF colorless transceiver is a tradeoff between several considerations (cost, energy consumption, modulation performance ...) while privileging high-bandwidth capable modulators.

M-R A U

(a) M-RAU (for upstream radio traffic)

M-H O L T

(b) M-HOLT
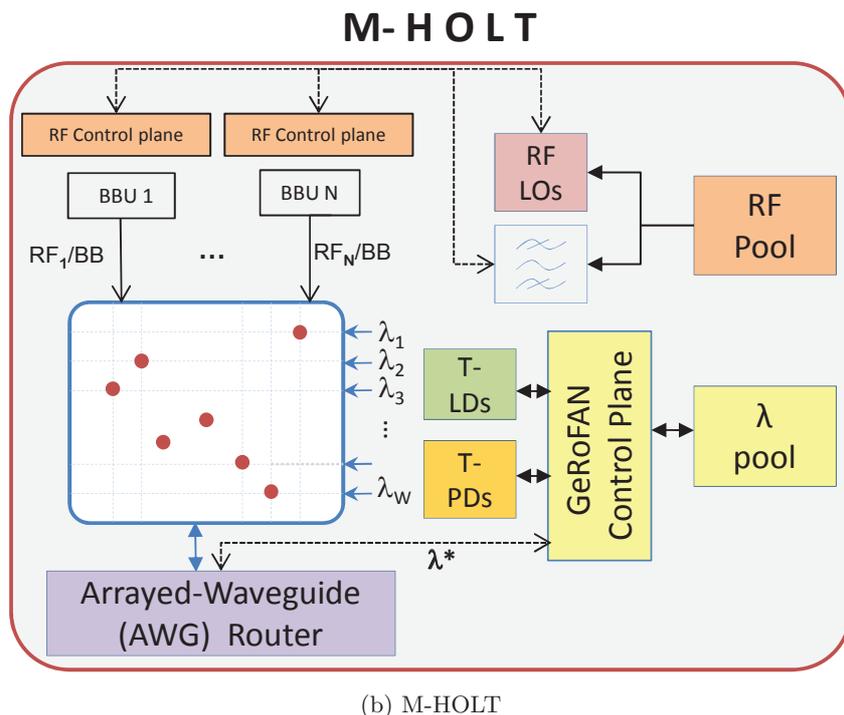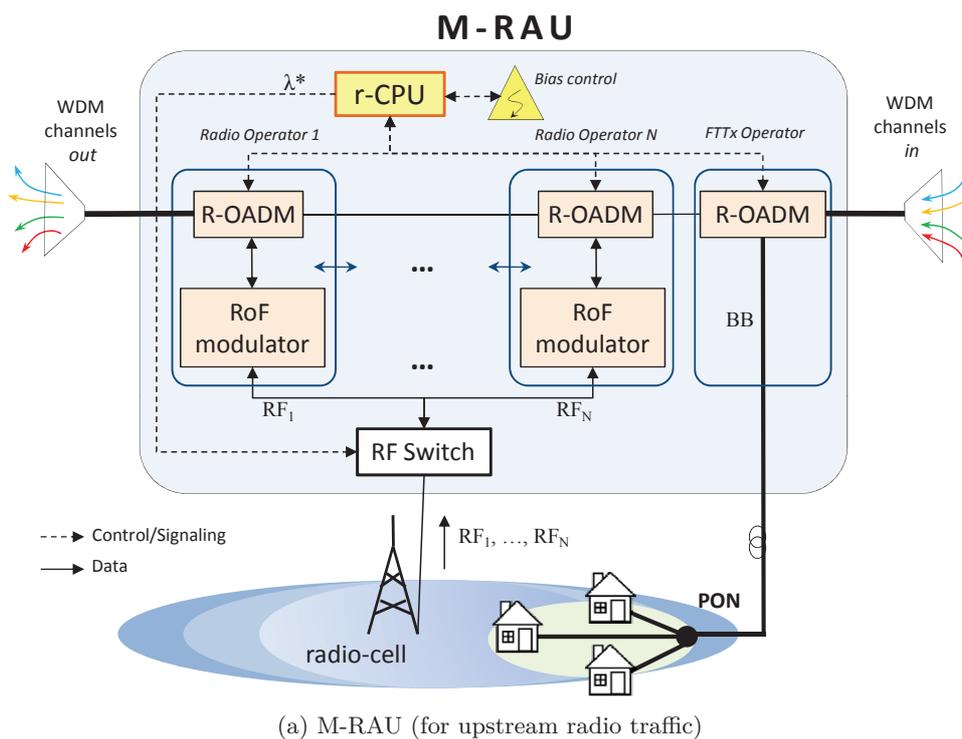
Figure 3.18: GeRoFAN accommodating multi-operator and multi-service operation.

3.4.2   GeRoFAN for multi-operator backhauling

The genericity of the GeRoFAN architecture enables to deal with several services/technologies or several operators within the same backhauling system. The architecture of the HOLT and the RAU are enhanced as illustrated in Figure 3.18. In the Multi-service HOLT (M-HOLT) (*c.f.* Figure 3.18b), several Base-Band Units (BBUs) process the traffic of different operators/services either wireless such as *4G WiMAX/LTE, 3G UMTS, Ultra-Wide Band (UWB)* or broadband fixed (FFTx). The internal architecture of the Multi-service RAU (M-RAU) shows a stack of several RoF-modulator/ROADM modules distributed among the multiple operators serving the same radio cell. Upstream multi-service radio traffic at an M-RAU is detected by a mutualized antenna and sent to an RF switch. Thanks to the GeRoFAN-CP, the RF switch is reconfigured to redirect each radio channel of a given mobile operator to its associated RoF-modulator/ROADM module. An FFTx operator benefits from the GeRoFAN infrastructure by sharing the same M-RAU as depicted in Figure 3.18a using an ROADM that drops the right optical channel modulated with BB users' data to serve FFTH subscribers of an overlying PON.
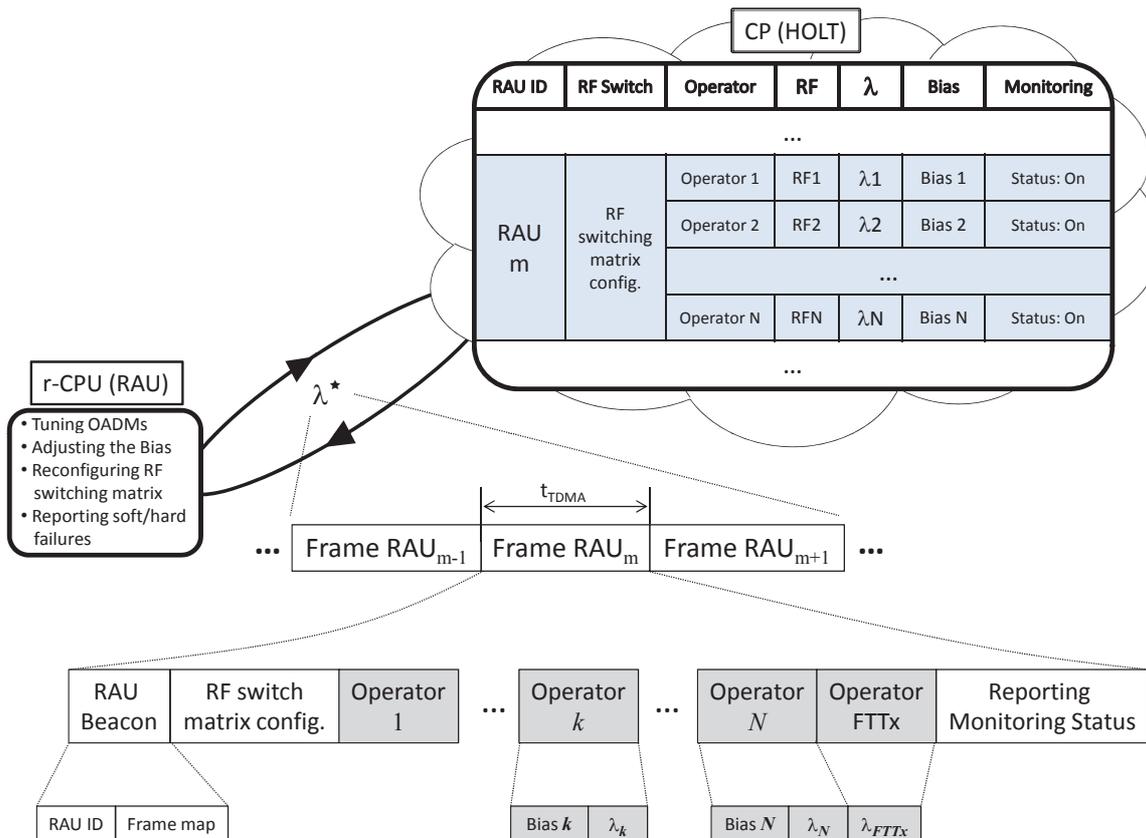
Figure 3.19: GeRoFAN-CP signaling and general frame structure of channel $\lambda^\star$.

3.4.3 GeRoFAN system control plane

3.4.3.1 System signaling

The direct benefit of traffic processing centralization at the HOLT is the possibility for the CP to acquire a global view of the load distribution across the cellular network and thus dynamically managing the bandwidth between RAUs using an out-of-band optical signaling channel $\lambda^\star$. The signaling channel is also used at the RAU level to enable the reconfigurability of the devices (automatic reconfiguration of the ROADM to drop/add the right OC, change of the bias of the RoF modulator to achieve optimal performance, reconfiguration of the switching matrix of the RF switch for M-RAU). The optical channel $\lambda^\star$ is accessed by RAUs on a TDMA basis; reconfiguration information are transported in base-band and processed by the remote CP Unit (r-CPU) equipping each RAU (*c.f.* Figure 3.17). Figure 3.19 illustrates the signaling mechanism between the CP and the r-CPU (at the RAU) using the control information encapsulated into a TDM $\lambda^\star$ frame in the general case where GeRoFAN is used for multi-operator backhauling.

3.4.3.2 Dynamic bandwidth management

To illustrate the dynamicity of the system, one may estimate that the activity of the business district does not coincide in time with the activity of the residential or leisure district served by GeRoFAN. The CP reconfigures the devices at the HOLT to dynamically assign, at a multi-hour scale, RFs and OCs to the district with increasing load. Shorter term horizon of the traffic fluctuation (*i.e*, cell localized load variation within the same district) keeps unchanged optical resources assigned to a given district, but reallocates RFs between the different RAUs within the same district. Such a reallocation of radio resources is carried out in accordance with radio cellular planning rules to minimize radio signal interference. Figure 3.20 illustrates how the GeRoFAN-CP enables optimal bandwidth management by shifting optical and radio resources at the two aforementioned time-scales.

3.4.3.3 Control plane design requirements

Dynamic bandwidth management realized by the control plane is achieved at a macroscopic time scale in terms of traffic fluctuations. This means that the GeRoFAN-CP deals with the aggregated traffic of the cell and ignores the packet time scale ($\sim ms$) which remains the focus of the radio mobile operator. Thus, the GeRoFAN system is a **radio MAC-agnostic**. By being MAC-agnostic, the GeRoFAN-CP is able to get applied to any radio system technology without need for costly and complex special engineering adaptations. It operates at time-scales ranging from few tens of minutes (shorter term traffic variations) to several hours (longer term variations). Indeed, the bandwidth relocation realized by the CP at the shorter term has to be
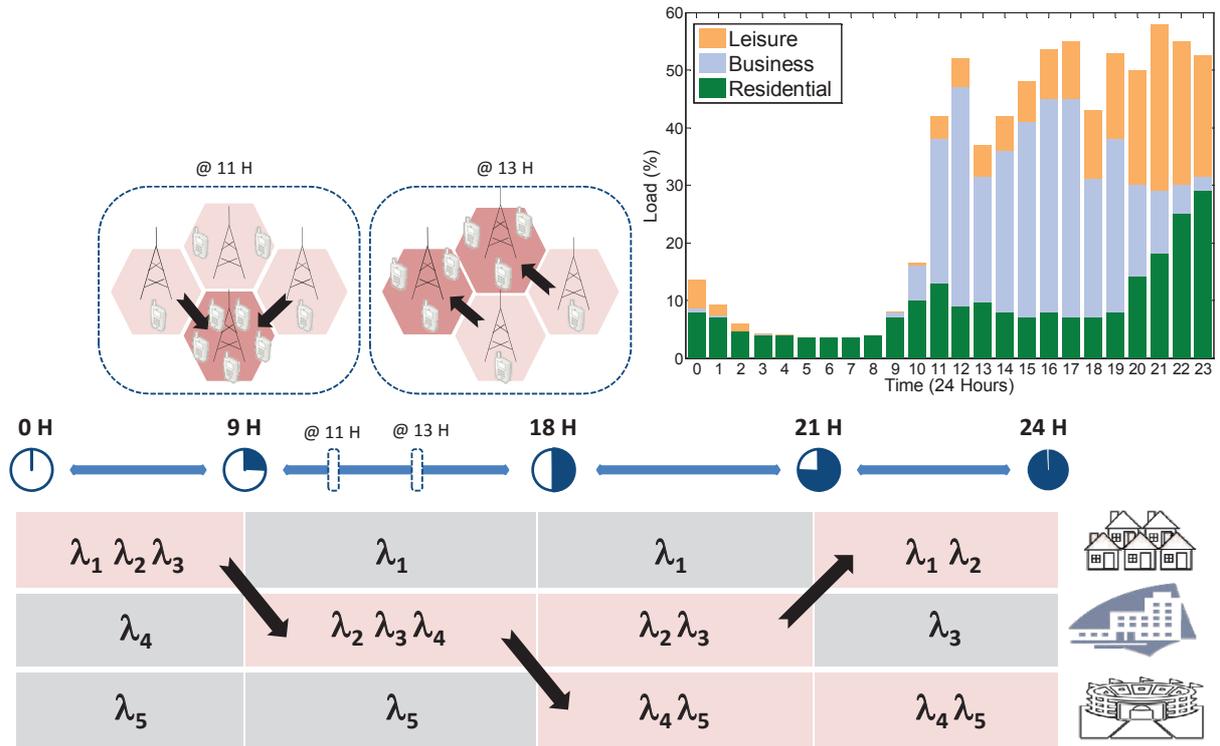
Figure 3.20: GeRoFAN-CP capacity management at short/long term time-scale.

Thanks to A-RoF, GeRoFAN acquires a global view of the traffic evolution. Supported by the CP, GeRoFAN performs dynamic bandwidth management at the short and medium/long term scales. Considering that GeRoFAN network is serving different functional districts, the CP exploits the daily pattern of the mobility of users to shift radio/optical resources among districts and cells. At multi-hours scale basis for instance, the CP shifts OCs from the housing area to the business area during usual working office hours time. At the end of the day, the CP allocates additional OCs to the leisure district since it becomes more solicited. At the evening, the traffic is more balanced between the housing and the leisure areas, as a consequence, there is no need to keep higher bandwidth at the business area where the load is decreasing. The shift of radio resources is achieved by the CP at a shorter time-scale. For instance, at $11 a.m$, a hot-spot is detected requiring to shift radio resources from neighboring cells where the load remains low. At the short time-scale, optical resources remain unchanged per district since the variation of the traffic matrix is triggered by some specific cells and not a set of cells.

achieved within the time-window at which the aggregated load in a given cell reaches its stable level[24].

In addition, as previously specified in Section 3.3, A-RoF transmission systems suffer from limited dynamic range, with link noise and RF distortions increasing with distance and the number of backhauled radio channels. In the contributions of [79] and [106] for instance, authors exploit the control centralization of A-RoF to propose optimized management of the radio/optical resources between RAUs without explicit consideration of physical layer impairments. To not loose the cost-effectiveness benefit of A-RoF (highlighted in Subsection 3.3.2), the GeRoFAN-CP has to be **Quality-of-Transmission(QoT)-aware**, to compensate for the various impairments stemming from A-RoF links. Unlike the compensation approach proposed in [43], where authors suggest the implementation at the RAU of costly pre-distortion and post-

[24]Actually the time-window is evaluated by monitoring the evolution of the aggregated traffic distribution based on real operation network. The time-window depends on the mobility pattern of subscribers, the size of radio cells, the network configuration (sectorization, inter-RAUs direct traffic pipelining using X2 interface in *LTE* for instance, type of area covered)...

distortion circuits based on adaptive learning algorithms, the QoT-aware CP has to mitigate RoF impairments through an original approach conducted from the HOLT and based on a deep knowledge of the physical layer.

In summary, supported by a radio MAC-agnostic and QoT-aware control plane, the GeRo-FAN architecture provides both an active and a non-intrusive cellular backhauling for the "hosted" radio system.

Part II

Physical Layer Study

Analog RoF Transmission Limitations in GeRoFAN

Contents

4.1   Introduction

RADIO signals transmission through A-RoF link is subject to several physical impairments that degrade the Signal-to-Noise Ratio (SNR) and by consequence the Shannon's capacity. Whatever the adopted network topology of the A-RoF system, it is necessary to characterize each relevant impairment and investigate the main parameters on which the GeRoFAN-CP could play to keep the Shannon's capacity as high as possible at the base stations. This chapter provides in Section 4.2 an overview of the main technological options for the RoF modulator and justifies the use of a reflective amplified absorption modulator as the most suitable candidate for GeRoFAN. A comprehensive analytical modeling of undergone physical limitations due to the different components of the GeRoFAN system is described in Sections 4.3, 4.4 and 4.5. Actually, several available simulation software tools[1] provides the opportunity to model physical layer impairments of analog optical transmission, however in most cases, these tools lacks the required genericity to accommodate any network or architecture configuration. Indeed, such tools are very useful to target a specific noise in a point-to-point network configuration. However, in our research, we put the focus on the mathematical development of GeRoFAN optical impairments in a networked configuration in order to understand the salient features of the physical mechanism behind each transmission noise. Such an approach enables to highlight the key parameters and variables that can be used by the CP as action levers to achieve an efficient cellular backhauling. Finally Section 4.6 draws out a big picture of our QoT-tool, a software programm[2] packaging the analytical modeling of GeRoFAN physical impairments. The QoT-tool enables the GeRoFAN-CP to integrate seamlessly the constraints of the physical layer and refine its backhauling strategy accordingly.

It is worth noting that the research scope of this chapter focuses only on evaluating the Shannon's radio capacity of the system for the upstream traffic[3].

4.2   RoF transceiver

The choice of the best transmitter equipping the RAU is subject to stringent requirements that have to be satisfied without penalizing the investment cost of the overall architecture. These requirements are summarized through some figures of merits such as: the link gain, the noise figure, the linearity and the dynamic range of the RoF link [96][34].

---

[1] For instance VPI Transmission Maker©, Simulink© or OptiSystem©.

[2] The QoT-tool is a programm developed in Matlab©, it is structured generically into modules, each module represents a specific impairment based on the mathematical modeling detailed in this Chapter. Depending on the GeRoFAN topology, the QoT-tool calls the different modules relevant to each step of the signal lightpath and updates the SNR of the optical carrier accordingly.

[3] Managing the radio capacity for upstream traffic is more challenging for a radio operator than the downstream traffic. Indeed, for the downstream traffic, the mobile operator knows *a priori* where the capacity would be redirected.

4.2.1 RoF transceiver technology survey

A first classification of RoF transmitter candidates can be made on whether these sources are wavelength-tunable or not. The tunability of the light source is mandatory to enable dynamic reconfiguration of the system. Thus, we identify two main categories for RoF transceivers at the RAU subject to whether the optical signal is generated locally or delivered remotely from the head-end node. Figure 4.1 depicts such a classification and main technologies used for each category.

4.2.1.1 RAU with locally generated optical signal
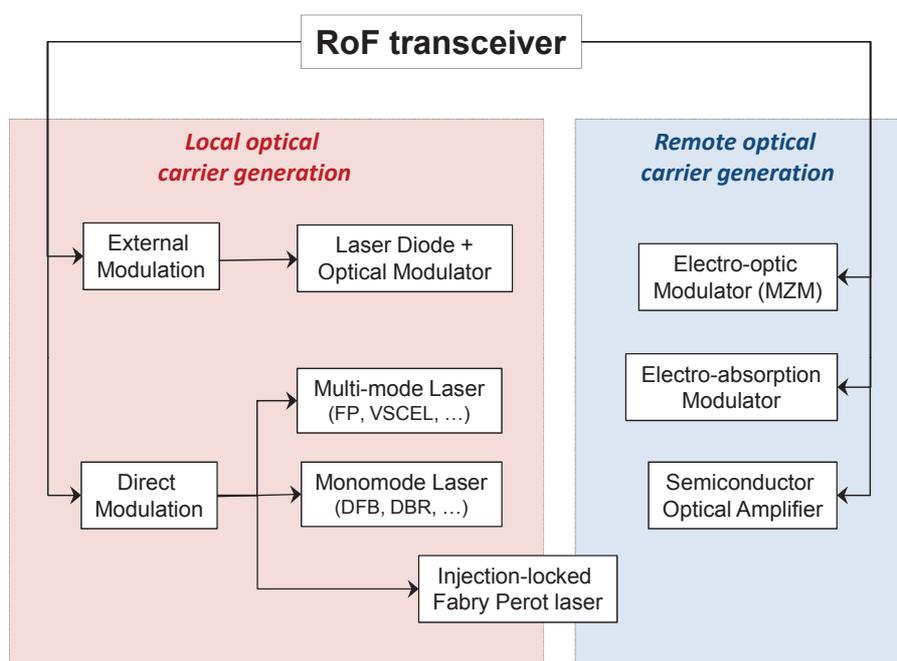
Figure 4.1: RoF transceiver technology classification.

With rapid wide scale deployment of broadband FFTx networks, remote light generation-based solutions become more attractive. Wavelength independent upstream transmission is enabled by several colorless components (electro-optic, electro-absorption, injection mode-locked, Semiconductor Optical Amplifier (SOA)). The similarity between the different solutions in terms of cost makes the dynamic range and the transmission performance as the key distinction criterion with respect to the target application.

Early RoF networks are deployed with a dedicated Laser Diode (LD) at the RAU. The optical signal generated by the LD may be either directly or externally modulated. In both cases, since each RAU is equipped with a LD, the investment cost of the overall system increases with the number of deserved remote cells which raises the problem of scalability in areas with high cell-density.

Two categories of optical sources are considered. Single mode longitudinal laser diodes (SMLD), DFB or DBR lasers, provide superior performance thanks to their high power, low intrinsic noise and their very narrow spectrum. They are widely adopted for long reach RoF

links with large dynamic range. However, since SMLD are still expensive, it seems economically not attractive to duplicate this cost at each RAU.

At the opposite, multi-mode laser diodes (MMLD) provide a more economical alternative for less demanding applications. Their utilization is restricted to short distance RoF links because of their low output optical power and high intrinsic noise. Fabry Perot (FP) laser diodes are the most common examples of MMLD. VCSEL MMLD [138] are also developed for remote antenna feeding and focus a great interest due to their low cost and performance for short range applications. Current VCSELs are available at 850 nm while DFB and FP lasers are operational around 1.3 and 1.5 μm [96]. While tunability of standard LDs raises several issues (cooling, control, cost, power consumption $\cdots$), Injected Mode-Locked (IML) FP lasers offer an elegant solution alloying low-cost and tunability. While IML-FP are well established, they suffer from limited spectral range. Note that the usage of Light Emitting Diodes (LED) has been also investigated in [71] but their poor performance compared to lasers restricts their utilization.

Operating at higher frequencies intensifies the limitations of direct modulation by approaching the limits of modulation efficiency. Therefore, using an external modulator in conjunction with the laser is preferable to ensure higher bandwidth with acceptable modulation performance [30].

4.2.1.2   RAU with remotely generated optical signal

For such a configuration[4], the RAU is equipped with an external modulator which is remotely fed by a high optical power laser diode (DFB) located at the head-end node. In addition to the RF equipment centralization, this configuration enables light source mutualization between different RAUs, thus reducing the system cost. Because the modulation at the RAU is carried out independently from the delivered optical carrier's wavelength, the RAU are classified as colorless. Electro-Optic Modulators (EOM) made with polymers, $LiNbO_3$ or III-V materials, are widely used as external modulators. Particularly, the electro-optic Mach-Zehnder interferometer Modulator (MZM) is recognized as the industry standard. However, MZMs suffer from some drawbacks such as non-linearity, low integration with semiconductors, and relative high cost [30].

Electro-Absorption Modulator (EAM) is an alternative to EOM. EAM relies on the Quantum Confined Stark Effect (QCSE) in quantum wells that leads to a change in the absorption profile of the incident light dependently on the applied electric field (which stands for the modulating voltage). Compared to MZM, EAMs have lower drive voltage, larger modulation bandwidth, and can be packaged with semiconductors through monolithic integration (EAM-DFB [77]). However, both MZMs and EAMs suffer from the non-linearity of their transfer function [156]. It is difficult to assess the superiority of one technology on the other due to the

---

[4]Also called as Centralized Light Seeding (CLS) configuration.

diversity of parameters as well as the continuous technological advances achieved by both of them. Nevertheless, an extensive comparison can be found in [120] based on a composite figure of merits.

A third interesting candidate for the RAU transmitter uses a Semiconductor Optical Amplifier (SOA) as a modulator [151]. By varying the bias current according to the RF sub-carrier, the gain of the SOA is modulated itself, thus modulating the optical carrier at its output. As opposed to the insertion loss of common external modulators (EAM, MZM), the amplification functionality of the SOA allows for relatively low power optical signal at its input. However, SOA modulators suffer from optical noise and non-linearity similar to directly modulated LDs [40].

Alternatively, monolithic integration can be achieved through EAM-SOA which corresponds to an amplified EAM. An EAM-SOA cumulates the advantages of the EAM as modulator with the amplification gain of the SOA. In the EAM-SOA design process, the performance of the integrated device are improved by shifting the amplification band of the SOA to coincide with the modulation peak of the EAM [39].

Finally, an Injection Mode-Locked Fabry Pérot (IML-FP) laser diode stands at a particular position as illustrated by the diagram of Figure 4.1. An IML-FP carries upstream data by direct modulation, the light is thus locally generated by stimulating the FP laser gain. Meanwhile, an external remotely generated continuous wave is injected into the FP cavity to lock the laser at the injected wavelength. The locked FP re-emits at the same wavelength than the injected one. The locking mechanism suppresses the original multi-mode nature of the FP laser, the locked device features a strongly single-mode operation with a Side Mode Suppression Ratio (SMSR) (used to assess how strong is the dominant mode of the laser spectrum) around 40 dB [99] (DFB laser displays 50 dB SMSR under appropriate bias [96]). Apparently, IML-FP cumulates both the advantage of the low-cost of the FP laser and the transmission benefits provided by the locking mechanism, however, the proprieties of the device is strongly dependant on the injected optical power that requires additional constraints to stabilize the locking mechanism.

4.2.1.3   Advances in external modulators:

• **Bulk-based device *vs.* Quantum Well (QW) structure:** For SOA modulators or semi-conductor LDs, compared to bulk materials, carrier density rises very sharply with the injected current into the active region which yields to a high differential gain [96]. For EAMs, the confinement of electrons and holes in the same physical QWs leads to the creation of excitons which interact with the applied voltage according to the QCSE effect [33]. In addition, using multiple QWs by piling up thin successive material layers helps increase both optical and carrier confinement that leads to enhanced performances. Moreover, multiple QW structures are preferable because the wavelength shift with the

temperature is potentially lower than with bulk devices, as well as polarization dependency [57]

- **Traveling Wave (TW) *vs.* Lumped structure:** Lumped devices are subject to *RC*-time constant which limits the bandwidth of the modulator at high RFs because the modulating signal is not constant during the transit time of the optical carrier through the modulator. For such high RFs, the lumped structure model is no longer valid. Instead, the concept of TW –where the capacitance is distributed along the modulator electrodes, is proposed. TW structures provide a broader bandwidth without degrading the modulation efficiency [156]. However, some design challenges related to velocity-match condition between the electrical signal and the optical carrier impact the efficiency of the TW modulator [30][96].

- **Reflective *vs.* Non-Reflective device:** Reflective modulators (REAM-SOA, RSOA, and REAM) are designed by adding a highly reflective coating at one side of the device. A reflective configuration enables to exploit the same single device twice. The RSOA and REAMSOA amplify both the incident optical carrier and the reflected one. The idea of a reflective device suits well the deployment of next-generation colorless (WDM)-PON architectures [20]. However, depending on the modulator length, a reflective configuration increases the transit time of the optical carrier through the device which may impede its use at very high data rates. Furthermore, RoF networks using reflective modulators are sensitive to Rayleigh Back-Scattering (RBS) whose penalty increases with the length of the fiber [144][59].

4.2.1.4   Full-duplex communication:

Although the modulation process is the most challenging step in the design of RoF link, the photo-detection process should not be neglected specially for downlink signals. For antenna remoting of cellular communication systems, all photo-detectors commercially available have a large bandwidth and a good detector responsivity. The most common receivers are based on the PIN structure [30]. Although these devices are relatively insensitive to temperature, some precautions are required in the packaging to minimize the fiber coupling loss and optical reflections as well as to improve the impedance matching. An additional interesting option for future RoF networks makes use of the same device to perform simultaneously modulation and detection functions achieving further cost savings. Besides the modulation functionality, photo-detection function has been reported for EAM [33] and SOA [143]. Simultaneous full-duplex operations of EAM and SOA requires balancing between modulation and detection efficiencies. By using a single device for full-duplex operation, the same bias point is set to satisfy both modulation and detection functionalities [4]. In-line with the concept of green networks, passive RAUs equipped with an unbiased electro-absorption transceiver have been proposed. However,

Table 4.1: RoF transceiver major impairments.

Direct modulation		External modulation		
FP LD	DFB LD	MZM	RSOA	REAMSOA
FP non-linearity	DFB non-linearity	MZM cosine characteristic	SOA non-linearity	EAM non-linearity
Low RF gain	Low RF gain	Insertion loss	Insertion gain	Insertion loss/gain
Mode partition noise	RIN	RIN	SOA ASE	SOA ASE
Mode hopping noise	Chirp	Very low chirp	Chirp	Relative low chirp
Chirp			Gain saturation	Polarization dependance
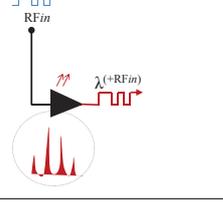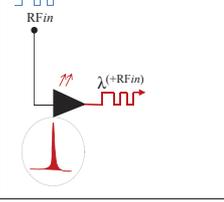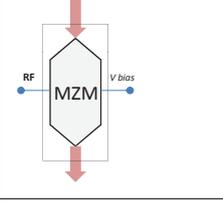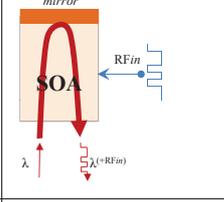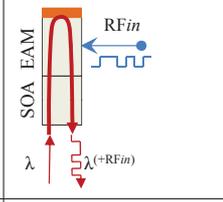
cascading several passive RAUs may be unfeasible due to the cumulated signal loss [35].

4.2.2 RoF transceiver physical impairments

Independently from the choice of the RoF transceiver, transporting RFs over optical fibers undergoes higher noise figure compared to traditional backhauling solution [34]. Since the RoF transmitter is the main source of signal distortion, we need to be aware of all noises and quality of transmission impairments that impact the RF signal. Table 4.1 shows the different physical impairments associated with five relevant configurations for the RoF transmitter namely: direct modulation with FP LD or DFB LD, external modulation using an electro-optic LiNbO$_3$ MZM, a RSOA and a REAMSOA.

4.2.2.1 Common impairments of RoF transceivers

Both LDs and external modulators present a nonlinear behavior of their response. This is the prime common physical impairment responsible for waveform distortion due to intermodulation between RF sub-carriers. Non-linearity of the transmitter can be corrected by inserting pre-distortion modules [74] or implementing either electro-optic or all-optical linearization methods [30]. However, implementations of common linearization schemes are rather expensive because they require an accurate modeling of the transfer function of the modulator depending on the particular order of distortion that one focuses on. The success of linearization techniques is achieved at the cost of bias-control complexity and induces an increase of the noise figure. Chirping which is the second common source of distortion shared between the different configurations. Created by an unwanted frequency modulation of the optical carrier, frequency chirping interplays with chromatic dispersion to generate distortions. Because of the multi-mode spectrum of FP LDs, the impact of chirping is generally neglected. MZMs are immune to chirping because optical carrier modulation is not achieved by modulating the carrier density

[30]. Nevertheless, MZMs suffer from their non-linear cosine transfer function [3]. While signal propagation impacts the link gain, RoF transmitter contributes also to the signal loss. Unlike directly modulated LDs, where link gain only depends on slope efficiencies, the gain of externally modulated LDs depends quadratically on the optical power, thus the power budget can be easily improved [30].

4.2.2.2 Specific Impairments of RoF transceivers

The multi-mode nature of FP LDs makes them vulnerable to Optical Beat Interference (OBI) between the different longitudinal modes, thus the intrinsic noise of the laser (Relative Intensity Noise (RIN)) is hard to deal with since it includes both mode partition noise and mode hopping noise. At the contrary, DFB LDs are assumed to have lower RIN, higher slope efficiency and consequently higher link gain. With EAM, a special care is made to select the right bias voltage and the right operation wavelength to improve the extinction ratio and to minimize the insertion loss. An SOA modulator suffers from the superposition of both static and dynamic non-linearities. However, it is shown that the latter kind of non-linearity prevails as static non-linearity can be suppressed by adjusting the bias [87]. In addition, SOA acts as an amplifier where the gain profile depends on the optical wavelength. For EAM-based or SOA-based external modulators, the polarization (TE/TM) of the incident light may impact the modulation performance[5], that could be overcome by using Polarization Controllers (PC) or strained (QW) EAM structures [75].

4.2.2.3 REAMSOA the most suitable RoF transceiver for GeRoFAN

As described earlier, different options of RoF transceiver can be selected to equip GeRoFAN RAUs, they range from direct *vs.* external modulation, the type of the light source (MMLD *vs.* SMLD) and the type of the modulator. The choice of the best candidate RoF transceiver for GeRoFAN is the outcome of a compromise between different criteria including:

- **Cost:** Cost criterion encompasses not only the cost of the device itself but also the cost of its deployment over all the system.

- **The optical power** intensity that feeds the RoF modulator or generated by the light source.

- **The electrical power** driving the device: In a context where designing low-energy consumption networks becomes mandatory, low voltage/current devices are highly privileged.

- **High Frequency:** This shows the ability of the device to handle high frequency or wideband modulating signals since GeRoFAN is designed also to support signals with frequencies above 10 GHz (such as *UWB* signals).

---

[5]Because heavy and light holes in the EAMSOA active region responds differently to incident light polarization.

Table 4.2: A comparison between different technologies for GeRoFAN RoF transceiver.

Comparative criteria	Cost	Optical Power	Electrical Power	HF	Link Gain	RIN	Chirp	Miniaturization Packaging ...
Direct modulation with FP LD at RAU	+	-	+	-	- -	- -	-	++
Direct modulation with DFB LD at RAU	- -	+	+	-	-	-	-	++
DFB LD at HOLT RSOA at RAU	+	+	+	+	+	+	-	++
DFB LD at HOLT MZM at RAU	+	+	-	-	-	+	++	++
DFB LD at HOLT IML-FP at RAU	+	-	+	+/-	-	+	+/-	+
DFB LD at HOLT REAMSOA at RAU	+	+	++	++	++	+	+/-	+

- **Physical impairments:** As explained earlier, while each RoF transceiver has it own specific transmission limitations, we focus here on 3 major impairments usually cited for performance comparison: Link gain, RIN and chirp.

- **Integration:** Significant technological advances have been made to improve the packaging, the integration and the miniaturization of the different devices.

Supported by the comparative study in [18], RoF transceiver candidates are ranked in Table 4.2 from the most (+) to the least convenient (-) according to the different criteria specified above.

The comparative ranking depicted in Table 4.2 shows the relative advantage of using REAM-SOA to equip GeRoFAN RAUs. The compromise achieved by the amplified absorption modulator in terms of cost-size-consumption effectiveness is summarized in the following items:

- In terms of system cost, equipping each RAU with a DFB laser diode is prohibitively expensive. Instead, the relative low-cost of FP lasers seems more attractive. Meanwhile, more expenses are required at some parts of the network (adding amplifiers, linearization circuits) to overcome the limited dynamic range of FP lasers and their low gain link. Thanks to RoF, DFB lasers are deported and pooled at the GeRoFAN head-end node. Remote light generation enables significant cost savings, flexible management and simplification of the RAU architecture. Size, packaging, required peripheral circuits and monolithic integration with other optical components, are also additional factors impacting the cost of the RoF transmitter device. LiNbO$_3$-based MZMs are difficult to work with and virtually impossible to integrate with electronic semiconductors, while a monolithic integration of EAM with DFB LDs is easily achieved [24]. Still, one of the main challenges

with the design of REAMSOA is to benefit from the SOA gain in an effective spectrum window by detuning the amplifier gain spectrum with respect to the EAM absorption edge. Design techniques like Selective Area Growth (SAG) have proved their effectiveness to achieve such a spectrum shift [17].

Currently, REAMSOA technology becomes more and more mature in the market, this makes the amplified absorption modulator a credible competitor to the emerging RSOA and the industry standard $LiNbO_3$ MZM. In addition, the same single REAMSOA at an RAU can be used both for modulation and photo-detection assuming the two signals belong to distinct bands to avoid interference issues.

- Thanks to the amplification feature provided by the SOA, a REAMSOA can be used for RoF links with longer reach than FP lasers or EAM external modulators, where an in-line amplification should be needed to compensate propagation and system components losses. Compared to a DFB laser diodes, RSOAs requiring relatively high current intensities or $LiNbO_3$ MZMs, REAMSOA operates with a low voltage (typically $1-3$ V).

- Compared to direct modulation options (FP, DFB LD) and external modulators (MZM and RSOA), electro-absorption modulators are capable of operating at high frequency and wide-band radio signals. With IML-FP, increasing the injected optical power consolidates the locking mechanism, on the contrary, the 3-dB bandwidth of the laser is strongly reduced.

- The comparison according to the physical impairments criterion is more balanced. In fact, thanks to the electro-optic mechanism, MZM are very less vulnerable to frequency chirping than direct modulation and RSOA. However, both REAMSOA and RSOA take advantage of the integrated amplification functionality to provide relatively higher link gain than MZM or direct modulation solutions. Finally, the impact of RIN is more serious with direct modulation (even it is still low with DFB than FP lasers) than external modulation solutions. Thanks to the injection-locking, the RIN of IML-FP is significantly reduced (similar to DFB lasers) but the chirp is increased with the injected optical power (chirp ranges between 1.5 - 4 [99]).

4.3 REAMSOA physical impairments

While the comparative study shown in Table 4.2 highlights definitely the advantage of selecting REAMSOA as the RoF transceiver for GeRoFAN, a deep insight on its main physical limitations is required to ensure a proper deployment and exploitation. We develop an analytical model describing the REAMSOA behavior in order to assess the intensity of the different noises.

4.3.1 REAMSOA working principle

The most crucial part of the REAMSOA stands for the EAM section where the modulation and photo-detection occur. The EAM is an external optical modulator based on a voltage-controlled absorption of light. EAMs are promising candidates for ultrahigh speed optical communications, due to their small size, light weight, relative low power consumption, high-frequency operating speed and the possibility for monolithic integration with other semiconductor devices. EAM can be realized using either a bulk semiconductor material or multiple quantum wells (MQW) positioned within an intrinsic region of a reverse biased p-i-n diode. Bulk and MQW-EAM rely on different physical quantum effects. While bulk EAM is driven by the Franz-Keldysh Effect (FKE) characterized by the direct band edge absorption, the working mechanism of a MQW-EAM is known as the Quantum Confined Stark Effect (QCSE) [150].

The main drawback of EA (Electro-Absorption) modulators consists in their link loss. The use of EAMs requires a careful adjustment of the bias voltage in order to achieve a low insertion loss. But, as discussed in the literature [156], the EAM is biased at a particular point leading to a compromise between the linearity of the modulator and its insertion loss. When an EAM is used for full duplex communication, the optimal bias voltage is selected as a compromise between photo-detection and modulation functions as suggested in [32]. To compensate for the power loss inherent to the modulation, the EAM can be integrated with an SOA to amplify the optical signal at the output of the modulator. Hence, the use of in-line optical amplifier becomes useless since the amplification function is already achieved through the new integrated amplified modulator. However, such integration is still facing some challenges such as maximizing the fiber coupling efficiency, the sensitivity to light polarization and shifting the amplification region of the SOA to coincide with the modulation region of the EAM [17][95].

The modulator considered in this study is a MQW-EA amplified modulator made of 10 quantum wells and 11 barriers based on *AlGaIn/GaIn* layers. One of the main original contributions of this Thesis is the design of a comprehensive analytical model describing the behavior of the MQW-EA amplified modulator. We provide in the **Appendix** the detailed description of the steps composing our methodology. Our analytical modeling of the amplified EAM has been validated by Mr *Christophe Kazmierski*, senior researcher within the *III-V Labs*[6] and international expert of the domain [104]. Mr Kazmierski estimates that the proposed approach to describe analytically the behavior of the EAM represents an original and interesting contribution. The approach is well suited to the description of the Stark effect in quantum wells, even if exciton effects are not the only ones to be considered to model the EAM behavior, especially under high reverse bias voltages (around 5 Volts). Meanwhile, at this level of the study, this remark does not question the final conclusions of following chapters in the manuscript.

---

[6]Alcatel-Thales III-V Lab., Alcatel-Lucent Bell Labs France. http//:www.3-5lab.fr/

The outcome of the calculations detailed in **Appendix** enables us to derive the absorption profile of the EAM with respect to the bias voltage at each optical channel. The absorption profile of the EAM stands for the transfer function of the device, through which we calculate the equation of the RF link gain.

4.3.2 The EAM section

The first figure of merit to characterize the performance of a RoF link is the link gain. The link gain G is defined as the ratio of the microwave output power P_{out} to the microwave electrical power P_{in} injected in the modulator:

$$G = \left| \frac{P_{RF,out}}{P_{RF,in}} \right| \tag{4.1}$$

For Intensity Modulation Direct Detection (IMDD) link, the link gain strongly depends on the transmitter device. In [30], the link gain has been evaluated for direct and external electro-optic modulation in RoF links. The impact of impedance matching on link gain and noise factor is addressed in [72] with a comparison between direct and external modulation. It is shown in [34] that for the RoF link gain G (in dB units) is negative (*i.e.* lossy link) for the case of direct modulation or external modulation using an EAM, while for the REAMSOA, one can take advantage from the amplifier functionality featured by the SOA to increase the link gain.

Like any external modulator, the link gain of EA modulator depends on the injected optical power and internal parameter of the device (capacitance of the electrodes, internal resistance etc.). EA modulators suffer from residual loss (residual absorption in the absence of external electric field) that may decrease the gain. For the case of TW-type EAM, the analysis is carried out based the mathematical approach developed in [64]. We express in Equation 4.2 the optical power at the output of the modulator as function of the input optical power, the absorption coefficient α_o of the active layer at 0 Volt, the optical confinement factor Γ of the EAM with length ℓ and the absorption change α across the modulation section due to the modulating voltage.

$$P_{out} = P_{in} \cdot \rho \cdot exp\left(-\alpha_o \ell\right) \cdot exp\left(-\Gamma \cdot \int_0^\ell \alpha(x)\, dx\right) \tag{4.2}$$

where ρ stands for the optical loss factor at each facet of the modulator (including fiber-coupling loss). A typical value of 3 dB for ρ is assumed. The applied voltage V to the EAM is expressed as the sum of its DC part (bias voltage V_b) and its AC part (modulating voltage V_{AC}). Using small signal approximation, we focus only on the AC part of Equation 4.2 to get:
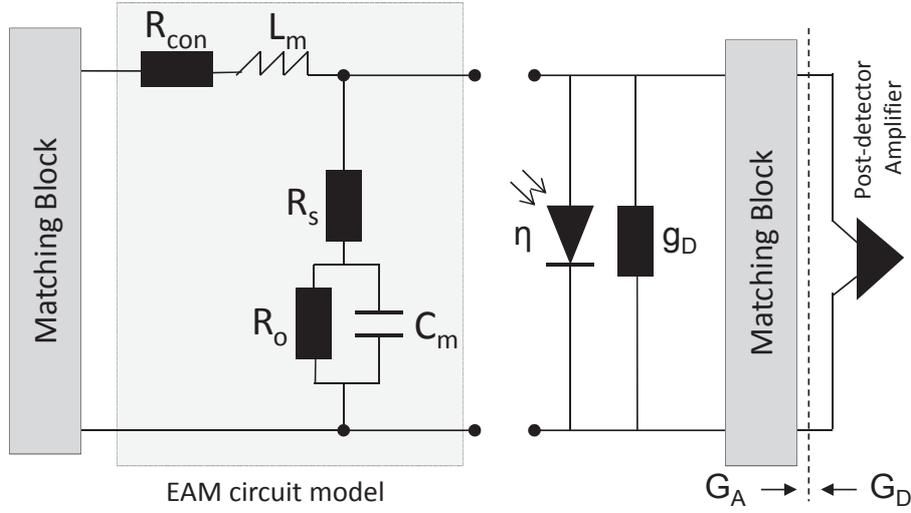
Figure 4.2: EAM quasi-static circuit model

A typical analog RoF link can be represented as a concatenation of an EAM equivalent circuit model, the fiber medium, a photo-detector equivalent circuit and eventually a post-detector amplifier. Matching blocks are inserted at the input and the output of the link. Impedance matching between the source and the EAM on one hand, the photo-detector and the amplifier on the other hand minimizes the power loss due reflection and increases the RF gain.

$$P_{out}^{AC} = P_{in} \cdot \rho \cdot exp\left(-\ell(\alpha_o + \Gamma\alpha_b)\right) \cdot \Gamma \cdot \frac{\mathrm{d}\alpha}{\mathrm{d}V}|_{V=V_b} \cdot \int_0^\ell V_{AC}(x) \ \mathrm{d}x \qquad (4.3)$$

where α_b denotes the absorption coefficient at V_b.

The AC part of the output optical power passes through a PIN photo-detector, the detected RF output power is:

$$P_{RF,out} = \left(\frac{q_e\eta}{hf}\right)^2 \cdot Z_L \cdot |P_{out}^{AC}|^2 \qquad (4.4)$$

where: η the photo-detector quantum efficiency, q_e the electron charge, h the Planck constant, f the microwave frequency of the modulating signal and $Z_L = \frac{G_D}{G_A \cdot g_D \cdot (1+\frac{G_D}{G_A})^2}$ the microwave impedance at the receiver computed through the quasi-static approximated circuit model of the TW-EA modulator. Parameters g_D, G_A and G_D correspond respectively to the photodiode admittance, the receiver equivalent impedance seen from both sides of the matching block as illustrated in Figure 4.2 .

The normalized gain (with respect of the ideal case where no loss is observed) is expressed in Equation 4.5:

$$G(f,\lambda,V_b) = \left| \frac{T}{1 - \Gamma_L\Gamma_S e^{-2\gamma_u\ell}} \cdot \left[\frac{e^{(\jmath\beta_o-\gamma_u).\ell}}{(\jmath\beta_o-\gamma_u).\ell} + \Gamma_L \cdot e^{-2\gamma_u\ell} \cdot \frac{e^{(\jmath\beta_o+\gamma_u).\ell}-1}{(\jmath\beta_o+\gamma_u).\ell} \right] \right|^2 \qquad (4.5)$$

Given, following the assumptions in [64]:

- $\gamma_u = \sqrt{\frac{R_{con}+\jmath 2\pi f Lm}{R_s+\frac{R_o}{1+\jmath C_m 2\pi f Ro}}}$ the microwave propagation constant.

- $\Gamma_L = \frac{Z_L - Z_m}{Z_L + Z_m}$ and $\Gamma_S = 1 - T$ are the modulator internal reflection coefficient at the load and the source ports respectively.

- $T = e^{-\Gamma \ell(\alpha_b - \alpha_o)}$ the amplitude transmission coefficient of the modulator.

- $Z_m = \sqrt{(R_{con} + \jmath 2\pi f L_m) \cdot (R_s + \frac{R_o}{1+\jmath C_m 2\pi f Ro})}$ the modulator impedance.

- β_o the wave number associated with the optical-wave group velocity, λ the wavelength of the optical carrier.

- $L_m, C_m, R_o, R_s, R_{con}$ are respectively: the (per-unit length) EAM inductance, capacitance, equivalent AC resistance, serial resistance and conduction resistance of the equivalent quasi-static circuit model of the modulator in Figure 4.2. The symbol $\jmath$ stands for the complex number where $\jmath^2 = -1$.

Three main remarks worth to be noticed when analyzing the RF gain of the modulator:

1. The RF gain depends on the waveguide microwave proprieties, the wavelength of the optical carrier λ and the bias voltage V_b. Therefore, one way to improve the RF gain should be to focus on enhancing the design parameters of the modulator-waveguide. Such an approach was followed in the study of [27], where authors investigate the optimal length of the modulator in order to maximize the RF gain.

2. The importance of the impedance matching between the modulator-waveguide and the source on one hand, and with the receiver on the other hand. In [72] and [29], the problem of impedance matching has been worked out through different matching scenarios.

3. The RF gain is proportional to the input EAM optical power squared. It suggests that, at some extent, one can minimize the link loss by increasing the optical power at the input of the modulator.

Because of the dependance of T with V_b, the optical bias point at each optical carrier is selected such that the modulation RF gain is maximized, *i.e* $V_b^* = \arg\max_{V_b} G(V_b)$. Figure 4.3 illustrates the optimal bias voltage V_b^* at different optical channels.

To characterize the performance of the modulator, the noise figure of the RoF link is a key performance indicator. The Modulation Penalty (MP) (*i.e.* the noise figure NF of the modulator) is related to the RF link gain G as expressed by Equation 4.6:

$$NF = \frac{N_{out}}{k \cdot T^K \cdot B \cdot G} \tag{4.6}$$
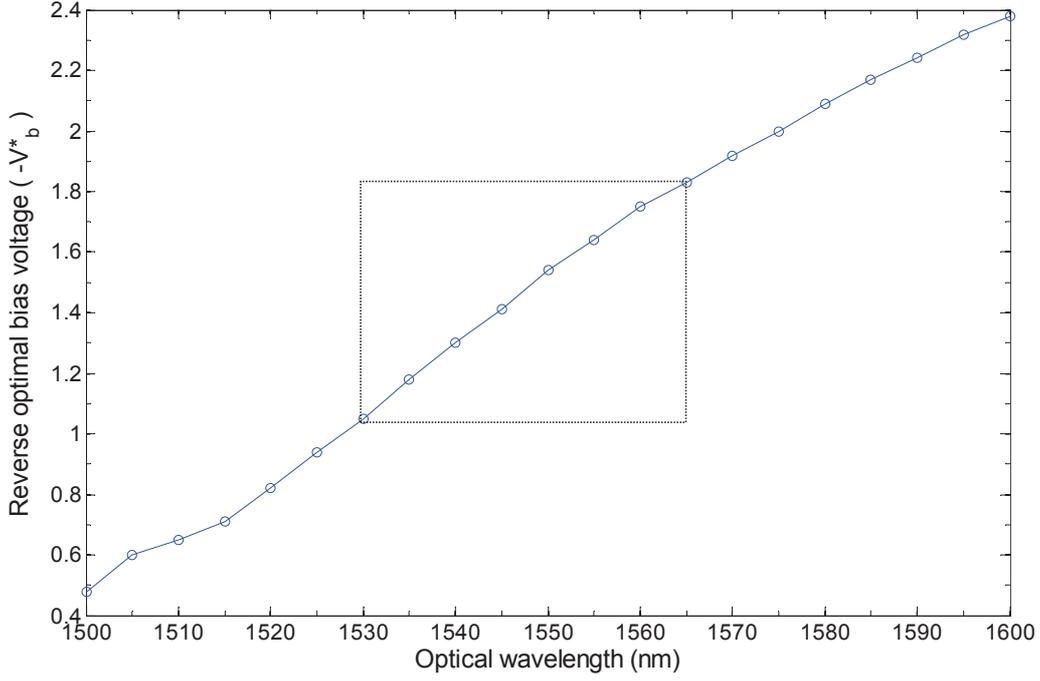
Figure 4.3: EAM Optimal Bias Voltage for each optical wavelength.

Unlike electro-optic modulators, EAMs work at smaller bias voltage. Optimal operation (in terms of RF gain) is achieved by biasing the device in the range $-1.8 \sim -1$ V to cover the conventional C-band (*cf.* squared area in the figure).

Given: N_{out} the noise power at the output of the amplified modulator, k The Boltzmann's constant, T^K the Kelvin temperature and B the noise bandwidth.

Figure 4.4 depicts the evolution of the RF link gain of the modulator according to the OC wavelength at 0 dBm and -10 dBm input optical signal power.

4.3.3 The SOA section

The REAMSOA takes advantage of the amplifier gain provided by the integrated SOA. The amplification operation is performed twice because of the reflective configuration of the device. To model the SOA gain profile, we follow the analytical development in [28]. If G_s denotes the single-pass gain at the operating wavelength λ, the maximum SOA gain expressed in Equation 4.7 is the fiber-to-fiber gain given from the transmittance function of the Fabry-Pérot cavity.

$$G_{soa}^{max}(\lambda) = \frac{(1 - R_1)(1 - R_2)G_s}{(1 - G_s\sqrt{R_1 R_2})^2 + 4G_s\sqrt{R_1 R_2}\sin(\frac{2\pi n_{eff}\ell_{soa}}{\lambda})^2} \tag{4.7}$$

Where: ℓ_{soa} the length of the SOA section, R_1, R_2 Input and output facet reflectivity of the cavity respectively, n_{eff} the effective refractive index of the amplifier waveguide expressed as in [28] and function of the *InGaAsP* active region refractive index, the cladding *InP* region refractive index and the optical confinement factor Γ^{soa} of the SOA.
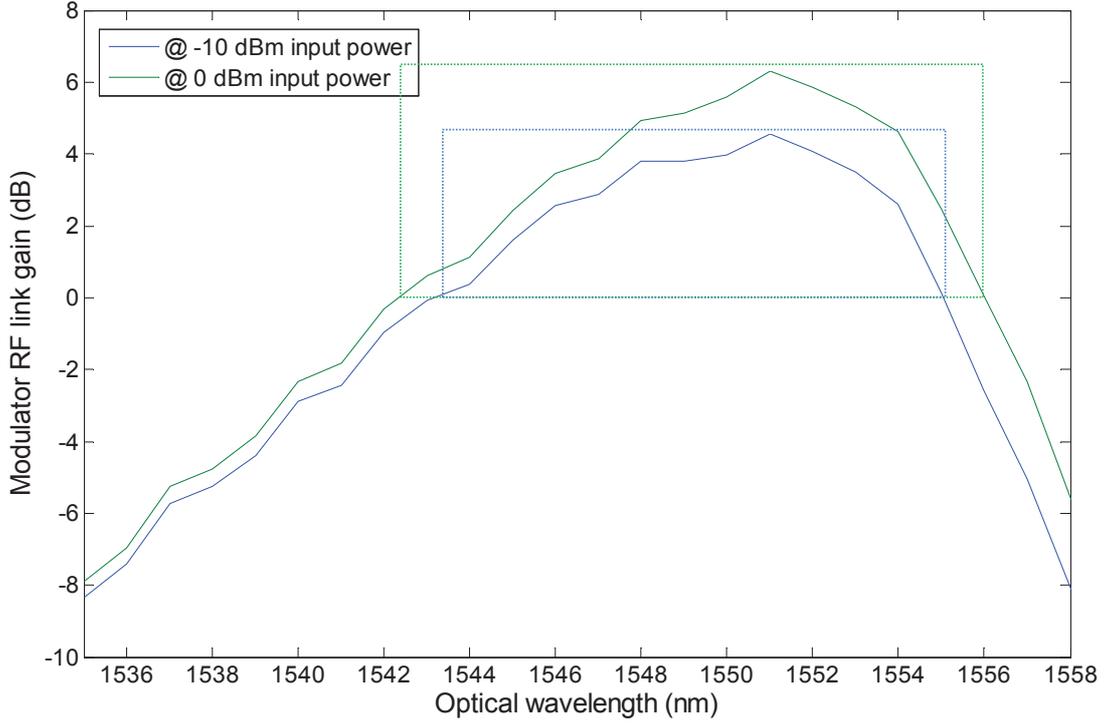
Figure 4.4: EAM RF Gain as function of the optical wavelength.

The RF gain of the modulator is computed at optimal bias voltage and under balanced impedance matching. The figure highlights two distinct regions of the RF gain: For some optical channels (*cf.* squared region in the figure), a positive RF link (in dB) is achieved, while at some other optical channels the RoF link is lossy. By increasing the optical power injected in the modulator, the RF gain increases as well and the range of optical channels leading to a positive gain is extended.

The single-pass gain depends on the material gain of the device which is *in-fine* carrier density dependant. The material gain coefficient g_m is estimated with respect to the optical wavelength and approximated by a parabolic extrapolation as carried out in [85].

Figure 4.5 plots the unsaturated gain of the SOA as function of the optical wavelength.

The gain saturation of the SOA is an important feature included in our analytical modeling. When the input optical power increases, the optical gain of the amplifier drops. The saturated gain of the SOA G_{soa} is related to the maximum gain according to Equation 4.8:

$$G_{soa} = \beta \cdot \ln\left(\frac{G_{soa}^{max}}{G_{soa}}\right) \tag{4.8}$$

The factor β stands for the ratio between the saturation optical power of the SOA (P_{sat}) and the input optical power.

Equation 4.8 indicates that for a low input optical power, the gain tends to reach its unsaturated value G_{soa}^{max}, while at very high optical power, the gain tends to 1 so that the input optical power equals to the output optical power. Equation 4.8 is solved using the Lambert W-function.

The saturation power P_{sat} of the SOA is expressed through Equation 4.9:
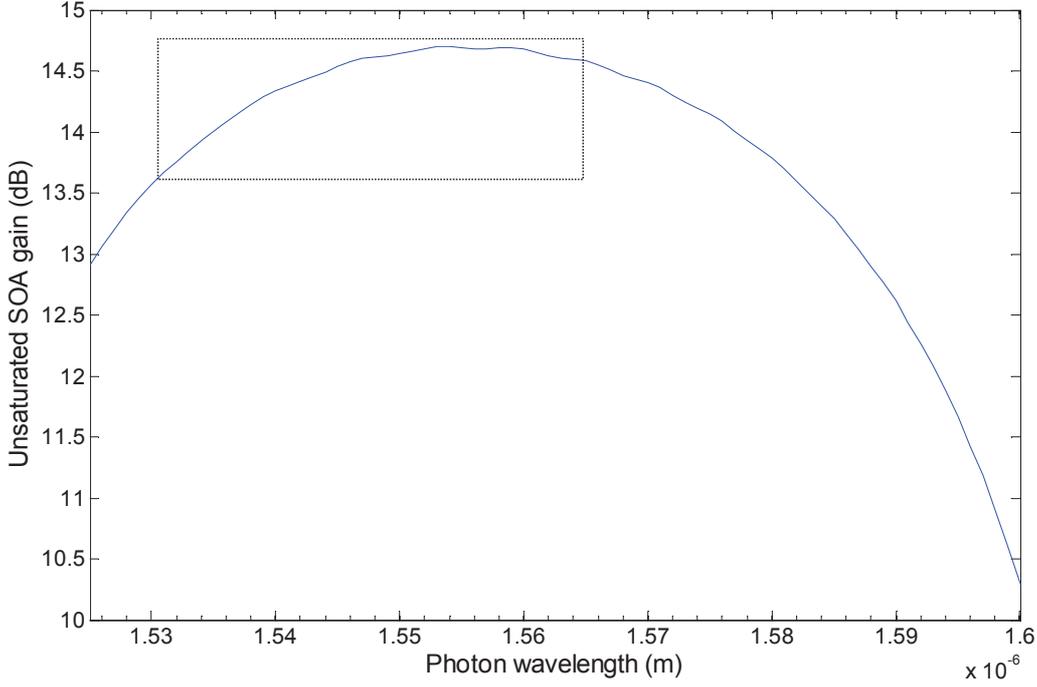
Figure 4.5: SOA unsaturated gain as function of the optical wavelength.

The unsaturated gain of the SOA is calculated assuming a bias of 120 mA and an input optical power of 0 dBm. The effective gain of the amplifier evolves with respect to the saturation power. When the input optical power is low, the effective gain tends to its unsaturated value, while at very high power the gain is equal to 1.

$$P_{sat} = \frac{E_{sat}}{\tau_c} = \frac{hc \cdot w_i t_i}{\tau_c \lambda \cdot \frac{g_m}{N_b - N_o}} \qquad (4.9)$$

Given: E_{sat} the saturation energy of the amplifier; τ_c the spontaneous carrier-life time; h the Planck constant; w_i and t_i the width and the thickness of the SOA active layer respectively; N_b and N_o the carrier density at bias current I_b and at transparency respectively.

Figure 4.6 illustrates the saturation optical power of the amplifier according to the wavelength.

The signal amplification by the SOA is accompanied by Amplifier Spontaneous Emission (ASE) noise. In general the ASE noise is very small (~ -70 dBm), but it may become a dominant noise source when numerous in-line amplifiers are inserted along the light-path. The ASE optical noise is computed through Equation 4.10 [5]:

$$P_{ase} = 2 \cdot n_{sp} \cdot h \cdot f \cdot (G_{soa} - 1) \cdot B_o \qquad (4.10)$$

Assuming: n_{sp} the population inversion parameter of the SOA; f_o the optical frequency; G_{soa} the amplifier gain computed according to Equation 4.8 and B_o the equivalent optical bandwidth.
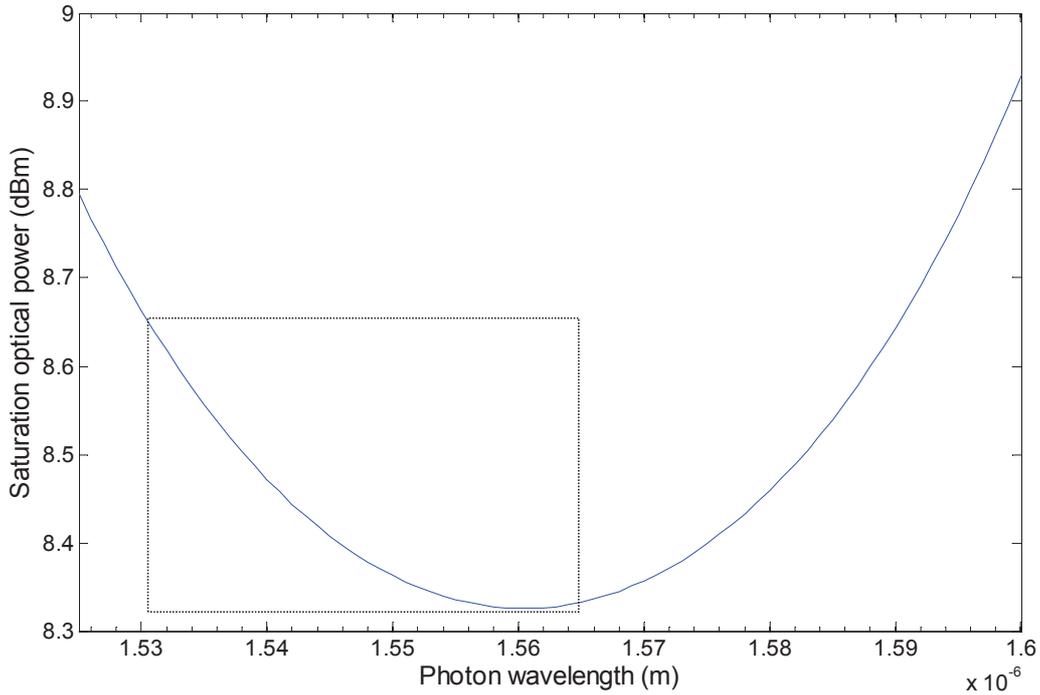
Figure 4.6: SOA Saturation optical power as function of the optical wavelength.

The saturation power of the SOA is computed assuming a bias of 120 mA and an input optical power of 0 dBm (*cf.* the C-band is delimited by the squared area in the figure).

4.3.4   Non-linearity and Intermodulation distortions

Intermodulation (IMD) distortions have been pointed out as the main impairment reducing the dynamic range of an analog RoF SCM transmission link [154]. Analog signal distortion occurs when multiple RFs transported by the same optical channel beat together to generate RF mixing products that may fall on a designated radio channel and degrade its SNR. For a REAMSOA, the phenomenon of intermodulation distortions is caused by 4 different physical impairments: Intermodulations proper to the intrinsic non-linearity of the Reflective Amplified Modulator (IMD-RAM), signal clipping, frequency chirping and specific intermodulations occuring when RF subcarriers are already OFDM modulated as high-speed *WiFi* (*802.11n/g* standard), *4G LTE* and *WiMAX* signals.

4.3.4.1   IMD-RAM

The transfer function of an EAM is intrinsically nonlinear [67]. Output optical power to input optical power ratio of the device depends on the absorption coefficient of the active region $\alpha(\lambda, V)$ which varies according to both the applied bias voltage V and the operating optical wavelength λ. Considering an EAM with an optical confinement factor Γ^{eam} and a length ℓ^{eam}, the transfer function $\mathfrak{f}$ of the modulator is expressed by Equation 4.11:

$$\frac{P_{out}}{P_{in}} = \mathfrak{f}(V) = \eta \cdot e^{-\alpha(V,\lambda) \cdot \Gamma^{eam} \cdot \ell^{eam}} \tag{4.11}$$

Where: η: the fiber coupling loss coefficient.

For a given operating wavelength, we consider V as a superposition of the DC bias voltage V_b and a variable modulating component V_m (RF modulating signal). We carry out the same mathematical development detailed in [67] to highlight the non-linear behavior of the device by expanding Equation 4.11 using Taylor series expansion around V_b:

$$\begin{aligned}
\mathfrak{f}(V) \simeq & \ \mathfrak{f}(V_b) + V_m \cdot \left(\frac{\mathrm{d}\mathfrak{f}}{\mathrm{d}V} |_{V=V_b} \right) + \frac{V_m^2}{2!} \cdot \left(\frac{\mathrm{d}^2\mathfrak{f}}{\mathrm{d}V^2} |_{V=V_b} \right) + \\
& \frac{V_m^3}{3!} \cdot \left(\frac{\mathrm{d}^3\mathfrak{f}}{\mathrm{d}V^3} |_{V=V_b} \right) + ... + \frac{V_m^n}{n!} \cdot \left(\frac{\mathrm{d}^n\mathfrak{f}}{\mathrm{d}V^n} |_{V=V_b} \right)
\end{aligned} \tag{4.12}$$

Under small signal approximation, Equation 4.12 is simplified up to the 3rd order derivative of $\mathfrak{f}$. For sub-octave bandwidth systems, second order IMDs (IMD-2) and third order Harmonic Distortions (HD-3) are not considered since they fall out of the signal band. However, these distortions must be considered for the case of multi-service system (for instance, *LTE* and *UWB* signals transported by the same optical channel) [125]. The IMD-3 optical noise generated by 2 tones (i, j) (respectively 3 tones (i, j, k)) that falls at RF $l = 2i \pm j$ (respectively $l = i \pm j \mp k$) is computed according to Equation 4.13a (respectively 4.13b):

$$N_{2i \pm j} = \frac{3}{4} \cdot \frac{K_3}{3!} \cdot V_b^3 \cdot m_i^2 m_j \cdot P_o \tag{4.13a}$$

$$N_{i \pm j \mp k} = \frac{3}{2} \cdot \frac{K_3}{3!} \cdot V_b^3 \cdot m_i m_j m_k \cdot P_o \tag{4.13b}$$

Given: m_i: Optical Modulation Index (OMI) of RF channel i; V_b: DC bias voltage of the EAM; $K_3 = \frac{\mathrm{d}^3\mathfrak{f}}{\mathrm{d}V^3}|_{V_b}$: 3rd order RAM non-linearity parameter computed at bias point and P_o: Average received optical power.

4.3.4.2 Clipping Noise

Restricted for a long time to direct modulations, external modulation links are also subject to clipping noise. Basically, clipping noise describes the distortion of the optical wave generated at the output of the modulator when the injection current/voltage overdrives (or under drives) the device beyond its clipping-free region [72]. Figure 4.7 illustrates through a phasor representation of the SCM modulating signal, how clipping occurs when some of the signal components get within clipping region of the modulator. When the signal is clipped, extra-harmonics and intermodulation products between the modulating subcarriers are generated. The study in [94] shows that compared to direct modulation systems and assuming the same optical depth and
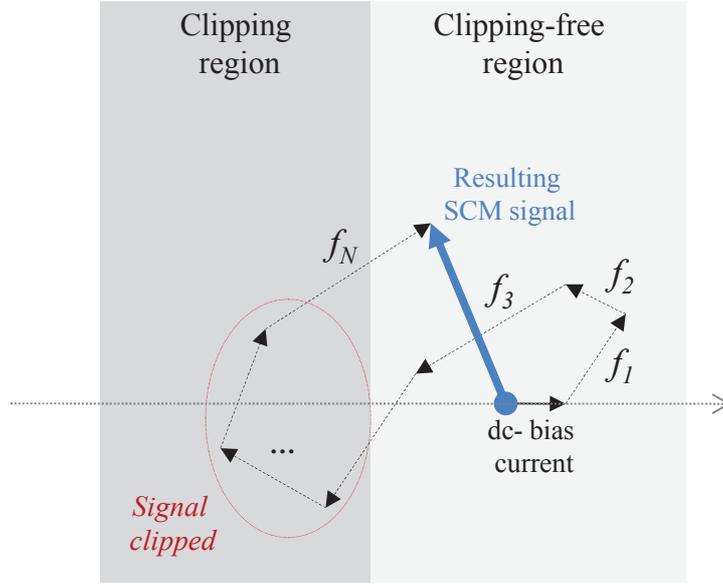
Figure 4.7: Illustration of clipping using a phasor representation of the SCM signal.

When N RF subcarriers modulates an optical channel, the resulting SCM signal will be clipped if the phasor of the signal is pushed within the clipping region of the modulator. Note that clipping may occur because of some of subcarriers although the phasor of the resulting SCM signal is outside the clipping region.

frequency planning scheme, externally modulated links suffer from an additional 6 dB clipping distortion penalty. Several publications have focused on clipping analytical modeling such as in [6] [137] and [82]. However, a more accurate approach detailed in [58] is followed in our modeling to assess the impact of clipping. Assuming an input SCM modulating electrical signal as a multiplex of N subcarriers $(f_1, ..., f_N)$ each with OMI m_i, the ratio of Carrier-to-Inter-Modulation Products of order n $CIMP^{(n)}$ computed at frequency f_i is expressed in Equation 4.14:

$$CIMP^{(n)}(f_i) = \frac{(4N)^{(n-1)} \cdot \pi \cdot (X^{(1)}n!)^2 \cdot exp(\frac{1}{\mu^2})}{H^2_{(n-2)}(\mu/\sqrt{2}) \cdot D^{(n)}_{f_i}} \tag{4.14}$$

Given: $\mu = \sqrt{\frac{\sum_{i=1}^{N} m_i^2}{2}}$: the total modulation depth of the RF multiplex signal; $D^{(n)}_{f_i}$: Number of IMD products of order-n; $X^{(1)} = 1 - \frac{erfc(\frac{1}{1\sqrt{2}\mu})}{2}$: The non-linear susceptibility of the effective transfer function of the modulator assuming to model the input SCM signal as a Gaussian process; $H_{(n-2)}(x)$: the Hermite polynomials of order $n-2$. For orders 2 and 3, it can be written as: 1 and x respectively.

4.3.4.3 Frequency Chirping Noise

Compared to directly modulated lasers, external optical modulators show lower frequency chirping which makes them very attractive for chirping sensitive optical communication systems. Chirping is typically between 4 and 6 for semiconductor diode lasers while it ranges between $+1$ and -2 for EA modulators [127]. Higher carrier densities are typical for laser diodes and do not allow for negative chirp factors, while because modulators are reverse biased, they exhibit a much lower carrier density in the quantum wells [75].

According to [80], there are two possible causes of frequency chirping in external modulators: one possible reason is the wavelength shift of the semiconductor laser feeding the modulator due to external reflection outside of the EAM. This kind of chirping can be mainly removed by adopting optical isolators and reducing the reflection by means of Anti-Reflection coating to the end-face of the modulator. The second cause of chirping is the phase modulation due to the refractive index change of medium inside the EAM. In the following analysis, we consider EAM frequency chirping due to the unwanted phase modulation of the optical signal by the modulating signal which is inherent to the working mechanism of the EAM. When coupled with chromatic dispersion, frequency chirping of an EAM, induces distortions of the signal through the generation of intermodulation products and harmonics. The intensity of these noisy frequency-dependant components depends on the phase variation with the modulating signal along the time. To estimate frequency chirping induced signal distortion in multiple quantum well EAMs (MQW-EAM), we follow the theoretical analysis carried out in [74]. Assuming that N radio signals at angular microwave frequencies $(\omega_1, ..., \omega_N)$ with OMIs $(m_1, ..., m_N)$ modulate the EAM, the outcome of our calculations (detailed in the **Appendix**) highlights the expressions of the optical noise $N_{opt}(\omega_l)$ of IMD3 products falling at angular frequency ω_l as in Equation 4.15:

$$N_{opt}(\omega_l) \simeq 2P_{in}10^{-aL}(I_{\omega_l}^2 + Q_{\omega_l}^2) \tag{4.15}$$

Where: P_{in}: the optical power at the input of the EAM; a: fiber attenuation coefficient; L: the optical fiber length; I_{ω_l} and Q_{ω_l} are In-phase and Quadratic-phase chirp-induced IMD3 noise falling at frequency ω_l and expressed as the following:

- For IMD3 with 2 tones falling at $\omega_l = 2\omega_i - \omega_j$:

$$I_c = a_1\beta^2 V_b \cdot m_i^2 m_j \cdot (\omega_i^2 + \frac{\omega_j^2}{2}) + 3a_1\beta^2 V_b \cdot m_i^2 m_j \cdot \omega_i(\omega_j - \frac{\omega_i}{2}) \tag{4.16a}$$

$$Q_c = a_2\beta^2 V_b \cdot m_i^2 m_j \omega_i(\omega_i - \frac{\omega_j}{2}) \tag{4.16b}$$

- For IMD3 with 3 tones falling at $\omega_l = \omega_i - \omega_j + \omega_k$:

$$I_c = a_1\beta^2 V_b \cdot m_i m_j m_k \cdot (\omega_i^2 + \omega_j^2 + \omega_k^2) + 3a_1\beta^2 V_b \cdot m_i m_j m_k \cdot (\omega_j\omega_i + \omega_j\omega_k - \omega_i\omega_k) \tag{4.17a}$$

$$Q_c = a_2\beta^2 V_b \cdot m_i m_j m_k \cdot \omega_i(\omega_i + \omega_j + \omega_k) \tag{4.17b}$$

Parameters β, a_1 and a_2 are defined in the **Appendix**.

4.3.4.4   IMD-OFDM

For a RF OFDM-modulated channel, such as in *4G LTE* or *WiMAX*, the non-linearity of the modulator generates IMD noises due to beating between OFDM Subcarriers (SCs). The analytical study in [100] shows that distortions spread out over a bandwidth three times larger than the RF bandwidth thus penalizing the SNR of the RF channel itself and its adjacent (left and right) neighbors. The detected intensity of third order IMDs falling at RF channel ℓ is:

$$I(\ell) = \frac{1}{6}d_{\ell-1}^2 + \frac{2}{3}d_\ell^2 + \frac{1}{6}d_{\ell+1}^2 \tag{4.18}$$

Given: $d_i^2 = \frac{(P_o K_3 m_o^2 V_b^3)^2}{2} \cdot \mathcal{M}(N_{sc})$: The relative amplitude of IMD noises created by OFDM SCs composing the RF channel i; m_o: OMI of single OFDM SC; $\mathcal{M}(N_{sc})$: total number of IMD3 composite products produced by the beating of N_{sc} equally-spaced OFDM SCs computed as in [101].

4.4   ROADM

ROADMs are the second key element in the GeRoFAN system. Substantial developments have been made on the architecture of ROADM subsystems to improve their tunability and reduce their insertion loss. A wide range of available ROADM structures are based on Arrayed Waveguide Gratings (AWGs), Fiber Bragg Gratings (FBGs) packaged along with optical switches, ring resonators, acousto-optic tuneable filters, micro-mirror arrays etc [129].

4.4.1   FBG-based ROADM

FBG-based ROADMs are selected for the GeRoFAN system as they cover a wide range of proposed OADM structures in the literature, showing relatively low loss compared to their counterparts (Mach-Zehnder Interfometer, AWG, etc.), low channel spacing. They are mature technology and available in the market at a relatively low cost [16]. Because tunability is an important feature to enable further control flexibility of the system, we are specially interested in tunable FBG based OADM. The tunability is achieved either through thermo-control or mechanic strain applied to the gratings. While this option may be attractive since it entails one single FBG, it presents some limitations on the tunability range of the device. To cover a large range of tunability, a set of gratings at different wavelengths separated by 2×2 optical switches are connected to each other in cascade within a single device. The switch routes the WDM signal from the input port through only the gratings at the add/drop wavelengths bypassing
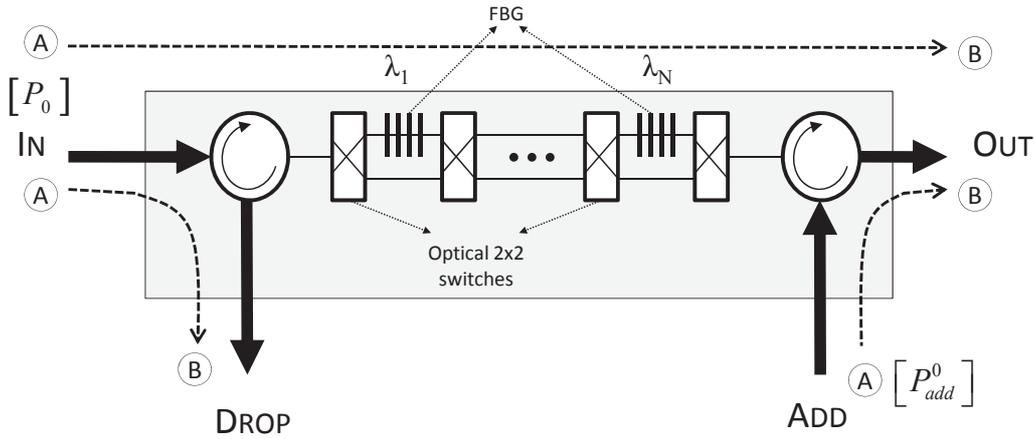
Figure 4.8: ROADM Structure used for GeRoFAN

Compared to other technologies, FBG-based OADM is considered as a mature low-cost technology. The reconfigurability of the OADM is achieved by driving the cross-bar configuration of multiple switches. Such a configuration prevents using filters (difficult to manage) to select the right optical channel. Each FBG is designed according to the optical wavelength to be dropped. The imperfections of FBGs, circulators, switches generate homodyne and heterodyne crosstalk which are accurately computed in our modeling.

the gratings at other wavelengths. A tuneable FBG-based OADM model minimizes filtering of the wavelength channels and subsequent induced signal distortions and eye closure [129].

Figure 4.8 illustrates the model of the Tuneable FBG-based OADM adopted in this study. Three possible paths of the optical signal are highlighted: a Drop path, an Add path and a Pass-through path.

4.4.2 OADM noises

OADM may degrade the quality of the optical signal due to the imperfect isolation of its optical components (optical switches, (de)multiplexers, gratings etc.). The degradation can be modeled by a leakage power, an optical interference between transiting channels or optical reflections. The generated crosstalk by these devices is classified either based on the phase difference $\triangle\Phi$ between the two optical carriers (Coherent *vs.* Incoherent Crosstalk) or on their wavelengths $\triangle\lambda$ (Homodyne *vs.* Heterodyne Crosstalk) [25].

In-band optical crosstalk (*i.e.* homodyne crosstalk) occurs if the crosstalk signal is at the same wavelength as the desired signal, while out-of-band crosstalk (*i.e.* heterodyne crosstalk) happens if the crosstalk signal is at a different wavelength. Coherent crosstalk occurs if the phase difference between the two signals is kept constant, while incoherent crosstalk takes place when the phase difference between the two signals varies randomly over the range $[0, 2\pi[$. We should notice that the heterodyne crosstalk is definitely non-coherent.

4.4.3   Homodyne Crosstalk

Homodyne crosstalk in Tuneable-FBG OADMs results from imperfections in FBGs, intermediate switches and circulators. For instance, within the OADM the added optical channel is reflected by the FBG and transmitted back to the GeRoFAN head-end node. However some of the added channel leaks through the grating and is received at the drop port of the OADM. Similarly, some of the dropped optical signal passes through the gratings and continues together with the added optical signal. Passing through channels are also affected by some power leakage. These leakages result either in an incoherent or coherent homodyne crosstalk increasing the noise level. SNR of the optical channel is also degraded because of a decrease in the power signal due to connectors or switches loss. To compute the degradation induced by homodyne crosstalk, we use the analytical model and crosstalk parameters described in [129]. Table 4.3 summarizes homodyne crosstalk equations for each path channel. Assuming an OADM with N FBGs, the dropped/added/passing-through channel corresponds to the wavelength at FBG with rank p[7].

Figure 4.9 shows the SNR penalty of an RF signal modulating an optical carrier in the C-band when the considered optical wave is dropped, added and passes-through the ROADM. Different ROADM structures are simulated assuming 8, 16, 24 and 32 build-in FBGs.

Whatever the path of the optical channel (drop, add or pass-through) through the ROADM, Figure 4.9 shows the higher the number of build-in FBGs, the higher the SNR penalty. In addition, least penalized channels differ from one path to another. Channels experiencing the lowest penalty correspond to longer optical wavelength channels for the ADD path. Short wavelength channels experience the lowest penalty for the DROP path, while channels located at the middle of the FBG sequence are the most privileged channels for the PASS-THROUGH path.

4.4.4   Heterodyne Crosstalk

Out-of-band (*i.e.* Heterodyne) crosstalk may be removed by adequate filtering at the receiver if the crosstalk and the desired optical signals are modulated by different subcarriers. When two optical channels at different wavelengths but modulated by the same radio frequency interfere with each other, the crosstalk noise depends on the subcarrier phase difference which is related to the fiber path length of each channel and chromatic dispersion [26]. In our model, the heterodyne crosstalk occurs within the FBG of the OADM system assuming that the interfered and the interfering channels are modulated by the same radio subcarrier (this particular kind of crosstalk noise is accounted only in the case of radio frequency reuse). When the dropped optical channel is reflected by the grating, a small part of the power of neighboring optical channels is

---

[7]$p \in \{1, 2, ..., N\}$

Table 4.3: Homodyne Crosstalk Equations for a Tuneable FBG-based ROADM.

ADD

The power of the added channel is attenuated by $(N + 2 - p)$ dB which stands for various insertion loss encountered along the channel path through the OADM, including circulators intermediate gratings and switches insertion losses. The signal power S_B (as well as the noise power N_B) at B is expressed according to the input level at A by:

$$S_B(dBm) = S_A(dBm) - (N + 2 - p) \tag{4.19a}$$

$$N_B(dBm) = N_A(dBm) - (N + 2 - p) \tag{4.19b}$$

A coherent crosstalk caused by a delayed version of the added signal is generated due to the circulator leakage which adds to the noise level a leakage of 50 dB of the signal power P_{add}^0 at the input of the ADD path:

$$N_B(mW) = N_A(mW) + 10^{\frac{P_{add}^0(dBm) - 50}{10}} \tag{4.20}$$

Another coherent crosstalk is created by switch imperfections. A pair of switches adds to the noise level a leakage of 66 dB of P_{add}^0. This noise is created $(N - p) \cdot (N - p - 1)$ times:

$$N_B(mW) = N_A(mW) + ((N - p) \cdot (N - p - 1)) \times 10^{\frac{P_{add}^0(dBm) - 66}{10}} \tag{4.21}$$

A third delayed version of the added channel comes from the IN port, this occurs because a fraction of the input signal at the IN port has not been dropped at the DROP port and passes through the OADM until it interferes with the added signal. Such an incoherent crosstalk increases the noise with a leakage of 41 dB of the power P_o at the OADM input, in addition, switches imperfections adds a leakage of -71 dB $p \cdot (N - p + 1)$ times:

$$N_B(mW) = N_A(mW) + 10^{\frac{P_o(dBm) - 41}{10}} + (p \cdot (N - p + 1)) \times 10^{\frac{P_o(dBm) - 71}{10}} \tag{4.22}$$

DROP

Similarly to added path channel case, the signal and noise power of the dropped channel is decreased by $(1 + p)$ dB:

$$S_B(dBm) = S_A(dBm) - (1 + p) \tag{4.23a}$$

$$N_B(dBm) = N_A(dBm) - (1 + p) \tag{4.23b}$$

The noise increases due to switches and FBG imperfections which cause power leakage at the IN-DROP port and the ADD-DROP port :

$$N_B(mW) = N_A(mW) + 10^{\frac{P_o(dBm) - 50}{10}} + 10^{\frac{P_{add}^0(dBm) - 41}{10}}$$
$$+ (p \cdot (p - 1)) \times 10^{\frac{P_o(dBm) - 66}{10}} + (p \cdot (N - p + 1)) \times 10^{\frac{P_{add}^0(dBm) - 71}{10}} \tag{4.24}$$

PASS-THROUGH

The signal of the pass-through channel is decreased by an amount of $(1 + N/2)$ dB which stands for various components losses encountered while traversing the OADM. It includes: IN connector insertion loss, OUT connector insertion loss, intermediate gratings transmission loss, intermediate switches insertion loss:

$$S_B(dBm) = S_A(dBm) - (1 + \frac{N}{2}) \tag{4.25a}$$

$$N_B(dBm) = N_A(dBm) - (1 + \frac{N}{2}) \tag{4.25b}$$

A delayed version of the signal is created by switch and FBG imperfections. The noise is increased by a leakage of 71 dB of the input power P_o, $((N - p)(N - p + 1) + p(p - 1))/2$ times:

$$N_B(mW) = N_A(mW) + \frac{((N - p) \cdot (N - p + 1) + p \cdot (p - 1))}{2} \times 10^{\frac{P_o(dBm) - 71}{10}} \tag{4.26}$$

Nota: The reference points "A" and "B" are to be related to the ADD, DROP and PASS-THROUGH paths illustrated in Figure 4.8.
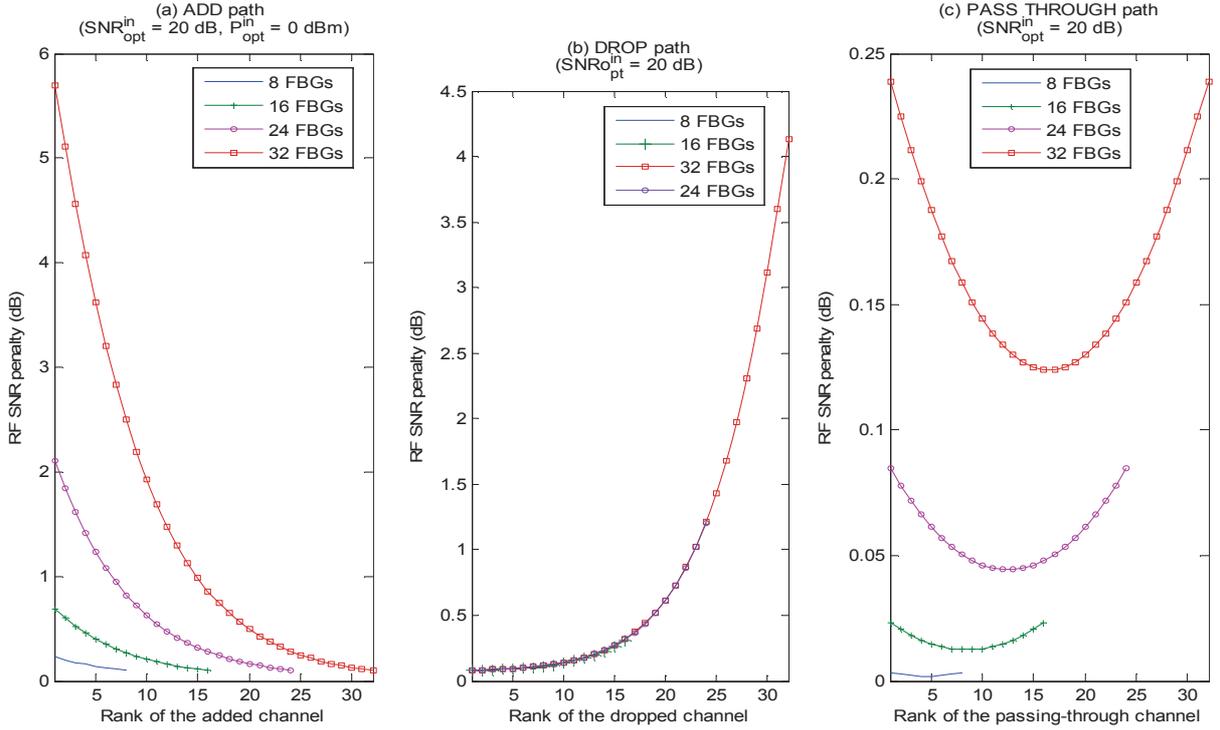
Figure 4.9: RF SNR penalty due to OADM Homodyne crosstalk for (a) the ADD path, (b) the DROP path and (c) the PASS-THROUGH path.

A higher number of optical channels increases the crosstalk penalty. We notice the dependance of the penalty distribution with the rank of the optical channel. In practice, optical wavelengths are mapped in an ascending order with FBGs from the left to the right side of the OADM. SNR_{opt}^{in} and P_{opt}^{in} stand for SNR and signal power at the input of the ROADM (at reference point "A" of the considered path) respectively.

reflected as well, causing interference with the dropped channel. To estimate the level of the crosstalk noise between reflected and transmitted signals, we focus on the reflectivity spectrum of the FBG. The choice of the FBG model is conditioned by key spectral characteristics including the flatness of its pass-band, the severity of pulse distortion related to the phase response of the grating, the strength of the out-of-band side-lobes and the symmetry of the reflectivity spectrum [130]. For simplicity, a standard uniform FBG model is assumed in our calculations.

Equation 4.27 expresses the complex reflectivity coefficient ρ of an FBG with respect to the optical wavelength λ:

$$\rho(\lambda) = \frac{-\kappa \sinh(\alpha \cdot \ell^{fbg})}{\sigma \sinh(\alpha \cdot \ell^{fbg}) + \jmath \cdot \alpha \cosh(\alpha \cdot \ell^{fbg})} \tag{4.27}$$

Given: σ, κ the DC and AC coupling coefficient respectively, ℓ^{fbg} FBG length and the coefficient $\alpha = \sqrt{\kappa^2 - \sigma^2}$ [140].

The power of Heterodyne crosstalk noise generated by optical channel j on optical channel i (modulated by the same radio-frequency f) is given by Equation 4.28:
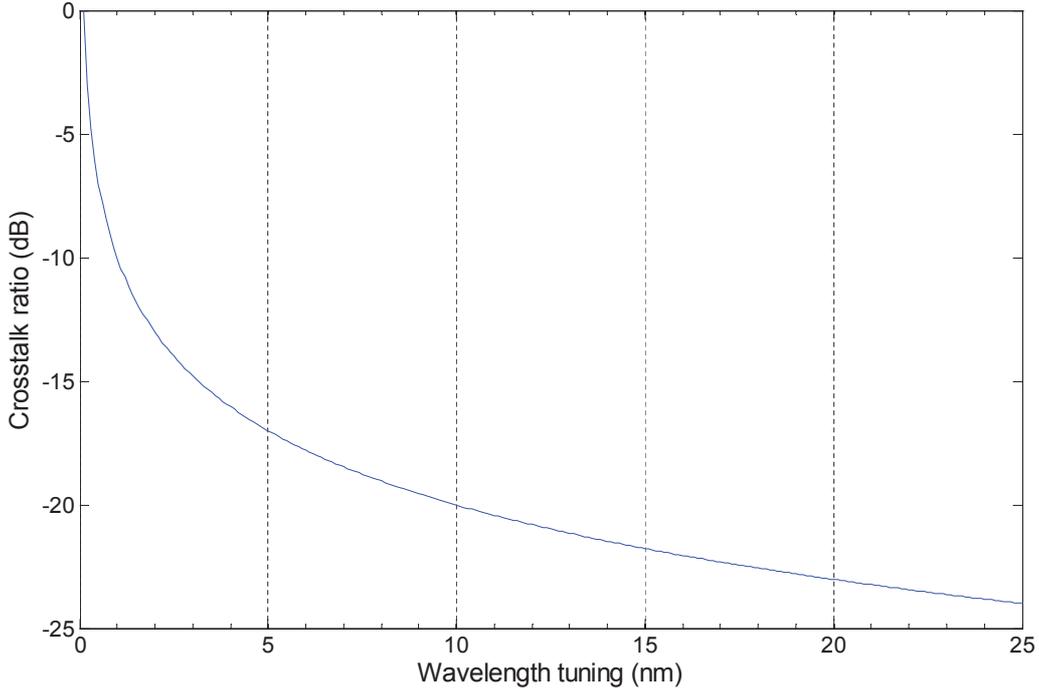
Figure 4.10: Crosstalk coefficient of a uniform BFG *vs.* wavelength tuning.

A uniform FBG model is used to compute reflected and transmitted signal spectra. A detuning of $1\ nm$ from the reflected wavelength causes a crosstalk coefficient of $-10\ dB$. To minimize the effect of heterdyne crosstalk, active optical channels should be enough spaced.

$$N_{j|i} = (x_{ij} \cdot \cos(2\pi f \tau_{ij}))^2 \cdot P_j \tag{4.28}$$

Given: P_j the RF power of the subcarrier modulating channel j, x_{ij} the crosstalk ratio between channels i and j, $\tau_{ij} = \tau_i - \tau_j$ the difference in time delay between channels i and j. The parameter $\tau_i = \tau_{prop,i} + \tau_{roadm,i}$ includes the time delay of channel i[8] due to fiber propagation ($\tau_{prop,i}$) and the add/drop/pass-through time delay ($\tau_{roadm,i}$) due to the ROADM. The parameter $\tau_{roadm,i}$ is calculated as: $\tau_{roadm,i} = \tau_{eamsoa} + (i \cdot \tau_{fbg})$ if channel i is dropped, $\tau_{roadm,i} = \tau_{eamsoa} + ((N - i + 1) \cdot \tau_{fbg})$ if channel i is added and $\tau_{roadm,i} = N \cdot \tau_{fbg}$ if channel i passes-through the ROADM; assuming: τ_{eamsoa} the propagation delay across the EAMSOA and τ_{fbg} the reflection/transmission delay of the FBG[9] and recalling that N refers to the number of FBGs in the ROADM system.

We compute the phase of the complex reflectivity ρ and its module to get τ_{fbg} and x_{ij} respectively. Figure 4.10 depicts the crosstalk ratio x_{ij} of a standard uniform FBG of length $\ell^{fbg} = 11\ mm$ with respect to wavelength tuning.

---

[8]The channel is considered of rank i in the FBG sequence within the ROADM. The delay caused by circulators is assumed to be negligible.

[9]We assume that the reflection and the transmission delays across the FBG are equivalent.

4.5 Fiber impairments

Analog RoF transmission is subject to optical propagation impairments. Both linear and non-linear fiber transmission limitations are considered in our QoT model. The major impairments include Chromatic Dispersion (CD), Polarization Mode Dispersion (PMD), Optical Beat Interference (OBI), Rayleigh Back-Scattering (RBS) and fiber Non-Linear Effects (NLEs).

4.5.1 Chromatic Dispersion

Thanks to its simplicity, GeRoFAN uses double side-bands modulation to modulate the optical carrier. However, because of CD, the OC, its sidebands, as well as their carried RF channels, propagate at different velocities. At the photo-detector, when beating the two sidebands of the optical channel to extract the radio signals, a power fading at each RF channel occurs due to their velocity mismatch [93]. After transmission over optical fiber of length L and CD coefficient D at OC λ, CD penalty is measured in terms of average squared Error Vector Magnitude (EVM) according to [24]:

$$\langle EVM^2 \rangle \simeq \frac{1}{N_{sc}} \cdot \left[(N_{sc}+1) + \sum_{n=-N_{sc}/2}^{N_{sc}/2} \eta^2 \cos\left(\frac{\omega_n^2}{2} - \frac{\lambda^2 DL}{2\pi c}\right)^2 - \right. \tag{4.29}$$
$$\left. 2\eta \cdot e^{\frac{-\sigma_\varphi^2}{2}} \sum_{n=-N_{sc}/2}^{N_{sc}/2} \cos\left(\frac{\omega_n^2}{2} - \frac{\lambda^2 DL}{2\pi c}\right) \right]$$

Given: $\eta = |\frac{J_1(m)}{J_o(m)}|$: the relative amplitude of the optical carrier to its first-order side-bands; J_i: the first kind Bessel function of order i; m: the total OMI of the SCM RF signal modulating the OC expressed with respect to the OMI m_i of each RF channel as in Equation 4.14; N_{sc}: the number of OFDM SCs of a RF channel; ω_n: the angular frequency of the nth OFDM SC and σ_φ: the average RF phase noise power.

The evolution of η with respect to the number of RFs modulating an OC and at different OMI m_i is depicted in Figure 4.11.

Considering the relation between SNR and EVM as $SNR = 1/\langle EVM^2 \rangle$, Figure 4.12 illustrates the effect of CD on optical SNR with weak (2.5%) to moderate (25%) values of η. A modulation depth of (5%) at 1.5 GHz modulating RF and a phase noise power of $\sigma_\varphi^2 = 5$ ‰ are assumed [24].

4.5.2 Polarization Mode Dispersion

In SCM analog optical systems, the composite electrical signal at the receiver is produced by heterodyne beating between the optical carrier and its subcarriers. To achieve a correct demodulation, it is necessary to align the State of Polarization (SoP) between the optical carrier
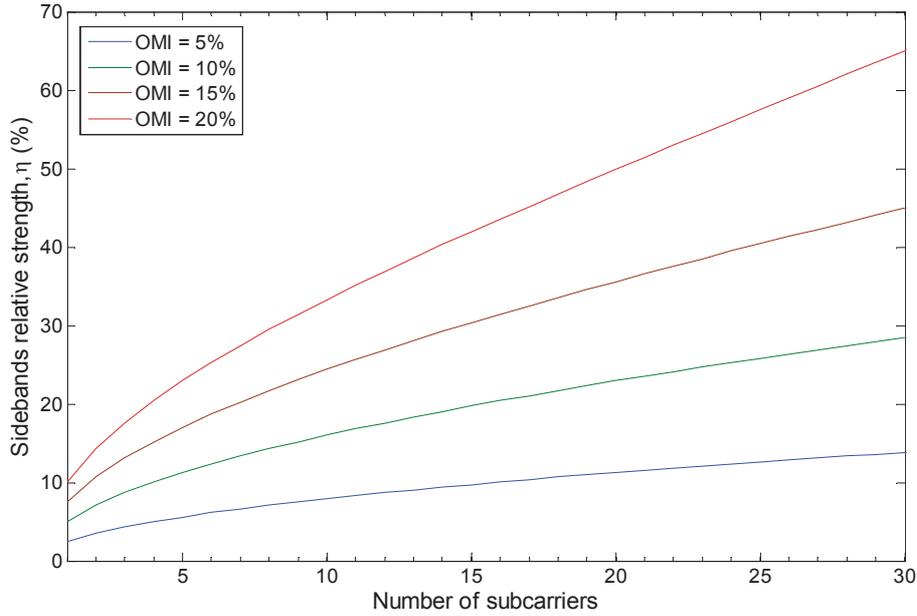
Figure 4.11: Evolution of η with the number of subcarriers and modulation depth.

Increasing the modulation depth per subcarrier increases the relative optical sideband intensity. In addition, as one "loads" the optical channel with more RFs, the velocity mismatch between the carrier and its subcarriers increases. In general, with double sideband modulation, the carrier absorbs the highest share of the injected optical power in the modulator, but as the number of subcarriers increases more and more optical power is shifted to the sidebands as shown by the increase of η with the number of RFs.

and its modulating subcarriers. The common birefringence of the optical medium makes the SoP to walk-off after propagation through the fiber, introducing fading in the beating signal. According to the analytical modeling in [114], the SNR power penalty δ caused by PMD at microwave frequency f over an optical link length L is expressed by Equation 4.30:

$$\delta = \cos(\pi \cdot f \cdot \tau) \tag{4.30}$$

Where: $\tau = \beta_{pmd} \cdot \sqrt{L}$: the differential group delay of the fiber; β_{pmd}: the PMD coefficient of the Single Mode Fiber (SMF).

4.5.3 WDM Non-linear Effects

In a WDM system, increasing the transmitted power to overcome the signal loss accumulated along the optical path is more prone to multi-channel crosstalk noise arising from fiber non-linearity. In [131], the impact of fiber non-linearity has been considered in Hybrid Fiber Coaxial-cable (HFC) system in order to find the optimal optical launch power intended to balance between receiver sensitivity and optical non-linear effects. Although the impact of NLEs on systems with optical reach smaller than 100 *Km* is relatively small [5], the main considered NLEs are Stimulated Raman Scattering (SRS) and Fourth Wave Mixing (FWM).
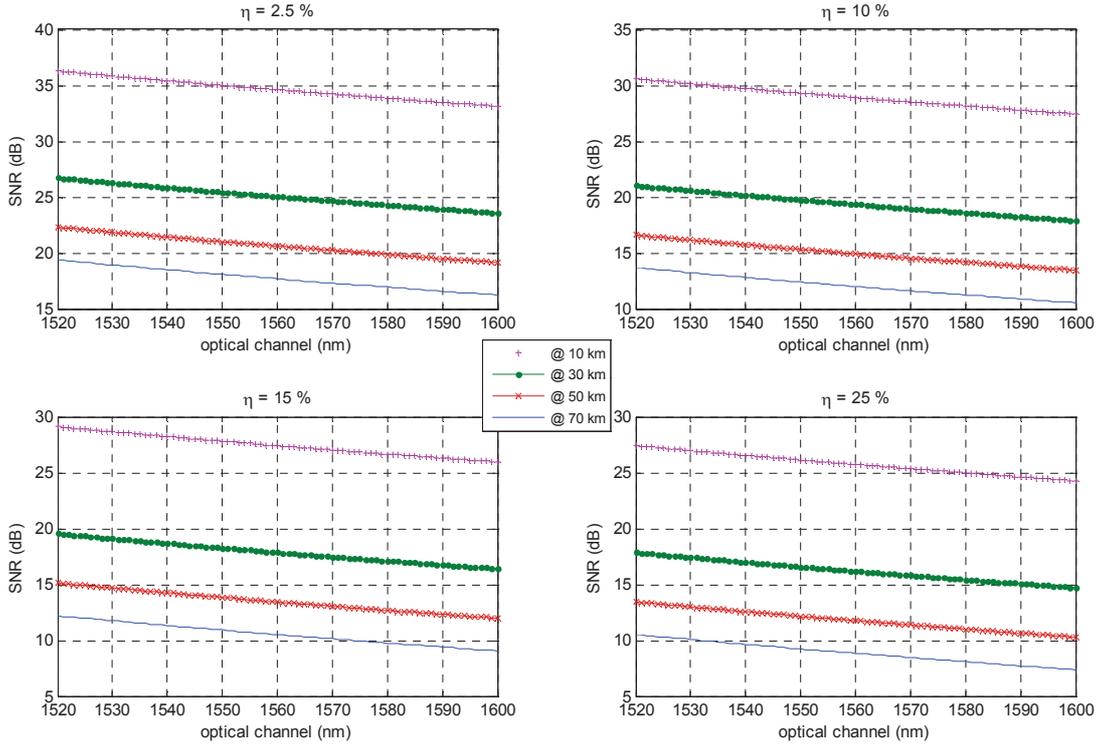
Figure 4.12: Impact of CD on optical SNR with 5% OMI at 1.5 GHz.

The figure shows the conjugation of 3 parameters impacting the CD penalty. The optical wavelength, the number of subcarriers per optical channel and the transmission distance.

4.5.3.1   Stimulated Raman Scattering:

In WDM systems, the fiber acts as a Raman amplifier such that the long-wavelength channels are amplified by the short ones as long as the wavelength difference is within the bandwidth of the Raman gain [5]. The power depletion from short wavelength channels at the benefit of long wavelengths, induces SNR penalty δ at each optical channel given by Equation 4.31:

$$\delta = -10\log(1 - D_R) \tag{4.31}$$

Where: D_R is the depletion factor of an optical channel [5].

4.5.3.2   Fourth-Wave Mixing:

FWM is another source of non-linear crosstalk created by *Kerr* effect in optical fibers. FWM-induced crosstalk induces optical signal distortions because of intermodulation products generated by propagating optical waves. The impact of FWM crosstalk becomes important whenever the optical channel spacing and fiber dispersion are small [5]. In the FWM generation process, three waves propagating at optical frequencies f_i, f_j, f_k combine together into IMD3 products to create a noisy product $f_l = f_i \pm f_j \mp f_k$ that may fall into the signal band. Two types of

FWM products are distinguished: degenerate (2 tones) and non-degenerate (3 tones) products. Assuming the worst case scenario where the phase mismatch between optical waves tends to 0, the variance of a single FWM product is given by [66] and expressed in Equation 4.32:

$$\sigma_{FWM}{}^2 = \left(\gamma \cdot M \cdot \frac{D_{deg}}{3} \cdot \frac{1 - exp(-\alpha L)}{\alpha} \right)^2 P_i P_j P_k \tag{4.32}$$

Given: D_{deg}: the degeneracy factor equals to 6 and 3 for non-degenerate and degenerate FWM products respectively; γ, α : the fiber non-linear and attenuation coefficient respectively; M: the number of traversed SOAs along the optical lightpath; and P_i, P_j, P_k: the average input optical power at channels i, j and k.

4.5.4 Rayleigh Back-Scattering

Rayleigh Back-Scattering (RBS) is particularly pointed out in bidirectional reflective transmission systems such as PONs [59]. RBS noise occurs when the Rayleigh back-scattered incident wave, caused by microscopic non-homogeneities of the fiber material, interferes with the reflected modulated optical wave. RBS results in signal power instabilities and in-band crosstalk causing degradation of the receiver sensitivity. The impact of RBS increases with the propagation inducing a limitation on the fiber length [63]. Some solutions are suggested to reduce the impact of RBS including: additional phase modulation, polarization scrambling and the deployment of low coherence light sources, while in [144] a proposed method is based on adjusting the modulator bias current/voltage.

Following the analytical approach in [148], we provide in Equation A.26 the mathematical expression of RBS Power Spectral Density (PSD) evaluated along an optical link of length L:

$$N_{rbs}(f) = \frac{10 R_{rb}^2 (2aL + e^{-2aL} - 1)}{9} \cdot \mathfrak{F}\langle |R_{\varepsilon_{sig}}|^2 \rangle \tag{4.33}$$

Given: $R_{\varepsilon_{sig}}$: The autocorrelation function of the signal electric field ε_{sig}; a: Fiber attenuation coefficient; R_{rb}: RBS reflectance of the SMF and $\mathfrak{F}$: denotes the Fourier transformation operator. The mathematical development of Equation A.26 is detailed in the **Appendix**.

4.5.5 Optical Beat Interference

In a WDM-PON system, two upstream OCs with the same wavelength may be modulated by distinct radio signals at RFs i and j, then combined at the optical coupler and detected. Because of the square-law of the detection process, the beating between the OCs generates IMD-like interference between their subcarrier RF channels that may fall on a designated RF channel $\ell = 2i \pm j$. The frequency spectrum of the interference term is determined by convolving the frequency spectra of the OCs. The PSD of the OC at the output of the DFB laser is approximated by a Lorentzian function with a line-width broadened by the frequency chirp of

the RAM. Following the development in [37], we express the Signal to Interference Ratio (SIR) defined as the ratio of the signal power to the OBI noise power falling within the bandwidth of RF channel ℓ as:

$$SIR = \frac{\frac{1}{2}\langle m_\ell^2 P_{o,\ell}^2 \rangle}{\int_{B_\ell} N_{ij}(f)\, \mathrm{d}f} \tag{4.34}$$

The PSD of the OBI noise due to the beating of OCs i and j is provided by Equation 4.35:

$$N_{ij}(f) = 4\sqrt{P_{o,i}P_{o,j}} \cdot \sqrt{f(V_i)f(V_j)} \cdot |\cos(\Phi)| \cdot (S_i(f) \otimes S_j(f)) \cdot \langle \cos^2 \theta_{ij} \rangle \tag{4.35}$$

Given: m_ℓ: the OMI of RF channel ℓ; B_ℓ: the bandwidth of RF channel ℓ; $S_k(f)$: The Lorentzian PSD of the electric field of OC modulated by RF k. $P_{o,k}$: Received optical power of OC modulated by RF k; Φ: the phase difference between the two optical carriers; θ_{ij}: the difference in polarization angle between fields i and j; $\otimes$: Convolution operator; $\langle \cdot \rangle$: Time average operator.

The analytical development of the OBI noise is detailed in the **Appendix**. The optical power of OBI-induced IMD3 noise falling on frequency $f_\ell = 2f_i - f_j$ is given by Equation A.37:

$$N_\ell^{obi} = \frac{\left.\frac{\mathrm{d}g}{\mathrm{d}V}\right|_{V_b} \cdot \left.\frac{\mathrm{d}^2 g}{\mathrm{d}V^2}\right|_{V_b}}{4} \cdot V_b^2 \cdot \sqrt{P_{o,i}P_{o,j}} \cdot m_i^2 m_j \cdot |\cos(\Phi)| \cdot \int\limits_{f_\ell - B_\ell/2}^{f_\ell + B_\ell/2} F(f - f_\ell)\mathrm{d}f \tag{4.36}$$

Given: $g = \sqrt{\mathfrak{f}}$: the root square of then EAM transfer function $\mathfrak{f}$; m_i and m_j: the OMI of RF channels i and j respectively; $F(\cdot)$: the Lorentzian distribution function detailed in the **Appendix**.

4.5.6   Other impairments

Apart RoF modulator, ROADM and fiber induced impairments, our QoT modeling include also receiver noises and other miscellaneous system penalties.

4.5.6.1   Receiver noises

Virtually all photo-detectors in use are based on the PIN structure. The main devices are: Avalanche Photo-Diode (APD) that provides a higher gain due to the avalanche effect, photo-conductors and direct illumination of phototransistors.

Photo-detectors offer a 3 dB bandwidth that is large enough to accommodate most link applications ranging from 10 GHz to more than 100 GHz. Meanwhile, such a high bandwidth comes at the expense of lower fiber-coupled responsivities especially at higher frequencies for which up to 20.4 dB contribution to the RF link loss is reported [30]. Another tradeoff is between linearity and optical power. Photodiode non-linearities are due to absorption saturation,

electric field screening due to an external circuit effect, or a space charge in the intrinsic layer [72]. Operating at high optical powers, increases the power density at the photodiode junction especially for photo-detectors with small illuminated surface, thus increasing the risk of non-linearities. Although for low-frequencies, photo-detectors are nearly ideal (responsivity, power handling and linearity), issues raise at higher frequencies. At these frequencies, the conflict linearity/power density can be reduced either by increasing the bias current or by changing the illumination geometry of the device as the case in edge-illuminated photo-detectors [30].

In the following, because the target application is remote antenna fiber optic link backhauling, photodiode non-linearities are neglected [72]. Indeed, at the receiver side, three main noise sources are expected to degrade the carrier-to-noise ratio: the thermal noise, the shot noise, the dark noise. While the thermal noise is common to any optoelectronic device, shot noise and dark noise are specific to the photo detection process of optical receivers.

- **Thermal noise:** Thermal noise of the receiver is modeled as a white noise process. The signal is quantified by the modulation depth m and a photocurrent I_o. The thermal white noise is relative to the ambient temperature and the noise factor of the receiver. The noise factor can be modeled through an equivalent noise current density i_N over the bandwidth B_e of the electrical filter. The CNR is expressed according to Equation 4.37:

$$CNR_{Th} = \frac{m^2 I_o^2}{2 i_N^2 B_e} \tag{4.37}$$

- **Shot noise:** Shot noise occurs because the light is composed of discrete packets of energy bursts of photons. The randomness of the arrival time of each photon generates a random noisiness in the current at the output of the photodiode. Shot noise can be considered as a white noise process and its associated CNR is computed through [6]. Let q_e stands for the electron charge. In case of APD diode, q_e equals to M times the electron charge since a single photon is expected to generate M electrons thanks to the avalanche effect. The expression of the CNR is given by Equation 4.38:

$$CNR_{sh} = \frac{m^2 I_o^2}{2 q_e I_o B_e} \tag{4.38}$$

- **Dark noise:** Dark noise is constant over the electric bandwidth of the signal. The dark noise current density expressed in A/Hz is specified for a given photo-diode. To get the dark noise over the signal bandwidth, the noise current density is simply multiplied by the electrical bandwidth of the RF signal.

4.5.6.2   Miscellaneous system penalties:

- **Beating noises at the receiver:** They include signal-ASE beating noise and ASE-ASE beating noise at the receiver. These noises are dependant of the signal photo-current, the noise-induced photocurrent, the electrical bandwidth of the signal and the optical bandwidth of the receiver. Analytical expressions of these beating noises are detailed in [105].

- **Splitter penalty:** A power penalty is considered each time the optical signal is splitted, while the splitter penalty increases with the splitting ratio [5].

4.6   Building a comprehensive QoT-tool

Given the physical layer modeling of RoF analog impairments, Table 4.4 identifies the least penalized optical channels in the WDM pool for each impairment.
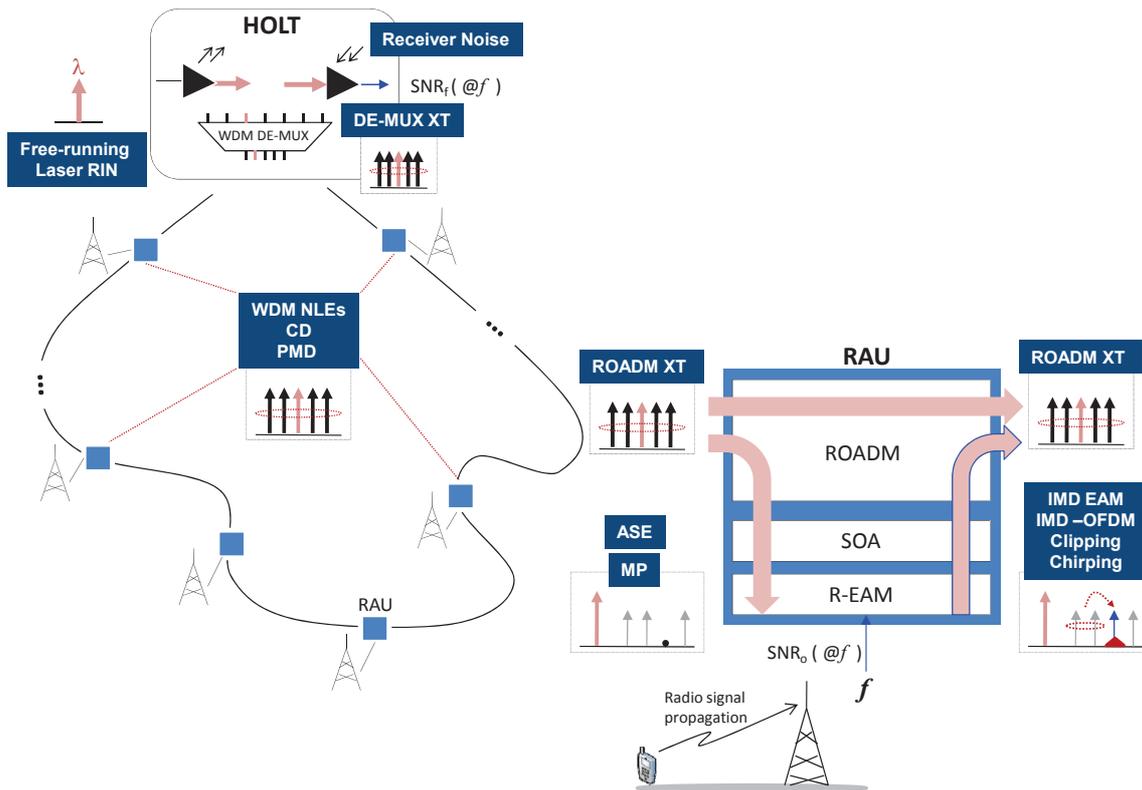
Figure 4.13: Illustration of the different impairments for a GeRoFAN loop network.

For a given radio-frequency, the SNR penalty is calculated as the ratio between the initial SNR (SNR_o) at the transmitter side and the SNR upon photo-detection and demodulation (SNR_f) at the receiver side.

The evaluation of optical layer limitations is tightly related to the GeRoFAN topology. We consider the most used access topologies: trees and loops. Figures 4.13 and 4.14 illustrate
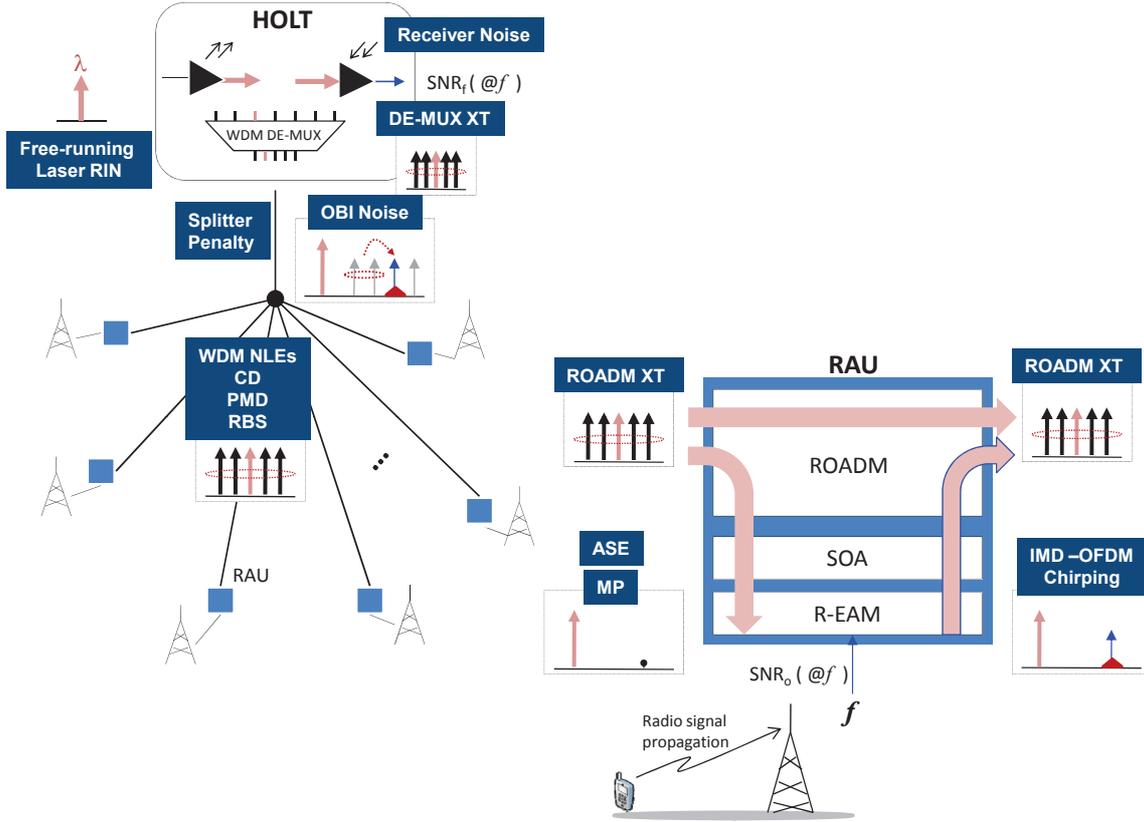
Figure 4.14: Illustration of the different impairments for a GeRoFAN tree network.

From the RAU until demodulation at the HOLT, the SNR of an uplink radio-frequency is penalized due to several impairments along the RoF backhauling link.

for each GeRoFAN topology how the different optical impairments considered in our model cumulate together. Impairments analytical modeling is formulated for both architectures and packaged into software program called *QoT-tool* which will be used by the GeRoFAN-CP to check the SNR relative to a given cellular backhauling strategy. Table 4.5 describes the relevant QoT impairments for each considered GeRoFAN topology. For each impairment, we highlight the relevant factors that contribute to impact the SNR. These factors, except L_{opt}, constitute the action levers exploited by the control plane of the GeRoFAN system. They include:

- **The optical channel:** It is represented by its wavelength value $[\lambda]$ and its relative rank with respect to the other co-propagating optical channels in the network $\lambda_{i|1\cdots W}$.

- W**:** The total number of optical channels per fiber.

- $N_{RF/\lambda}$**:** The number of RF channels transported by the same optical carrier.

- **The subcarrier radio channel f:** It is represented by its microwave frequency $[f]$ and its relative position with respect to other RF channels sharing the same optical carrier

Table 4.4: Selection rules of optical channels for each impairment, WDM channels in the C-band ("+" denotes least penalized OCs, "-" denotes most penalized OCs)

Optical carrier (OC)	short OCs	middle OCs	long OCs
Modulation Penalty (MP)	-	+	-
IMD	-	-/+	+
OADM Homodyne XT, Drop path	+	+/-	-
OADM Homodyne XT, Add path	-	-/+	+
OADM Homodyne XT, Pass path	-	+	-
Rayleigh Back-Scattering (RBS)	+	-	+
Chromatic Dispersion (CD)	+	+/-	-
WDM NLEs, SRS	-	-/+	+

Table 4.5: Analog RoF limitations for GeRoFAN loop and tree topologies.

Impairment	W	$[\lambda]$	$\lambda_{i|1\cdots W}$	$N_{RF/\lambda}$	$[f]$	$f_{i|1\cdots F}$	L_{opt}	**Loop**	**Tree**
MP[10]		✓		✓	✓		✓	✓	✓
IMD[11]		✓		✓	✓	✓		✓	
IMD-OFDM		✓		✓	✓	✓		✓	✓
ROADM-XT[12]	✓		✓	✓	✓			✓	✓
OBI		✓		✓	✓	✓	✓		✓
RBS		✓		✓			✓		✓
CD		✓		✓	✓		✓	✓	✓
NLE[13]	✓	✓	✓	✓			✓	✓	✓
PMD		✓			✓		✓	✓	✓
Receiver noises		✓			✓			✓	✓
Splitter penalty				✓					✓

$f_{i|1\cdots F}$.

- L_{opt}: The length of the optical link which is constant once the network has been deployed.

Both topologies are subject to common impairments like fiber non-linearities, chromatic dispersion, polarization mode dispersion and RoF Modulator Penalty (MP). Because of the cascaded optical carrier modulation in a loop, noise accumulates at each RAU which increases modulator penalty at each stage. In a tree configuration, a continuous-wave OC is splitted before getting broadcasted to the RAUs where it will be modulated by RF upstream traffic. Hence the splitter penalty decreases the SNR of the optical carrier at the input of the modulator. In a loop topology, RF channels are more prone to interact together within the modulator (through IMDs) or the ROADM (Heterodyne CrossTalk (XT)). Meanwhile, interaction between RFs in a

---

[10]MP designates the noise figure of the RoF link.

[11]Including IMD-RAM, clipping and chirping. Note that when several RFs modulate the OC at the same RAU, an optical tree topology is also subject to IMD.

[12]An optical tree is only subject to Homodyne crosstalk.

[13]Including FWM and SRS impairments.

tree occurs through optical beat interference and eventually within the modulator if several RFs are present at the same RAU. Finally, only the tree topology may suffer from Rayleigh back-scattering noise since the incident optical signal and the reflected modulated signal propagate in opposite directions on the same optical fiber.

Part III

GeRoFAN-CP Algorithmic Design

Impairment-aware CP Design for Static Traffic

Contents

5.1 Introduction

As outlined in Chapter 3, the main originality of the GeRoFAN-CP is to be radio MAC-agnostic to accommodate generically a wide variety of mobile systems. This CP takes into consideration the impact of signal impairments inherent to RoF transmission. Our objective is to make the cellular backhauling provided by the GeRoFAN-CP as much as as possible transparent to the mobile system. In this chapter, we investigate how the backhauling strategy of the CP can be formulated and solved through an optimization problem. This chapter assumes a uniform distribution of the traffic load across all cell sites, it is structured as follows. In Section 5.2, we describe the architecture of the GeRoFAN-CP and its interaction with the radio layer.

Section 5.3 formulates the rationale of the CP through an exact optimization approach. In Section 5.4, we present an alternative approach based on evolutionary algorithms to solve the CP optimization problem. Finally, we investigate in Section 5.5 the impact of overlaying several radio channels per cell site on the system capacity.

5.2 The cross-layer architecture of the GeRoFAN-CP
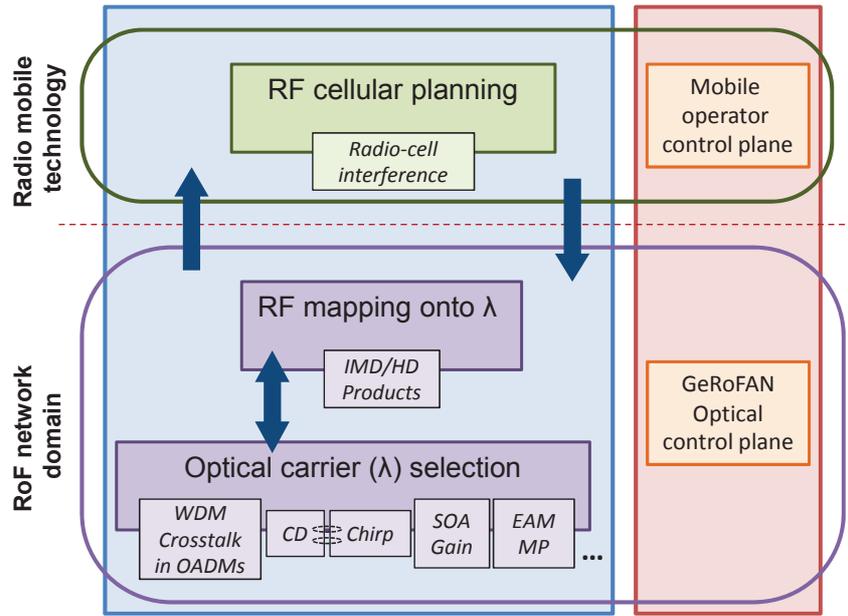
Figure 5.1: The cross-layer architecture of the GeRoFAN-CP.

The GeRoFAN-CP investigates the optimal backhauling strategy that aims at maximizing the capacity utilization of the optical carrier while minimizing for each RF channel the SNR penalty that stems from the optical part of the system. Thus, dealing with non-ideal RF front-ends are out-of-the scope of the GeRoFAN-CP and their effects are assumed to be compensated by the radio operator at the HOLT. RF front-end devices main impairments include co-channel radio cellular interference, DC offsets[1], I/Q imbalance[2], non-linearities of the Power Amplifier (PA), oscillator frequency drift[3] and aperture clock jitter of the ADC/DAC[4] [43]. The effects of RF front-ends can be mitigated from the HOLT by the radio CP through dedicated stabilization

---

[1] DC-offset occurs due to self mixing of the signals caused by non-perfect isolation between the LO and the PA at the HOLT for downstream traffic.

[2] I/Q imbalance denotes the imperfect orthogonality of the in-phase and quadrature components during the complex mixing process. In today's commercially available components, the image signal is multiple orders of magnitude weaker than the information carrying signal [43].

[3] Called also Phase Noise, the mixing radio frequency of the LO drifts slightly from its original value due to abrupt small changes of the controlling voltage, this results in phase distortions of the signal.

[4] In ADC, a clock-driven switch performs the sample-and-hold action by disconnecting quickly the hold capacitor from the input buffer amplifier. This action requires a short time interval called the aperture time of the ADC. The aperture clock jitter designates commonly the variation of the aperture time from one sample to another.

circuits (DC-offsets, I/Q-imbalance, phase noise of LOs), adequate pre-distortion techniques (to tackle non-linearities arising from practical PAs[5]), Peak-to-Average Power Ratio (PAPR) reduction techniques[6] and more efficient radio planning schemes[7] (to mitigate radio-cell interference). Particular coding and bit-interleaving techniques can help compensate RF front-end impairments. The different aforementioned RF front-end impairment compensation techniques require either a processing at the level of the individual connection (radio packet scale) or playing with the radio specifications of the cellular system (like those based on power control), which make them definitely out-of-scope of the GeRoFAN-CP.

Although mitigating radio cellular interference is the responsibility of the radio operator, the GeRoFAN-CP acquires the quality of the radio channel at the input of the antenna (for uplink channel) to apply the appropriate optical transport policy. For instance, according to the Signal to Interference Noise Ratio (SINR) of the uplink RF channel received by the antenna, the GeRoFAN-CP selects the right OCs and elaborates the optimal mapping of RFs onto OCs such that the RF channel upon reception at the HOLT undergoes the lowest degradation to guarantee a successful demodulation. The interaction between the radio layer and the GeRoFAN-CP (optical) layer is illustrated in Figure 5.1.
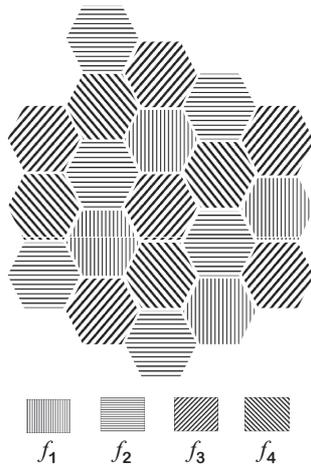
Figure 5.2: A 4 frequency reuse planning.

Carrier radio frequency	2.5 GHz
Radio channel bandwidth [133]	5 MHz
UE RF transmit power	+10 dBm
Inter-RAU distance	$\sqrt{3} \cdot 500\ m$
User location	@250 m
Pathloss exponent	3.65
(Log-distr.) Shadowing variance	3 dB
Free-space propagation loss	25.5 dB
Antenna isotropic RF gain	15 dBi
RF amplifier gain	15 dB
RF amplifier noise figure	5 dB
Noise power per OFDM SC	−140 dBm

Table 5.1: *LTE* radio parameters.

5.3 An exact optimization approach for GeRoFAN-CP

To investigate the feasibility and the ultimate gain of the GeRoFAN-CP backhauling strategy, we propose to formulate the optimal RF-onto-OCs mapping by a Mixed-Integer Linear Programm (MILP). The MILP performs an exact combinatorial optimization through the finite discrete search space. While an MILP insures the optimality of the backhauling solution, the main

---

[5]Non-linearity of the PA/LNA can be mitigated also by reducing the peak-to-average power ratio of the OFDM signal.

[6]Many methods have been proposed to reduce the PAPR including clipping, constellation extension, and Partial Transmit Sequence (PTS) with or without feedback side information from the receiver [81].

[7]Like Fractional Frequency Reuse or Two Level Power Control frequency reuse schemes [65].

difficulty raises from its scalability with the size of the problem due to an increase of the number of radio-cells, the size of the optical pool or the complexity of the radio planning. To make the optimization tractable, we consider for this section a 20-cells radio network, with a cellular planning of four RFs reused regularly across the network as illustrated in Figure 5.2, while at the optical layer we assume a WDM pool of 11 OCs whose wavelengths range from 1532 *nm* to 1562 *nm* with 3 *nm* channel spacing. The second main challenge raised by the MILP is the linearity of its constraints to get the problem solved. Since several QoT impairments modeled in Chapter 4 are intrinsically non-linear, only a subset of these impairments can be included in the MILP formulation. The MILP considers impairments which are either linear, linearizable or that can be accounted by their asymptotic values[8]. In the following subsections, we provide the MILP formulation when a GeRoFAN loop and tree are considered.

5.3.1　ILP optimization for GeRoFAN loop

5.3.1.1　Modeling RAU operating modes
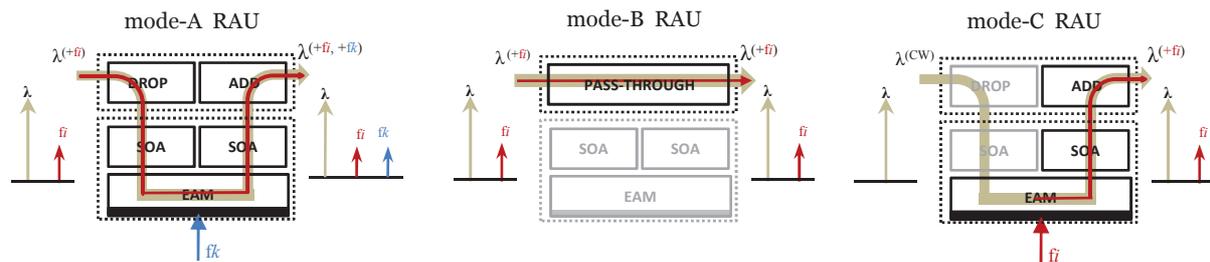
(a) Modeling RAU operating modes.
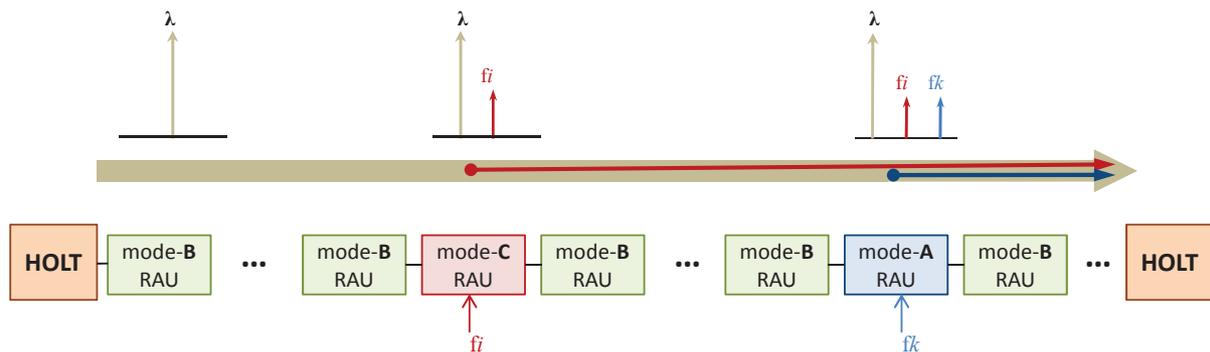
(b) An example of lightpath build as cascaded RAUs as seen by RF f_i.

Figure 5.3: Lightpath modeled as a cascade of RAU operating modes.

When an optical loop is deployed to backhaul the radio cells, the GeRoFAN system can be modeled as a cascade of several RAUs connected by fiber segments. At each RAU, the composite

---

[8]Unlike the heuristic approach presented later, the MILP uses asymptotic values instead of the exact value of the impairment penalty because the MILP does not call the QoT-tool during the optimization procedure.

radio/optical signal undergoes one of the three operating modes of an RAU as illustrated by Figure 5.3a. At a given RAU, the SNR penalty can be evaluated as a function of the various physical impairments and their interaction; the impact of a given impairment being either magnified or dominated by another impairment. Given the SNR penalty due to each operating mode, one can estimate the overall penalty of an RF channel along the optical loop. The three operating modes of an RAU are:

- **Passing-through the RAU (Mode-A)**: An optical carrier λ, previously modulated by f_i, is first dropped by the ROADM before being modulated by an another RF f_k and then re-inserted in the optical loop. In this case, f_i is subject to the add/drop penalties of the ROADM and the absorption/amplification penalties of the REAMSOA.

- **Modulation in the RAU (Mode-C)**: This is the case of f_k in the previous example. The RF f_k is subject to the absorption/amplification penalties of the REAMSOA as well as the add penalty of the ROADM.

- **By-passing the RAU (Mode-B)**: Finally, an optical carrier λ, previously modulated by f_i, may bypass the RAU without any modulation. Only the pass-through penalty of the ROADM is expected to impact the signal quality of f_i.

Figure 5.3b depicts an example where RF f_i undergoes the three different operating modes when it traverses the cascaded RAUs along the loop. It is worth noting that a given radio channel f_i undergoes, along the GeRoFAN optical loop, only a single Mode-C RAU (where it modulates the OC), but many Mode-B RAUs (where its optical carrier passes-through the ROADMs) and some few Mode-A RAUs.

5.3.1.2 SNR penalty

When the RAU operates in Mode-C, the impact of the modulator on the RF signal quality is crucial. Indeed, the SNR degradation due to the REAMSOA is twofold: the penalty due to the modulation itself and the signal distortion due to the non-linear transfer function of the modulator. On one hand, the modulation efficiency depends on the SNR of the optical carrier at the input of the modulator and decreases with the number of hops [99]. On the other hand, the non-linearity of the REAMSOA induces signal in-band distortions caused by the beating between the OFDM sub-carriers composing an *LTE* RF channel [100]. This beating noise increases with the power of the modulated optical carrier.

In a WDM GeRoFAN loop, a large number of RAUs operate in Mode-B with regard to a given OC. Thus, we investigate, in a first step, the impact of the number of consecutive Mode-B RAUs traversed by a given OC before being modulated again at an RAU (Mode-A).
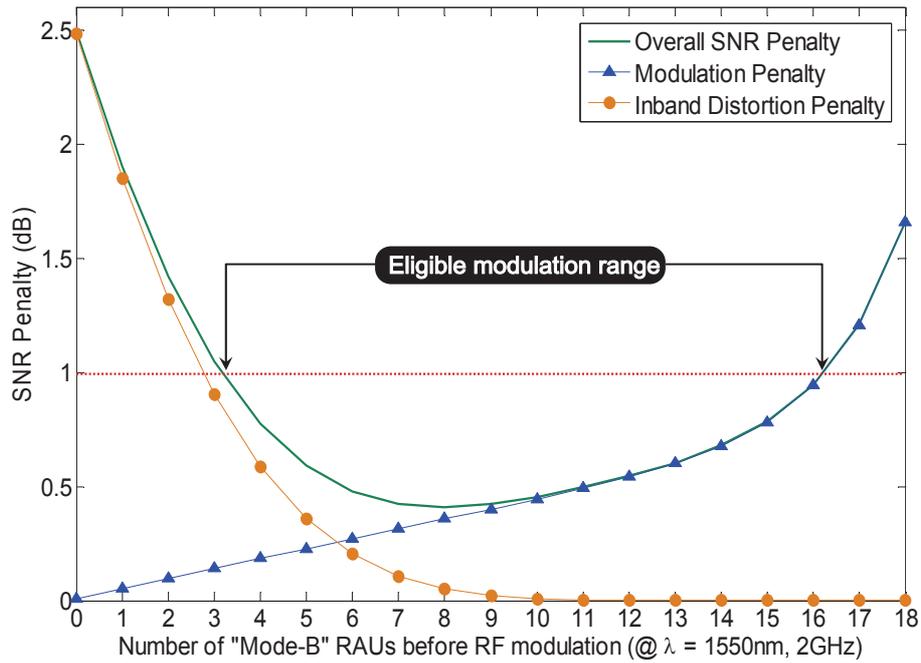
Figure 5.4: SNR penalty *vs.* the number of Mode-B RAUs.

Figure 5.4 illustrates the overall SNR penalty observed by the transported RF channels at the output of a Mode-A RAU *vs.* the number of previously traversed Mode-B RAUs. One notices the non-monotonicity of the overall SNR penalty. This can be explained by the interaction of the two SNR degradations of the REAMSOA. As the number of traversed Mode-B RAUs increases, the power and the SNR of the optical carrier, at the input of the modulator of Mode-A RAU, decrease (no amplification being carried out). On one hand, the modulation penalty increases as the SNR of the optical carrier decreases. On the other hand, the modulator non-linear distortion decreases as the optical power decreases. The overall penalty is dominated by one of the aforementioned penalties with an optimal region where the overall penalty is kept under a predefined threshold. This region delimitates a range of traversed Mode-B RAUs before a modulation could be performed. In a second step, we investigate the SNR penalty[9] induced by a single Mode-B RAU with respect to the optical channel rank. GeRoFAN loops with $W =$ 8, 10, 12, and 16 wavelengths respectively are considered and their penalties are illustrated in Figure 5.5. The lowest penalty is observed at the central wavelength of the considered optical pool. Moreover, the SNR penalty increases with the number of OCs W.

---

[9]The penalty accounts for the homodyne optical crosstalk when the OC passes-through the ROADM.

Table 5.2: Eligible ranges for the first 4 modulations and corresponding average SNR penalties in dB.

$\omega:\lambda_\omega(nm)$	$\Gamma_{1,\omega} - \Gamma'_{1,\omega}$	$\Upsilon_{1,\omega}$	$\Gamma_{2,\omega} - \Gamma'_{2,\omega}$	$\Upsilon_{2,\omega}$	$\Gamma_{3,\omega} - \Gamma'_{3,\omega}$	$\Upsilon_{3,\omega}$	$\Gamma_{4,\omega} - \Gamma'_{4,\omega}$	$\Upsilon_{4,\omega}$	$\varepsilon(\times 10^{-3})$
1 : 1532	0 - 15	0.52	0 - 11	0.85	0 - 9	0.88	2 - 9	0.92	8
2 : 1535	0 - 14	0.99	0 - 12	0.70	0 - 11	0.81	4 - 7	0.92	6.7
3 : 1538	2 - 14	0.80	1 - 12	0.82	2 - 11	0.90	3 - 11	0.92	5.7
4 : 1541	2 - 14	0.94	2 - 12	0.69	2 - 12	0.72	6 - 8	0.85	5
5 : 1544	2 - 14	0.77	1 - 12	0.89	2 - 12	0.90	6 - 7	0.93	4.5
6 : 1547	1 - 15	0.80	2 - 11	0.89	6 - 8	0.97	7 - 8	0.82	4.4
7 : 1550	3 - 16	0.62	0 - 12	0.75	1 - 11	0.82	3 - 10	0.93	4.5
8 : 1553	0 - 14	0.45	0 - 12	0.74	0 - 11	0.79	2 - 11	0.83	5
9 : 1556	0 - 13	0.27	0 - 13	0.86	0 - 10	0.92	3 - 9	0.85	5.7
10 : 1559	0 - 13	0.24	0 - 13	0.85	0 - 11	0.75	2 - 9	0.97	6.7
11 : 1562	0 - 14	0.58	0 - 11	0.80	0 - 11	0.83	0 - 9	0.90	8

The eligible range of RAUs where modulation can be achieved at low penalty decreases as the number of previously performed modulations increases. Little choice is left for the position of the fourth modulation compared to previous ones. The meaning of the different variables mentioned in this Table are provided in the MILP formulation.
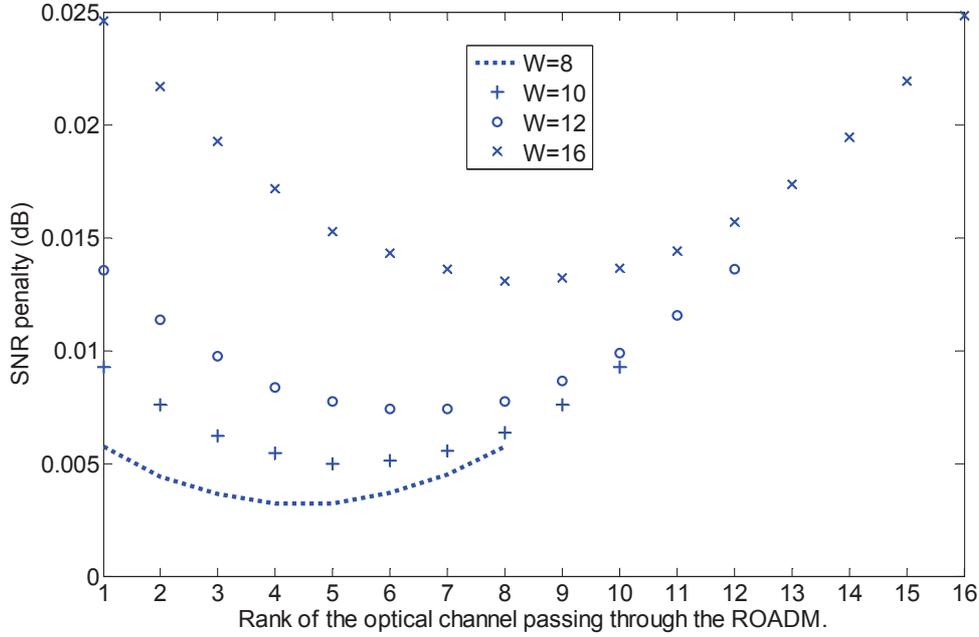
Figure 5.5: SNR penalty when passing through the ROADM.

5.3.1.3 Rules for eligible modulation placement

If the maximum authorized SNR penalty at the output of an RAU operating in Mode-C (Mode-A resp.) is fixed to 1 dB (0.25 dB resp.), we can conclude that the optimal modulation range for the first RF modulation on the 1550 nm wavelength should occur between the 3rd and the 16th RAU along the loop. More generally, we can compute, by means of an analytical model of the SNR penalty, the eligible range where the nth modulation should be performed for the 11 considered OCs in the C-band. Table 5.2 summarizes eligible RAU location ranges for the first

four RF modulations and their induced SNR penalties.

5.3.1.4 Mathematical formulation

We formulate the MILP using the following parameters:

- The number N of radio cells and W the maximum number of OCs in the GeRoFAN system.

- The number F of frequencies used in the considered cellular system.

- The maximum number I of RFs that modulate a single OC ($I \leq F$). The value of I is constrained by the penalties due to the different RAU operating modes of GeRoFAN.

- Subscripts/indices $n = 1 \cdots N$, $\omega = 1 \cdots W$, $j = 1 \cdots F$ and $i = 1 \cdots I$.

- According to Table 5.2, let $\Gamma_{i,\omega}$ and $\Gamma'_{i,\omega}$ be respectively the minimum and maximum number of operating Mode-B RAUs that OC ω can tolerate after the ith modulation.

- $\Upsilon_{i,\omega}$: the SNR penalty incurred by the RF channel modulated onto OC ω as the ith modulation.

- ε: the SNR penalty incurred by any RF modulated onto OC ω when it passes-through an RAU.

- ξ_ω: the additional SNR penalty incurred by any RF modulated onto ω when it bypasses a single RAU after the last modulation.

- $F_{n,j}$: a binary parameter representing the radio-mobile cellular deployment. $F_{n,j} = 1$, if the RF f_j is used at cell n. $F_{n,j} = 0$, otherwise.

- A large number $\mathcal{M} \ggg 1$ used to linearize some constraints.

  The ILP optimizes the following variables:

- The binary variables $\mathfrak{y}_{i,n,\omega}$. $\mathfrak{y}_{i,n,\omega} = 1$, if the RF of the nth cell is modulated onto ω as the ith modulation. $\mathfrak{y}_{i,n,\omega} = 0$, otherwise.

- The binary variables $\eta_{n,\omega}$. $\eta_{n,\omega} = 1$, if the RF of the nth cell is modulated onto ω. $\eta_{n,\omega} = 0$, otherwise.

- The non-negative integer variables $\mathfrak{x}_{i,\omega}$ representing the consecutive number of RAUs that are bypassed by ω before the ith modulation. If ω is not modulated for the ith time, $\mathfrak{x}_{i,\omega} = 0$.

- The non-negative integer variables δ_ω representing the consecutive number of RAUs that are bypassed by the wavelength ω after the last modulation. If ω has never been modulated, $\delta_\omega = 0$.

- The binary variables $\theta_{i,\omega}$. $\theta_{i,\omega} = 1$, if ω has been dropped at an ROADM for the ith time. $\theta_{i,\omega} = 0$, otherwise.

- The non-negative integer variables $\vartheta_{n,\omega}$ denoting the number of additional modulations carried out by ω after the jth cell.

- The binary variables $\mu_{i,\omega}$ and the non-negative real variables $\varpi_{n,\omega}$ both used for intermediate calculation.

- The non-negative real variables $\pi_{n,\omega}$ representing the penalty that will be induced by the RF of the nth cell if it modulates OC ω.

- The non-negative real variables Π_n stands for the total SNR penalty computed at the nth cell.

The ILP is solved subject to the following constraints:

- Each cell must modulate a single OC. $\forall n = 1 \cdots N$,

$$\sum_{i=1}^{I} \sum_{\omega=1}^{W} \mathfrak{H}_{i,n,\omega} = 1 \tag{5.1}$$

- Constraint 5.1 is consolidated by these redundant equations:

$$\begin{array}{c|c} \forall n = 1 \cdots N \\ \forall i = 1 \cdots I \end{array} \; \sum_{\omega=1}^{W} \mathfrak{H}_{i,n,\omega} \leqslant 1 \tag{5.2}$$

$$\begin{array}{c|c} \forall n = 1 \cdots N \\ \forall \omega = 1 \cdots W \end{array} \; \sum_{i=1}^{I} \mathfrak{H}_{i,n,\omega} \leqslant 1 \tag{5.3}$$

$$\sum_{i=1}^{I} \sum_{n=1}^{N} \sum_{\omega=1}^{W} \mathfrak{H}_{i,n,\omega} = N \tag{5.4}$$

- The relation between $\eta_{n,\omega}$ and $\mathfrak{H}_{i,n,\omega}$ is given by: $\forall n = 1 \cdots N, \forall \omega = 1 \cdots W$,

$$\mu_{n,\omega} = \sum_{i=1}^{I} \mathfrak{H}_{i,n,\omega} \tag{5.5}$$

- The variables $\theta_{i,\omega}$ are related to $\mathfrak{H}_{i,n,\omega}$ by: $\forall i = 1 \cdots I, \forall \omega = 1 \cdots W$,

$$\theta_{i,\omega} = \sum_{n=1}^{N} \mathfrak{H}_{i,n,\omega} \tag{5.6}$$

- An OC can not be modulated for the ith time if it was not modulated before.

$$\theta_{i,\omega} \leqslant \theta_{i-1,\omega} \tag{5.7}$$

- The cell where an OC ω is modulated for the ith time can only occur after the cell where ω was previously modulated (except if ω was not modulated for the ith time). $\forall i = 2 \cdots I$, $\forall \omega = 1 \cdots W$,

$$\sum_{n=1}^{N} n.\mathfrak{y}_{i-1,n,\omega} + 1 \leqslant \sum_{n=1}^{N} n.\mathfrak{y}_{i,n,\omega} + (N+1).(1-\theta_{i,\omega}) \tag{5.8}$$

- The number of bypasses $\mathfrak{x}_{i,\omega}$ between two consecutive modulations must verify the constraints on the acceptable range of modulation in order to keep the SNR penalty below the predefined threshold. $\forall i = 1 \cdots I$, $\forall \omega = 1 \cdots W$,

$$\theta_{i,\omega}.\Gamma_{i,\omega} \leqslant \mathfrak{x}_{i,\omega} \leqslant \theta_{i,\omega}.\Gamma'_{i,\omega} \tag{5.9}$$

- Equation 5.10 addresses the number of bypasses between two consecutive modulations. $\mathfrak{x}_{i,\omega}$ should be set to zero if the OC ω is not modulated for the ith time. $\forall i = 2 \cdots I$, $\forall \omega = 1 \cdots W$,

$$\sum_{n=1}^{N} n.\mathfrak{y}_{i,n,\omega} - \sum_{n=1}^{N} n.\mathfrak{y}_{i-1,n,\omega} - 1 \leqslant \mathfrak{x}_{i,\omega} \leqslant \mathcal{M}.\mu_{i,\omega} \tag{5.10a}$$

$$\mathfrak{x}_{i,\omega} - \sum_{n=1}^{N} n.\left(\mathfrak{y}_{i,n,\omega} - \mathfrak{y}_{i-1,n,\omega}\right) + 1 \leqslant \mathcal{M}.(1-\mu_{i,\omega}) \tag{5.10b}$$

- The number of bypasses between the HOLT and the first modulation. $\forall \omega = 1 \cdots W$,

$$\mathcal{M}.\mu_{1,\omega} \geqslant \mathfrak{x}_{1,\omega} \geqslant \sum_{n=1}^{N} n.\mathfrak{y}_{1,n,\omega} - 1 \tag{5.11a}$$

$$\mathfrak{x}_{1,\omega} - \sum_{n=1}^{N} n.\mathfrak{y}_{1,n,\omega} + 1 \leqslant \mathcal{M}.(1-\mu_{1,\omega}) \tag{5.11b}$$

- The number of bypasses δ_ω between the last modulation and the HOLT is:

$$\delta_\omega = N.\theta_{1,\omega} - \sum_{i=1}^{I} \mathfrak{x}_{i,\omega} - \sum_{i=1}^{I} \theta_{i,\omega} \tag{5.12}$$

- The number of additional modulations carried out by ω after the jth cell is:

$$\vartheta_{n,\omega} = \sum_{j=n+1}^{N} \sum_{i=1}^{I} \mathfrak{y}_{i,j,\omega} \tag{5.13}$$

- The SNR penalty cumulated by the RF channel of the nth cell if it was transported by ω which includes the penalty incurred at its modulation, the penalty when it passes through an RAU, and the penalty when it bypasses an RAU after the last modulation of its bearer OC. This penalty is computed as follows:

$$\pi_{n,\omega} = \sum_{i=1}^{I} \Upsilon_{i,\omega}.\mathfrak{y}_{i,n,\omega} + \varepsilon.\vartheta_{n,\omega} + \xi_\omega.\delta_\omega \tag{5.14}$$

- The SNR penalty incurred by the RF channel of the nth cell: $\forall n = 1 \cdots N$,

$$\Pi_n = \sum_{\omega=1}^{W} \varpi_{n,\omega} = \sum_{\omega=1}^{W} \pi_{n,\omega} . \eta_{n,\omega} \tag{5.15}$$

- The variable $\varpi_{n,\omega}$ is the product of the two variables $\pi_{n,\omega}$ and $\eta_{n,\omega}$, and can be equivalently expressed as the minimum of $\pi_{n,\omega}$ and $\mathcal{M}.\eta_{n,\omega}$. This latter expression can be formulated linearly as: $\forall n = 1 \cdots N$, $\forall \omega = 1 \cdots W$,

$$\varpi_{n,\omega} \leqslant \pi_{n,\omega} \tag{5.16a}$$

$$\varpi_{n,\omega} \leqslant \mathcal{M}.\eta_{n,\omega} \tag{5.16b}$$

$$\varpi_{n,\omega} - \pi_{n,\omega} \geqslant \mathcal{M}.(\eta_{n,\omega} - 1) \tag{5.16c}$$

- The different cells modulated onto the same OC ω can not have the same frequency. $\forall \omega = 1 \cdots W$, $\forall j = 1 \cdots F$,

$$\sum_{n=1}^{N} \eta_{n,\omega} . \mathcal{F}_{n,j} \leqslant 1 \tag{5.17}$$

The objective of the GeRoFAN-CP is to:

- minimize the number of used OCs expressed as $\sum_{\omega=1}^{W} \theta_{1,\omega}$,

- and minimize the SNR penalty $(\Pi_n)_{\forall n=1..N}$ in each cell which minimizes the rejection ratio of the radio system.

5.3.1.5   RF-onto-OCs optimal mapping for a loop
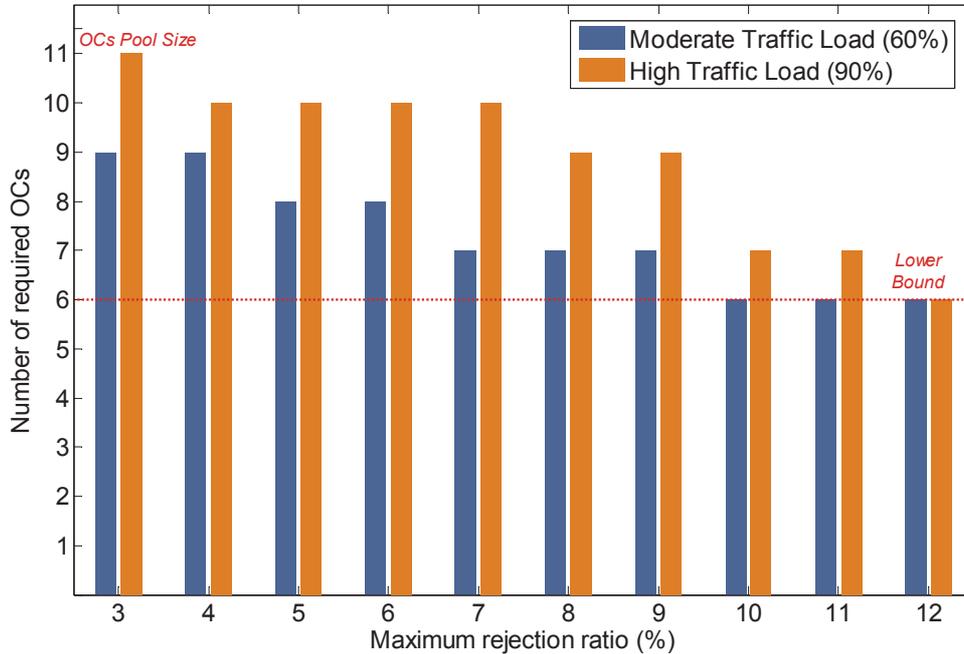
Figure 5.6: Optimal number of required OCs for a target maximum rejection ratio.

Simulations are carried out assuming the *LTE* cellular system. The noise due to the radio interface (including signal propagation loss, radio noise and cellular interference) is evaluated using the analytical fluid-based model[10] described in [65]. The MILP is run using Cplex programming solver[11] on a 2 GHz CPU machine. The optimization programm runs until an optimal solution is found[12]. The capacity of the RF channel is computed using the Shannon's capacity which is based on the SINR of the RF channel accounting for both radio and optical degradations. Once the cell capacity is derived, the rejection ratio of the system is calculated with respect to the case where no RoF link is used. For the rejection ratio calculation, we assume a voice connection requesting 32 kbps[13]. More generally, radio parameters of the simulation are summarized in Table 5.1. Figure 5.6 provides the evolution of the number of required OCs to meet the target maximum (averaged over all cells) rejection ratio at moderate (60%) and high (90%) traffic loads. It does worth noting that with the assumed 4 RFs regular reuse scheme (*c.f* Figure 5.2), the lower bound of the number of required OCs is equal to 6.

---

[10]Although originally defined for downlink transmission, some parameters of the model are modified (such as the transmit power and radio shadowing) to make it valid for uplink transmission.

[11]IBM ILOG Cplex optimizer at: *www.ibm.com/software*

[12]The MILP iterates until the gap of optimality equals 0%.

[13]The assumption of a 32 kbps-voice call connection in our model may not change the performance of the optimization algorithm since we have been dealing with the Shannon's capacity.

5.3.2 ILP optimization for GeRoFAN tree

The formulation of the optimization problem for the case a GeRoFAN tree is simpler compared to the GeRoFAN loop formulation since an optical tree does not accumulate noises along RAUs, thus no particular constraints are required on the minimum and maximum range of modulation. The MILP formulation for a GeRoFAN tree considers the following RoF transmission impairments: the in-band OFDM distortion penalty occurring at the RF and its neighbors, the modulation penalty, the ROADM crosstalk and the splitter penalty.

5.3.2.1 Mathematical formulation

Unless specified, we consider the same notations adopted in Subsection 5.3.1.4. In addition, we introduce the following parameters:

- ϕ_n^ω: in-band OFDM distortion penalty occurring on neighboring channels of the RF modulating the OC ω at cell n.

- φ_n^ω: includes MP, ROADM optical crosstalk and splitter penalties when OC ω is modulated at cell n.

For a GeRoFAN tree, the MILP is required to solve for the following variables:

- $\delta_\omega = 1$ if OC ω is used. $\delta_\omega = 0$ otherwise.

- $x_n^\omega = 1$ if OC ω is dropped at cell n. $x_n^\omega = 0$ otherwise.

- $\chi_{n,m}^\omega = 1$ if OC ω is dropped at both cells n and m. $\chi_{n,m}^\omega = 0$ otherwise.

- ζ_n: non-negative variable standing for the IMD-OFDM SNR penalty at cell n.

- Π_n: non-negative variable standing for the total SNR penalty of RFs at cell n.

The objective of the CP for a tree is the same as the previous MILP, *i.e.*:

- minimize the number of used OCs expressed as $\sum_{\omega=1}^{W} \delta_\omega$ and;

- minimize $(\Pi_n)_{\forall n=1..N}$ that gives the rejection ratio in each cell.

The specific MILP constraints for a GeRoFAN tree are:

- Each cell must modulate a single OC: $\forall n = 1..N$,

$$\sum_{\omega=1}^{W} x_n^\omega = 1 \tag{5.18}$$

- An OC cannot be modulated twice by the same RF: $\forall \omega = 1..W$, $\forall j = 1..F$,

$$\sum_{n=1}^{N} x_n^{\omega} \cdot F_{n,j} \leq 1 \tag{5.19}$$

- δ_{ω} are related to x_n^{ω} by: $\forall n = 1..N$, $\forall \omega = 1..W$,

$$x_n^{\omega} \leq \delta_{\omega} \leq \sum_{n=1}^{N} x_n^{\omega} \tag{5.20}$$

- The IMD-OFDM penalty occurring at the right and the left channels of the RF modulating cell n is: $\forall n = 1..N$,

$$\zeta_n = \sum_{\substack{m=1 \\ m \neq n}}^{N} \sum_{\omega=1}^{W} \sum_{\substack{j=2 \\ F_{n,j}=1 \\ F_{n,j-1}=1}}^{F} \chi_{n,m}^{\omega} \cdot \phi_m^{\omega} + \sum_{\substack{m=1 \\ m \neq n}}^{N} \sum_{\omega=1}^{W} \sum_{\substack{j=1 \\ F_{n,j}=1 \\ F_{n,j+1}=1}}^{F-1} \chi_{n,m}^{\omega} \cdot \phi_m^{\omega} \tag{5.21}$$

- The total SNR penalty at cell n is:

$$\Pi_n = \zeta_n + \sum_{\omega=1}^{W} x_n^{\omega} \cdot \varphi_n^{\omega} \tag{5.22}$$
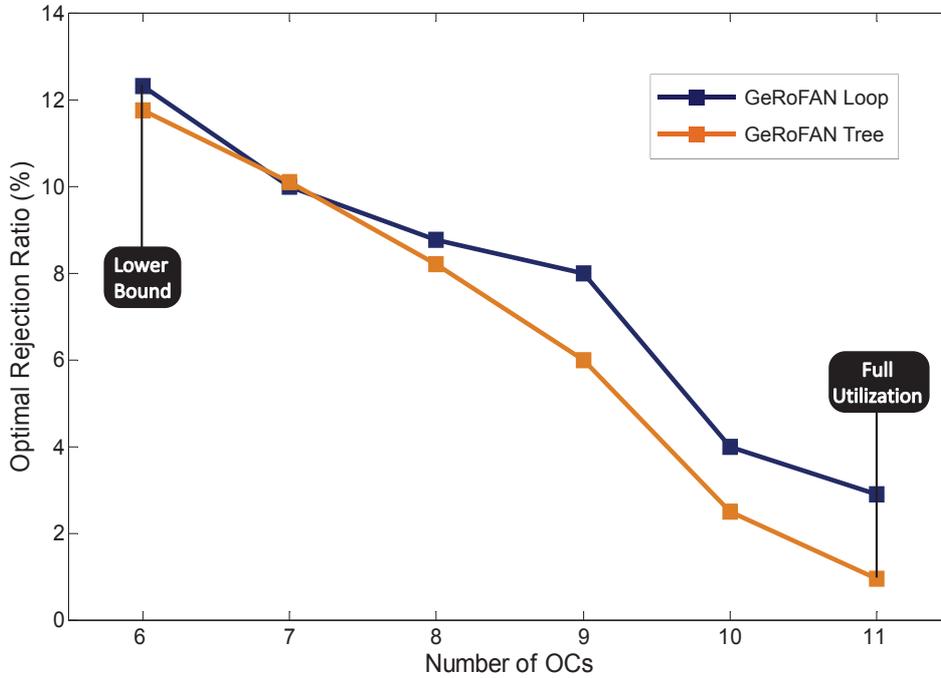
Figure 5.7: GeRoFAN Tree *vs.* Loop MILP optimization.
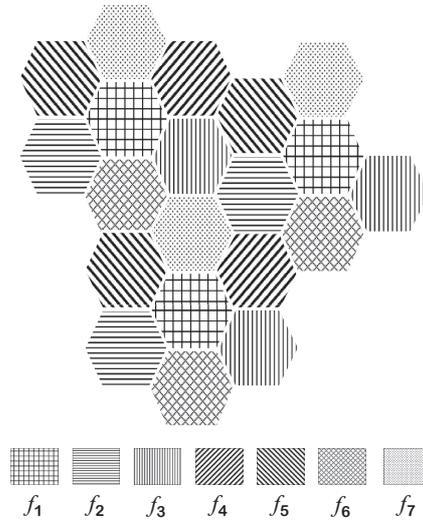
Figure 5.8: A 7 frequency reuse planning.

5.3.2.2 RF-onto-OCs optimal mapping for a tree

For the sake of comparison between both GeRoFAN topologies, we plot in Figure 5.7 the optimal achievable rejection ratio (assuming a traffic load of 90%) at different number of OCs (starting from the lower bound to a full utilization of the optical pool). In both topologies, the higher the number of used OCs, the lower the achievable rejection radio. However, the general trend shown in Figure 5.7 demonstrates that a GeRoFAN tree architecture achieves lower rejection ratios at the same number of required OCs than a GeRoFAN loop architecture does. In fact, at the assumed load, a GeRoFAN loop requires in average a ~ 0.5 OC higher to get the same rejection ratios as archived by a GeRoFAN-based tree network. While such an OC gap seems not very penalizing, we will show in Section 5.4 that the gap gets wider between the two topologies when all QoT impairments are considered in the optimization model.

5.4 PaGeO: a heuristic approach for GeRoFAN-CP

Since the QoT-tool relies on numerical simulations to evaluate the impact of QoT impairments, and because the MILP approach is unable to encompass both linear and non-linear impairments, we propose a heuristic optimization, called **Pa**reto-based **Ge**netic **O**ptimization (PaGeO). PaGeO is a multi-objective heuristic using the concepts of genetic algorithms and Pareto optimization [41]. By allying both concepts, PaGeO takes benefit of the robustness of

evolutionary optimization[14] and the compromise ensured by Pareto optimality[15].
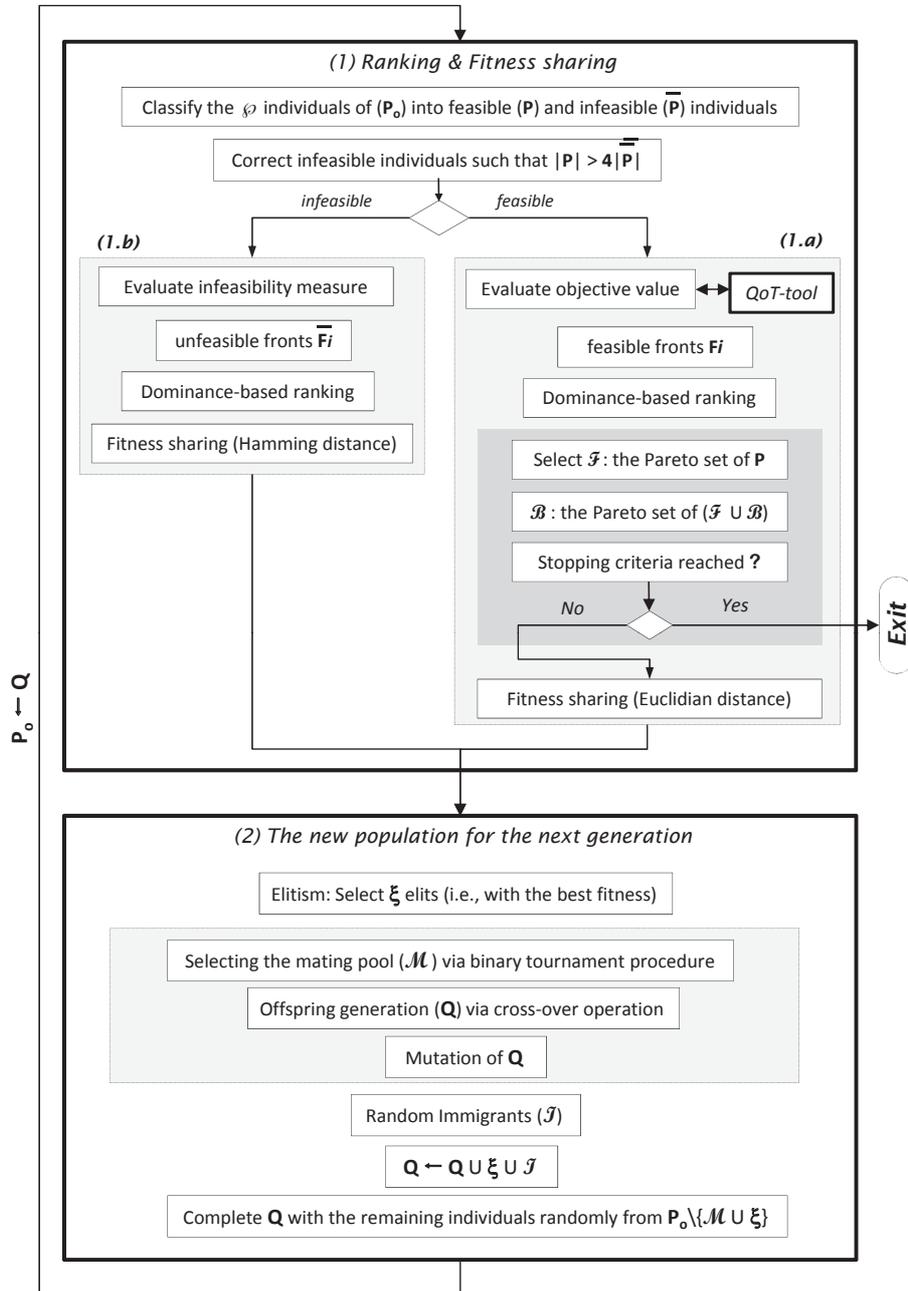
Figure 5.9: The PaGeO algorithm flowchart.

---

[14]Evolutionary optimization are based on the notion of competition between individuals to derive the solution which best-fits the objective function. Evolutionary algorithms are stochastic meta-heuristics inspired by the same principles of natural evolution, exploiting strategies like mutation, crossing genes and elitism [41].

[15]The optimal solution for a multi-objective optimization is not a single solution, but a set of solutions called Pareto optimal solutions, that leaves a greater flexibility for the decision maker to select among the Pareto set, the solution that fits its need. Pareto optimal solutions represent the compromise solutions between the different conflicting objectives. With the Pareto concept, we do not need to transform the multi-objective optimization problem into a mono-objective problem by weighing each objective with respect to the other, which like in our case seems hard to get a fair weighting [41].
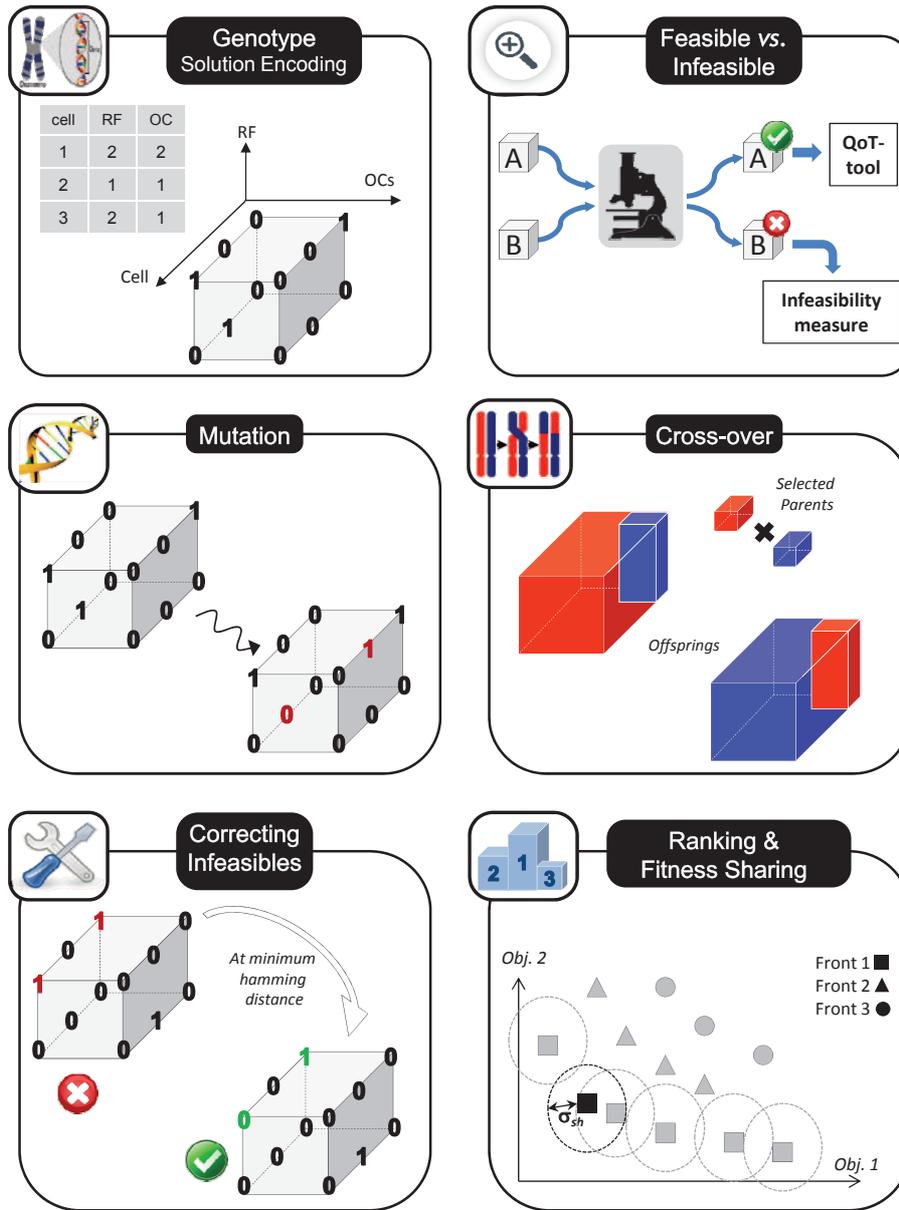
Figure 5.10: Illustration of the key steps of PaGeO.

5.4.1 PaGeO Algorithm

The flowchart of PaGeO and its algorithmic parameters are provided in Figure 5.9 and Table 5.3 respectively. In the following, we describe the different steps of the algorithm.

The first population P_o is created by generating randomly 100 individuals (*i.e.* solutions). A solution x, *a.k.a* chromosome, is encoded by a 3 dimensional binary matrix $[\Psi \times \Lambda \times F]$, where Ψ is the set of cells, Λ the set of OCs and F the set of RF channels. The chromosome is defined as: $x_{i,j,k} = 1$ if the OC j is used at cell i to transport the RF k; $x_{i,j,k} = 0$ otherwise.

The multi-objective function that PaGeO optimizes is an objective vector f =

$(f_1,...,f_{|\Psi|+1}) = ((\rho_i)_{i=1..\Psi}, \Lambda^\star - \Lambda_{min})$ of length $|\Psi| + 1$, where ρ_i is the rejection ratio at cell i, $\Lambda^\star$ is the number of used OCs and Λ_{min} is the OCs lower bound.

The randomness of the evolutionary process can lead to some infeasible individuals. Infeasible chromosomes are produced each time when the constraints of the optimization problem (maximum number of RFs carried by an OC, a carrier must not be modulated twice by the same RF etc.) are violated.

Different strategies are investigated in the literature to handle constraints [78]. In Step 1 of the algorithm, PaGeO splits the current population into two sub-populations: feasible individuals P and infeasible individuals $\overline{P}$. To insure the majority for feasible individuals, some infeasible chromosomes are corrected by choosing the nearest feasible chromosome according to the Hamming distance. Feasible chromosomes are treated in Step 1.a by evaluating, via the QoT-tool developed in Chapter 4, their objective vector. Since several objectives are addressed at the same time, we use the concept of non-dominated front which is the set of solutions that do not dominate each other[16]. This concept is in-line with Pareto optimality. The latter specifies that for a multi-objective optimization, an improvement on one objective is sacrificed by a degradation on another one. Following the step-by-step procedure described in [78], different levels of non-dominated fronts F_i are identified by sweeping iteratively the subpopulation P.

Once solutions are classified into non-dominated fronts, they are ranked according to the density-based strategy as defined in [78]. To avoid local minima, solutions with the same fitness (*i.e.* the same rank) are discriminated using the Euclidian distance-based niche count nc_E (computed as in Table 5.3). A niche count of a given solution is proportional to the number of solutions located within its immediate neighborhood [23]. Using the niche count, the fitness of the chromosome is then updated according to Equation (5.23), where $y \succ x$ denotes chromosome y dominates x[17].

For infeasible chromosomes (Step 1.b), the infeasibility measure, defined as the total number of violated constraints by an infeasible individual, is used instead of the objective value vector. Based on the infeasibility measure, infeasible non-dominated fronts $\overline{F_i}$ are identified and chromosomes are ranked accordingly. To maintain a diverse infeasible population, a niche count nc_H based on the Hamming distance (*c.f.* Table 5.3) is used to update the ranks of too close infeasible chromosomes as in Equation (5.23). The population of the next generation is formed by selecting ξ elite individuals from P. Offsprings Q are produced by crossing, with a probability p_X, the genes of each couple of parents selected from the mating pool $\mathcal{M}$. Individuals of Q are then mutated with a probability p_m. A fraction of immigrants $\Im$, made of randomly generated individuals, are added to Q in order to increase the diversity of the population.

---

[16]Chromosomes x and y do not dominate each other, if and only if, x performs better than y in at least one objective, while y outperforms x in another one.

[17]Note that $y \succ x$, if and only if, $f_i(y) \leq f_i(x)$ for $i = 1, .., |\Psi| + 1$ and $f_j(y) < f_j(x)$ for at least one objective function j.

Table 5.3: Parameters setting for PaGeO.

Population size ($\wp$)	100
Parents selection	tournament selection strategy [78]
Mating pool ($\mathcal{M}$) size	50% of $\wp$
Mutation rate p_m	0.001 [78]
Cross-over rate p_X	0.6 [78]
Immigrants ($\Im$) size	25% of $\wp$
Number of elites (ξ)	5% of $\wp$
Max. number of generations	1000
Euclidian-based $nc_E(x)$	$\displaystyle\sum_{\substack{y \in P \\ r(y)=r(x)}} max\left\{\frac{\sigma_{sh} - d_E(x,y)}{\sigma_{sh}}, 0\right\}$ [23]
Hamming-based $nc_H(x)$	$\displaystyle\sum_{\substack{y \in \overline{P} \\ r(y)=r(x)}} max\left\{1 - \frac{d_H(x,y)}{\overline{\sigma}_{sh}}, 0\right\}$
Euclidian distance $d_E(x,y)$	$\displaystyle\sqrt{\sum_{i=1}^{|\Psi|+1}\left(\frac{f_i(x) - f_i(y)}{f_i^{max} - f_i^{min}}\right)^2}$ [23]
Hamming distance $d_H(x,y)$	$\displaystyle\sqrt{\sum_{i=1}^{|\Psi|}\sum_{j=1}^{|\Lambda|}\sum_{k=1}^{|F|}\left(x_{i,j,k} - y_{i,j,k}\right)^2}$
Niche radius σ_{sh}	≈ 0.44 [78]
Niche radius $\overline{\sigma}_{sh}$	2
Threshold $\delta^\star$	1%

$$r(x) = \begin{cases} \dfrac{1 + \sum_{\substack{y \succ x \\ y \in P}} r(y)}{nc_E(x)} & \text{if } x \in P \\[3ex] \dfrac{1 + \sum_{\substack{y \succ x \\ y \in P}} r(y) + \sum_{\substack{y \succ x \\ y \in \overline{P}}} r(y)}{nc_H(x)} & \text{if } x \in \overline{P} \end{cases} \qquad (5.23)$$

The performance of the current generation is evaluated by selecting the Pareto set ($\mathcal{F} = F_1$) of the feasible subpopulation P. A set of Pareto optimal solutions ($\mathcal{B}$) is updated at each generation with elements of $\mathcal{F}$. Stopping criteria are checked to decide wether to stop or to continue with the next generation. PaGeO terminates when the maximum generation number is reached or the lowest relative deviation δ from a targeted objective value vector $f^{\star}$[18] goes below a predefined threshold $\delta^\star$. Denoting f the objective function, δ is defined according to Equation 5.24:

$$\delta = min_{x \in \mathcal{B}} \frac{|f(x) - f^\star|}{|f^\star|} \qquad (5.24)$$

The key moments of the PaGeO algorithm are illustrated in Figure 5.10, including: the representation of the chromosome (genotype: solution encoding), the dispatching of individuals

---

[18]The ideal objective vector targets the lower bound in terms of required OCs and the required capacity with an excess ranging from 2% to 5% as a margin to secure eventual fluctuation of the traffic load.

between feasible and infeasible ones, evolution operators (mutation and cross-over), correcting an infeasible chromosome while preserving as most as possible its genetic information, individuals ranking and fitness sharing.

5.4.2   Numerical performance of PaGeO

Unlike Section 5.3, we consider a 7 RF regular reuse scheme as depicted in Figure 5.8 which decreases the lower bound of OCs to 3 channels. The WDM pool is increased to 24 OCs in the C-band with 1 nm channel spacing.

5.4.2.1   Convergence quality analysis

In a multi-objective Pareto-based optimization, two proprieties are examined to evaluate the quality of the algorithm convergence. The first propriety deals with the convergence to the Pareto optimal front, which ensures the generation of near-optimal Pareto solutions. The second propriety indicates a good distribution of the obtained solutions around the Pareto optimal front, so that all the search space is covered. These two properties are evaluated through two metrics: the contribution and the spread of the Pareto set [41].

The **contribution measure** is a convergence-based indicator which evaluates the effectiveness of the solutions in terms of closeness to the optimal Pareto front. The contribution of $\mathcal{F}$ to $\mathcal{B}$, which represents the proportion of Pareto solutions given by $\mathcal{F}$ in the Pareto set of $\mathcal{F} \bigcup \mathcal{B}$. Given $\mathcal{D}_{\mathcal{F} \succ \mathcal{B}}$ the set of solutions in $\mathcal{F}$ that dominate some solutions in $\mathcal{B}$, $N_{\mathcal{F}}$ the set of non comparable solutions of $\mathcal{F}$, $\mathcal{D}_{(\mathcal{F} \bigcup \mathcal{B})}$ the Pareto set of $\mathcal{F} \bigcup \mathcal{B}$ and $\|X\|$ denotes the size of set X, the contribution is computed at each generation according to Equation 5.25 [41]:

$$Cont_{\mathcal{F}/\mathcal{B}} = \frac{\frac{\|\mathcal{F} \bigcap \mathcal{B}\|}{2} + \|\mathcal{D}_{\mathcal{F} \succ \mathcal{B}}\| + \|N_{\mathcal{F}}\|}{\|\mathcal{D}_{(\mathcal{F} \bigcup \mathcal{B})}\|} \tag{5.25}$$

The ability of PaGeO to maintain a diverse population is assessed by **the spread of the Pareto set** $\mathcal{B}$ which measures the dispersion of $\mathcal{B}$. The spread of $\mathcal{B}$ is computed according to Equation 5.26 [41]:

$$I_S(\mathcal{B}) = \frac{\sum_{x \in \mathcal{B}} \|y \in \mathcal{B} : |f(x) - f(y)| > 0.75 \cdot \sigma_{sh}\|}{\|\mathcal{B}\| - 1} \tag{5.26}$$

Histograms showing the statistical distribution of the contribution and the spread metrics for a given instance of PaGeO are provided in Figures 5.11a and 5.11b respectively. Results indicate that, in average, 75% of the solutions of the non-dominated set of $\mathcal{F} \bigcup \mathcal{B}$ are provided by $\mathcal{F}$, which denotes the high performance in terms of convergence to the Pareto front. Moreover, with a spread $I_S(\mathcal{B})$ higher than 70% in average, PaGeO is able to maintain a good diversity

of the Pareto set which provides the GeRoFAN manager a large range of (Pareto-)equivalent
solutions.
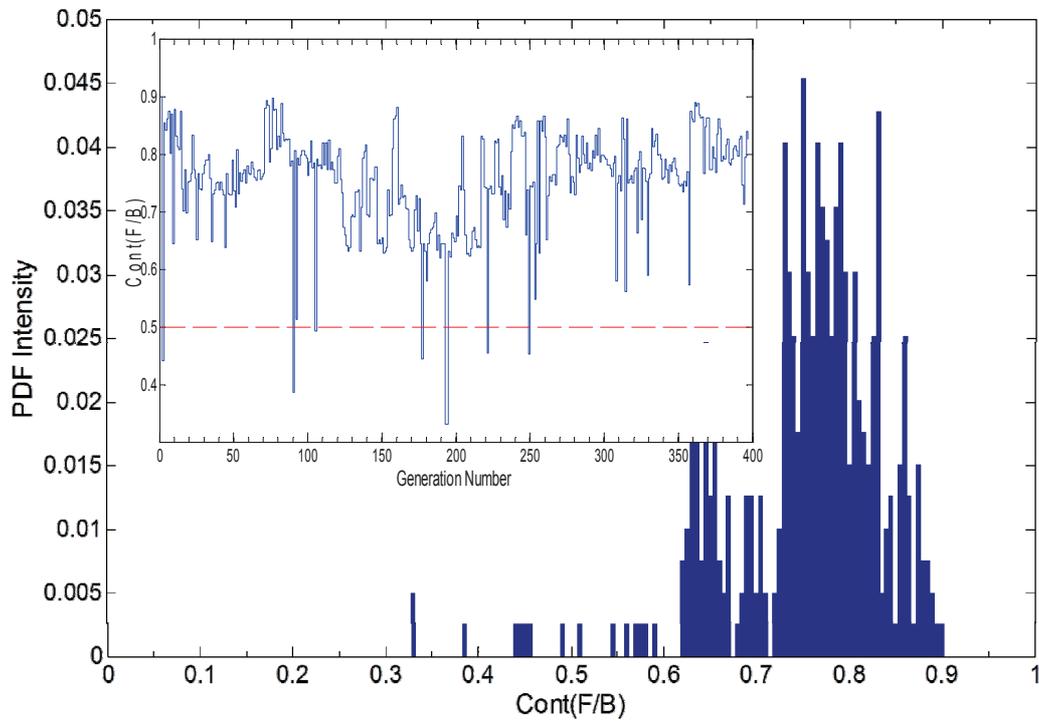
(a) PDF of $Cont_{\mathcal{F}/\mathcal{B}}$. Inset: $Cont_{\mathcal{F}/\mathcal{B}}$ evolving with generations.
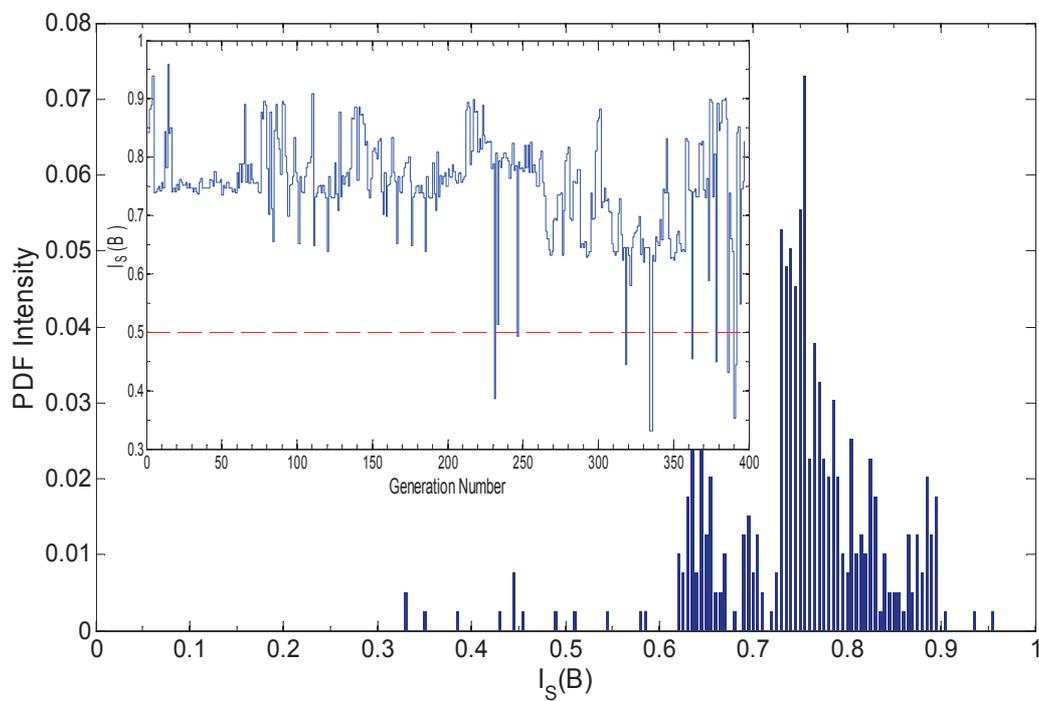
(b) PDF of $I_{S\mathcal{B}}$. Inset: $I_{S\mathcal{B}}$ evolving with generations.

Figure 5.11: Convergence quality analysis of PaGeO.

5.4.2.2   GeRoFAN Tree *vs.* GeRoFAN Loop

Figure 5.12 shows the rejection ratio achieved by PaGeO as well as the number of required OCs for GeRoFAN tree and loop topologies. Results indicate the performance superiority of an optical tree compared to a loop. In terms of rejection ratio, a tree achieves a gain between 25% at a high traffic load and up to 90% at a moderate load. Significant savings (up to 57%) in terms of the number of OCs are also reported; with the lower bound of required OCs (equals to 3) being reached at moderate loads. In fact, the cumulative nature of the noise in an optical loop induces a higher SNR penalty which leads to a higher loss in the radio capacity. To mitigate the increasing impact of IMD noises and optical crosstalk, a loop topology has to use more OCs than a tree.

The comparison between the two topologies is also carried out in terms of QoT profiling depicted in Figure 5.13. To facilitate the analysis of the share of each physical impairment in the total SNR penalty for both GeRoFAN topologies, we classify the different noises into four categories: The first category (Cat.I) designates the modulation penalty (MP), while the second category (Cat.II) includes all IMDs impairments (IMD-RAM, IMD-OFDM, and OBI). The third category (Cat.III) gathers all fiber-induced impairments and are sub-categorized as the following: Cat.III-A for PMD and RBS, Cat.III-B for WDM NLEs and Cat.III-C for CD. Finally, the fourth category (Cat.IV) encompasses ROADM/AWG optical crosstalk (XT) and all other GeRoFAN system penalties (mainly the splitter penalty, SOA ASE noise etc.). Figure 5.13 highlights the heavier impact of IMDs on the total SNR penalty in a GeRoFAN loop than a tree. Due to the cumulative aggregation of noises along RAUs in an optical loop, the QoT profiling points out a significant increase of the share of MP (Cat.I) and IMDs (Cat.II) in the total penalty for a loop compared with a tree. Meanwhile, one notices on one hand the decrease of the share of the fourth category noises (16% for a tree and 11% for a loop) since no splitter is required for a GeRoFAN loop, and on the other hand the very marginal contribution ($< 1\%$) of Cat.III-A noises (PMD+RBS) for an optical loop due to the absence of RBS in the SNR penalty calculations.

5.4.3   Alternative heuristic backhauling policies

Since we demonstrated that a tree topology outperforms a loop topology, the following investigations assumes an optical tree for the GeRoFAN system.

To evaluate the benefit of the cross-optimization achieved by the GeRoFAN-CP, we compare PaGeO with four cellular backhauling policies, namely:
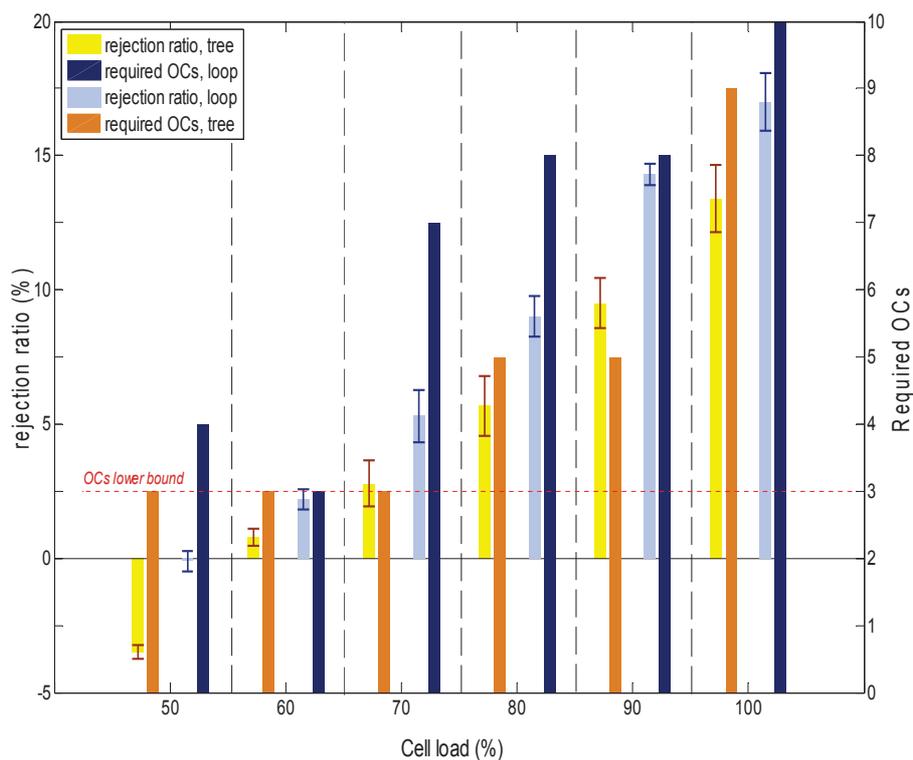
Figure 5.12: Comparison at different traffic loads between GeRoFAN loop and GeRoFAN tree in terms of rejection ratio (left axis) and number of required OCs (right axis). Error bars stand for deviation from the mean value. Negative rejection ratios indicate excess capacity beyond required by the traffic load.
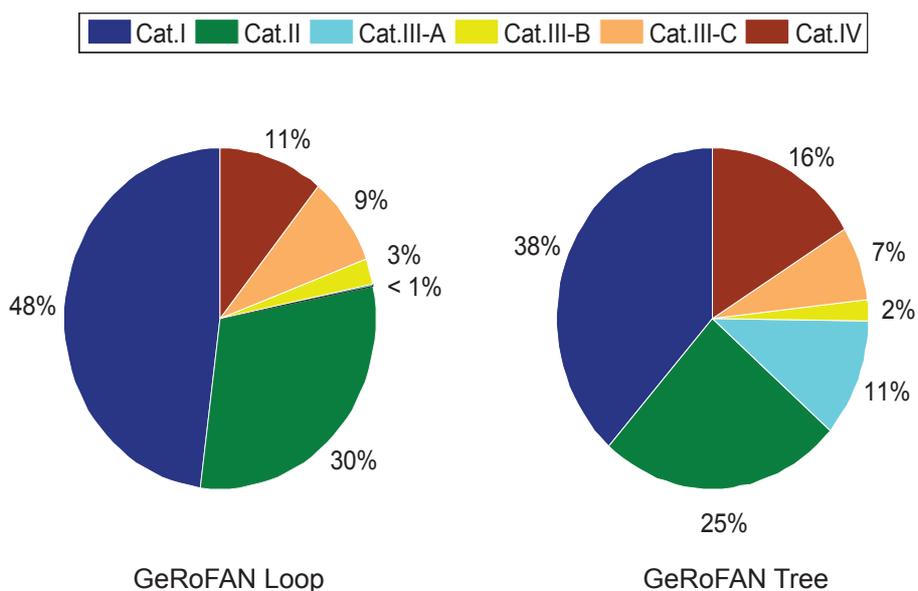
Figure 5.13: QoT profiling: Share of each impairment category in the total SNR penalty for GeRoFAN tree and GeRoFAN Loop.
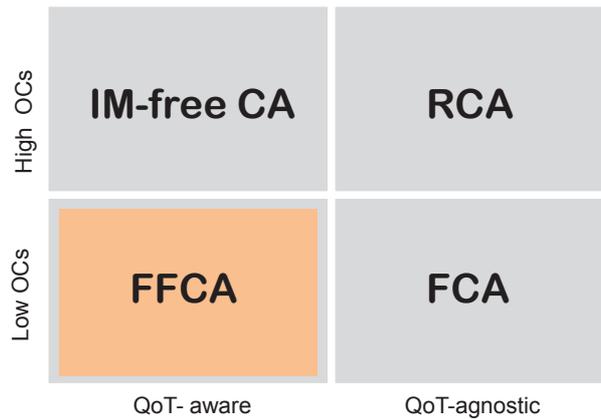
Figure 5.14: A conceptual 2-by-2 matrix positioning of alternative backhauling policies.

- *First Channel Assignment (FCA)*: an RF channel is placed on the first listed available OC.

- *Random Channel Assignment (RCA)*: an RF channel is placed on a randomly selected available OC.

- *First Fit Channel Assignment (FFCA)*: an RF channel is assigned to the first listed available OC that fits the rejection ratio threshold. If no OC is able to meet such a requirement, the RF placement is iterated with a new relaxed threshold. The pseudo-code of FFCA is provided in Algorithm 2.

- *Intermodulation-free Channel Assignment (IM-free CA)*: RFs are assigned to the lowest number of OCs such as IMD3 products are eliminated. To achieve an IMD-free RF assignment, RF channels are placed according to position marks specified by the Golomb ruler [13].

Note that FFCA and IM-free CA are QoT-aware backhauling strategies, while FCA and RCA are QoT-agnostic strategies. Figure 5.14 illustrates the key positioning of the four strategies according to two dimensions: the level of QoT-impairments embedding and the number of required OCs. In the following, we show how PaGeO gets well positioned at the target square shadowed in Figure 5.14. The performance of PaGeO are compared with the four backhauling strategies described previously in terms of rejection ratio and number of required OCs. Numerical results of the comparison are depicted in Figure 5.15 at different network traffic loads. By bin-packing RFs on the first available channels, FCA achieves by default the lowest number of required OCs, but at the detriment of the highest level of rejection ratio among all policies. Although being QoT-agnostic, the RCA policy mitigates QoT impairments thanks to the random selection of OCs and RFs placement, however, this comes at a cost of the highest number of

---

Algorithm 2: Pseudo-code of FFCA backhauling policy.

    input : $\mathcal{N}$: Set of radio-cells. W: OCs Pool.

    output: $\Lambda^\star$: Selected OCs for backhauling. $(\rho_n)_{n=1..N}$: Rejection ratio at each cell.

    // Routine initialization ...

1 $\rho_{max} \leftarrow 0\%$;

2 $\Lambda^\star \leftarrow \emptyset$;

3 $n \leftarrow 1$;

4   **while** $n \leq \mathcal{N}$ **do**

5 $\Omega \leftarrow$ Set of candidate OCs from W able to carry the RFs of cell n;

6   Select *the first listed* OC $\lambda^\star \in \Omega$ such that: $\forall i = 1..n, \rho_i \leq \rho_{max}$;

7   **if** $\lambda^\star \neq \emptyset$ **then**   // OC $\lambda^\star$ is selected to backhaul RFs of cell n

8 $n \leftarrow n + 1$;

9 $\Lambda^\star \leftarrow \lambda^\star$;

10   **else**   // OC $\lambda^\star$ does not exist

11 $n \leftarrow 1$;

12 $\Lambda^\star \leftarrow \emptyset$;

13 $\rho_{max} = \rho_{max} + 0.1\%$;   // Relaxing the constraint on ρ_{max}

14   **end**

15   **end**

OCs ($\sim 70\%$ of the λ-pool). Since it can be considered as the QoT-aware version of FCA, FFCA consumes in average 3 OCs more than FCA, but at the benefit of lower rejection ratios (up to 85% of decrease compared to FCA). Results show also that we need 7 OCs more than the lower bound of required OCs to achieve an IM-free RFs backhauling. Compared to FFCA and QoT-agnostic policies, IM-free CA reduces the rejection ratio by canceling IMDs penalty. However, the residual values of rejection ratio of IM-free CA, especially at higher loads, show that consuming more OCs to avoid IMDs strengthens some impairments (WDM-NLE, ROADM/DEMUX XT) whose penalties may increase with the number of used OCs.

Coming to our algorithm, one notices that, among all policies, PaGeO achieves the best tradeoff between the rejection ratio and the number of required OCs. On one hand, PaGeO consumes in average 2 OCs lower than FFCA, while achieving 2 times the lower bound (at moderate load). On the other hand, rejection ratios achieved by PaGeO are close to IM-free CA. In fact, rejection ratios obtained with IM-free CA show that preventing the occurrence of IMDs, while ignoring the other impairments (particularly those arising at high number of OCs), doesn't suffice to totally preserve the radio capacity. This advocates for a comprehensive management of all RoF impairments which is achieved by PaGeO while consuming a few of OCs. Finally, thanks to its multi-objective Pareto optimization, PaGeO achieves its good performance
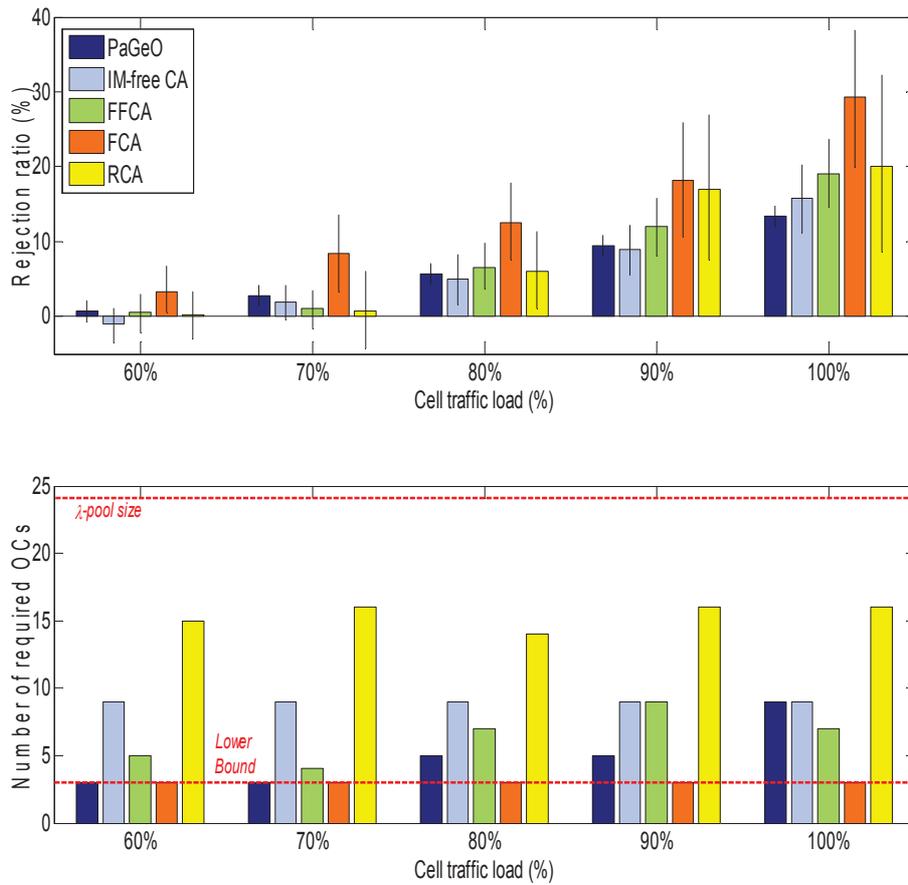
Figure 5.15: PaGeO vs. Other Policies (RCA, FCA, FFCA, IM-free CA) at different traffic loads. Error bars stand for deviation from the mean value. Negative rejection ratio means excess capacity more than the required load.

of rejection ratio more uniformly between radio cells compared to the other policies[19].

5.5   Overlaying multiple radio channels per cell site

In the following, we investigate the impact of increasing the number of RFs per radio cell. Overlaying several radio channels in a cell site is typically observed in real networks when a mobile operator aims to increase the radio capacity of that cell. However, increasing the number of radio channels per cell while keeping the same total bandwidth (for instance 5 MHz) in the cell would not offer more capacity to that cell, instead, doing so provides the mobile operator with a more flexibility in managing the radio resources between cell sites. In fact, overlaying more RFs having thinner granularity (smaller bandwidth per RF) within a cell enables to carry out the radio planning with smaller increments and thus to adjust more suitably the capacity provided to the cell with respect to its traffic load.

---

[19]It can be seen from the length of the standard deviation (STD) bars of PaGeO compared to other policies.
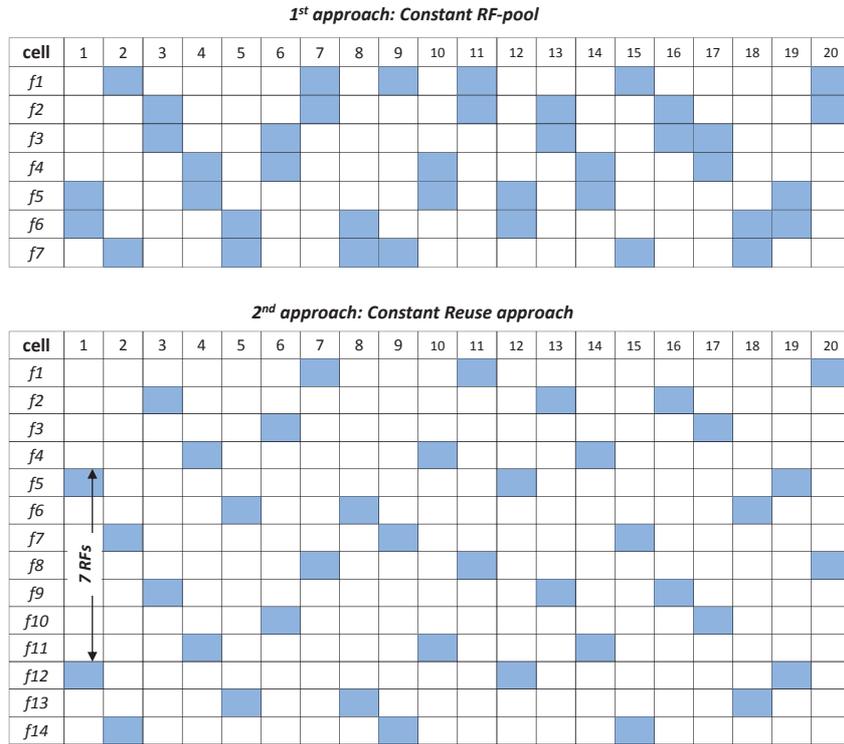
Figure 5.16: Illustration of both RF planning approaches for 20 cells network (2 RFs/cell).

Overlaying several radio channels per cell site can be achieved through different radio planning schemes. We investigate two radio cellular planning approaches to increase the number of RFs per cell either by increasing or keeping constant the RF-pool:

- **Constant RF-pool approach**: To get n radio channels for a given cell, assuming that the latter was attributed with RF channel i in the original RF planning (1 RF/cell), we assign to that cell the n following RFs $\{\bigcup_{j=0}^{n-1} ((i+j) \equiv [7])\}$, where: $(k \equiv [\ell])$ stands for k modulo ℓ. Such an approach keeps the same RF pool $\{f_1, ..., f_7\}$ while decreasing the cellular reuse factor as n increases.

Table 5.4: Minimum number of OCs, the lower bound Λ_{min} and $\Delta\mathcal{B}_{min}$ for both approaches.

Approach	n	1	2	3	4	5
1st	Λ_{min}	3	6	9	12	15
approach	$\Lambda^\star - \Lambda_{min}$	0	0	1	2	3
(Const. RF-pool)	$\Delta\mathcal{B}_{min}$ (in RBs)	2.6	3	4	6	8.5
2nd	Λ_{min}	3	3	3	3	3
approach	$\Lambda^\star - \Lambda_{min}$	0	0	0	1	2
(Const. Reuse)	$\Delta\mathcal{B}_{min}$ (in RBs)	2.6	2.7	3	4.2	4.5

• **Constant Frequency Reuse approach**: The second approach keeps the same reuse factor whatever the number of radio channels per cell, but includes new RFs (requested from the radio broker for instance) thus the size of the RF pool increases as well. To achieve n RFs for a cell provided with radio channel i in the original RF planning, we assign to that cell the n following RFs $\{\bigcup_{j=0}^{n-1}(i + 7 \times j)\}$.

We illustrate both RF cellular planning approaches in Figure 5.16 when two radio channels are overlaid per cell.

5.5.1 Equivalent Bandwidth Loss

With the increase of RFs per cell, IMDs are expected to increase and radio capacity of the cell is degraded as well. The capacity loss is converted into bandwidth $\Delta\mathcal{B}$, called equivalent bandwidth loss, which can be interpreted as the amount of "misused" bandwidth [142]. For a cell with n RF channels each with a bandwidth B_i[20], and given η_i^o the spectral efficiency of the ith RF without RoF and $\eta_i^{\star}$ the spectral efficiency of the ith RF after the RoF link, EBL is computed as in Equation (5.27):

$$\Delta\mathcal{B} = \sum_{i=1}^{n} B_i \cdot \frac{\eta_i^o - \eta_i^{\star}}{\eta_i^{\star}} \tag{5.27}$$

In *4G LTE* mobile systems, the concept of Resource Block (RB) is commonly used to designate the smallest bandwidth unit that can be scheduled for transmission. Given 12 OFDM SCs (occupying each 15 KHz bandwidth) per RB for *LTE* uplink transmission, a single RB occupies thus 180 KHz in the frequency domain [126]. Hence, from a radio operator perspective, it is more meaningful to express the EBL in terms RBs instead of Hz units

We compare both RF planning approaches by running PaGeO to compute the minimum number of OCs required to achieve the lowest EBL ($\Delta\mathcal{B}_{min}$).

Results of both approaches, summarized in Table 5.4, show that EBL increases with the number of RFs per cell. This advocates for reducing the number of RFs per cell to avoid an excessive EBL, while it's worth noting that it is easier for an operator to reallocate radio resources between cells with thin grain RFs capacity. In addition by comparing the two approaches, we notice a slower increase of the EBL with the number of RFs per cell for the constant RF reuse approach than the constant RF-pool approach. Since the EBL represents RBs radio spectrum slices that are definitively lost and cannot longer be allocated to mobile users for traffic transmission, a mobile operator –using GeRoFAN for cellular backhauling– may define a threshold for the maximum EBL that can be tolerated to achieve a cost-effective network planning. Such a threshold can be equal to the radio bandwidth overhead specified by the *LTE* standard which

---

[20]Recalling that $\forall n, \sum_{i=1}^{n} B_i = 5$ MHz

accounts for the relative guard bands and common/control channels and synchronization for a given *LTE* RF channel. Since 5 RBs are required as overhead for a 5 MHz *LTE* radio channel according to the *LTE* standard specifications [133], we deduce that the second approach is more attractive than the first approach. In fact, with such a threshold, a mobile operator adopting the constant RF-pool approach can overlay up to 3 RFs per cell while the constant reuse approach enables to pile up at least 5 RFs per cell without incurring an excessive bandwith loss.

The attractiveness of the second approach compared to the first one is also confirmed by results of Table 5.4 showing of the evolution of the number of required OCs to achieve $\Delta\mathcal{B}_{min}$. By increasing the number of RFs per cell, more OCs are needed to achieve the lowest EBL. Unlike the constant RF pool approach in which the lower bound (Λ_{min}) increases with the number of RFs per cell, the constant RF reuse approach keeps the same lower bound of required OCs ($\Lambda_{min} = 3$ OCs). We notice also that the number of required OCs increases more slowly for the second approach than the first approach.

In summary, since a constant RF reuse approach extends the RF-pool to increase the number of RFs/cell, it is likely to be more expensive for a mobile operator than a constant RF-pool approach. Meanwhile, as highlighted by the results of Table 5.4 the constant RF reuse approach is more capacity and OCs-usage efficient than the constant RF-pool approach. Thus, the tradeoff should lay between both approaches to achieve a cost-effective network planning for the radio system backhauled by GeRoFAN.

5.5.2 QoT analysis

Figure 5.17 displays the share of each QoT impairment category in the total penalty for the two approaches. In this figure, the level of the SNR penalty (high penalty or low penalty) is depicted by the size of its corresponding circle graph for the two RF cellular planning approaches.

In-line with results of Table 5.4, the first approach suffers from higher SNR penalty than the second one. An increase of the SNR penalty ranging from 12.4% to 83% depending on the number of RFs/cell is shown in Figure 5.17. For the first approach, MP and 4th category noises (occupying in average 39% and 24% respectively of the total SNR penalty) are the two impairments with the highest increase with the number of RFs/cell. In fact, by increasing the reuse of RFs, the SNR of the RF signal at the input of the RAM is degraded (since radio cellular interference is increased), increasing *de facto* the MP. In addition, by requiring more OCs, the first approach increases NLEs and WDM-XT noises[21].

Since it uses lower number of OCs, the second approach packs more RFs onto a single OC, thus increasing IMD penalty (IMDs contribute with 44.2% in average to the total penalty). Apart IMDs and although representing only 4.11% of the total pie, CD increases the most

---

[21]the increase of the 4th category noises is attributed systematically to ROADM/AWG WDM-XT since the splitter penalty does not change with the number of RFs/cell.

(a) Basic scenario: A single RF per cell.

(b) Two RFs per cell.

(c) Three RFs per cell.

(d) Four RFs per cell.

(e) Five RFs per cell.
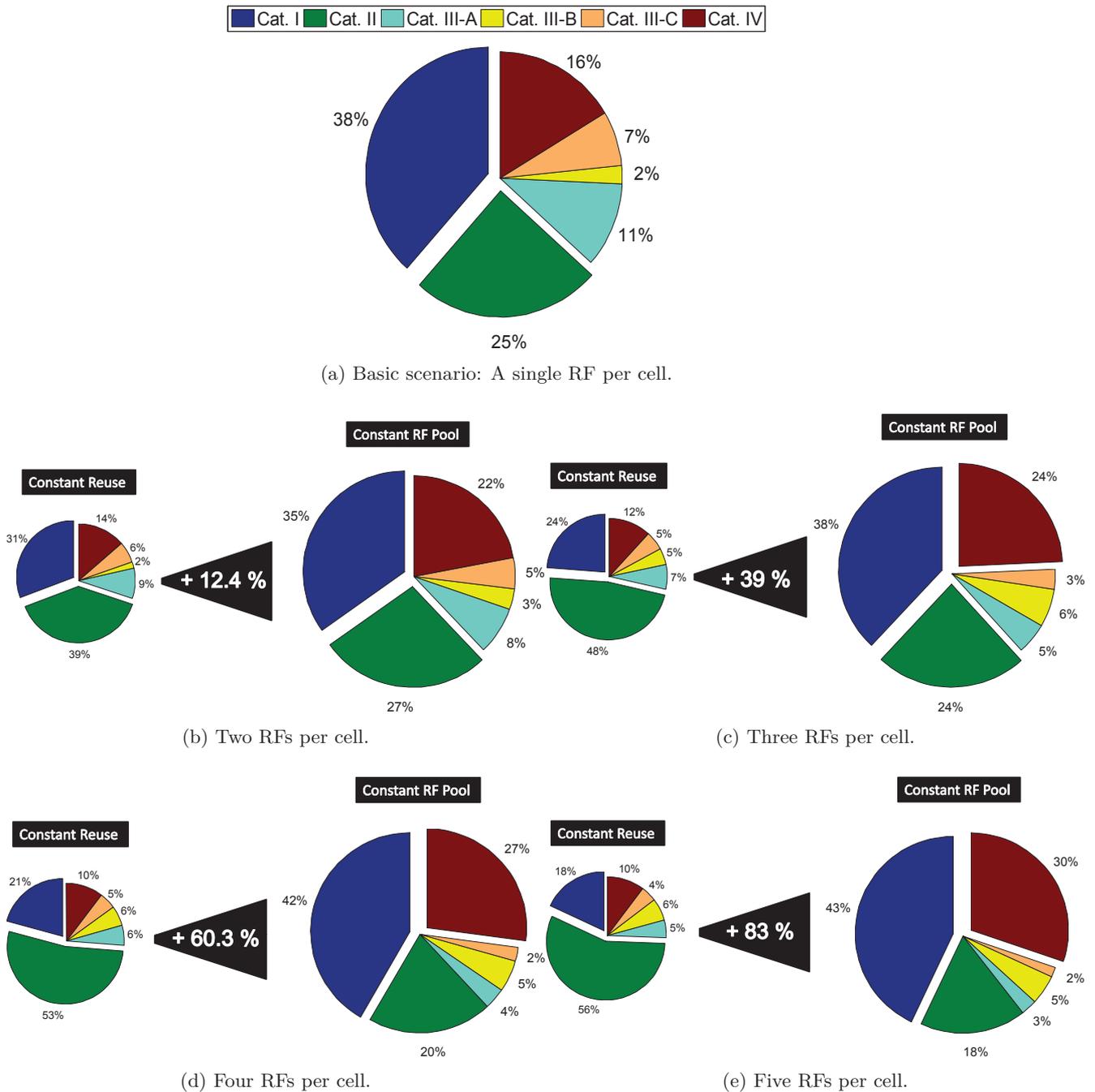
Figure 5.17: Pie chart of the penalty share of QoT categories for both RF planning approaches.

significantly with the number of RFs per OC. We note that for both approaches, the most penalizing factors for radio capacity are: categories I, II and IV, while fiber impairments contribute to less than 10% to the total penalty. Thus, the ROADM and the modulator devices are more penalizing than the signal propagation. This conclusion can be justified by the very limited range ($\sim$ 20 Km) of GeRoFAN.

5.6 Summary

In this Chapter, we proposed an extensive performance evaluation of the control plane of the GeRoFAN system applied to the backhauling of *LTE* cell sites. To the best of our knowledge, the cross-optimization performed by the GeRoFAN-CP–either based on an exact (MILP) or a heuristic search (PaGeO), is the first approach enabling to mitigate the impact of A-RoF transmission limitations on cellular capacity while consuming the lowest number of OCs. Both MILP and PaGeO point out the superiority of a tree topology compared to a loop for GeRoFAN.

Compared to alternative cellular backhauling policies either being QoT-aware (FFCA, IM-free CA) or QoT-agnostic (FCA, RCA), the GeRoFAN-CP exploiting PaGeO achieves an excellent tradeoff between preserving the capacity of the radio system while using efficiently the optical pool. Our numerical results outline that for a given traffic load, for a same total radio bandwidth per cell (5 MHz), it is preferable to exploit a single RF channel per cell than overlaying multiple RFs with thinner granularity. Thus, the operator faces a trade-off: overlaying several radio channels per cell site enables a more flexible management of RFs between cells, but it comes at the price of a loss in the effective radio capacity because of higher intermodulations between radio channels.

Differentiated Backhauling Service for Dynamic Traffic

Contents

6.1   Introduction

U NLIKE Chapter 5 where static distribution of the traffic is assumed, the PaGeO algorithm is not suited for the situation where the cell load fluctuates with time, in fact, the convergence time of PaGeO ranges from 1 hour to 3 hours for instances with a high number of OCs. Such a long convergence time makes PaGeO impractical for on-line execution. On the other hand, in a dynamic environment, the new optimal backhauling strategy should not differ completely from the previous solution which is not the case of PaGeO since it carries out a global optimization. Chapter 6 aims at proposing a new meta-heuristic called Differentiated Backhauling Service (DBS) intended for on-line execution (fast convergence time) where the new solution delivered by DBS is build by realizing minor changes to the previous one. The DBS algorithm is driven by a decision support tool, which consists of a set of rules to manage the impact of A-RoF impairments on cellular capacity. The DBS algorithm relies on an iterative optimization

technique aiming at adjusting the Shannon's capacity at each cell according to its actual traffic load, thus preventing either a situation of shortage or useless excess of capacity. The chapter is organized as follows. Based on the QoT-tool developed in Chapter 4, Section 6.2 formulates the set of rules which are used as a decision support tool by the GeRoFAN-CP to select optimally OCs and to assign RFs onto these OCs. Section 6.3 is dedicated to the description of the DBS algorithm. In Section 6.4, we comment numerical results outlining the efficiency of the DBS algorithm in the context of *4G LTE* backhauling. Finally, in Section 6.5, we describe how the DBS algorithm can be exploited as a key part of an efficient cross-layer resource management carried out with the radio broker. Such an interaction with the radio broker enables radio-frequency virtualization and yields as it will be shown to significant savings in terms of radio bandwidth usage. In this Chapter and on the basis of the results of Chapter 5, only the tree topology is considered for GeRoFAN.

6.2 Rules to manage A-RoF impairments

In a dynamic and heterogenous traffic context, where all radio cells are not subject to the same load, our main challenge consists in determining the *optimal* SNR at each cell that adjusts the Shannon's capacity to the requested bandwidth in the cell. This means that too high SNRs, thus leading to a higher Shannon's capacity than required, have to be prevented if they are achieved at the detriment of insufficient SNR at other radio cells subject to a high traffic load. To assess the impact of the various RoF impairments on the SNR of an RF channel, we exploit the QoT-tool, a comprehensive analytical model described in Chapter 4, that packages all noises inherent to the GeRoFAN system. Figure 6.1 illustrates the penalty of MP, IMD-RAM, RBS and CD with respect to the optical channel wavelength λ and other relevant factors such as the number of RFs per OC and the optical link length. For each depicted impairment in Figure 6.1, we highlight the range of OCs, within the WDM-pool that leads to the lowest penalty.

From the analytical modeling of each impairment, we get the behavior of its amplitude with respect to its associated action levers. This enables to derive rules $\mathcal{R}_\ell$ in order to manage the SNR penalty of each impairment. To quantify the degree of compliance of an OC λ to a given
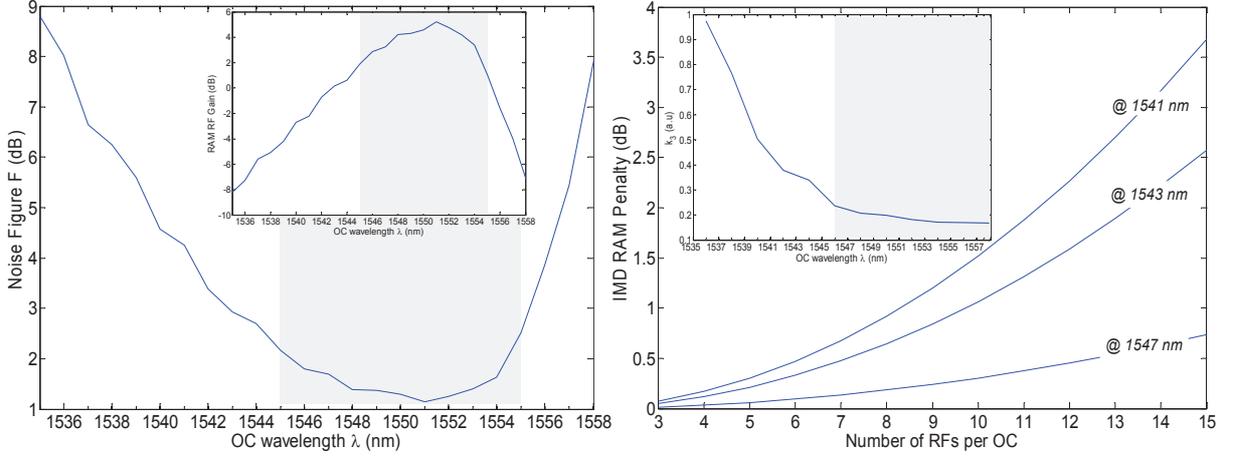
(a) Noise figure of the EAM *vs.* λ at $10mW$ input optical power. Inset: Modulator RF Gain.

(b) IMD penalty at different OCs assuming an equally spaced RF mapping. Inset: 3rd order RAM non-linearity parameter (k_3).
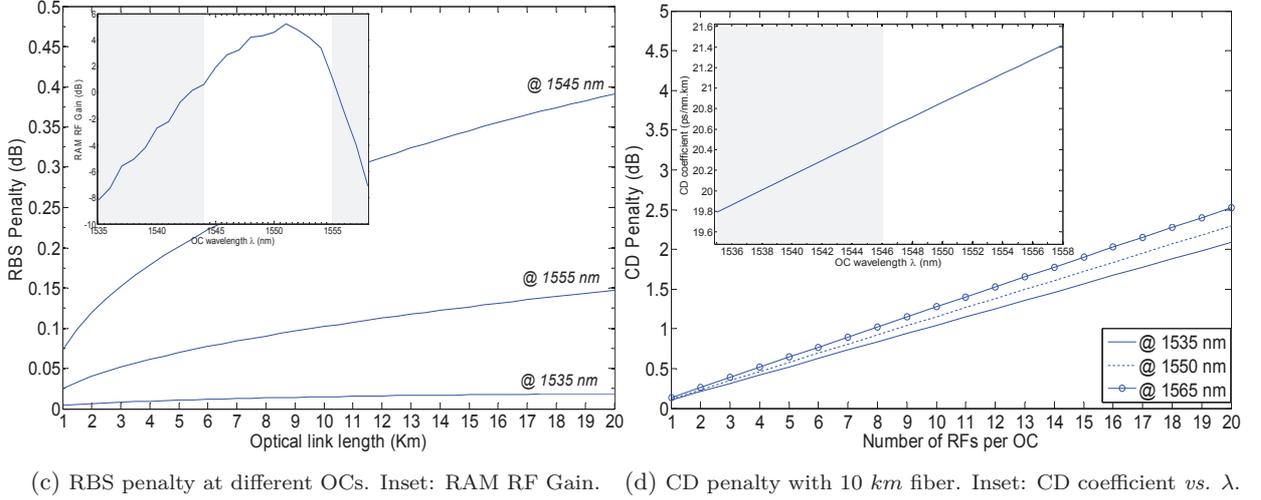
(c) RBS penalty at different OCs. Inset: RAM RF Gain.

(d) CD penalty with $10\,km$ fiber. Inset: CD coefficient *vs.* λ.

Figure 6.1: SNR Penalty of MP, IMD-RAM, RBS and CD function of the OC wavelength. Dashed grey area in each sub-figure highlights the privileged OCs (*i.e.* with low penalties.).

rule $\mathcal{R}_\ell$, we compute its rank $r_{\mathcal{R}_\ell}(\lambda)$. A rank $r_{\mathcal{R}_\ell}$ of an OC is a non-negative real function from the λ-pool $\{\lambda_1, \ldots, \lambda_W\}$ into $[0, 1]$ designed such that the higher the value of the rank, the higher the compliance of that OC to the rule $\mathcal{R}_\ell$.

The set of rules $\mathcal{R}_\ell$ of each impairment $\mathcal{I}$ and their associated rank equations $r_{\mathcal{R}_\ell}$ are detailed in Table 6.1. They constitute a decision support tool used by the GeRoFAN-CP to investigate the optimal RF backhauling solution.

Figure 6.2 depicts the rank of an OC for MP, IMD-RAM, RBS and CD impairments.

Table 6.1: Action levers of each impairment $\mathcal{I}$ and rules $\mathcal{R}_\ell$ to mitigate its impact.

$\mathcal{I}$	Levers	Rules $\mathcal{R}_\ell$ to mitigate the impairment $\mathcal{I}$ and rank equations
MP	$[\lambda]$	$\mathcal{R}_1$: **Select the middle-right OCs of the λ-pool.** For a λ-pool with size W OCs, the rank of an OC with index k is: $r(\lambda_k) = \left(\frac{W}{2} - k\right)^{-2}$ if $k < \lfloor W/2 \rfloor$ and $r(\lambda_k) = \left(k - \frac{W}{2} + 1\right)^{-1}$ otherwise, where $\lfloor x \rfloor$ denotes the integer floor of x.
IMDs	$[\lambda]$	$\mathcal{R}_1$: **Select the outside-right position OCs of the λ-pool, i.e. long wavelengths.** For a λ-pool with size W OCs, the rank of an OC with index k is: $r(\lambda_k) = (W-k)^{-2}$ if $k < \lfloor W/2 \rfloor$ and $r(\lambda_k) = (W-k+1)^{-1}$ otherwise, where $\lfloor x \rfloor$ denotes the integer floor of x.
	$f_{i|1..F}$	$\mathcal{R}_2$: **IMD-free RF mapping.** To achieve IMD-free RF mapping, radio channels are placed according to position marks specified by the Golomb Ruler as in [13]. Assuming $\mathcal{P}_{f_i \in \lambda_k}$ the number of IMD3 products within λ_k and falling on RF f_i, δ_i^k a binary variable equals to 1 if f_i modulates λ_k and 0 otherwise, then: $r(\lambda_k) = 1 - \dfrac{\sum_{i=1}^{F} \delta_i^k \cdot \mathcal{P}_{f_i \in \lambda_k}}{1 + \sum_{i=1}^{F} \sum_{\ell=1}^{W} \delta_i^\ell \cdot \mathcal{P}_{f_i \in \lambda_\ell}}$
		$\mathcal{R}_3$: **Two neighboring RFs should not be carried by the same OC (Mitigates IMD-OFDM).** Since the maximum number of overlapping noises in an OC due to IMD-OFDM is equal to $2(F-1)$, the rank of an OC with index k is: $r(\lambda_k) = 1 - \dfrac{\sum_{i=1}^{F} \delta_i^k \cdot (\delta_{i-1}^k + \delta_{i+1}^k)}{2(F-1)+1}$
	F	$\mathcal{R}_4$: **Minimize the number of RF carried by an OC.** $r(\lambda_k) = 1 - \dfrac{\mathcal{F}(\lambda_k)}{F+1}$, where: $\mathcal{F}(\lambda_k)$ the number of RFs carried by λ_k and F the total number of distinct RFs in the cellular system.
RBS	$[\lambda]$	$\mathcal{R}_1$: **Select outside (right or left) position OCs of the λ-pool, i.e. long or short wavelengths.** For a λ-pool with size W OCs, the rank of an OC with index k is: $r(\lambda_k) = \dfrac{\frac{W}{2} - k}{\frac{W}{2} - 1}$ if $k \leq \lfloor W/2 \rfloor$ and $r(\lambda_k) = \dfrac{2(k - \frac{W}{2})}{W}$ otherwise, where $\lfloor x \rfloor$ denotes the integer floor of x.
CD	$[\lambda]$	$\mathcal{R}_1$: **The lower the OC wavelength, the lower the CD penalty.** The rank of an OC with index k in the λ-pool of size W is: $r(\lambda_k) = \dfrac{W + 1 - k}{W}$
	F	$\mathcal{R}_2$: **Minimize the number of RFs carried by an OC.** $r(\lambda_k) = 1 - \dfrac{\mathcal{F}(\lambda_k)}{F+1}$, where: $\mathcal{F}(\lambda_k)$ the number of RFs carried by λ_k and F the total number of distinct RFs in the system.
XT, NLEs	$\lambda_{i|1..W}$	$\mathcal{R}_1$: **Increase the channel spacing between OCs that modulate the same RF (Mitigates both XT and NLEs).** Defining $\mathcal{I}_{i,k} = \{\ell \in \{1..W\} \backslash \{k\}; f_i \in \lambda_\ell\}$: the index of all OCs, except λ_k, that carry RF f_i. The rank of an OC λ_k is: $r(\lambda_k) = 1 - \dfrac{\sum_{i=1}^{F} \sum_{\ell \in \mathcal{I}_{i,k}} \frac{\delta_i^k}{|k-\ell|}}{\sum_{j=1}^{W} \sum_{i=1}^{F} \sum_{\ell \in \mathcal{I}_{i,j}} \frac{\delta_i^j}{|j-\ell|}}$
		$\mathcal{R}_2$: **Select long wavelength OCs (Mitigates SRS).** The rank of an OC λ_k is: $r(\lambda_k) = \dfrac{k}{W}$.
		$\mathcal{R}_3$: **Select FWM-free OCs (Mitigates FWM).** To achieve FWM-free OCs, optical channels are selected according to position marks specified by the Golomb Ruler as in [13]. Assuming $\mathcal{P}_{k \in 1..W}$ the number of FWM tones generated due to the presence of λ_k in the pool $\{\lambda_1..\lambda_W\}$, then: $r(\lambda_k) = 1 - \dfrac{\mathcal{P}_{k \in 1..W}}{1 + \sum_{\ell=1}^{W} \mathcal{P}_{\ell \in 1..W}}$.

Nota: The terminology "middle-right", "outside-right/left" OCs mentioned for MP, IMDs and RBS rules refer to the range of the most efficient OCs in the C-band to mitigate the effect of these impairments. These ranges have been determined empirically from Figure 6.1 where they are identified by grey dashed areas. For instance, in Figure 6.1a, "middle-right" OCs correspond to the range [1545 nm, 1555 nm].
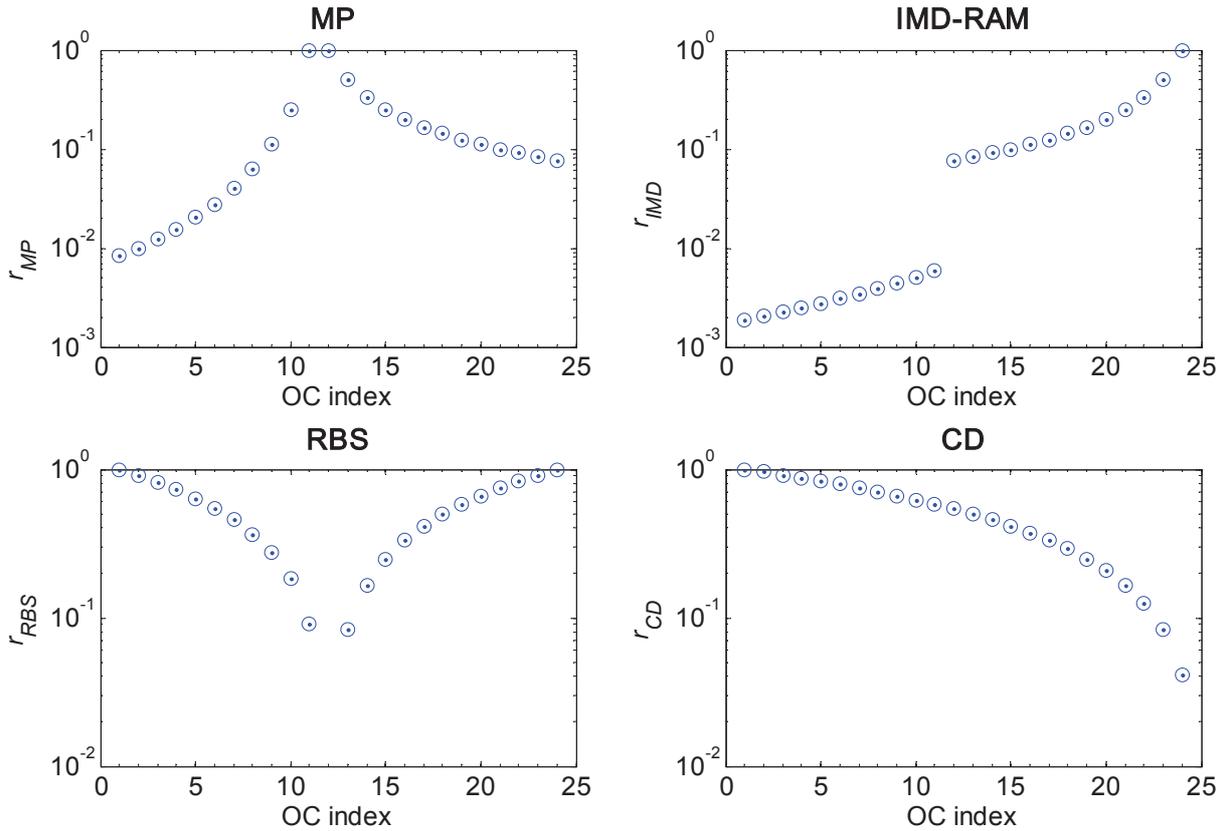
Figure 6.2: OCs ranking for MP, IMD-RAM, RBS and CD impairments. A WDM pool of 24 OCs with 1 *nm* channel spacing in the C-band is assumed. Y-axis is log-scaled.

6.3 The DBS algorithm

The GeRoFAN-CP acquires at the HOLT a global view of the system dynamics (traffic load distribution). This CP keeps a steady monitoring of the evolution of the aggregated traffic load at each cell in the network. Upon the observation reported by the traffic load manager, the CP activates the Differentiated Backhauling Service (DBS) algorithm which is illustrated in Figure 6.3. The DBS algorithm relies on an iterative procedure aiming to adjust the Shannon's capacity within each cell according to its actual traffic load. Two variants of the DBS algorithm, namely DBS^- and DBS^+, are executed by the CP in case of traffic decrease or increase respectively.

If a traffic load increase and decrease are observed at the same time in two different cells respectively, the CP averages both magnitudes of these two fluctuations and decides accordingly to launch the appropriate variant of the DBS. Once DBS achieves the optimal RF-onto-OCs mapping solution, reconfiguration information are encoded into the signaling OC $\lambda^{\star}$[1] and broadcasted to each RAU.

---

[1] The signaling mechanism of GeRoFAN described in Section 3.4.3 of Chapter 3.
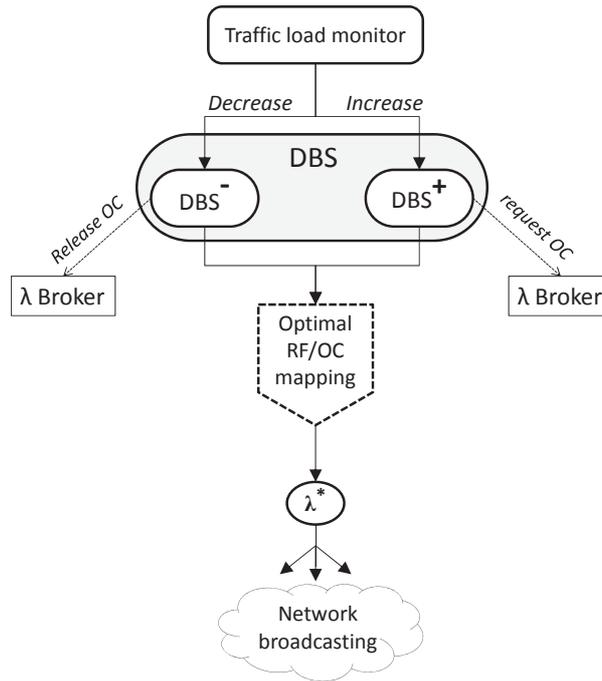
Figure 6.3: DBS activation by the GeRoFAN-CP and interaction with the λ-broker.

Assuming $\zeta = \{C_k, 1 \le k \le |\zeta|\}$ the set of radio cells, $F = \{f_i, 1 \le i \le |F|\}$ the set of distinct RFs used in the cellular planning and $\Lambda = \{\lambda_j, 1 \le j \le p\}$ the set of required OCs ($p \le W$), the DBS algorithm investigates the optimal RF-onto-OCs placement solution by modifying the $|F| \times p$ matrix $S^{(p)}$ defined as: $S_{ij}^{(p)} = C_k$ meaning that RF f_i assigned to cell C_k is carried by OC λ_j. By convention, $S_{ij}^{(p)} = 0$ means that there is no cell served by RF f_i transported by OC λ_j. It has to be noted that if multiple RFs are assigned to the same cell C_k, the value C_k appears several times on the same column of $S^{(p)}$. Since the RF-onto-OCs remapping has to keep unchanged the cellular RF planning, the modification of $S^{(p)}$ is achieved by circular shift along the same row of the matrix (*i.e.* by permutating $S_{ij}^{(p)}$ and $S_{i\ell}^{(p)}$). To evaluate the impact of the new placement on the capacity provided to each cell, we define similarly to $S^{(p)}$, the $|F| \times p$ matrix ρ. Element ρ_{ij} expresses the ratio of the gap between the offered and the required capacities normalized to the required capacity at cell $S_{ij}^{(p)} = C_k$. In consequence, $\rho_{ij} > 0$ indicates an excess in the offered capacity, while $\rho_{ij} < 0$ means that only a fraction of the offered load is provisioned.

6.3.1 DBS at traffic load increase (DBS$^+$)

The CP runs the DBS$^+$ algorithm when an increase of the traffic load is reported by the traffic monitor. DBS$^+$ provides hot-spot cells with the needed radio capacity by remapping RFs-onto-OCs while requesting from the λ-broker, the lowest additional number of required OCs. The

algorithm takes in input the traffic load distribution among cells and the best RF-onto-OCs mapping solution $S^{(p)^*}$ achieved with p OCs. Considering $\zeta^\uparrow$ the set of cells experiencing an increase of the traffic load, then the quality of a given solution $S^{(p)}$ is evaluated using the quadratic mean Ω of the radio capacity computed as in Equation 6.1:

$$\Omega = \frac{\sqrt{\displaystyle\sum_{(i,j);S_{ij}^{(p)}\in\zeta^\uparrow} \rho_{ij}^2}}{|\zeta^\uparrow|} \tag{6.1}$$

The lower the value of Ω, the better is the RF-onto-OCs mapping solution. The use of the quadratic mean in Equation 6.1 instead of a simple average makes the minimization of Ω yielded by the minimization of all its elements $|\rho_{ij}|$.

As depicted in the flowchart of Figure 6.4a, DBS$^+$ investigates the best mapping solution that can be achieved with at most p OCs. For that sake, it calls two main algorithmic blocks namely the Blind Search Box (BSB) and the Guided Search Box (GSB) whose detailed working is described respectively in subsections 6.3.3 and 6.3.4. Unless BSB or GSB triggers an exit, the quality of solutions $S^{(p-1)^*}$ and $S^{(p)^*}$ are compared, making DTS$^+$ either to carry out a new iteration with an additional OC or to exit with $S^{(p-1)^*}$.

6.3.2 DBS at traffic load decrease (DBS$^-$)

When a decrease of the traffic load is reported in some cells, a capacity excess is likely to occur in that cells. The CP runs the DBS$^-$ algorithm which targets to pack RFs more closely together into the minimum number of OCs. Hence, freshly vacant OCs can be released and given back to the λ-broker (*c.f.* Figure 6.3). However, because a dense packing of RFs into OCs is likely to increase the beating between RFs and thus to degrade their radio capacities, DBS$^-$ carries out the RF packing process iteratively over all used OCs. By doing so, the algorithm ensures that only the most *least penalizing* OCs are released. We call *least penalizing* OCs, those whose release remains compatible with the satisfaction of the new traffic load. To check the quality Ω of a given solution $S^{(p)}$, DBS$^-$ uses Equation 6.2 which not only focuses on $\zeta^\downarrow$, the set of under-loaded cells, but also includes cells of set $\widetilde{\zeta} = \{S^{(p)}{}_{ij} \in \zeta; \rho_{ij} < 0\}$ which experience a need in capacity subsequent to the RF packing:

$$\Omega = \frac{\sqrt{\displaystyle\sum_{(i,j);S^{(p)}{}_{ij}\in\zeta^\downarrow\bigcup\widetilde{\zeta}} \rho_{ij}^2}}{|\zeta^\downarrow| + |\widetilde{\zeta}|} \tag{6.2}$$

The flowchart of DBS$^-$ is depicted in Figure 6.4b. Similarly to DBS$^+$, DBS$^-$ calls the BSB and GSB blocks to search for the best RF-onto-OC mapping. To identify the *least penalizing* OC $\widetilde{\lambda}$ that should be released, the algorithm runs a Tabu-search among all OCs using a Tabu

list $\mathcal{Z}$. The release of $\widetilde{\lambda}$ is made effective when the quality of the solution $S^{(p-1)^*}$ (which doesn't require $\widetilde{\lambda}$) is at least equal to the solution $S^{(p)^*}$ (which uses $\widetilde{\lambda}$). Unless BSB or GSB triggers an exit, the algorithm stops either when the Tabu list becomes full or the theoretical lower bound of required number of OCs is achieved.

6.3.3   The Blind-Search Box (BSB)

The DBS algorithm relies on the BSB algorithmic block whose flowchart is illustrated in Figure 6.5a. The rationale of the BSB is to feed cells that need capacity (*i.e.* cells with $\rho_{ij} < 0$) with the capacity excess observed in under-loaded cells (*i.e.* cells with $\rho_{ij} > 0$). BSB adjusts the radio capacity to the load level by permutating OCs transporting under-loaded RFs with OCs carrying overloaded RFs.

BSB starts an iteration t by identifying the cell whose RF i should be relocated from its OC j to another OC $j^\star$. If DBS$^+$ is applied, the targeted cell is $S^{(p)}{}_{ij} = \{S^{(p)}{}_{k\ell} \in \zeta^\uparrow; \max_{k\ell} |\rho_{k\ell}|\}$, while for DBS$^-$ it would be $S^{(p)}{}_{ij} = \{S^{(p)}{}_{k\ell} \in \zeta^\downarrow \bigcup \widetilde{\zeta}; \max_{k\ell} |\rho_{k\ell}|\}$.

$$r(\lambda_k) = \begin{cases} |\rho_{ij} - \rho ik| & \text{if } S^{(p)}{}_{ik} \neq 0 \\[2mm] \max_{\ell=1..|\Lambda|} r(\lambda_\ell) & \text{if } S^{(p)}{}_{ik} = 0 \end{cases} \tag{6.3}$$

To find OC $j^\star$, BSB ranks all OCs according to Equation 6.3. After rank normalization, BSB checks whether the rank of the OC $j^\star_{t-1}$, i.e. the OC selected at the previous iteration $t-1$, equals to $\max_{k=1..|\Lambda|} r(\lambda_k)$. In that case, ranks are updated as in Equation 6.4 to prevent the OC $j^\star_{t-1}$ from being selected at the current iteration t, however if $r(\lambda_{j^\star_{t-1}}) < \max_{k=1..|\Lambda|} r(\lambda_k)$ then there is no need for BSB to update the ranks.

$$\begin{cases} r(\lambda_k) = r(\lambda_k) + \dfrac{r(\lambda_{j^\star_{t-1}})}{2(|\Lambda| - 2)} \\[3mm] r(\lambda_{j^\star_{t-1}}) = \dfrac{r(\lambda_{j^\star_{t-1}})}{2} \end{cases} \tag{6.4}$$

Equation 6.4 penalizes the rank of OC $j^\star_{t-1}$ by dividing it by 2 at the profit of the other OCs (except the original OC j).

We evaluate the capacity matrix ρ of the new RF-onto-OCs mapping solution obtained by relocating RF i from OC j to the OC $j^\star$ with the highest rank. Using Equation 6.1 (respectively Equation 6.2) if DBS$^+$ (respectively if DBS$^-$) is applied, the quality Ω of the new mapping solution is compared with the best quality achieved Ω^*. The BSB algorithm is iterated once again, however, it can lead to an exit if Ω^* achieves a threshold value Ω^{th}, or it moves to the GSB block if a local counter α attains a threshold value α^{th}.

The example depicted in Figure 6.6 illustrates the working principle of BSB and the GSB algorithms for a network with 10 cells using 3 radio channels mapped onto 4 optical channels.

6.3.4 The Guided-Search Box (GSB)

The flowchart of the GSB algorithm is presented in Figure 6.5b. GSB identifies the RF i to relocate similarly to BSB. Nevertheless, unlike BSB, the GSB algorithm relocates RF i from its OC j to a new OC $j^\star$ using a guided optimization approach. In fact, supported by the QoT-tool, GSB quantifies the share of each impairment in the total SNR penalty of RF i in order to identify the most penalizing impairment $\mathcal{I}$ responsible for such a capacity degradation. Using the rules $\mathcal{R}_\ell$ recommended to manage the impairment $\mathcal{I}$ in Table 6.1, GSB computes the rank $r_{\mathcal{R}_\ell}(\lambda_k)$ of each OC $k \neq j$. Note that the rank of an OC k is computed after assuming an RF permutation between OC k and OC j. To prevent the selection of the same OC j, we set $r_{\mathcal{R}_\ell}(\lambda_j) = 0$. When $\mathcal{L}$ rules are involved for impairment $\mathcal{I}$, we compute the aggregated rank[2] $r(\lambda_k)$ of an OC k as in Equation 6.5. Once the highest ranked OC has been selected as the OC $j^\star$, the algorithm is continued similarly to BSB.

$$r(\lambda_k) = \prod_{\ell=1}^{\mathcal{L}} r_{\mathcal{R}_\ell}(\lambda_k) \tag{6.5}$$

6.4 DBS performance: Numerical results

To evaluate the performance of the DBS algorithm, we consider an *LTE* mobile network with 20 radio cells. We use the same parameters for the radio model provided in Table 5.1 in Chapter 5. Radio cells are backhauled via the GeRoFAN optical tree by selecting the splitting node at the center of the cellular network so that all RAUs are uniformly distributed around the splitting node. The radio spectrum pool is made of 7 radio channels regularly reused among cells as illustrated in Figure 5.8 of Chapter 5.

---

[2]We choose a product instead of a simple normalized sum in order to depict the impact of each rank taken individually on the aggregated rank. Such a mathematical formulation of the aggregated rank is achieved by analogy with the probability of simultaneous rules (of equal importance).
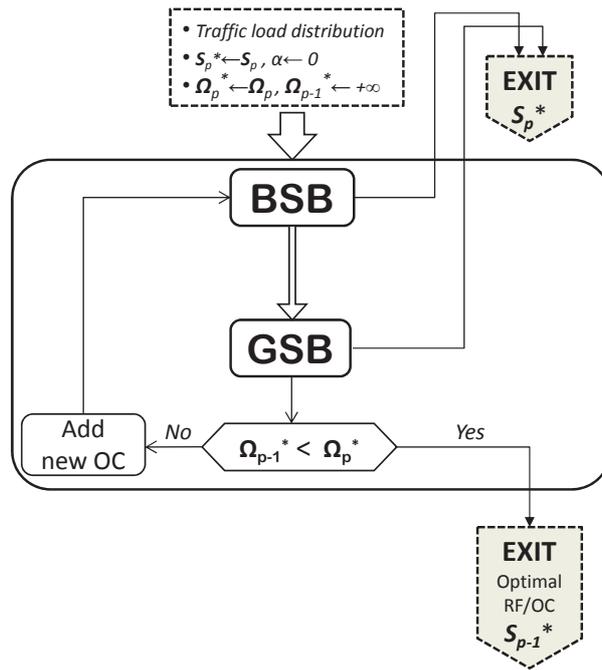
(a) DBS$^+$ algorithm flowchart.
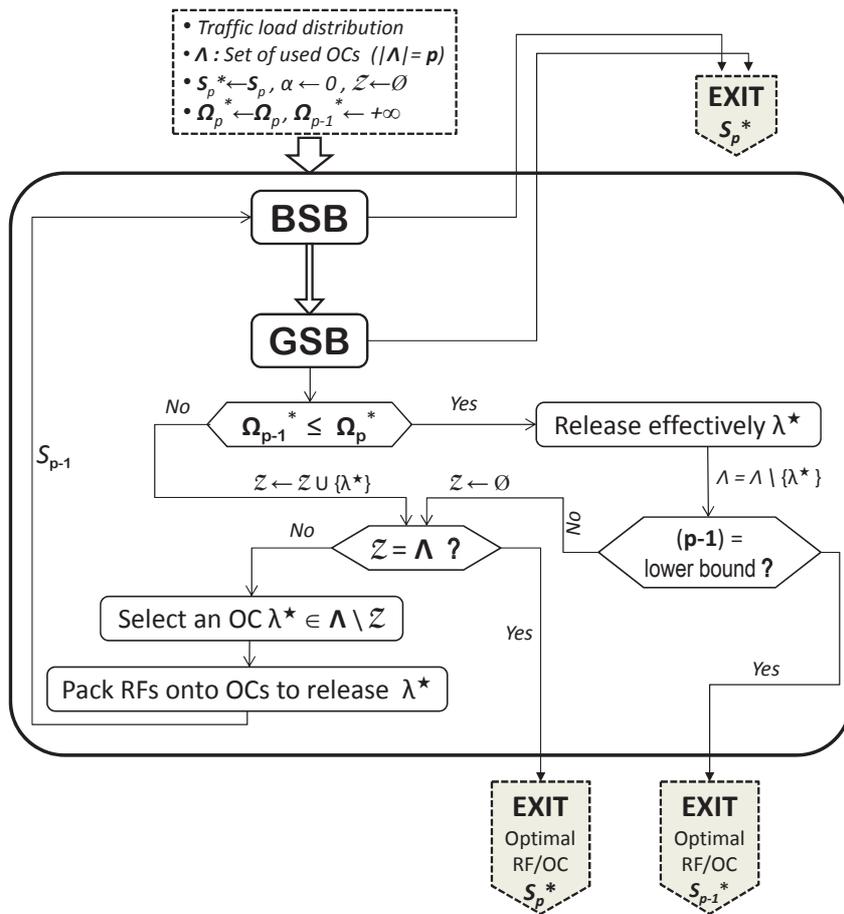
(b) DBS$^-$ algorithm flowchart.

Figure 6.4: The two variants of the DBS algorithm.
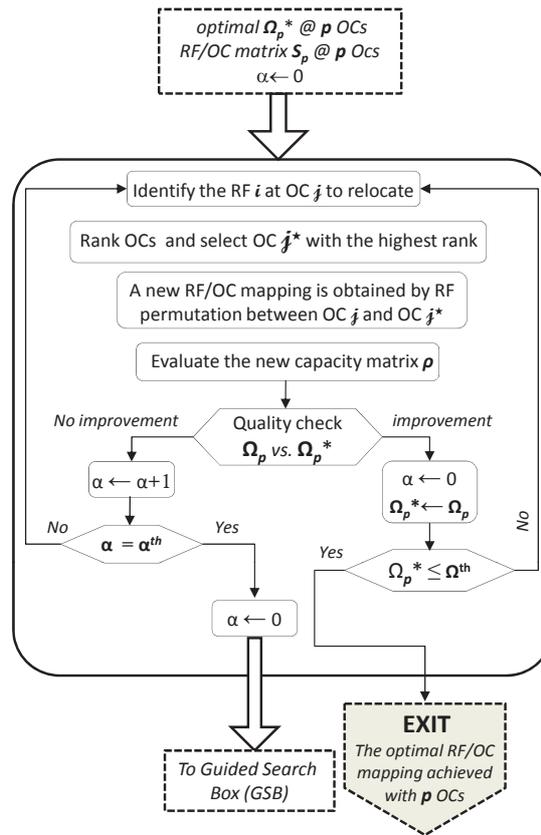
(a) Blind Search Box (BSB) flowchart.
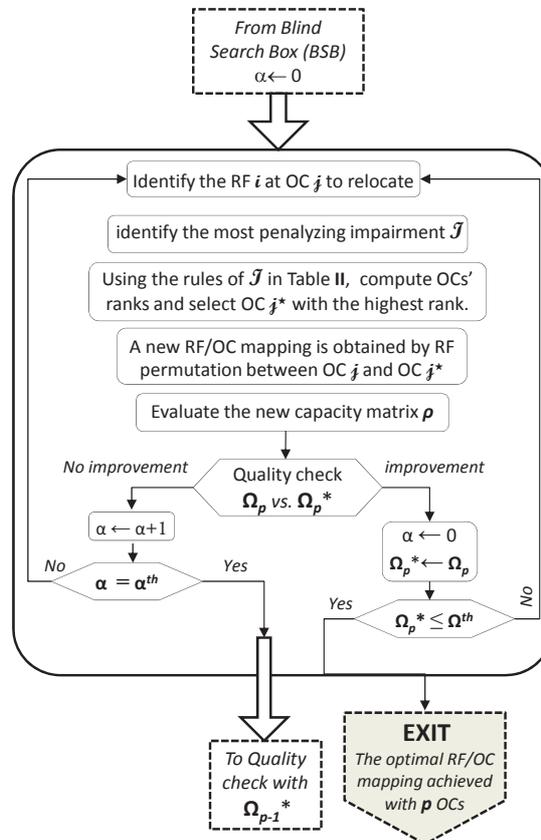
(b) Guided Search Box (GSB) flowchart.

Figure 6.5: Guided and Blind Search Boxes of the DBS algorithm.

Blind Search Box (BSB) example

S_4 (10 cells, $F=3$, $|\Lambda|=4$)

	λ_1	λ_2	λ_3	λ_4
f_1	1	4	0	7
f_2	0	2	6	9
f_3	8	5	10	3

ρ matrix (in %)

-0.9	0.5		1
	0.5	5	1
-0.5	-0.3	7	3

Normalized Ranking
- $r(\lambda_1) = 0$
- $r(\lambda_2) = 0.27$
- $r(\lambda_3) = 0.365$
- $r(\lambda_4) = 0.365$

Update ranks ($\lambda^{\star}_{(t-1)} = \lambda_3$)
- $r(\lambda_1) = 0$
- $r(\lambda_2) = 0.361$
- $r(\lambda_3) = 0.182$
- $r(\lambda_4) = 0.456$

New mapping S_4

	λ_1	λ_2	λ_3	λ_4
f_1	7	4	0	1
f_2	0	2	6	9
f_3	8	5	10	3

Guided Search Box (GSB) example

| S_4	λ_1	λ_2	λ_3	λ_4
f_1	7	2	1	4
f_2	0	5	6	9
f_3	3	0	10	8

ρ matrix (in %)

2	1	-0.2	1
	-0.2	3	2
4		1	-0.4

Identify Impairment $\mathcal{J}$

penalty: XT/NLE, CD, RBS, IMDs, MP

Ranking according to rules $\mathcal{R}_\ell$

	$\mathcal{R}_1$	$\mathcal{R}_2$	$\mathcal{R}_3$	$\mathcal{R}_4$	Π ($\times 10^{-3}$)
λ_1	0.008	1	1	0.5	4.15
λ_2	0.01	0.7	0.6	0.5	2.1
λ_3	0.012	0.7	0.25	0.25	0.53
λ_4	0	0	0	0	0

New mapping S_4

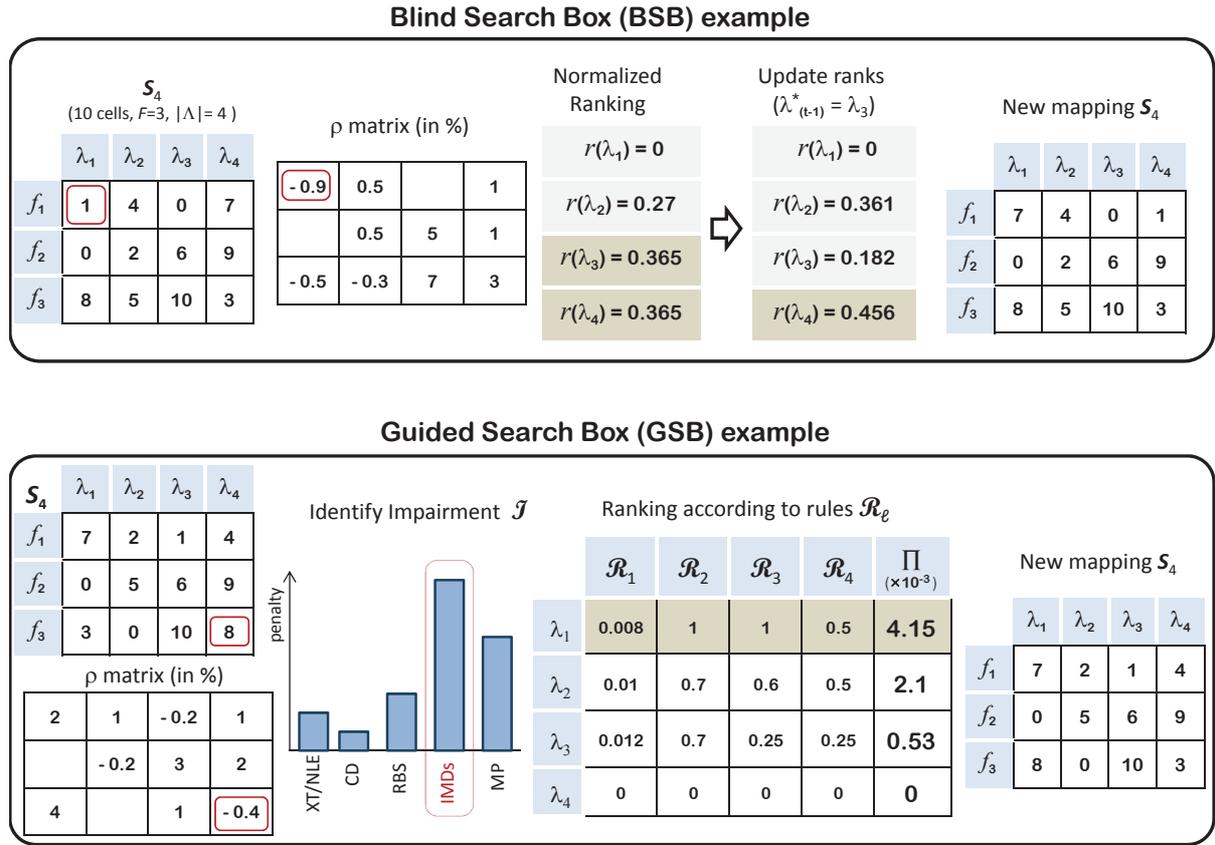|	λ_1	λ_2	λ_3	λ_4
f_1	7	2	1	4
f_2	0	5	6	9
f_3	8	0	10	3

Figure 6.6: An example of the main steps of the BSB and GSB blocks.

Let consider a network of 10 cells using 3 distinct RFs mapped onto 4 OCs as illustrated by matrix $S^{(4)}$. Assuming that BSB is called during the execution of DBS$^+$ algorithm, the former identifies RF f_1 assigned to cell 1 as the RF to relocate from its OC λ_1. The 4 used OCs are ranked according to Equation 6.3. Since OC λ_3 has been selected as OC $j^\star$ at the previous iteration, BSB updates the ranks according to Equation 6.4. The updated ranking enables OC λ_4 to be selected for RF permutation with OC λ_1. With the new RF-onto-OC mapping solution, BSB exploits the QoT-tool to compute its capacity matrix ρ and to evaluate its quality according to Equation 6.1.

To illustrate the main steps of the GSB algorithm, let consider again the previous case of a 10-cells network using 3 distinct RFs mapped onto 4 OCs from a λ-pool of $W = 24$ OCs. As depicted in Figure 6.6, GSB identifies RF f_3 of cell 8 as the most degraded RF that should be relocated from its OC λ_4. Supported by the QoT-tool, the algorithm computes the share of each impairment and identifies IMDs as the most penalizing noise $\mathcal{I}$. According to Table 6.1, 4 rules can be exploited to mitigate IMDs. Once all OCs are ranked with respect to each rule $\mathcal{R}_\ell$, the aggregated rank is computed as in Equation 6.5 while the rank of OC λ_4 is set to 0. Showing the highest rank, OC λ_1 is selected for RF permutation with OC λ_4. Given the new RF-onto-OC mapping solution, GSB uses the QoT-tool to evaluate its capacity matrix ρ before computing its quality Ω.

The simulation scenario is initialized by considering that all cells are subject to the same load set to 50%. As a starting point, RFs are mapped optimally using PaGeO onto the lower bound of required OCs (equals to 3 OCs). We select randomly 4 radio cells in the network to emulate hot-spots. The load in hot-spots is increased by an increment of 5% over consecutive time snapshots[3]. Such an increment granularity makes the radio cell activity easily tracked by the traffic load monitor. At each snapshot, the GeRoFAN-CP runs DBS (in this case DBS$^+$) to investigate the optimal RF-onto-OC mapping solution able to provision the required capacity with the lowest number of OCs. DBS calculates the optimal RF-onto-OC mapping solution

---

[3]The simulation scenario is build through consecutive snapshots. A new snapshot corresponds to an increase of the traffic load in the hot-spots with an increment of 5%.

Table 6.2: Average rejection ratios, Ψ^* and required number of OCs $|\Lambda^\star|$ achieved by DBS$^+$ when 4 hot spot cells experience an increase of the traffic load. DBS ends with an incompressible excess capacity $\xi \simeq 27\%$.

	load (%)	rejection (%)	Ψ^* (%)	$|\Lambda^\star|$	DBS achieved by:
Figure 6.7a	50	0	133	3	no specific action required.
	55	0	127 ± 0.5	3	no specific action required.
	60	0	116 ± 0.5	3	RF/λ remapping.
	65	0	107 ± 0.5	3	RF/λ remapping.
Figure 6.7b	70	0	105 ± 0.7	4	RF/λ remapping + Adding a new OC.
	75	0	101 ± 1	4	RF/λ remapping.
	80	0	100.8 ± 1	5	RF/λ remapping + Adding a new OC.
	85	3 ± 0.5	96.7 ± 1.5	6	RFλ remapping + Adding a new OC.
Figure 6.7c	90	5 ± 0.5	92.3 ± 1.5	7	RF/λ remapping + Adding a new OC.
	95	9.5 ± 1	89 ± 2	7	RF/λ remapping.
	100	11.6 ± 1.8	86 ± 2	7	RF/λ remapping.

corresponding to the new traffic load by starting its search from the optimal solution achieved at the previous snapshot[4]. We run DBS with the following parameters: $\alpha^{th} = 25$ and $\Omega^{th} = 10^{-5}$.

Two metrics are used to track the performance of the DBS algorithm. We define Ψ as the ratio of the provisioned capacity to the requested capacity, averaged over all hot-spots. To highlight how the algorithm achieves the transfer of radio capacity to feed hot-spots with the required capacity, we define the excess capacity ξ ($\xi \geq 0$) as the the ratio of the gap between the offered and the required capacities normalized to the required capacity. ξ is averaged over all cells except the hot-spot cells. Let Ψ^* be the value of Ψ achieved by the optimal RF-onto-OCs mapping solution at each load of the hot-spot cells. In addition to Ψ^*, Table 6.2 shows the rejection ratio, the required number of OCs and specifies the main actions undertaken by the DBS algorithm to achieve the optimal solution. Since the 4 hot-spots are selected randomly among the 20 radio cells, results in Table 6.2 stand for the value averaged over $\binom{4}{20} = 4845$ possible scenarios and the standard deviation margin is also specified. Numerical results of Table 6.2 are reported to Figures 6.7a, 6.7b and 6.7c illustrating the evolution of Ψ and ξ along iterations when the load at hot-spots increases from 50% to 65% (moderate load), then to 85% (high load) and finally to 100% (very high load) respectively.

Let's analyze the behavior of the DBS algorithm when the load increases. When hot-spots

---

[4]Such a working approach, *i.e* starting the search from the previous optimum to attain the new one, is used to simulate the performance of the DBS algorithm as if it was executed on-line.

are subject to moderate load (*i.e.* up to 65%), the CP is able to provision the required capacity by optimizing the placement of RFs onto OCs. The needed capacity in hot-spots is filled at the detriment of the other cells (subject to lower load) as highlighted by the decrease of the excess capacity in Figure 6.7a. Note that at 65% traffic load, an excess capacity of 7% can be derived at hot-spots, while for loads up to 55% no specific action is needed by the CP to satisfy the load apart reassigning uniformly the excess capacity among hot-spots. However, when the hot-spot is subject to high load (*c.f.* Figure 6.7b), it may be necessary to add new OCs when only a remapping of RF-onto-OCs is not sufficient to provision the required capacity. According to Table 6.2, first optimal solutions leading to rejection are obtained when the load lies between 80% and 85%. Such a particular value of the load is called *critical load*. It is worth noting that when the load at hot-spots attains the critical load, the DBS backhauling solution cannot "absorb" completely the load. In that case, only providing a new RF (from the radio broker) is able to provision the capacity required to serve all calls. On Figure 6.7b, we distinguish the two optimization approaches constituting the DBS algorithm. Under BSB, Ψ increases as a stair function with small amplitudes and large step iterations, while with GSB this stair function is characterized by large amplitudes and small steps. Thus, BSB and GSB correspond respectively to a disruptive and an incremental evolution of Ψ. At very high loads, DBS is not able to provide the requested capacity as outlined by the values of rejection ratios and $\Psi^* < 100\%$. Figure 6.7c shows that for loads higher than 95%, providing a new OC is worthless while the excess capacity achieves a plateau (equal to $\simeq 27\%$) called the *incompressible capacity*. The *incompressible excess capacity* is the ultimate limit of ξ beyond which the rationale of DBS–consisting in feeding hot-spots with capacity drawn from the excess of "cold" spot cells, becomes ineffective.

Figure 6.8 illustrates the incompressible excess capacity (ξ) and the critical load computed by DBS according to the number of hot-spot cells in the network. Up to 12 hot-spots, an incompressible excess capacity ranges between 20% and 30% hosted in the other 8 under-loaded cells. Such an unused capacity could be exploited by the radio operator by applying promotional fees in under-loaded cells in order to exploit the system at its full capacity. Such an approach benefits to both mobile users and the radio operator, it is in-line with the *Pricing for Profit* paradigm as depicted in Figure 6.9, where the radio operator exploits a dynamic pricing approach based on patterns of excess capacity. According to a *Nokia Siemens Networks* research white paper [135], by combining customers insights and service-capacity knowledge, Pricing for Profit enables communication service providers to increase revenues by at least 5%.

Critical load *vs.* the number of hot-spot cells is also depicted in Figure 6.8. If we consider an operator serving an urban area, such an operator knows *a priori* the ratio of hot-spots in the considered area. From the critical load depicted in Figure 6.8, whatever the density of hot-spots up to 50%, the operator does not need additional RFs than the same RFs already considered. If
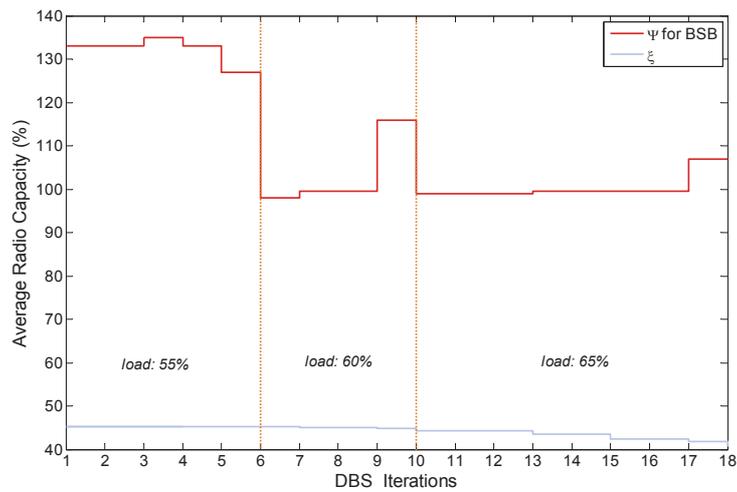
(a) Hot-spots load increasing from 50% to 65%.
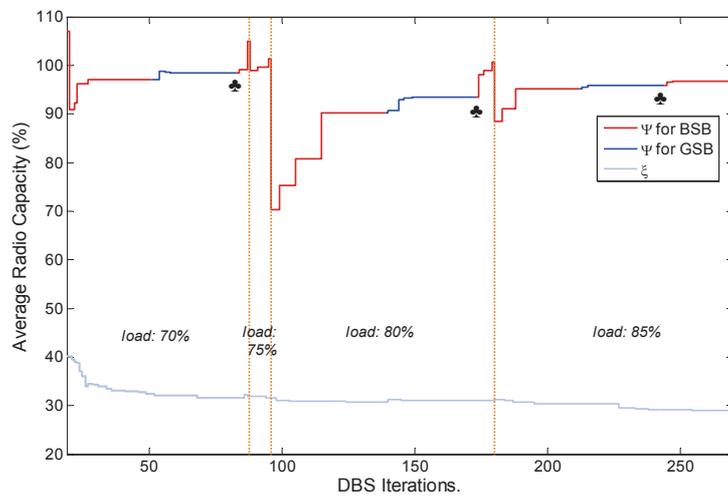
(b) From 65% to 85%.
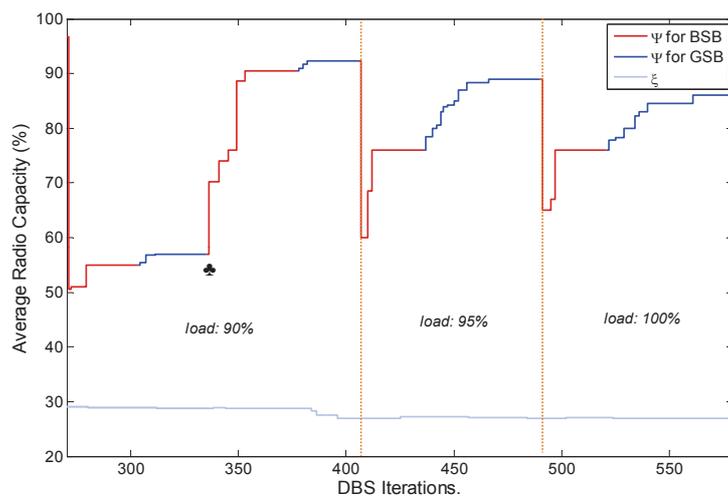
(c) From 85% to 100%.

Figure 6.7: Running the DBS algorithm as the load in hot-spots increases. ♣ denotes the adding of a new OC. Attained *Incompressible Capacity* $\simeq 27\%$.

the hot-spot density is higher than 50% one notices that the probability the operator requests additional RFs from the RF-broker increases with the number of hot-spots. Since purchasing an additional RF is very expensive for an operator according to the current regulatory environment, this highlights the benefit of the DBS algorithm exploited by the GeRoFAN-CP.
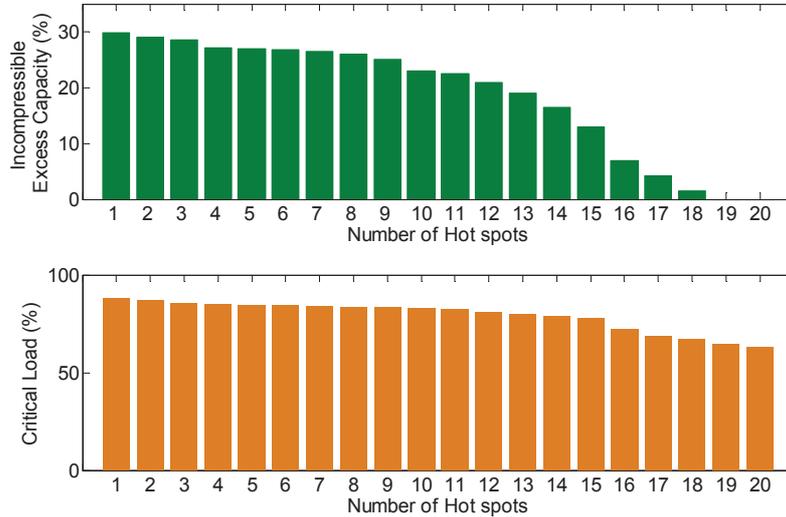

Figure 6.8: Incompressible excess capacity and critical load *vs.* the number of hot spot cells in the cellular network.

6.5   Interaction with the RF-broker

In Sections 6.3 and 6.4, we highlighted the benefit of exploiting the DBS approach by the GeRoFAN-CP to adjust, at either minimum OCs cost or maximum OCs savings[5], the capacity of the cell to its actual traffic load. However, it was previously shown that at higher loads, the radio operator would require sooner or later an additional radio channel from the RF-broker when the DBS technique does not lead to any improvement. When an operator requests additional RFs due to a load increase, the capacity provided may excess the actual load at the hot-spot, which constitutes an opportunity for activating the DBS$^-$ algorithm to achieve OCs savings if it is possible. Similarly, when an operator releases some of the overlaying RFs in under-loaded cells[6], the remaining capacity may fall slightly below the required load at these cold-spots, which requires the activation of the DBS$^+$ algorithm to fulfill the gap at a minimum optical cost. Both described situations advocate for a cross-layer approach between the GeRoFAN-CP (exploiting DBS) and the RF broker in order to investigate the best timing for an operator to request/release a radio channel. The Rf broker "trades" radio resources on-

---

[5]Depending on the variant of the DBS algorithm.

[6]Obviously, the radio site is never completely turned off, at least a single RF is maintained in such under-load cells to serve its vegetative state.
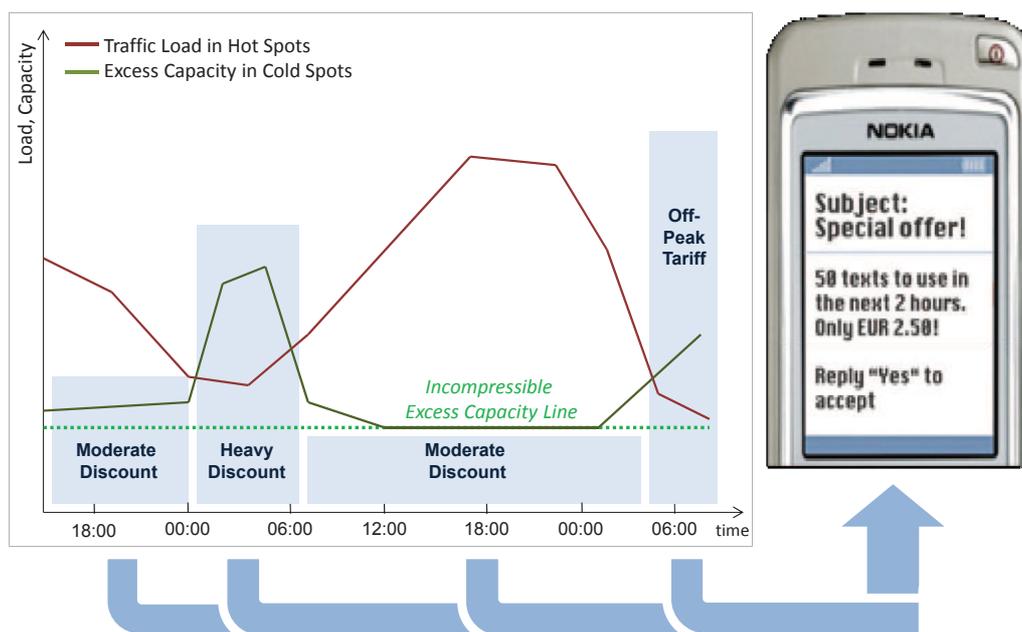
Figure 6.9: DBS enabling the "Pricing for Profit" paradigm as advocated by NSN [135].

As the traffic load in hot spots increases, the excess capacity in underloaded cells decreases. In fact, the DBS algorithm feeds hot spots cells with capacity derived from the unused capacity in cold spots similar to a water-filling problem in communicating vessels. Depending on the level of the excess capacity in cold spots, the mobile operator applies different discount schemes (moderate or heavy discounts) that are advertised instantaneously to mobile users located in these cold spots. The principle of the *Pricing for Profit* detailed by NSN enables operators to avoid excess capacity left unexploited and by consequence to increase revenues up to 5% according to the estimations in [135]. This is an example how the DBS strategy fits well the operators need for an accurate and adjusted radio capacity management (a kind of "lean capacity management") only by acting on the optical layer. Such an optimized capacity management can be further enhanced by well orchestrating the interaction with the radio broker such that to help the mobile operator with the best timing of requesting/releasing a radio channel from/to the broker. This is detailed in Section 6.5.

demand with the mobile operator while the GeRoFAN-CP (using DBS) adjusts the provisioned capacity to the traffic load with an efficient use of optical resources. Figure 6.10 illustrates the flow-chart of the iterative process performing the radio/DBS cross-layer management approach for the case of a traffic increase[7].

Compared to legacy mobile backhauling[8], the cross-layer management approach of the GeRoFAN-CP offers the mobile operator with bandwidth savings achieved by delaying in time the systematic need for a additional radio resources from the RF-broker. Such an economic saving is illustrated through Figure 6.11a. Indeed, in a prospective horizon, mobile operators trades on-demand radio resources with an RF broker, the latter being a regional or nation-wide regulator. To price such a spectrum trading, a common discussed approach [112] consists in multiplying the traded radio channel bandwidth with the elapsed time during which the RF has been used by the mobile operator. From the mobile operator perspective, the incurred cost is considered as an OpEx. Thus, we highlight the relevance of the cross-layer management

---

[7]The process performing the radio/DBS cross-layer management approach for the case of a traffic decrease follows the same steps with minor changes: the order of applying the two DBS variants are reversed and the mobile operator releases RFs in under-loaded cells to the RF-broker.

[8]Not capitalizing on the benefits of A-RoF in terms resources mutualization and flexible management of the bandwidth, enabled by the GeRoFAN-CP.
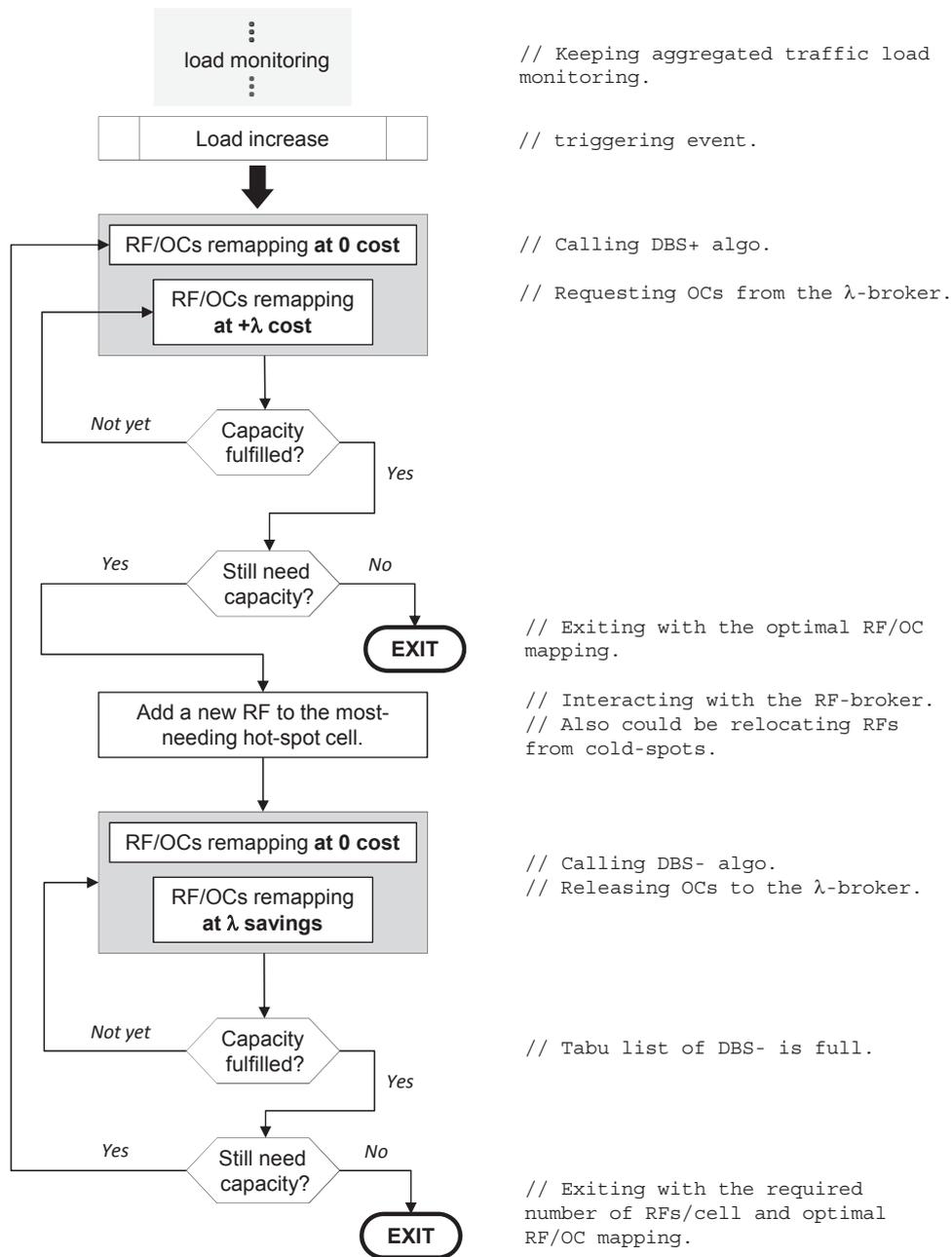
Figure 6.10: Flowchart of the radio/DBS cross-layer management approach for the case of a traffic increase.

approach promoted by the GeRoFAN-CP.

To assess the gain achieved by the RF/DBS cross-layer approach, we consider an *LTE* network with 20 radio-cells and the same radio model assumed in Chapter 5. The dynamic traffic model adopted is inspired from the simulation tool in [136]. We highlight in the following the key features of the model.

For a given simulation instance, k cell sites are selected at random among the 20 radio
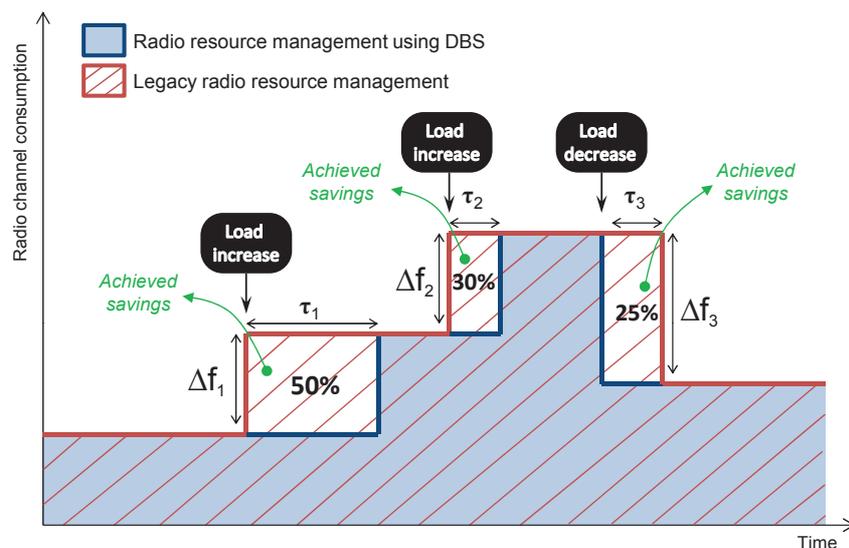
(a) Illustrating achieved savings.
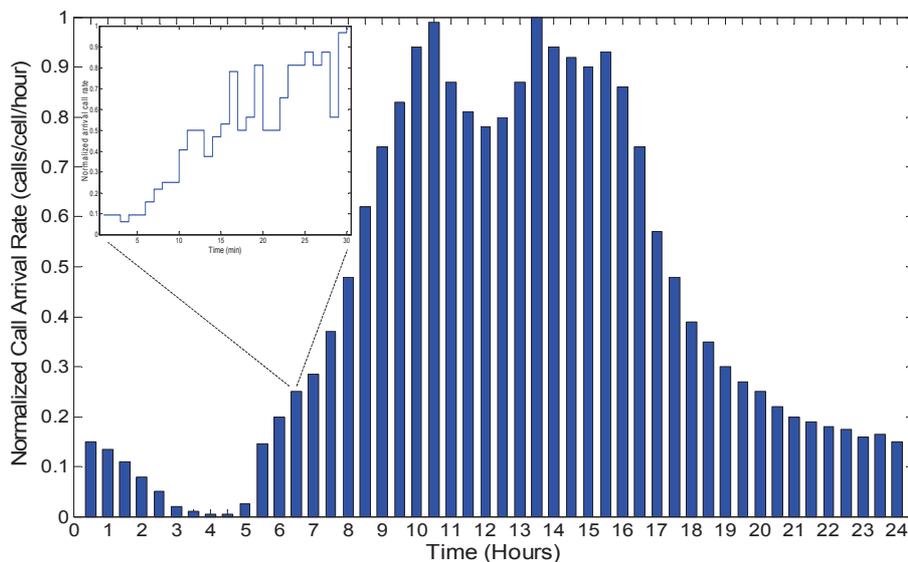
(b) Normalized daily radio traffic profile (from [136]).

Figure 6.11: Example of RF/DBS cross-layer approach achieved savings. Realistic traffic profile for a mobile network operator.

Figure 6.11a: The RF/DBS cross-layer management approach enables significant savings in the radio bandwidth consumption compared to legacy radio resource management (in our case, the cellular backhauling policy is based on FFCA algorithm). When the load increases at hot-spots, radio bandwidth savings can be achieved by postponing the need for an additional radio channel. As illustrated, during elapsed times τ_1 and τ_2, the radio mobile operator exploits the benefits of DBS$^+$ to postpone the need for radio bandwidth Δf_1 and Δf_2 achieving savings up to 50% and 30% respectively. Similarly, when the load decreases, the cross-layer management approaches exploits DBS to anticipate the release of some RFs to the radio broker, leading to savings up to 25% as illustrated in the figure.

Figure 6.11b: Typical daily traffic pattern based on real statistics from a mobile operator. Two peak loads are noticed between 9 am and 5 pm. Inset figure illustrates the load activity at the scale of a call. During that time-window, call arrivals are modeled using the Poisson distribution. A birth/death process is highlighted, while the general trend of the load is increasing from 22% to 25% between 6 and 6.30 am. Note that the GeRoFAN-CP deals only with the aggregated traffic load, *i.e* the CP remains agnostic to the Poisonous evolution of the number of calls depicted in Inset Figure.

cells to play the role of hot-spots. The simulation scenario is based on successive snapshots. A snapshot represents the activation/desactivation of user calls. The call arrivals per hot-spot evolves according to a Poisonous process with an intensity λ_p[9]. New calls are generated in a hot-spot through two different ways. On one hand, calls may be activated due to users mobility from a cold spot (selected randomly among the neighbors of the hot spot). On the other hand, activated calls may be emanating from the hot-spot itself. User mobility-induced new calls occur with a probability p_a while hot-spots self-generated new calls occur with a probability $1-p_a$. Once the hot-spots are clearly identified for a given instance, the simulation is initialized by assuming 50% of traffic load in cold-spots. The evolution of the aggregated traffic load in a given hot-spot cell is depicted in Figure 6.11b. The GeRoFAN-CP deals only with the aggregated traffic and the RF/DBS cross-layer approach depicted in Figure 6.10 is executed at each 30 min time window. The savings provided by the cross-layer approach is calculated with respect to a QoT-aware cellular backhauling approach namely FFCA. The FFCA algorithm presented in Chapter 5, achieves an optimal RF-onto-OCs mapping by assigning RFs to the first-fit available OC, the same approach is carried out by FFCA when a new RF is solicited from the radio broker.

Let $BW_n^{x-layer}$ and $\Delta\tau_n^{x-layer}$ (BW_n^{FFCA} and $\Delta\tau_n^{FFCA}$ respectively) be the RF bandwidth used by the mobile operator and the time duration of its usage in cell n when the cross-layer approach is exploited (respectively when FFCA is used), the averaged saving χ achieved by the cross-layer approach is expressed according to Equation 6.6.

$$\chi = \frac{1}{N} \cdot \sum_{n=1}^{N} \frac{BW_n^{x-layer} \cdot \Delta\tau_n^{x-layer}}{BW_n^{FFCA} \cdot \Delta\tau_n^{FFCA}} \tag{6.6}$$

Figure 6.12 provides the evolution of the achieved gain with the number of hot-spot cells k among $N = 20$ for three possible scenarios $p_a = 1$, $p_a = 0.5$ and $p_a = 0$.

Numerical results of Figure 6.12 show that the RF/DBS cross-layer approach of the GeRoFAN-CP yields to radio bandwidth savings compared to the situation where only FFCA is used. The gain decreases with the number of hot-spots. In fact, as demonstrated in the previous section, the benefit of the DBS algorithm is noticed as long as cold-spot cells exist to feed hot-spots with the required capacity. Figure 6.12 highlights that the highest gain is achieved with $p_a = 1$ and decreases when p_a decreases as well. Indeed, the dynamics of the transfer of capacity carried out by the DBS algorithm are relevant as long as there is a gap of traffic load between hot-spots and cold spots. With a high p_a, cold-spots become more and more under-loaded as the new activated calls in hot-spots are due to mobile users originating from neighboring cold-spots. However, at $p_a = 0$, where all new calls are self-generated within the hot-spots themselves thus keeping constant the load at cold-spots, a small gain (under 2.5%) or even no gain at all is reported which confirms the relevance of the cross-layer approach only

---

[9]Call holding times are thus exponentially distributed with a mean of 120 sec [136].
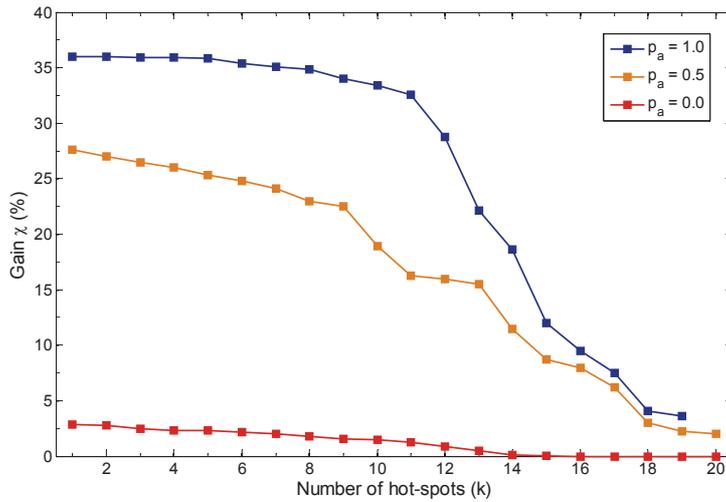
Figure 6.12: Gain χ of the RF/DBS cross-layer management approach at various p_a values.

when there is a gap in the traffic load between cells to favor the transfer of capacity between them.

6.6 Summary

In this chapter, we demonstrated the GeRoFAN-CP capabilities to perform an efficient cellular backhauling strategy in a dynamic traffic context. Supported by the QoT-tool, a set of rules has been derived to manage the impact of A-RoF transmission limitations on cellular capacity. Such rules constitute a decision support tool for the GeRoFAN-CP that runs a Differentiated Backhauling Service (DBS) to adjust dynamically the Shannon's capacity in each radio cell according to the traffic load by optimizing the RF-onto-OCs mapping. The efficiency of the DBS approach has been demonstrated through numerical simulation scenarios. Its "fast" convergence time, ranging from 7 min (for simple instances) to 15 min (for complex instances), makes the DBS suited to on-line execution[10]. Given the scarcity of the RF resource and the cost of radio licences, the GeRoFAN-CP applies an efficient RF/DBS cross-layer management approach to differ the need for additional RFs for the operators when the load at hot-spots increases thus helping them leverage on significant cost savings. Our numerical results show that the gain of the cross-layer approach compared to a classical approach based on the FFCA strategy ranges between 2.5% and 35%. Results confirm the relevance of the RF/DBS cross-layer approach only when there is a gap in the traffic load distribution between cells to favor the transfer of capacity between them. In that sense, an analogy can be found in the rationale of the DBS approach with the water-filling problem in a system of connecting vessels.

Since it is possible to assign optical channels to different operators and thanks to optical

---

[10] Further reductions of the computation time are also possible by optimizing the software implementation of the algorithm.

transparency, GeRoFAN can be viewed as an enabler for mobile backhauling mutualization. Such an environment necessitates an evolution of the regulatory context where the GeRoFAN infrastructure is managed by a third party (either a regional authority or a private independent backhaul operator). The next chapter will focus on the economics of the GeRoFAN system and the integration of business strategies in the DBS in order to facilitate radio resources mutualization between several operators at the benefit of both the GeRoFAN manager and radio operators.

Part IV

Economics and Business Relevance of GeRoFAN

GeRoFAN: a Prospective Approach

Contents

7.1 Introduction

IN this chapter, we aim at evaluating the business value of the GeRoFAN network from mobile carriers' new regulatory environment perspective. In Section 7.2, we describe the GeRoFAN eco-system and the crucial role played by the GeRoFAN operator as a third party. As an illustration, we outline in the same section different business cases for GeRoFAN infrastructure deployment, either short term-oriented or prospective. Based on Capital Expenditures (CapEx) and Operational Expenditures (OpEx) models, we study in Section 7.3 the economics of the GeRoFAN architecture. We assess the profitability of GeRoFAN compared to an alternative investment project backhauling network architecture based on WDM-PON and D-RoF technology

considered in the literature as the most credible solution for fiber-based next generation mobile backhauling. In Section 7.4, we investigate the best-suited business models for GeRoFAN. A two-tiers and a three-tiers business models are considered to study how the business value of the cellular backhauling service is shared among the stake-holders of each model. Finally, we conclude this chapter by summarizing the key findings of our investigations and outlining the main open issues conditioning the viability of the new business model promoted by GeRoFAN.

7.2   The GeRoFAN operator: a Third party

7.2.1   Structuring the GeRoFAN eco-system

The GeRoFAN architecture assumes a new commercial and regulatory environment in the metropolitan area in the sense where a third party operator could manage the GeRoFAN infrastructure. Thanks to the genericity of the GeRoFAN architecture and the MAC-agnostic feature of its CP, the GeRoFAN infrastructure can be mutualized by fixed or mobile operators.

The new ecosystem promoted by the GeRoFAN network is depicted in Figure 7.1 and structured around three functional layers: The resource layer (OC and RF brokers), the telcos' layer and the end-users' layer. The operator of the GeRoFAN infrastructure is positioned at the upper layer. It provides the optical backhaul infrastructure for the different telecom operators. In line with the target of a flexible radio spectrum usage achieved through spectrum markets, we assume that the radio broker allocates on-demand RFs to mobile operators according to the exploited radio system. Similarly, the GeRoFAN operator acts as an OC-broker in charge of provisioning dynamically both fixed and mobile operators with the required OCs to transport their baseband/radio traffic. Two methods are envisioned to manage optical channels for the OC-broker. The first method consists in dividing the WDM pool into sub-pools, each of them being used exclusively by a given operator. The borders between these sub-pools could shift according to the market share of the different operators. The balance between the different operators while sharing the WDM pool can be determined as the outcome of an auction process or based on game theory equilibrium[1]. The second method for optical pool mutualization, consists in sharing the same optical channel by different operators. Such a full sharing approach offers a more efficient management of the WDM pool. However, we estimate that such an approach is technically more challenging, a special care being necessary in the placement of the different traffics (associated to different operators) on the same optical channel in order to avoid inter-operator interference. The OC-broker implements specific incentives policies[2] to encourage operators to share their assigned OCs with other operators. In addition to the dynamic management of OCs, the OC-broker dynamically assigns the corresponding ROADM/REAMSOA

---

[1]For instance based on a Nash equilibrium assuming a non-cooperative game between the competing operators.

[2]For instance, the higher the rate of sharing of an OC, the lower the leasing price of that OC.

module to each operator (*c.f* Section 3.4 of Chapter 3). Thus, another major originality of
GeRoFAN consists in favoring the emergence of an innovative business environment where each
operator can be viewed as a a fixed and/or mobile Virtual Network Operator (VNO). Since
the investment of all operators in the infrastructure is equivalent, service innovation and op-
timization of the traffic management would be the key factors to make the difference in such
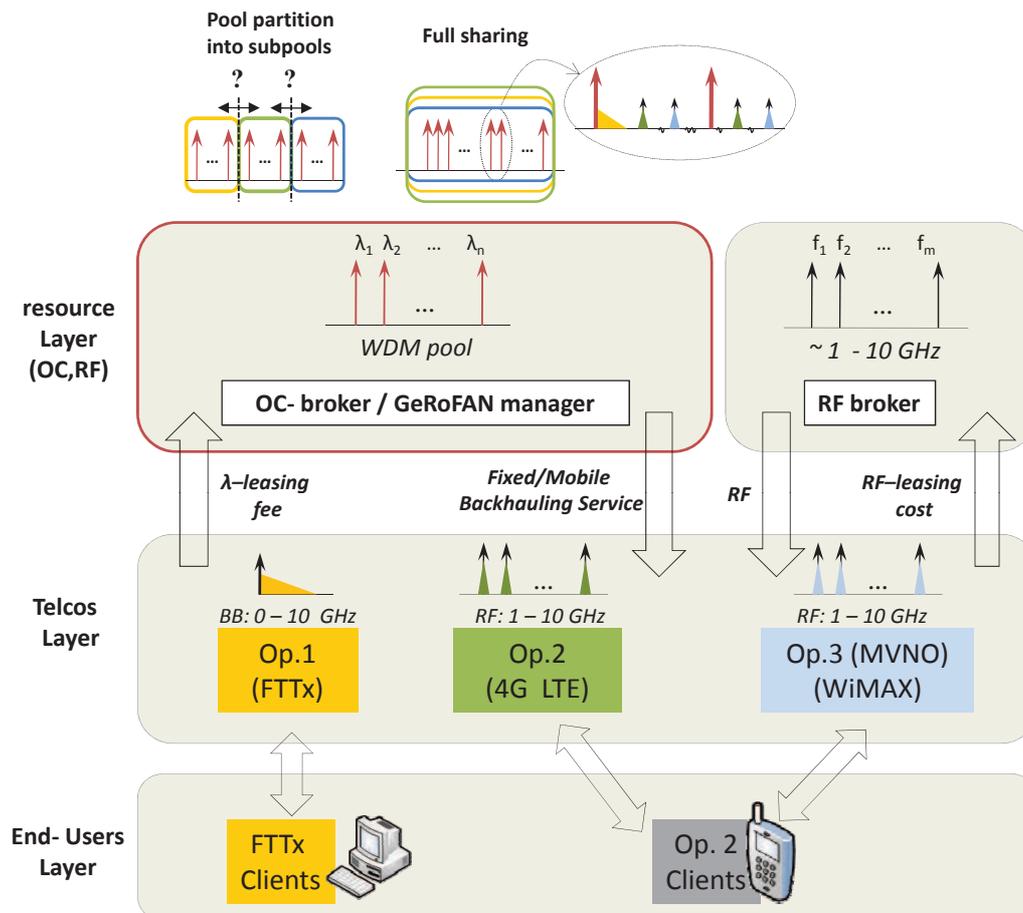commercial competitive multi-tenants environment.

Figure 7.1: The GeRoFAN new eco-system business model.

7.2.2   Business cases for GeRoFAN

The successful implementation of the GeRoFAN system requires a full involvement of the dif-
ferent stake-holders. A new regulatory environment is required to encourage the mutualization
of the backhauling infrastructure, the dynamic provisioning of radio and optical resource (the
emergence of RF-broker and OC-broker). Indeed, municipalities,regional authorities or joint-
venture companies set up through a private/public partnership could play the role an OC-broker.
Incumbent operators could benefit from outsourcing the backhaul activity to a third party since

such a new environment could help them be more focused on their core competencies (innovative telecom service provisioning, network radio planning etc.). Finally, small operators/new entrants/VNOs would see GeRoFAN as a springboard to shorten their time-to-market and expand their business activity. At the time being and since all these requirement are not fulfilled yet, the deployment of the GeRoFAN system in public outdoor environment is still considered as a prospective business case. Instead, the GeRoFAN network could be realistic for the short-term horizon if deployed in semi-private large domains like airports, a major railway station like in [11], exhibition centers, commercial centers or sports complex. In these domains, multiple public radio-mobile operators could rent the GeRoFAN infrastructure provided by the private company that also manages the telecommunications facilities on the whole site. In such domains, significant savings could be achieved in terms of radio resources management (through RoF mutualization) and power consumption (by shutting down unused equipments) provided by the GeRoFAN network by correlating the usage of network resources with traffic fluctuations. For such semi-private large domains, the time[3] and space fluctuations of the traffic matrix are mainly predictable. In an airport [1], the traffic distribution is tightly related to flights departures and arrivals in the different operating terminals, while in a sports complex facility, the competition planning determines the time/space variation of the traffic distribution.

7.3   Economics of the GeRoFAN system

In this section, we investigate the economics of the GeRoFAN system. In a comparison with a WDM-PON architecture exploiting D-RoF technology for cellular backhauling. Both architectures backhaul the same number of radio cells (20 *4G LTE* radio cells) and are subject to the same traffic load detailed later.

7.3.1   GeRoFAN *vs.* D-RoF WDM-PON architecture

The network architecture of the D-RoF WDM-PON is depicted in Figure 7.2 and is taken from [36]. Several Remote Radio Heads (equivalent to the RAU) are federated to the head-end node called Main Unit (MU, equivalent to the HOLT) using a WDM-PON infrastructure. An RRH manages both upstream and downstream radio traffic of its associated *LTE* cell. The D-RoF WDM-PON architecture exploits bandpass sampling theory to digitize/reconstruct the analog signal using an ADC/DAC without needing RF oscillators, thus simplifying the RRH architecture. The digitized stream is mapped into an Optical Module (OM) port which uses WDM-PON. The OM is a bidirectional colorless optical transceiver (SFP or SFP+) constituted by a TOSA (remotely-fed uncooled reflective modulator), a ROSA (High-speed APD) and a Printed Circuit Board (PCB) implementing in FPGA a high speed path for Inverted Return

---

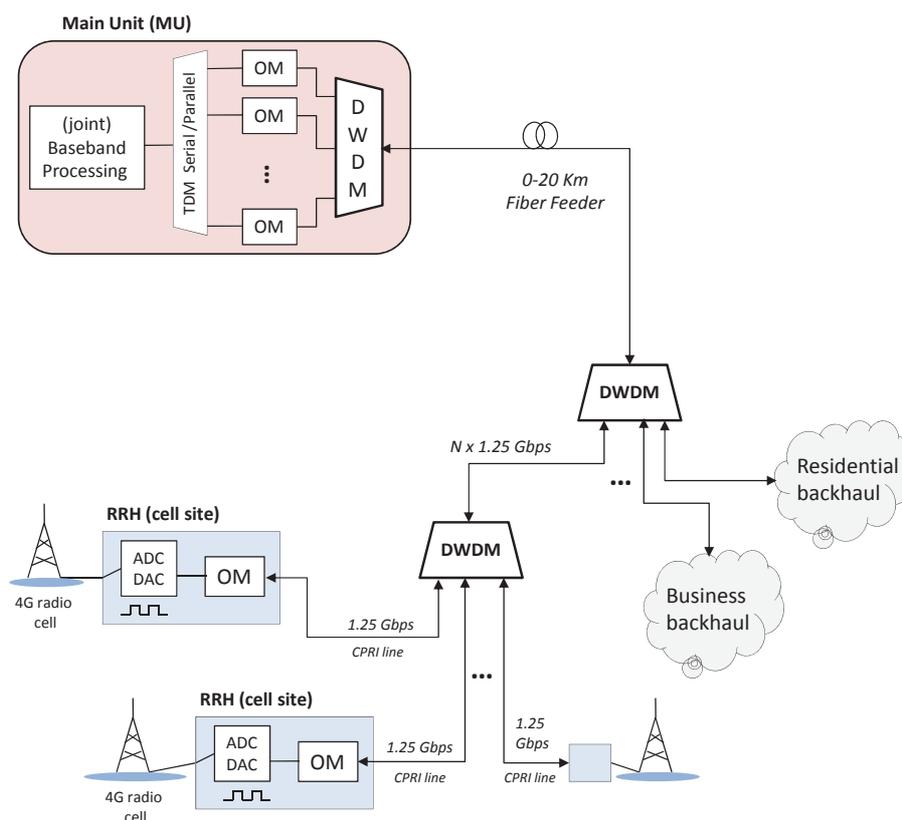[3]In the range of few tens of minutes as considered in Chapter 5.

Figure 7.2: D-RoF WDM-PON network architecture

to Zero/Return to Zero (IRZ/RZ) translation[4]. RRH links are aggregated to the MU using a DWDM multiplexer/demultiplexer. At the MU, each RRH digital link is demodulated using a dedicated OM. Parallel digital streams are serialized using a high-speed TDM multiplexer and joint-baseband processed at the CP of the MU.

The GeRoFAN and the D-RoF WDM-PON architectures show several similarities. First, both systems rely on the centralized light-seeding concept combined with reflective colorless modulators to facilitate wavelength management and to prevent the need for costly light-sources at the RRH/RAU. Second, both systems exploit the benefits of the DWDM technology in the optical distribution network (traffic isolation, transparency, "unlimited" bandwidth etc.). Finally, both architectures take advantage of the centralization at the head-end node to implement either joint baseband processing for D-RoF WDM-PON or QoT-aware backhaul and aggregated capacity management for the GeRoFAN system. However, the main difference between the two systems is the optical transmission technology used for backhauling: A-RoF for GeRoFAN, while the alternative architecture relies on D-RoF.

---

[4]The PCB translates data coding from IRZ to RZ. The latter is more efficient against the RBS noise which is expected to be one of the main impairment in high-speed WDM-PON [36].

7.3.2 Methodology

The techno-economic study of GeRoFAN and D-RoF WDM-PON systems is carried out following the methodology depicted in Figure 7.3. Our methodology is inspired from techno-economic research studies developed in [109], [51], the economic frameworks presented in [47] and [141] and the financial model developed for cable television in [149].

Assuming a traffic evolution scenario which depicts the annual increase of the backhaul capacity per cell site, we determine how the network should be dimensioned to fulfill the projected capacity. The CapEx cost consists of the infrastructure costs of the network calculated using the dimensioning model. The CapEx cost includes the infrastructure cost of the head-end node (HOLT/MU), the infrastructure cost of the RAU/RRH and the outside plant cost (civil works for fiber deployment, housing/cabinet[5] etc.). In addition, we include in the CapEx calculation the potential savings due to sharing and reuse of existing infrastructure. Substantial proportion of existing ducts/trenches can be reused for fiber deployment according to a report of Analysys Masons [7]. The report points out a reuse rate of the infrastructure up to 80% in the distribution segment near the head-end node (*i.e* between the HOLT/MU and the fiber node cabinet) as well as 30% in the final drop near the premises (*i.e* between the fiber node cabinet and the RAU/RRH). The OpEx is composed of three major parts: the Installed First Cost (IFC), the OpEx for a network that is up and running (power consumption cost, diagnosis/repair and maintenance costs) and the fixed costs for network operation and administration. Once OpEx and CapEx are calculated for a given traffic scenario, the overall cost of the system is distributed over the study period fixed at 10 years. To calculate the discounted cashflow savings achieved by the investment, we evaluate the OpEx cost incurred by the operator if it still relies on the legacy backhauling strategy based on T1/E1 leased lines. The OpEx incurred by legacy T1/E1-based backhauling includes the T1/E1 line leasing fee, the line activation fee and the associated operation and administration expenses.

For the final techno-economic evaluation of the network solution, critical financial indexes, such as Net Present Value (NPV), Internal Rate of Return (IRR) and Payback period of the project are calculated in order to decide about the profitability of the investment. The reader may refer to Table 7.1 which summarizes the definition of the key financial indexes used to assess the business profitability of the investment.

7.3.3 Traffic scenario

In our study, we use the yearly statistics of the traffic per cell site as reported by Yankee Group Research [110] from 2000 to 2012. Assuming a study period of 10 years ranging from 2010 to 2020, statistics of the traffic evolution per cell site for the $2012 - 2020$ period are derived

---

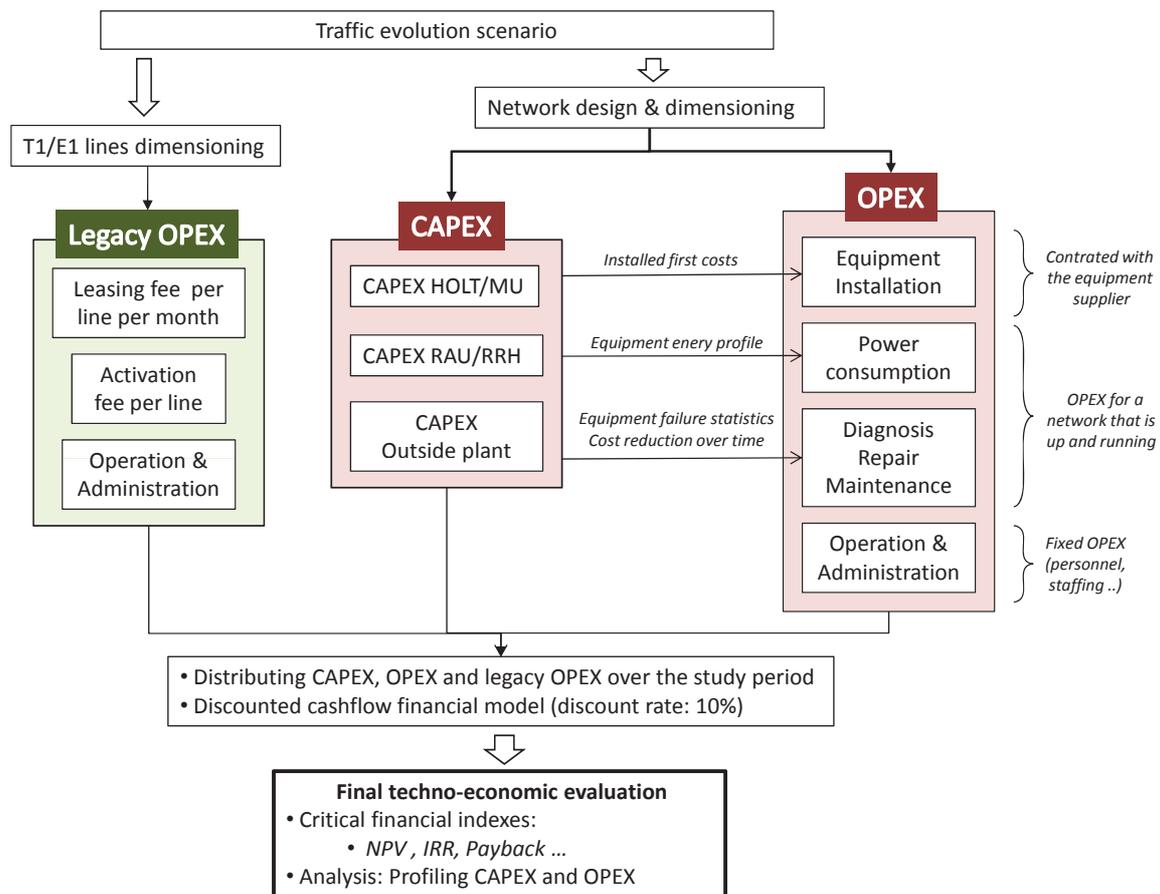[5]The cabinet hosts either the DWDM-MUX or the optical splitter.

Figure 7.3: The techno-economic study methodology.

Table 7.1: How to assess project investment profitability ? [45]

The **Net Present Value (NPV)** describes today's value of the sum of resultant discounted cashflows (CapEx, OpEx, Revenues, Savings, etc.) by taking into account the time value or opportunity cost of money expressed by the discount rate. If the NPV is positive, the project is acceptable. The higher the NPV of the investment project, the higher its business profitability.
The **Internal Rate of Return (IRR)** gives a good indication of the business value achieved with respect to the money invested to set up and run the project. is the interest rate resulting from an investment and income (total net discounted cashflow) that occur over a the study period. To assess the business profitability of a project, we compare the IRR with the discount rate used for the analysis. The project investment is profitable as long as its IRR is higher than the discount rate.
The **Payback Period** is the specific point in the life time cycle of the project when the accumulated discounted cashflow (cash balance) turns positive. Starting from the first year of investment, the payback period represents the time needed to recover the required amount of funding.

through projections. Three possible scenario projections are considered in our study: the first scenario assumes a 5% yearly traffic growth rate, the second scenario considers a 10% yearly growth rate while a rate of 20% is assumed for the third scenario. The three considered traffic evolution scenarios are shown in Figure 7.4.
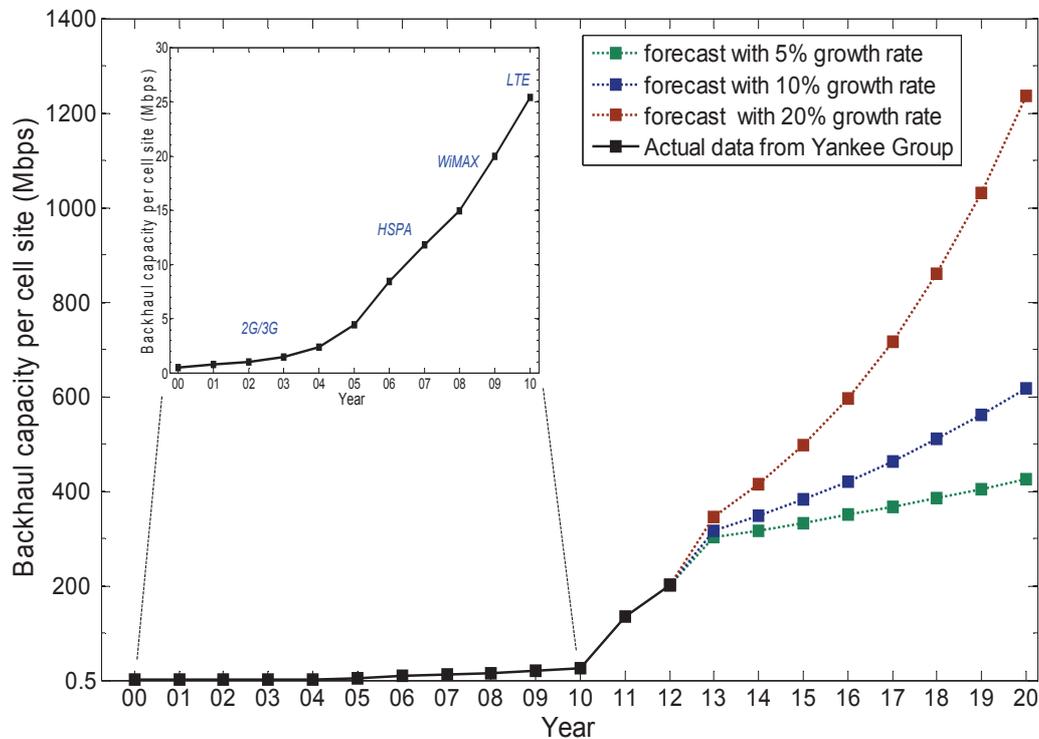

Figure 7.4: The three scenarios considered for backhaul capacity evolution.

7.3.4   CapEx valuation model

For both network architectures, a number of cost components are assigned to different parts of the network (HOLT/MU, RAU/RRH and Outside plant). Major CapEx components are detailed in Table 7.2. For all components, we assume that the equipment life time is equal to 10 years. In order to be able to calculate the yearly capital equipment costs, the total cost of the component is divided by the equipment life-time.

7.3.5   OpEx valuation model

The OpEx cost is the aggregation of four operational costs.

- First, IFC which stands for OpEx associated with equipment installation is determined together with the CapEx cost of the equipment. For real scenario, the IFC is contracted as a negotiation with the equipment vendor. For our study, some values of the IFC are

---

[6]For instance the Spartan-6 FPGA family from *www.xilinx.com*

Table 7.2: CapEx costs (G: GeRoFAN, D: D-RoF WDM-PON).

	Component	Cost (€)	IFC (€)	Source	G	D
HOLT/MU, RAU/RRH	TOSA-DFB-LD @ HOLT/MU	920	276	[115]	●	●
	ROSA-APD @ HOLT/MU	700	210	[115]	●	●
	FPGA-based RF-onto-OCs switching matrix	500	150	Xilinx Corp[6].	●	
	High speed TDM S/P	7000	2100	[34]		●
	FPGA PCB for joint Baseband processing	500	150	Xilinx Corp.		●
	DWDM ROADM (25 GHz spacing.)	1500	450	Ciena	●	
	TOSA-REAMSOA @ RAU	3000	900	[115]	●	
	ROSA-WB APD @ RAU	700	210	[115]	●	
	RF duplexer @ RAU/RRH	260	78	[115]	●	●
	r-CPU: BOSA (FP-LD/APD) @ RAU	250	75	[115]	●	
	r-CPU: FPGA PCB ($\lambda\star$) @ RAU	100	30	Xilinx Corp.	●	
	BOSA-EAT WDM-SFP 1GbE @ RRH	3850	1115	[34]		●
	BOSA-EAT WDM-SFP+ 10GbE @ RRH	5000	1500	[34]		●
	BOSA-EAT WDM-XFP/SFP+ 40GbE @ RRH	9800	2940	[34]		●
	ADC/DAC 250MS/sec (8bits) @ RRH	3000	900	National Instruments		●
	ADC/DAC 500MS/sec (8bits) @ RRH	4000	1200	National Instruments		●
	ADC/DAC 1GS/sec (8bits) @ RRH	6000	1800	National Instruments		●
	ADC/DAC 2GS/sec (8bits) @ RRH	10850	3255	National Instruments		●
Outside Plant	DWDM MUX/DEMUX (up to 40 λ)	12000	3600	[51]	●	●
	Optical Splitter (1:32)	100	-	CSMG [109]	●	
	Fiber node cabinet/closures	2450	-	CSMG [109]	●	●
	Optical Cable24Fiber	1220/Km	900/Km	Analysys Masons [109]	●	●
	Digging/ducting cost (Urban)	60000/Km	-	CSMG [109]	●	●
	RAU/RRH site civil work	1000	-	Analysys Masons [109]	●	●

taken from [109] if available, otherwise IFC is estimated as the assumptions in [51] to be 30% of the CapEx costs. Values of IFC for the different components are specified in Table 7.2.

- The second operational cost represents the energy consumption of network components. Average power consumptions are estimated from the energy consumption model developed in Section 3.3 of Chapter 3 and from data reported in [73] and [147]. We consider, according to the assumptions in [51], a price of 0.08 € per KWh to determine the cost of the energy consumption.

- The third operational cost encompasses the expenditures associated with failure diagnosis/monitoring, repair and equipment maintenance. The maintenance cost $OpEx_M$ of an equipment is evaluated on a yearly basis according to the following formula in Equation 7.1 reported from [45]:

$$OpEx_{Mi} = \frac{V_{i-1} + V_i}{2} \cdot (P_i \cdot R_{class} + P_l \cdot \frac{MTTR}{MTBF}) \tag{7.1}$$

where: V_i the equipment volume in year i, P_i the price of the equipment in year i, R_{class} is the maintenance cost percentage for every cost component assumed according to [109] as 7% of CapEx for the equipment, P_l the hourly cost of the staff in charge of maintaining the equipment assumed to be 1.5 times the minimum wage. $MTTR$ and $MTBF$ represent the mean time to repair and the mean time between failures respectively. The first item between the parenthesis in the Equation represents the cost of repair parts while the second item stands for the cost of repair work. Nominal values of availability statistics ($MTTR$ and $MTBF$) of the different network components are taken from [51]. The evolution of the price of a component P_i follows a decreasing trend over years described by the following learning curve formula taken from [45]:

$$P_i = P_0 \cdot \left[\frac{1}{n(0)} \cdot \left\{ 1 + \exp\left[\ln(\frac{1}{n(0)} - 1) - \frac{2\ln(9)}{\tau} \cdot i \right] \right\}^{-1} \right]^{\log_2(k)} \tag{7.2}$$

Given: P_0 the initial price of the component at the reference year (2010), τ the time required for the accumulated production volume to grow from 10% to 90% (here assumed to be 10 years), k is a learning curve coefficient set at 98% [109] and $n(0)$ reflects the relative cumulative volume taken as 0.5 for components that already exist in the market and their price is expected to decrease due to aging rather than due to the production volume (RF duplexers, LD, APD, fiber, splitter etc.), 0.1 for mature components (ROADM, DWDM MUX, WDM-PON SFP, moderate speed ADC/DACs etc.) and 0.01 for new to very

Table 7.3: Personnel/staffing overhead cost inspired from [50].

Activity	Overhead
Technical (field)	× 2.5
Network Operation Center	× 2
Adminstrative/helpdesk	× 2
Engineering, R&D	× 3

Table 7.4: Other yearly recurring OpEx taken from [109].

OpEx	Valuation (€/year)
Site rental for HOLT/MU (urban area)	3000
Housing: cabinets/closures	5% of CapEx for closures
Civil works	3% of CapEx for civil works

new components in the market (WDM-PON XFP/SFP+, very high speed ADC/DACs, EAT/REAMSOA etc.).

- The last OpEx item stands for Operation and Administration (*O&A*) costs. The latter includes the cost of the operational activities (network technical operations, helpdesk/administrative tasks) calculated as the hourly cost of the employee multiplied by the average duration required to perform the activity. following the approach of [51], an overhead factor is included in the salary estimation in order to fully account the cost of this person for the company. The overhead factor accounts for the tools, transport and training needed for personnel performing difficult or high qualifying tasks. Table 7.3 provides the personnel cost for each activity type. At this stage of the study, only administrative/hepldesk and technical field personnel are considered.

- Finally other yearly recurring operation costs are also considered and summarized in Table 7.4.

7.3.6 Economic results and discussion

We investigate the techno-economics of both investment projects and we calculate the discounted cashflow achieved savings with respect to a legacy backhaul using T1/E1 leased lines. The details of the OpEx associated with the legacy backhaul are provided in Table 7.5:

Table 7.5: OpEx for a T1/E1 leased-lines backhaul [110].

Leasing fee of a single T1/E1 line	300€/month
Contracted line activation fee	10% of the leasing fee
Required dedicated staff	1 technical, 1 administrative

Figure 7.5 provides the evolution of the amount of achieved savings for both architectures with the three traffic scenarios assuming a 10% discount rate. The evolution of the cashflow savings shows that the GeRoFAN investment project is more profitable compared to the D-RoF WDM-PON project at high rate increase of the radio traffic. In fact, at such higher rates, higher speed electronics and optical transceivers are required for the D-RoF based network architecture. Regarding the current cost of such components and the high level of power consumed, the CapEx and OpEx of D-RoF WDM-PON is increased as well which decreases the achievable savings compared to GeRoFAN. At 5% of the traffic rate increase, results show that the D-RoF architecture is more cost-effective with a little higher achieved cashflow savings. Such results are in-line with the results in Chapter 3 where we pointed out the economic advantage of A-RoF compared to D-RoF only at higher traffic loads.
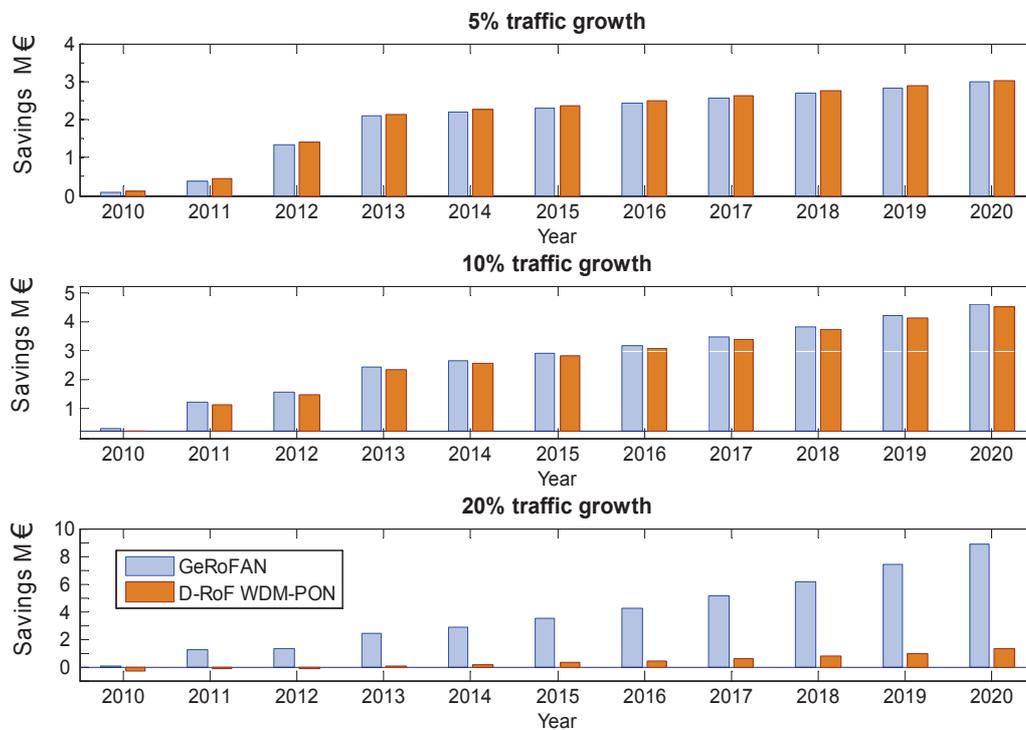
Figure 7.5: Year-by-year discounted cashflow savings achieved by GeRoFAN and D-RoF WDM-PON for the three traffic scenarios.

The trend of cashflow savings shown in Figure 7.5 is confirmed by the financial summary provided in Table 7.6. Higher IRRs and NPVs as well as lower payback periods are reported for GeRoFAN compared to D-RoF WDM-PON especially at higher rates of the radio traffic increase. Particularly, the cost-effectiveness of the GeRoFAN investment is confirmed with the third scenario (20% of yearly traffic increase rate). Indeed, the D-RoF WDM-PON investment project shows 94.5% lower NPV, lower IRR (lower than the cost of capital (10%)) and higher payback period (6× the payback needed by GeRoFAN). Note that all these statistics are subject to

Table 7.6: Financial summary of both investments.

	Scenario	GeRoFAN	D-RoF WDM-PON
NPV	1	1.057 M€	1.104 M€
	2	1.280 M€	1.215 M€
	3	1.892 M€	103.18 K€
IRR	1	25 %	≃ 30.8 %
	2	≃ 27.7 %	≃ 32.62 %
	3	≃ 34.1 %	≃ 8.5 %
Payback	1	≃ 1 year, 2 months	≃ 1 year, 2 weeks
	2	≃ 1 year, 3 weeks	≃ 1 year, 1 month
	3	≃ 1 year, 1 month	≃ 6 years, 6 months

modification if substantial technological development is carried out by equipment manufacturers to lower the cost of high speed opto-electronics required by the D-RoF architecture and increase the power efficiencies of such devices.

OpEx and CapEx costs are analyzed for both architectures in Figure 7.6. Unlike the D-RoF WDM-PON architecture, we have noticed no significant change of the OpEx and CapEx cost for the GeRoFAN architecture at the different traffic scenarios. We can conclude that GeRoFAN is economically much less sensitive[7] to the traffic evolution than D-RoF WDM-PON.

For both investment projects, the outside plant represents the major part of the CapEx cost (dominated mainly by the deployment cost of the fiber). It's worth noting that the share of the outside plant can be significantly reduced by favoring a higher mutualization of network facilities and cable ducts. Apart the outside plant and excepting the first scenario where the relatively low traffic increase rate (5%) makes the RRH less expensive, Figure 7.6a shows that the RRH/RAU captures a major share of the CapEx (at the third scenario, RRHs occupy 29% of the total network CapEx).

The OpEx profiling illustrated in Figure 7.6b shows that the maintenance/repair cost and the power consumption are the two major costs constituting the structure of the OpEx. Note that at higher traffic increase rates (10% and 20%), energy consumption costs over-dominate the total OpEx (80% of OpEx) for the D-RoF WDM-PON architecture, while the cost structure is more relatively balanced for GeRoFAN (although energy consumption costs are still prevailing). These results indicate how the GeRoFAN architecture takes advantage of its higher optical transparency to lower the OpEx and the share of the energy consumption cost almost driven by electronics.

---

[7]Although a sensitivity analysis is required to assess exactly how much each architecture is economically sensitive to variations of the used parameters in the model (components cost, T1/E1 leasing fee, the price of a KWh etc.), we expect that such a sensitivity analysis would not change the results of ours study.
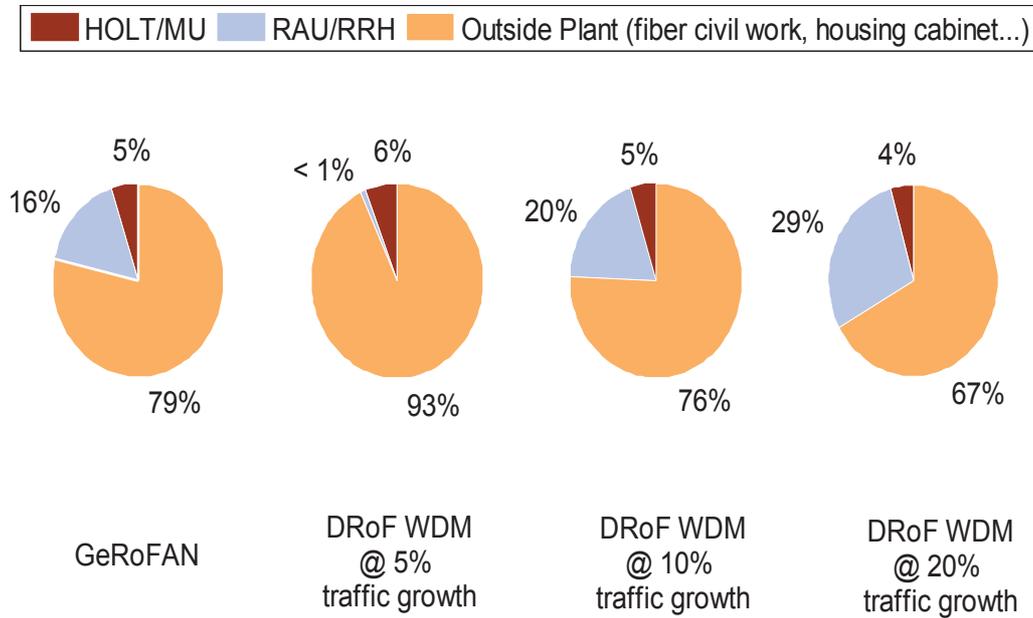
(a) CapEx Profiling for the two network architectures.
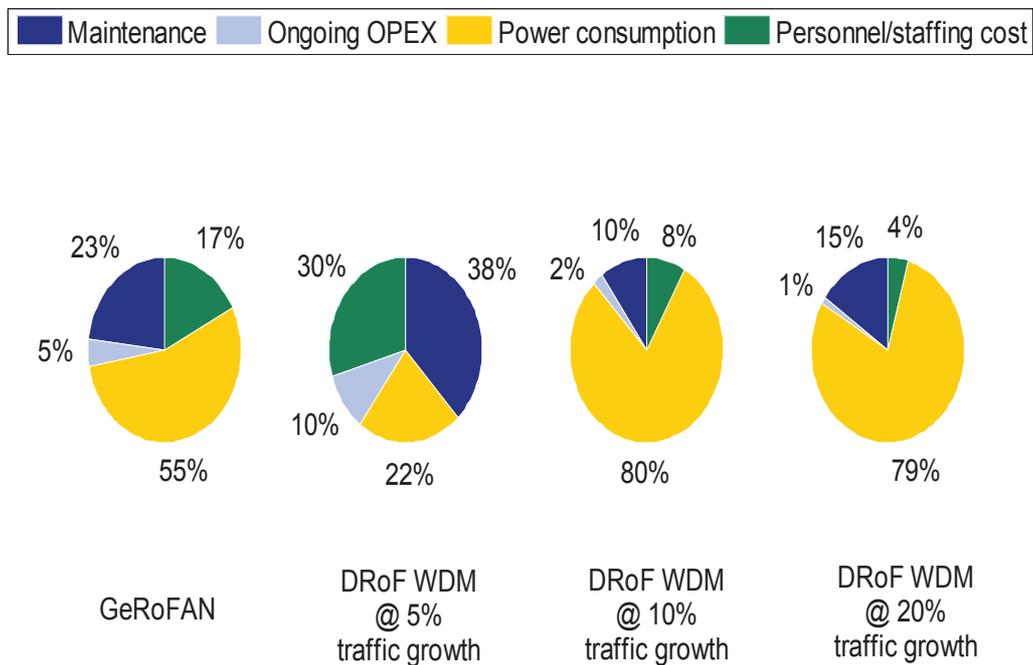
(b) OpEx Profiling for the two architectures.

Figure 7.6: CapEx and OpEx profiling analysis.

7.4   Sharing the business value among stake-holders

After assessing the profitability of the GeRoFAN investment, we investigate in this section the requirement for an economically attractive exploitation of the GeRoFAN system. As outlined, the GeRoFAN architecture offers the radio operator the opportunity to outsource the backhauling activity. Two models are proposed in this section to structure the value chain of the cellular backhauling activity and to orchestrate the interaction between the different stake-holders.

7.4.1   A two-tiers business model

In the two-tiers model, depicted in Figure 7.7a, the value chain is achieved by two players: the GeRoFAN operator and the radio mobile operator. The latter outsources the backhauling activity to the GeRoFAN operator who is in charge of installing and maintaining the GeRoFAN infrastructure. In addition, the GeRoFAN operator acts also as a Backhaul Service Provider (BSP) to backhaul the traffic of the radio operator at a given fee and subject to a given Service Level Agreement (SLA). The SLA of the backhaul service provided by the GeRoFAN operator is related to the efficiency of the backhauling, *i.e* the rejection ratio imposed to the mobile operator due to the physical layer impairments of the backhaul transmission through the GeRoFAN network. Thus, the more efficient the backhauling strategy carried out by the GeRoFAN operator, the higher the compliance with the SLA, but also the more expensive such a strategy would be to get implemented[8]. Once the backhauling strategy selected, the non conformity to the SLA, *i.e* the loss in the radio system capacity, is translated into a penalty cost that the GeRoFAN manager refunds back to the radio operator. Our aim is to price the backhauling service provided by the GeRoFAN operator and its associated penalty cost in order to achieve a balanced sharing of the business value between the GeRoFAN operator and the radio mobile operator.

Unlike the techno-economic assessment in Section 7.3 which does not need any assumption about the backhauling strategy applied by the GeRoFAN operator, the current study requires the determination of the average number of OCs needed to carry out the considered backhauling strategy together with its incurred rejection ratio. We assume that the GeRoFAN operator applies the FFCA backhauling strategy described in Chapter 5. In the following, we describe the methodology, illustrated in Figure 7.8, to calculate the backhauling fee (α) and the penalty cost (β).

1. The first step consists in determining the hourly evolution of the traffic per cell site for a given year i. This is calculated by "modulating" the amount of traffic reported at year i (considering traffic statistic for an increase rate of 5% in Figure 7.4) with the daily traffic

---

[8]Optimal backhauling strategies like those investigated in the previous chapters (DBS, PaGeO, FFCA etc.) are more complex to design and to implement compared to QoT-agnostic backhauling policies.

(a) Interaction between the two business model players.

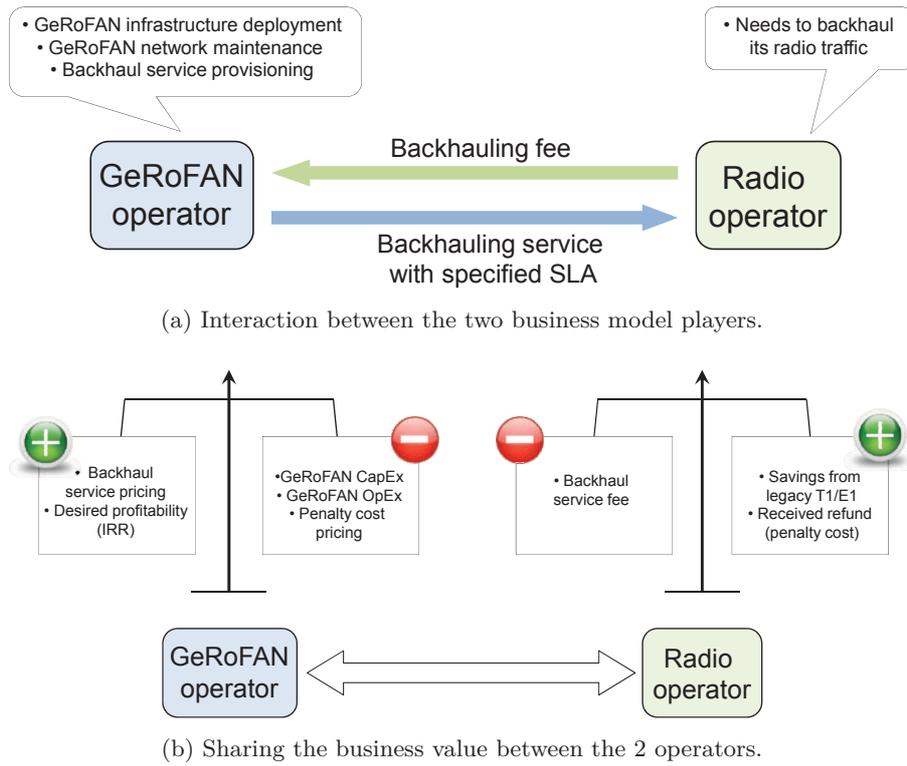(b) Sharing the business value between the 2 operators.

Figure 7.7: A two-tiers business model

distribution shown in Figure 6.11b of Chapter 6. To differentiate hot-spot cells from other cells, the obtained distribution is multiplied by a cell activity factor which equals to 1 for hot-spots and 0.5 for a non-hot-spot cell.

2. Once the hourly evolution of the traffic per cell site is determined for year i, we deduce in the second step the required RF bandwidth using the classical Shannon's formula. For that sake, we consider the radio spectral efficiency γ calculated from the analytical radio propagation model of [65] and assuming a regular frequency reuse factor of 7. The calculated RF bandwidths are mapped into *4G LTE* radio channels[9].

3. In the third step, we run successively the FFCA algorithm at each hour of the evolution of the traffic per cell site for an average daily traffic pattern along year i. An *LTE* network with 20 cells is considered with 4 hot-spots selected randomly within the radio system network.

   Results of the different FFCA instances (each executed for a given hour) are averaged to get the number of required OCs per hour (n_i^{FFCA}) and the average rejection ratio per hour (τ_i^{FFCA}) for the considered year i. Values of n_i^{FFCA} and τ_i^{FFCA} for the investment

---

[9]According to the current 3GPP specifications [133], the *LTE* system supports the deployment of the following bandwidth blocks: 1.4 MHz, 3 MHz, 5 MHz, 10 MHz, 15 MHz and 20 MHz. A radio channel bandwidth of 100 MHz is also possible using the technique of carriers aggregation.
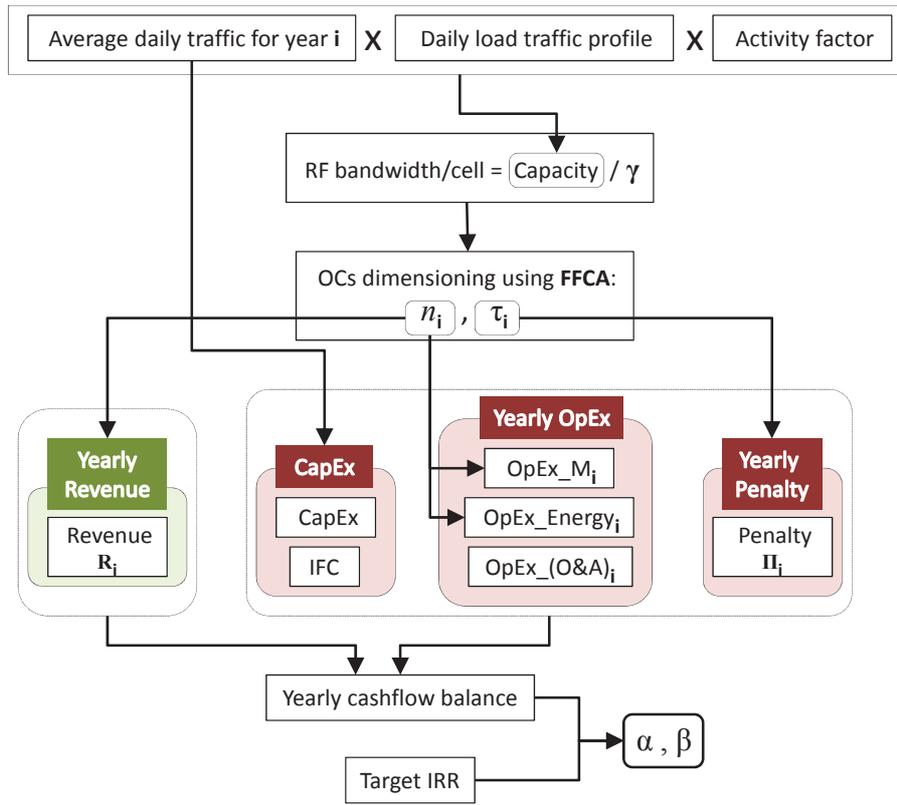
Figure 7.8: Methodology of the economic assessment for the two-tiers business model.

study period (10 years) are provided in Table 7.7.

4. The economics of the GeRoFAN system and its backhauling service are evaluated in the fourth step. CapEx costs ($CapEx$) (including infrastructure capital cost and IFC) are evaluated similarly to Section 7.3. As in the previous techno-economic assessment, OpEx costs at year i ($OpEx_i$) aggregates maintenance costs ($OpEx_{Mi}$), energy consumption costs ($OpEx_{Ei}$) and operation and adminstration costs ($OpEx_{(O\&A)_i}$). However, unlike the OpEx calculations in Section 7.3, maintenance and energy consumption costs are evaluated on the basis of effectively activated equipments (*i.e* n_i^{FFCA} OCs), while 2 additional personnel (sale and Network Operation Center (NOC) personnel) are added to the operation and adminstration costs.

Given β the penalty cost per hour and due to 1% incurred rejection ratio, we compute the yearly penalty Π_i as: $\Pi_i = (24 \times 356) \times \beta \times \tau_i^{FFCA}$. At the same step and using the calculated average number of required OCs per hour (n_i^{FFCA}), we evaluate the yearly revenue R_i of the GeRoFAN operator as: $R_i = (24 \times 356) \times \alpha \times n_i^{FFCA}$ given α the price of the usage of a single OC per hour[10].

---

[10]We assume that all OCs are subject to the same price, while in reality, OCs of the WDM pool would be priced differently since they do not display the same quality as highlighted in the previous chapters.

Table 7.7: Yearly required *LTE* RF channels per cell, averaged n_i and τ_i for FFCA and DBS.

Year	2010	2011	2012	2013	2014	2015	2016	2017	2018	2019	2020
LTE RFs (MHz)	5	15	15, 20	2×20, 10	2×20, 10	2×20, 10, 3	2×20, 15	2×20, 15, 3	3×20, 1.4	3×20, 5	3×20, 10
n_i^{FFCA}	6.05	6.15	6.6	7.15	7.15	7.6	7.15	7.6	7.6	7.9	8.6
τ_i^{FFCA} (%)	2.9	3.5	3.6	4.16	4.16	4.48	5	5.57	6.11	6.8	7.53
n_i^{DBS}	3.5	3.65	4.15	4.6	4.8	5.17	5	5.5	5.5	5.75	6
τ_i^{DBS} (%)	0.85	1.06	1.12	1.4	1.4	1.7	2	2.4	2.9	3.5	4.1

Nota: Rejection ratios are computed on the basis of the number of rejected voice calls, each requiring 32 *kbps* (*c.f.* Chapter 4 and Chapter 5).

5. Using the yearly cash-inflow and cash-outflow of the project, we compute the cash balance at year i as: $R_i - \Pi_i - OpEx_i$. The question at this stage is how the GeRoFAN operators should price α and β such that all expenditures can be recovered by the generated revenues with an additional profit margin. In this context, the IRR is a key indicator to decide about the profitability of the business project. From an investment perspective, the GeRoFAN operator estimates the pricing of α and β according to which a desired IRR value ($IRR^\star$) is achieved. Analytically, the optimal pricing is decided according to Equation 7.3:

$$CapEx = \sum_{i=1}^{10} \frac{R_i - \Pi_i - OpEx_i}{(1 + IRR^\star)^i} \qquad (7.3)$$

The key to implementing the two-tiers business model successfully is aligning the backhauling fee expectations of the mobile operator with the investment profitability the GeRoFAN operator is able to achieve. The requirement for a balanced sharing of the business value between the two stake-holders (GeRoFAN operator and mobile operator) is illustrated in Figure 7.7b. Indeed, the proposed business model is attractive for the mobile operator as long as the backhauling service fee is still lower than the received refund (from the GeRoFAN operator as a penalty cost) added to the estimated yearly cost of legacy backhaul ($OpEx_i^{T1/E1}$) based on leased T1/E1 lines. Such a requirement is formulated according to Equation 7.4:

$$\sum_{i=1}^{10} \frac{(R_i - \Pi_i)}{(1 + r)^i} \leq \sum_{i=1}^{10} \frac{OpEx_i^{T1/E1}}{(1 + r)^i} \qquad (7.4)$$

Figure 7.9 depicts the possible pair solutions (α, β) evolving along the different curves each of them corresponding to a given targeted $IRR^\star$ by the GeRoFAN operator. In addition, we highlight the particular region where a balanced sharing of the business value between the two operators can be realized. On one hand from the GeRoFAN operator perspective, the investment is profitable as long as the IRR is higher than the cost of capital (*i.e* the discount rate of 10%). On the other hand from the mobile operator perspective, it is worthy to get involved in the business model as long as the condition expressed in Equation 7.4 is fulfilled, that sets an upper

limit on the price of an OC beyond which the backhauling service fee becomes prohibitive. Thus, the optimal pricing (α, β) within the highlighted eligible region on which both operators should agree would be the outcome of the business negotiation between the two stake-holders.
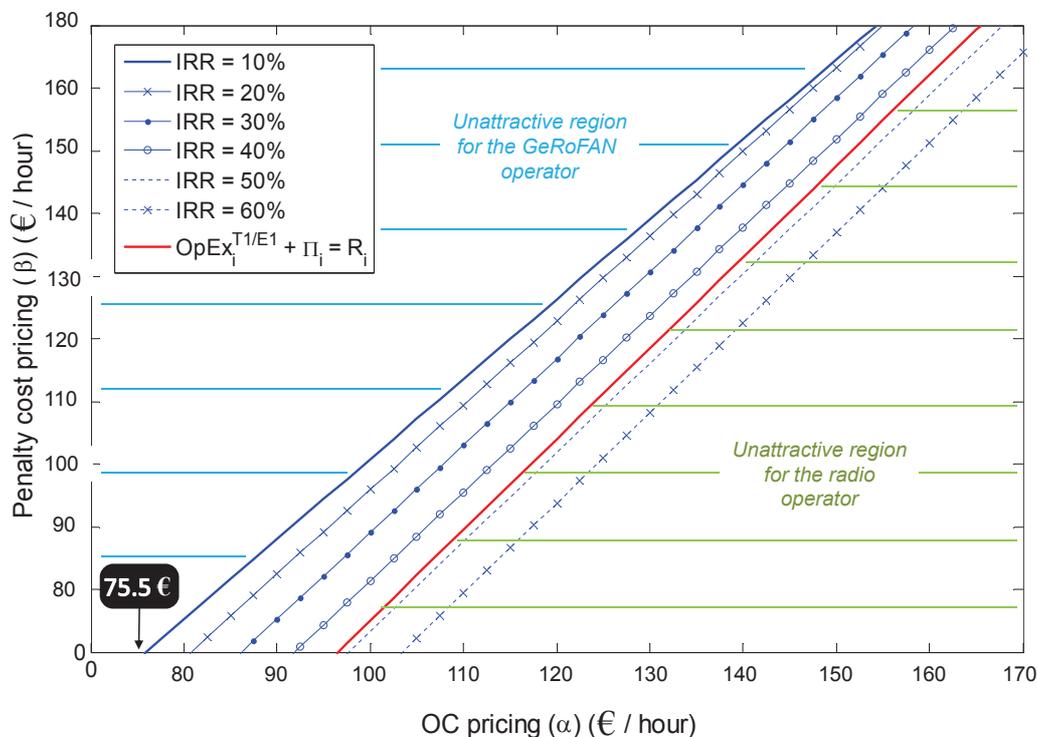

Figure 7.9: OCs and penalty cost pricing (α, β) for a balanced business value sharing in a two-tiers model.
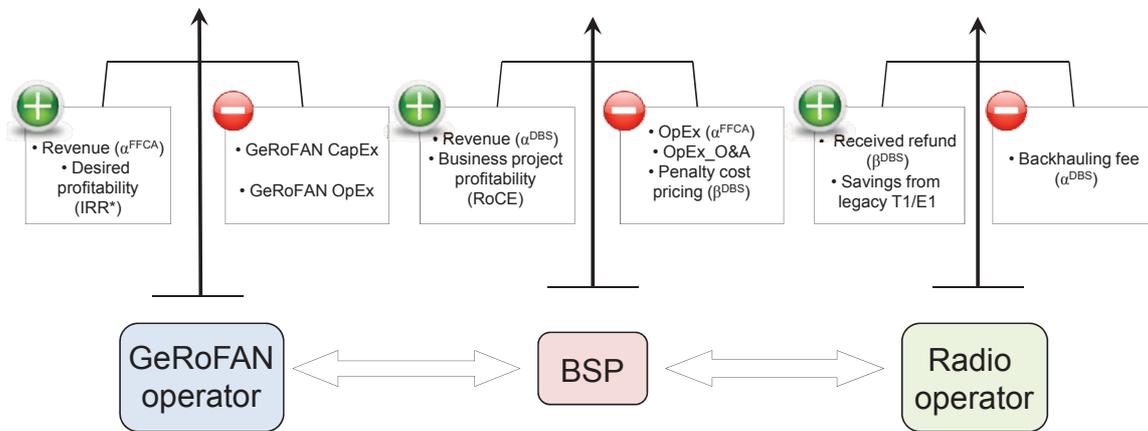
7.4.2 A three-tiers business model

One may argue that the role of the GeRoFAN operator consists in deploying and maintaining the optical network infrastructure and leasing it to any potential customer (FTTx operator, radio mobile operator etc.). Unlike the two-tier model, the new business model assumes a new player in the market, called *Backhaul Service Provider* (BSP), who is in charge of provisioning the traffic backhauling service for a mobile operator subject to a specified SLA. In the three-tiers model, the BSP is positioned in the value chain as an intermediary player between the mobile operator and the GeRoFAN operator. Since the value is shared between three stake-holders instead of only two as described in the previous model, the BSP has to implement an efficient and cost-effective backhauling strategy to ensure its business viability. Figure 7.10a illustrates how interactions are orchestrated between the GeRoFAN operator, the mobile operator and the BSP in the new business model.

Unlike the two-tiers model, the global balance achieved by the players in the three-tiers
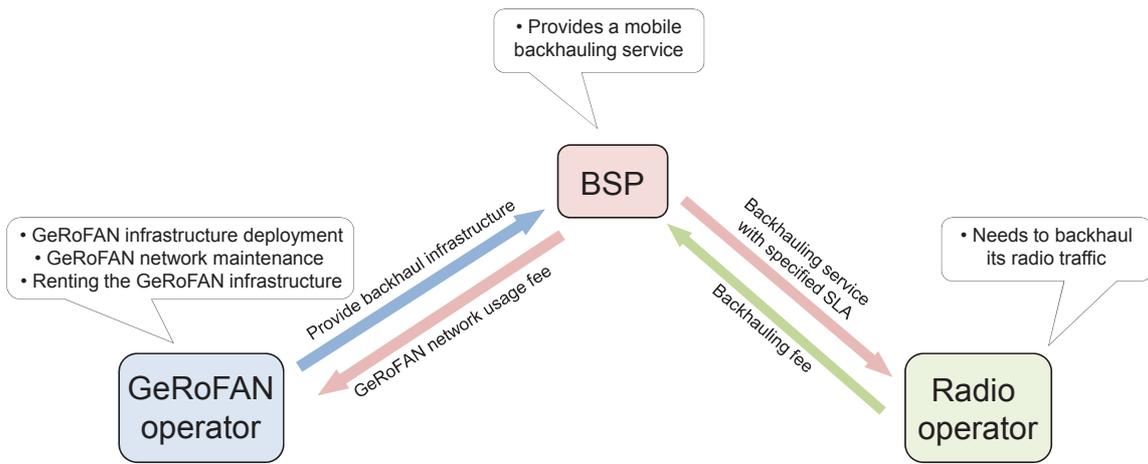
(a) Interaction between the three player in the new business model.

(b) Sharing the business value between the 3 stake-holders.

Figure 7.10: A three-tiers business model.

model is constituted by two-sided balances as depicted in Figure 7.10b. Indeed, at the left side of the model a first balance regulates the interaction between the GeRoFAN operator and the BSP, while a second balance at the right side ensures that the business is viable for the BSP and the mobile operator. The complexity of the three-tiers model consists in the fact that the two balances have to be realized at the same time in order to achieve a balanced sharing of the business value among the three players.

To solve the two aforementioned balances, we need to understand the motivations and expectations of each player from getting involved in the business model.

7.4.2.1 The GeRoFAN operator

The GeRoFAN operator rents out the usage of its OCs to the BSP who backhauls the traffic of its customer (the mobile operator). Hence, the GeRoFAN operator selects the right pricing of

the leasing fee (*i.e* the price of an OC per hour) according to a desired investment profitability (*i.e* a target IRR). Similarly to the calculations of the two-tiers model, the GeRoFAN operator dimensions for each year (along the 10 years project life-time) the average number of OCs expected to be used per hour by the BSP. Because the GeRoFAN operator does not know *a priori* the backhauling strategy the BSP would apply, the GeRoFAN operator estimates the number of required OCs assuming the FFCA backhauling strategy (*i.e* n_i^{FFCA}). However, unlike the calculations carried out by the GeRoFAN operator in the previous model, the latter does not assume any penalty cost since in the three-tiers model the GeRoFAN operator does not provide a backhauling service but simply rents the usage of its network infrastructure[11]. Thus, by removing the penalty cost represented by Π_i, Equation 7.3 is modified as the following to get the optimal pricing (α^{FFCA}) of an OC that should be charged by the GeRoFAN operator to the BSP.

$$CapEx = \sum_{i=1}^{10} \frac{R_i - OpEx_i}{(1 + IRR^\star)^i} \qquad (7.5)$$

Given: $Ri = 24 \times 356 \times (\alpha^{FFCA} \cdot n_i^{FFCA})$ and $OpEx_i(n_i^{FFCA})$ the "expected" revenue and OpEx cost respectively of the GeRoFAN operator for year i. Note that as in the calculations of the two-tiers model, $OpEx_i(n_i^{FFCA})$ depends on the number of "expected" activated OCs (n_i^{FFCA}) for each year.

Figure 7.11 illustrates the evolution of the leasing price of an OC per hour with respect to the desired IRR by the GeRoFAN operator. Since the latter targets an IRR at least equal than the cost of capital, the minimum charged price of an OC would be 50 € per hour. We notice that this price is roughly 33% lower than the minimum price (75.5 €) of the GeRoFAN operator determined in the two-tiers model. This is explained by the fact that in the three-tiers model, the charged price refers only to the cost of the usage of the GeRoFAN infrastructure, while the two-tiers model pricing reflects both the usage of the infrastructure and the provided backhauling service[12].

7.4.2.2 The BSP

From the BSP perspective, its involvement in the business model is worthy as long as the business contracted with the mobile operator on one hand and the GeRoFAN operator on the other hand are profitable. Since the BSP builds up its business without any CapEx (unlike the case of the GeRoFAN operator in the two tiers model), the business model for the BSP is profitable if the revenues generated from the backhauling service recover all operational expenses

---

[11]This is a key subtle difference between two business models. In the two-tiers model, the GeRoFAN operator acts as both a backhaul service and infrastructure provider, while in the three-tiers model, the GeRoFAN operator provides only the infrastructure to realize the backhaul value chain.

[12]By a rule of a thumb, the price of the provided backhauling service can be estimated here to 25.5 €.
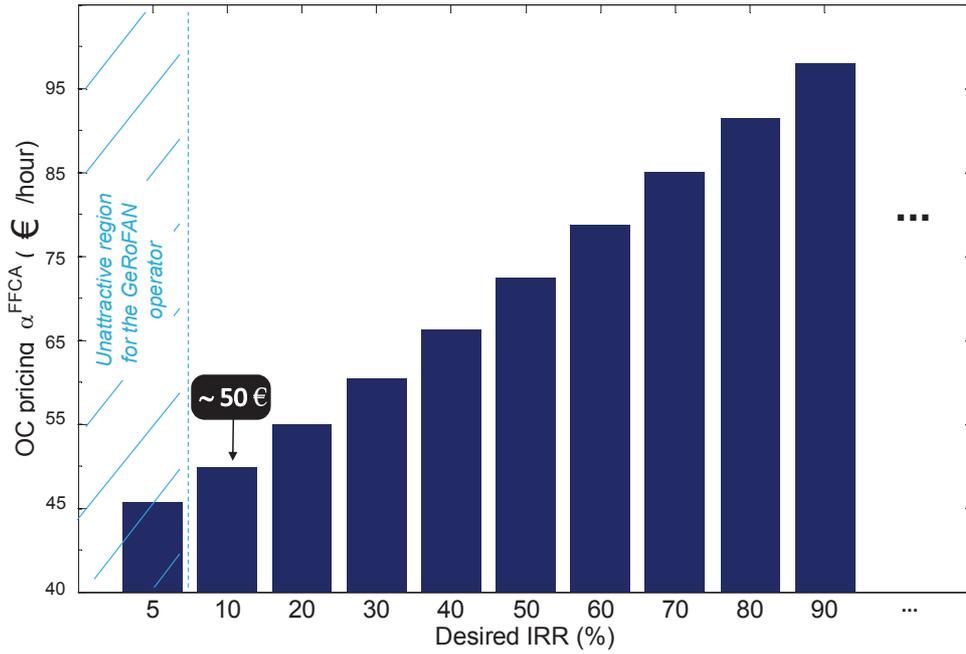
Figure 7.11: OC leasing price per hour as charged by the GeRoFAN operator to BSP.

needed to provide that service. The key competitive advantage of the BSP is to use the DBS backhauling strategy which carries out the backhauling with lower number of required OCs and at lower rejection ratio. Similarly to the approach carried out in the two-tiers model for FFCA, the BSP estimates at each year i the number of required OCs (n_i^{DBS}) and rejection ratio (τ_i^{DBS}) if the DBS is used. Results of n_i^{DBS} and τ_i^{DBS} are summarized in Table 7.7. Let α^{DBS} the price of an OC per hour proposed by the BSP, the revenue (R_i^{BSP}) of the BSP at year i will be: $R_i^{BSP} = (24 \times 356) \times \alpha^{DBS} \times n_i^{DBS}$. The total yearly OpEx ($OpEx_i^{BSP}$) of the BSP can be defined as: $OpEx_i^{BSP} = (24 \times 356 \times \beta^{DBS} \times \tau_i^{DBS}) + (24 \times 356 \times \alpha^{FFCA} \times n_i^{DBS}) + (OpEx_{O\&A})$. Three major costs constitute the total yearly OpEx of the BSP. The first term between parentheses stands for the penalty cost paid back to the mobile operator because of the loss of capacity induced by the DBS backhauling (non conformity to the SLA). The second term stands for the leasing fee charged by the GeRoFAN operator to the BSP, noting that only effectively used OCs are charged (*i.e* n_i^{DBS}). Finally the last term refers to the operation and adminstration costs assumed to account mainly for the staffing/personnel cost. Unlike FFCA for instance, the BSP applying the DBS algorithm would support a higher "human" operational cost (high qualified engineers/R&D team are needed to set up and operate the DBS strategy). Once the yearly revenue and the OpEx costs are evaluated and discounted[13], the BSP uses for instance the Return on Capital Employed (RoCE) to assess the profitability of its business. Expressed according to Equation 7.6, RoCE is defined as the ratio of the profit of the business to the

---

[13]Since the calculated revenue and OpEx costs are future values, the corresponding cashflows are discounted with a discount rate r of 10% to determine their present value.

amount of capital invested to launch that business[14], the result being divided by the overall study period to get the yearly RoCE.

$$RoCE = \frac{1}{10} \cdot \sum_{i=1}^{10} \frac{R_i^{BSP} - OpEx_i^{BSP}}{24 \times 356 \times \alpha^{FFCA} \times n_i^{DBS}} \qquad (7.6)$$

From the BSP perspective, the business is theoretically profitable as long as the RoCE is non-negative. The higher the value of the RoCE, the higher the expected return.

7.4.2.3 The radio mobile operator

Similarly to the two-tiers model, the radio mobile operator finds beneficial to outsource the backhauling activity to the BSP as long as the backhauling service fee does not overcome the the potential savings from legacy T1/E1-based backhauling including the refund received from the BSP in terms of penalty cost. The mobile operator contracts with the BSP as long as the condition of Equation 7.7 is fulfilled.

$$24 \times 356 \times \sum_{i=1}^{10} \frac{\left(\alpha_i^{DBS} \cdot n_i^{DBS} - \beta_i^{DBS} \cdot \tau_i^{DBS}\right)}{(1+r)^i} \leq \sum_{i=1}^{10} \frac{OpEx_i^{T1/E1}}{(1+r)^i} \qquad (7.7)$$

In Figure 7.12, we illustrate for each IRR targeted by the GeRoFAN operator, the possible pricing solutions (α^{BSP}, β^{BSP}) for the BSP to achieve a given RoCE. We note that for each IRR scenario the range of RoCE is constrained within an eligible region where the pricing couple should be selected. In fact, the eligible region is delimitated by the mobile operator condition set by Equation 7.7 (which fixes an upper value on the achievable RoCE) together with the profitability requirement of the BSP ($RoCE \geq 0$). The figure shows also the necessity to reach a compromise between the objective of the GeRoFAN operator to target higher IRRs and the aim of the BSP to reach higher RoCEs. In fact, the higher the IRR targeted by the GeRoFAN operator, the lower the maximum bound of RoCE achievable by the BSP. Finally, we note that the minimum OC pricing proposed by the BSP (*i.e* the pricing such that RoCE = 0) would be $\sim$ 69 €[15], this is nearly 8.6% lower than the minimum pricing proposed by the GeRoFAN operator if it acts as a BSP (*c.f* in the two-tiers model) which demonstrates the relevance of the three-tiers model.

The maximum achievable RoCE for the BSP is bounded by the requirement of the mobile operator expressed in Equation 7.7. Figure 7.13 depicts the evolution of the maximum RoCE with respect to the target IRR by the GeRoFAN operator. As indicated in the comment of Figure 7.12, the higher the target IRR (the higher pricing α^{FFCA} charged by the GeRoFAN

---

[14]We assume in our study that the amount of capital required by the BSP to launch its business is equal to the OCs leasing fee paid to the GeRoFAN operator.

[15]We recall that based on the minimum pricing of 75.5 € determined by the GeRoFAN operator in the two-tiers model, we have estimated by a rule of thumb that the backhaul service (considered separately from the GeRoFAN infrastructure usage price) accounts approximately for 25.5 €, which is 43.5 € cheaper than the minimum pricing of the BSP in the three-tiers model.
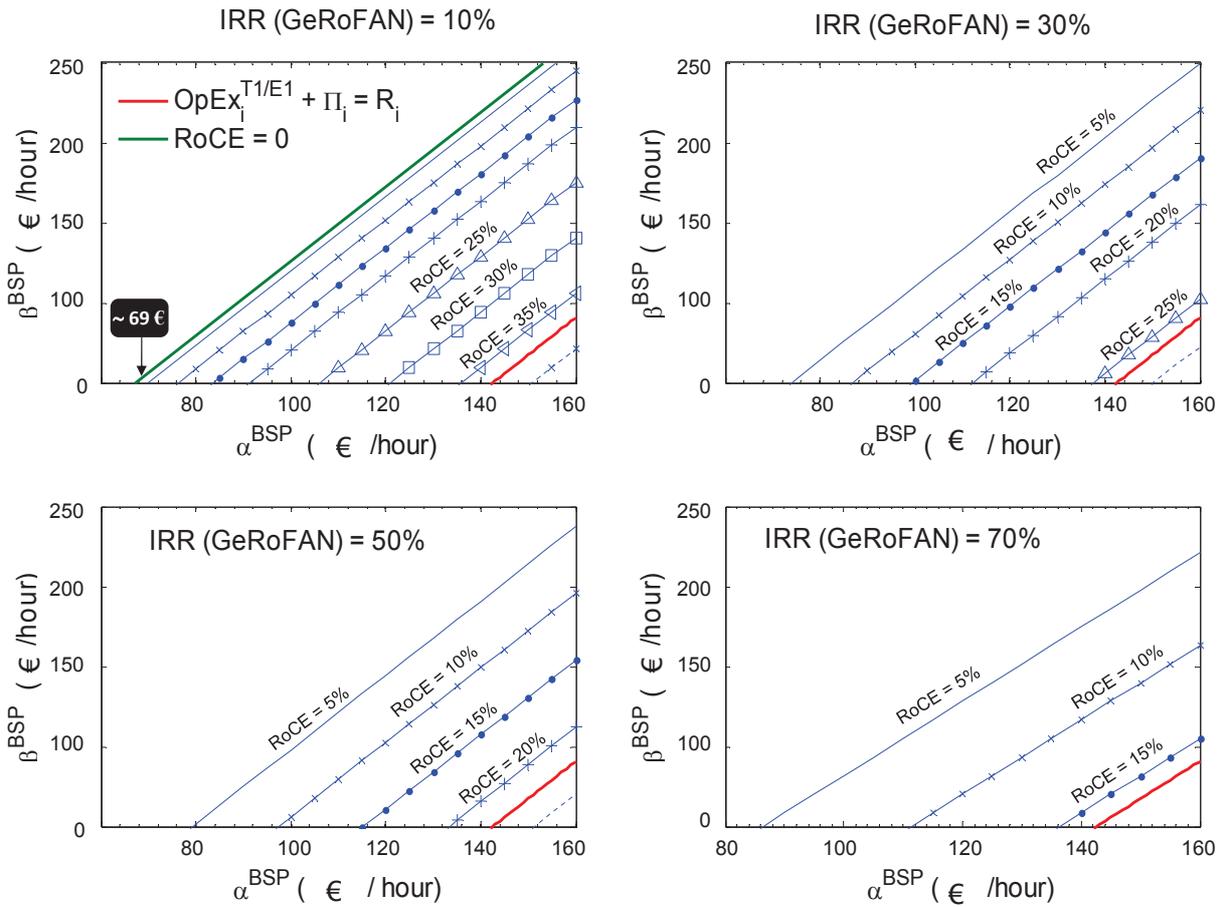
Figure 7.12: OCs and penalty pricing of the BSP for each target RoCE.

operator), the lower the profit margin of the BSP which decreases in turn the maximum RoCE. Such a result points out the compromise to be found between the GeRoFAN operator and the BSP in sharing the added value. We illustrate in Figure 7.13 the revised IRR for the GeRoFAN operator. In fact, the target IRR* was determined by the GeRoFAN operator based on an OC pricing calculated while assuming the FFCA backhauling strategy. Nevertheless, since the BSP exploits the DBS algorithm instead of FFCA, the BSP capitalizes on the higher performance of its innovative backhauling strategy to use actually a lower number of required OCs than planned by the GeRoFAN operator. Since a lower number than expected of OCs are effectively used, the benefit margin of the GeRoFAN operator is revised downward as well the target IRR. The figure shows that the revised IRR values are in average 25.3% lower than the initially planned IRR. As it can be seen in Figure 7.13, the revised IRR values extends also the unattractive region for the GeRoFAN operator (the region for which IRR is lower than the cost of capital).
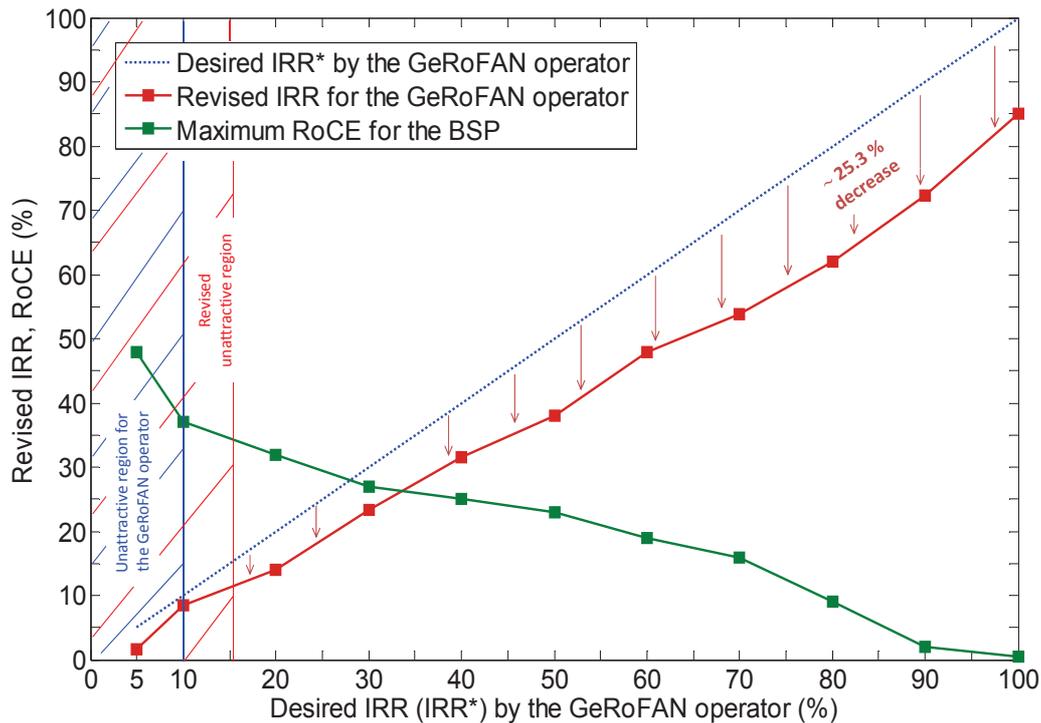
Figure 7.13: Revised IRR⋆ for the GeRoFAN operator and Maximum achievable RoCE for the BSP.

7.5   Summary and open issues

In this chapter, we investigated the economical prospects of GeRoFAN. From an investment perspective and compared to a D-RoF WDM-PON network architecture, results show that the GeRoFAN investment project remains profitable especially at higher increase rates of the radio traffic. The economic advantage of GeRoFAN on the D-RoF WDM-PON architecture depends mainly on the cost evolution of high-speed digital WDM transceivers and required high-speed electronics to digitize the signal. Since the power consumption contributes with more than a half of the total OpEx of the D-RoF WDM-PON architecture, the economic advantage of GeRoFAN could be jeopardized with the design of more power-efficient devices used by the D-RoF architecture.

We have also investigated two possible business models to structure the GeRoFAN eco-system. In a two-tiers model, the GeRoFAN operator acts as a third party installing and maintaining the infrastructure as well as providing the backhauling service for the mobile operator. For such a business model, we investigated the optimal pricing of OCs and the penalty cost (non-conformity with the SLA due to the radio capacity loss induced by the FFCA-based backhauling) able to achieve a target profitability for the GeRoFAN operator. Meanwhile, the determined pricing should guarantee for the mobile operator that outsourcing the backhauling

to GeRoFAN is still attractive. An alternative innovative three-tiers business model is also investigated. Such a new business model limits the role of the GeRoFAN operator to an infrastructure leaser and introduces a new "unusual" player called BSP in charge of providing the cellular backhauling service to the mobile operator with an optimized backhauling strategy (DBS). The BSP brings its added values in the three-tiers business model by capitalizing on the advantages of the DBS algorithm compared to FFCA, *i.e* by using lower number of OCs and offering an improved quality of service for backhaul (lowering the penalty cost thanks to the lower rejection ratios of DBS).

The key benefit of the three-tiers models consists in enriching the value chain of the backhauling service by outsourcing it to a specialized player able to capitalize on its innovation potential in order to deliver mobile operators with a competitive service (performing higher QoS at lower cost).

Despite the attractiveness of the three-tiers business model, some issues have to be addressed. The major issue is related to the complexity of implementing such a model. Indeed the successful implementation of the tree-tiers model relies on defining exactly the requirments/expectations of each player and implementing, through a best practice framework, an efficient protocol to orchestrate a Business-to-Businesses (B2B) cooperative interaction between the involved actors [91].

The regulation framework needed to support the new business model could get inspired from similar evolutions initiated either in sectors other than telecom (such as the energy retail market [119] and the transportation sector) or in activities that are related to telecom (like the study in [56] that investigates the cost-effectiveness of an outsourced green-power procurement model for mobile operators and develops a best practice guide to achieve its successful implementation for the case of the Indian telecom market).

Conclusion

Contents

8.1 Summary of Thesis Achievements

THE objective of the research conducted in this thesis is to investigate the potentiality of GeRoFAN, an all-optical network architecture exploiting A-RoF technology, to backhaul next generation radio cellular systems.

Thanks to its MAC-agnostic feature and its system flexibility provided by A-RoF, the GeRo-FAN architecture is suited for multi-technology and multi-radio system backhauling which points out its genericity. The GeRoFAN architecture takes benefit of equipment centralization at the head-end node (HOLT) enabled by A-RoF to acquire a global view of the traffic distribution in the area served by the GeRoFAN system. GeRoFAN is supported by an innovative Control Plane (CP) exploiting network resources mutualization at the HOLT to carry out a dynamic bandwidth management according to the space and time variations of the traffic matrix. However, achieving cellular backhauling using A-RoF is subject to several physical layer impairments degrading the signal quality and thus the Shannon's capacity of the radio channel. We outlined in Chapter 2 that such a limitation can be overcome by designing a QoT-aware CP able to mitigate RoF transmission impairments and thus preserving the radio system capacity. Doing so, the key innovation of the GeRoFAN-CP is to make the cellular backhauling as transparent as possible to the radio system.

Designing an efficient QoT-aware CP for GeRoFAN requires a deep knowledge of the physical layer impairments inherent to RoF link transmission. For that sake, we conducted in Chapter 3 an extensive modeling and analysis of the various noises involved in the GeRoFAN network. Indeed, we proposed a mathematical modeling describing the behavior of the reflective

electro-absorption amplified modulator considered as the key component of the GeRoFAN architecture. In addition, we carried out a modeling of the different noise sources inherent to the GeRoFAN network (fiber transmission impairments, ROADM noises, intermodulation radio signal distortions and optical crosstalk inherent to SCM/WDM multiplexing used by GeRoFAN). Considering two main possible network topologies for GeRoFAN (a tree and a loop), the outcome of the research was to package the various impairments inherent to each topology into a comprehensive analytical model called QoT-tool. The latter will be exploited by the GeRoFAN-CP to set up an optimized cellular backhauling strategy.

Assuming a static and uniform traffic distribution throughout the radio network, we investigated in Chapter 4 the optimal backhauling strategy operated by the GeRoFAN-CP able to preserve the radio system capacity while using efficiently the optical pool. Such a cross-optimization was first solved through an exact MILP formulation. Then we proposed a heuristic approach (PaGeO) based on a genetic algorithm with Pareto optimization. Our numerical results pointed out the superiority of an optical tree compared to an optical loop for GeRoFAN. In comparison to alternative backhauling policies either being QoT-aware or QoT-agnostic, the GeRoFAN-CP exploiting PaGeO achieves an excellent tradeoff between preserving the radio capacity while using efficiently the optical pool. Moreover, we have investigated the compromise that an operator faces between overlaying several radio channels per cell to enable a more flexible management of radio resources between cells and the loss in the effective radio capacity induced by such an overlaying because of the deleterious effect of intermodulation distortions between radio channels.

The focus of Chapter 5 was to extend the capabilities of the GeRoFAN-CP to perform an efficient cellular backhauling in a dynamic and non-uniform traffic context. In such a particular environment, an on-line calculation of the backhauling strategy is required by the CP, a requirement that PaGeO is unable to afford despite its good performance. Instead, we designed for the GeRoFAN-CP a meta-heuristic, called DBS, based on a set of rules exploiting the modeling of the physical layer impairments provided the QoT-tool. The main originality of the DBS is to perform a differentiated backhauling policy that aims at adjusting dynamically the Shannon's capacity in each radio cell according to its actual aggregated traffic load. We carried out extensive simulations that demonstrated the capability of the GeRoFAN-CP using DBS to achieve radio capacity virtualization. Indeed, DBS exploits the gap in the traffic load between cells, inherent to such a dynamic context, to realize a transfer of the radio capacity between them in a similar way to a water filling problem in a system of communicating vessels. In that sense, the relevance of the DBS approach is to perform a kind of a *lean management of the radio capacity*[1] of the mobile system by "piping" the required bandwidth where it is needed at the detriment

---

[1]By analogy to the lean principle that enables an efficient resource management. The objective of a lean strategy is to avoid either a waste or a shortage of capacity by designing a flexible workflow process.

of areas where resources are under-used, thus enabling significant savings/gains for the mobile operator.

The last chapter of the thesis focuses on the business value and the economics of GeRoFAN. From an investment perspective, we highlighted through a comprehensive CapEx/OpEx valuation model the profitability of the GeRoFAN cellular backhauling system compared to a D-RoF WDM-PON network architecture. Two business models, namely a two-tiers and a three-tiers model, structuring the GeRoFAN eco-system were investigated. In both business models, the cellular backhauling service is outsourced either to the GeRoFAN operator (who also deploys and maintains the GeRoFAN network infrastructure) or to a specialized third party called BSP who provides the backhauling service to mobile operators using an optimized backhauling strategy (such as DBS). The economic comparison between the two models showed that the BSP enriches the business value chain gathering the different stake-holders (mobile operator, BSP and GeRoFAN operator) by capitalizing on the competitive advantage offered by its backhauling strategy (DBS) to deliver mobile operators a cellular backhaul with a higher QoS and at lower cost. We concluded our research study by outlining the main issues conditioning the successful implementation of the new business model promoted by GeRoFAN.

8.2 GeRoFAN in the real world

The achievements of the thesis find their application for different players, including the following:

- **Incumbent operators:** Today incumbent operators strive to upgrade their backhauling network at a low cost in order to cope with the continuous increase of the radio traffic. As highlighted by the study from the telecom consultancy company Heavy Reading [38], several mobile carriers across the world are considering the best alternatives to legacy leased T1/E1 backhaul. While an aggressive shift to microwave-based backhauling is considered profitable as short-term solution for several operators[2], the strategic direction will certainly be focused on fiber-based backhauling by means of RoF technology as the most sustainable solution able to accommodate the dramatic increase of the traffic. Such a strategic direction would open new prospects for a unified broadband fixed/mobile convergence. In that sense, the GeRoFAN architecture and its innovative control plane enabling an efficient QoT-aware cellular backhauling is a strong candidate to reinforce the strategic direction of Telcos to evolve their backhaul.

- **Potential new comers/ small operators / MVNOs:** The GeRoFAN concept (system, architecture and the promoted business model) is by excellence a strong ally for new telecom operators entering the market as well as MVNOs. Small carriers, new comers

---

[2]According to Heavy Reading, such a strategy is strongly applied by Vodafone in UK, Sprint in US, SFR in France.

and virtual operators have lower capabilities (they cannot afford the high CapEx of radio network deployment) than incumbent operators. Since the GeRoFAN infrastructure investment is under the responsibility of a third party, the GeRoFAN architecture facilitates the introduction into the market of such long ago considered small players. Thanks to its MAC-agnostic feature, different operators serving different radio technologies can be supported by the GeRoFAN network. Since the investment of all operators (either incumbent or new comers/MVNOs) in the infrastructure is equivalent, innovation in services offered to radio mobile subscribers will be the key factor of differentiation in such a commercial competitive multi-tenants environment.

- **Optical network infrastructure provider:** Optical network infrastructure providers like Syringa[3] in the US or those promoted by the FFTH Council Europe[4] can easily play the role of a GeRoFAN operator. Instead of simply renting out its optical network to broadband FFTx operators, the optical infrastructure provider can reuse its optical network for cellular backhauling as advocated by GeRoFAN. With the current trend of network component cost evolution, we have demonstrated that investing in GeRoFAN is more profitable than an alternative D-RoF WDM-PON architecture. As shown in our research, the optical network infrastructure provider playing the role of a GeRoFAN operator can either act as a backhaul service provider or simply focus its business on a backhaul infrastructure provider.

- **Backhaul Service Provider (BSP):** Several studies like [139] and [38] have pointed out the increasing role expected from the BSP. As highlighted in the thesis, the nature of the BSP evolves from a third party who provides backhaul for mobile operators by renting out its T1/E1 copper line assets to an engineering service company delivering a competitive backhauling service for radio operators with a higher QoS and at lower cost. Either named, according to Heavy Reading [38], as a *Backhaul Network Optimization Consultancy* or a *Backhaul Service Provisioning Company*, the BSP is able to enrich the value chain of the Business-to-Business (B2B) telecom market by outsourcing the backhauling to a specialized player who acts as a broker between its supplier (the GeRoFAN operator) and its customers (mobile operators).

- **Telecom regulators:** As outlined in our research, the GeRoFAN concept supports a new challenging commercial and regulatory environment, with increased interactions between the different stake-holders. The key for a successful implementation of the GeRoFAN ecosystem relies on a full involvement of regulatory authorities and institutions to set up the best practices and implement an efficient legal framework. The role of regulators is crucial

---

[3] *www.syringanetworks.net*

[4] *www.ftthcoucil.eu*

to conceive incentive policies for mutualization according to a suited road-map[5]. In some cases, where large incumbent operators are reluctant to take "the GeRoFAN plunge", it is up to regulators to pave the way for opening the market. In that sense, GeRoFAN could be an attractive solution to achieve that aim.

- **Equipment vendors/Bakchaul technologies suppliers:** They are also concerned by the GeRoFAN solution in particular and the challenges raised by the backhaul in general. As shown in the thesis, one of the key components of the GeRoFAN system is the advantages offered by the reflective electro-absorption amplified modulators. Telecom equipment companies like the *Alcatel-Lucent III-V Lab* sitting at mid-range between research/engineering and business are at the front line to promote the quick introduction into the market of advanced opto-electronic and photonic components able to speed up the road-map for a real implementation of bold architectures like GeRoFAN.

Regarding their level of involvement in the GeRoFAN concept, the aforementioned players are positioned in Figure 8.1 within different circles ranging from directly impacted/involved (inner circles) or indirectly impacted/involved players (outer circles).

8.3 Areas of future works

Thanks to its radio MAC-agnostic CP, the GeRoFAN architecture can be mutualized by several mobile operators exploiting the same or different radio technologies. In such a multi-operator environment, the different carriers may serve the same region and compete together to provide enhanced user-experience for mobile subscribers. Thanks to Cognitive Radio, mobile subscribers use devices equipped with a multi-technology radio-access card which enables them to get an instant access to any radio system being sensed[6]. The different mobile operators compete not only on the market share, but also on two other resources: radio frequencies managed dynamically on a leasing-basis by a radio broker, and optical channels from the WDM pool managed by the GeRoFAN manager. The multi-operator/multi-service GeRoFAN architecture described in Chapter 2 can be the cellular backhauling network platform for such a multi-tenants environment. Unlike the research of this PhD that focuses on the interaction between operators (B2B framework), the future research should include also end-users' expectations. Indeed, end-users are willing to shift at the connection basis between operators looking for the best QoS and the lowest service subscription price. Therefore, the future research deals with

---

[5]See the case of the French Telecom regulator ARCEP in the article published in "Le Monde" written by Cecile Ducourtieux (Service Economie) and entitled "Vers une mutualisation des réseaux" [Towards networks mutualization]: *http://www.lemonde.fr/idees/article/2012/06/13/vers-une-mutualization-des-reseaux_1717636_3232.html*, accessed 06/13 2012.

[6]The different systems are advertised via their beacon radio signals broadcasted within the cells. As a key enabler of Cognitive Radio, Software Defined Radio (SDR) implements by software most signal processing tasks usually carried out in hardware. SDR can serve a wide variety of changing radio protocols in real time and thus enables mobile users to shift seamlessly (even at a connection basis if allowed by the regulatory environment) from one radio technology/operator to another.
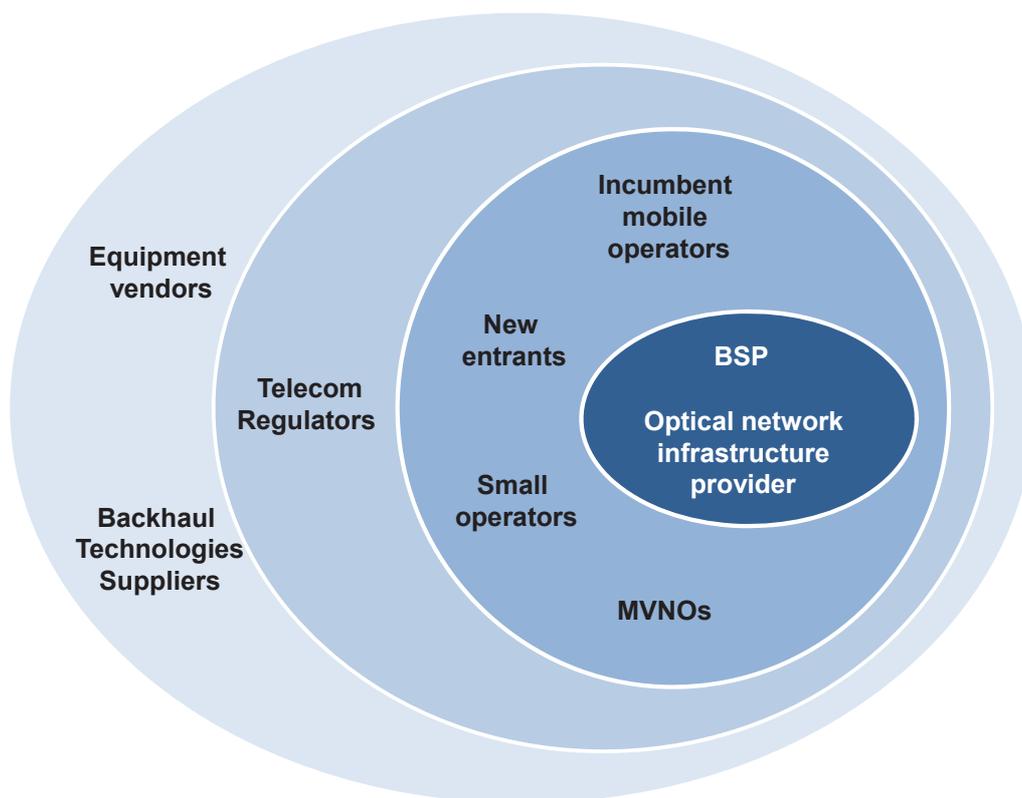
Figure 8.1: Positioning the different players impacted/involved in the GeRoFAN concept.

two overlaying interaction frameworks: B2B (interactions between mobile operators/GeRoFAN manager/Radio broker) and B2C (Business-to-Customer interactions orchestrating the relations between the mobile operators and their "potential"[7] customers). In that sense, the results of the current research can be exploited as a valuable input together with mathematical models like **Game Theory** techniques managing the strategies adopted by the different players involved in the B2B interaction framework. While **Utility Functions enriched with a Learning Process**[8] describing the behavior of the mobile users can be used to orchestrate the B2C framework.

---

[7] So called because of their ability to shift from one operator to a competitor (offering a better QoS or/and a more attractive service price). Hence, operators are constantly challenged to offer a more attractive service in order to retain their customers as long as possible and thus to lead the competition.

[8] A machine learning process makes utility functions evolve with time. In fact, one can imagine that mobile users are not totally agnostic during their interactions with the different mobile operators. Indeed, a mobile operator who "disappoints" a given customer for several times, would be penalized (by appropriately weighing the utility function) in the next round choice of that customer. Although more complicated to model and implement, Utility function including a learning process enables to translate the perceived QoS (*a.k.a* Quality of Experience) by the customer as the latter learns from his/her previous experience and modifies his/her objective accordingly. A learning process-based Utility function ensures also a minimum stability of the system by avoiding the "ping-pong" effect caused by the excessive move of subscribers between operators.

Appendix

A.1 EAM Analytical Modeling

Figure A.1 illustrates the methodology followed for EAM analytical modeling. Considering the case of a Multi-Quantum Well (MQW)-EA modulator, the absorption coefficient α is Voltage (V)-dependant and optical carrier (λ)-dependant. For simplicity, only the ground state heavy/light-hole (E_1-(H/L)H_1) energy transition is considered in the model since it is expected to be the major participant in the photo-absorption process [49]. We describe in the following the different steps to compute α. The mathematical development is inspired from a semi-empirical model proposed in [84][152] for MQW-based modulators.

First, the unperturbed (ground-state) wave-functions of electrons and holes (heavy/light) Ψ_x^o and their energies E_x^o are computed from the Schrodinger equation, where x denotes the considered particle (*i.e.* e, lh and hh for electron, light hole and heavy hole respectively). Assuming that modulator layers are piled up along the z axis, the unperturbed Hamiltonian H_o is provided by Equation A.1:

$$H_o(\Psi_x^o) = E_x^o \cdot \Psi_x^o = \frac{-\hbar^2}{2m_{x,b/w}^*} \cdot \frac{-\mathrm{d}^2 \Psi_x^o}{d^2 z} + V_x(z) \cdot \Psi_x^o(z) \tag{A.1}$$

Given: $m_{x,b/w}^*$ the effective mass of particle x at the barrier (b) or the well (w); $V_x(z)$ the electric potential seen by particle x at z and $\hbar$ the reduced Planck constant.

Solutions of Equation A.1 for the steady-state are the superposition of two plane-waves, an incident wave and a reflected wave. Depending on the location of the particle, the wave expression is:

$$\Psi_x^o(z) = \begin{cases} A \cdot \exp\left(\jmath k_x z\right) + B \cdot \exp\left(-\jmath k_x z\right) & \text{for a well-located particle} \\ A' \cdot \exp\left(\jmath K_x z\right) + B' \cdot \exp\left(-\jmath K_x z\right) & \text{for a barrier-located barrier} \end{cases} \tag{A.2}$$

Given: $k_x = \sqrt{(\frac{2m_{x,w}^*}{\hbar^2})(E_x^o - V_x(z))}$ and $K_x = \sqrt{(\frac{2m_{x,b}^*}{\hbar^2})(V_x(z) - E_x^o)}$ the wave-numbers for particle x respectively within the well and the barrier; A, B, A' and B' are constants and $\jmath$ the complex number ($\jmath^2 = -1$).

In a QW modulator, a rectangular potential is assumed and expressed as function of the gap-energy of each quantum layer. Assuming that only an evanescing wave is considered within
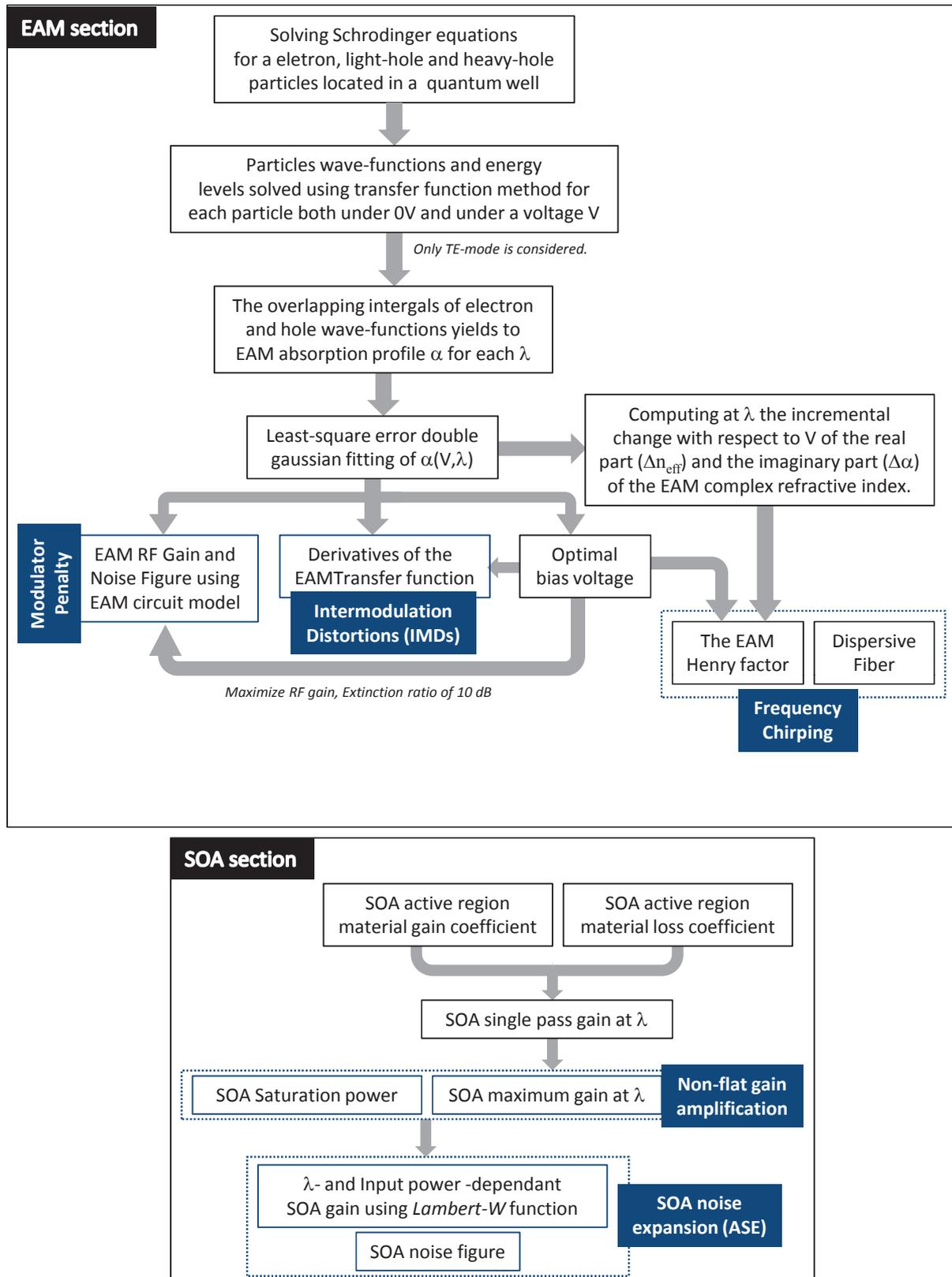
Figure A.1: Methodology of EAM-SOA analytical modeling.

We follow a step-by-step modeling methodology inspired from [52] and [28] to get an analytical formulation of the working principle of the REAMSOA. One of the key aspect of the model is to highlight the dependance with the optical wavelength, that will be exploited for the optimization carried out by the GeRoFAN control plane. EAMSOA-induced major impairments are also highlighted in blue.

the barrier and only propagating waves within the well, the wave-function is written depending on the location of the particle as the following Equation system A.3:

$$
\begin{cases}
\Psi^o_{1,x}(z) = a \cdot \exp\left(K_x z\right) & z \leq -\frac{\ell_w}{2} \\
\Psi^o_{2,x}(z) = b \cdot \exp\left(\jmath k_x z\right) \pm \exp\left(-\jmath k_x z\right) & -\frac{\ell_w}{2} \leq z \leq \frac{\ell_w}{2} \\
\Psi^o_{3,x}(z) = -a \cdot \exp\left(-K_x z\right) & z \geq \frac{\ell_w}{2}
\end{cases}
\tag{A.3}
$$

Where: ℓ_w the width of the quantum well; a and b are real constants.

The equation system A.3 shows the superposition of two possible solutions within the well, a symmetric (*i.e.* when: $\Psi^o_{2,x}(z) = b \cdot \cos(k_x z)$) or asymmetric propagating wave (*i.e.* when: $\Psi^o_{2,x}(z) = b \cdot \sin(k_x z)$).

In a quantum-well, the energy level is quantized. To compute the discrete energy levels for a given particle x, we exploit the continuity condition of the wave-function Ψ^o_x and its first derivative $\frac{d\Psi^o_x}{dz}$ at the well/barrier boundaries (i.e. at $z = \pm \ell_w/2$), thus leading to $K_x = k_x \cdot \tan(\frac{k_x \ell_w}{2})$ and $K_x = -k_x \cdot \cot(\frac{k_x \ell_w}{2})$ for symmetric solutions and asymmetric solutions respectively. Equations of wave-numbers for symmetric and asymmetric solutions are solved graphically for each particle to find energy levels E^o_x. We use the normalization constraint related to the probability density function (*i.e* $\int_{-\infty}^{+\infty} |\Psi^o_x|^2 dz = 1$) to find the value of constants a and b.

We apply our analytical model on an EAM designed by the joint-venture Alcatel-Thales III-V Lab [39]. The modulator is made of 10 quantum wells and 11 barriers with the following features:

- Barrier: $Al_{210}Ga_{190}In_{600}As$ with width $\ell_b = 9.4\ nm$.

- Well: $Ga_{517}In_{483}As$ with width $\ell_w = 9.4\ nm$.

The band-gap energy $Eg_{b,x}$ and $Eg_{w,x}$ for particle x in the barrier and well respectively are computed by taking into account the alloy composition of both well and barrier materials using the method presented in [54]. Related data at room temperature including the energy gap of basic elements (Ga, In, Al and As), Luttinger parameters for particle effective masses in the well and the barrier are extracted from [53]. Wave-functions and energy levels of a given particle x at each quantum level in the absence of external field (*i.e* $F = 0$) are summarized in Table A.1. Figure A.2 depicts first quantum level unperturbed wave-functions of each particle for 1550 nm.

Given I_x the number of energy levels of particle x (*i.e* $I_e = 2$, $I_{lh} = 2$ and $I_{hh} = 4$), the set of wave-functions $\Psi^o_{x_i(1 \leq i \leq I_x)}$ shown in Table A.1 form a orthonormal basis of a vector sub-space of $\mathcal{L}^2$[1], *i.e.* for a given particle x and quantum level i and j, $\int_{-\infty}^{+\infty} \Psi^o_{x_i} \cdot \Psi^o_{x_j} dz = \delta_{ij}$[2]

With an applied electric field F, the perturbed Hamiltonian is written as in Equation A.4:

---

[1] $\mathcal{L}^2$: Hilbert space, i.e vector space of 2nd power integrable functions.

[2] δ_{ij} stands for the Kronecker notation: $\delta_{ij} = 1$ if ($i = j$) and 0 otherwise.

Table A.1: Wave-functions and energy levels for each particle at 0 V.

x_i	E_x^o (eV)	$\Psi_x^o(z)$ (well)	$\Psi_x^o(z)$ (barrier)
e_1	0.4115	$1.2206 \cdot 10^4 \cdot \cos(2.361 \cdot 10^8 \cdot z)$	$9.5473 \cdot 10^4 \cdot \exp(\pm 6.0993 \cdot 10^8 \cdot z)$
e_2	0.567	$1.1723 \cdot 10^4 \cdot \sin(4.828 \cdot 10^8 \cdot z)$	$\pm 5.323 \cdot 10^4 \cdot \exp(\pm 3.782 \cdot 10^8 \cdot z)$
lh_1	-0.3701	$1.1212 \cdot 10^4 \cdot \cos(2.0795 \cdot 10^8 \cdot z)$	$2.6291 \cdot 10^4 \cdot \exp(\pm 3.0489 \cdot 10^8 \cdot z)$
lh_2	-0.4528	$7.8696 \cdot 10^3 \cdot \sin(3.673 \cdot 10^8 \cdot z)$	$\pm 1.1784 \cdot 10^4 \cdot \exp(\pm 8.848 \cdot 10^7 \cdot z)$
hh_1	-0.3623	$1.2807 \cdot 10^4 \cdot \cos(8.2099 \cdot 10^8 \cdot z)$	$-2.7907 \cdot 10^5 \cdot \exp(\pm 7.1579 \cdot 10^8 \cdot z)$
hh_2	-0.41334	$1.0343 \cdot 10^4 \cdot \sin(1.0557 \cdot 10^9 \cdot z)$	$\pm 2.7201 \cdot 10^4 \cdot \exp(\pm 2.124 \cdot 10^8 \cdot z)$
hh_3	-0.4524	$1.3304 \cdot 10^4 \cdot \cos(2.7906 \cdot 10^8 \cdot z)$	$5.0816 \cdot 10^5 \cdot \exp(\pm 1.0647 \cdot 10^9 \cdot z)$
hh_4	-0.4781	$1.3173 \cdot 10^4 \cdot \sin(5.549 \cdot 10^8 \cdot z)$	$\pm 5.673 \cdot 10^5 \cdot \exp(\pm 9.447 \cdot 10^8 \cdot z)$
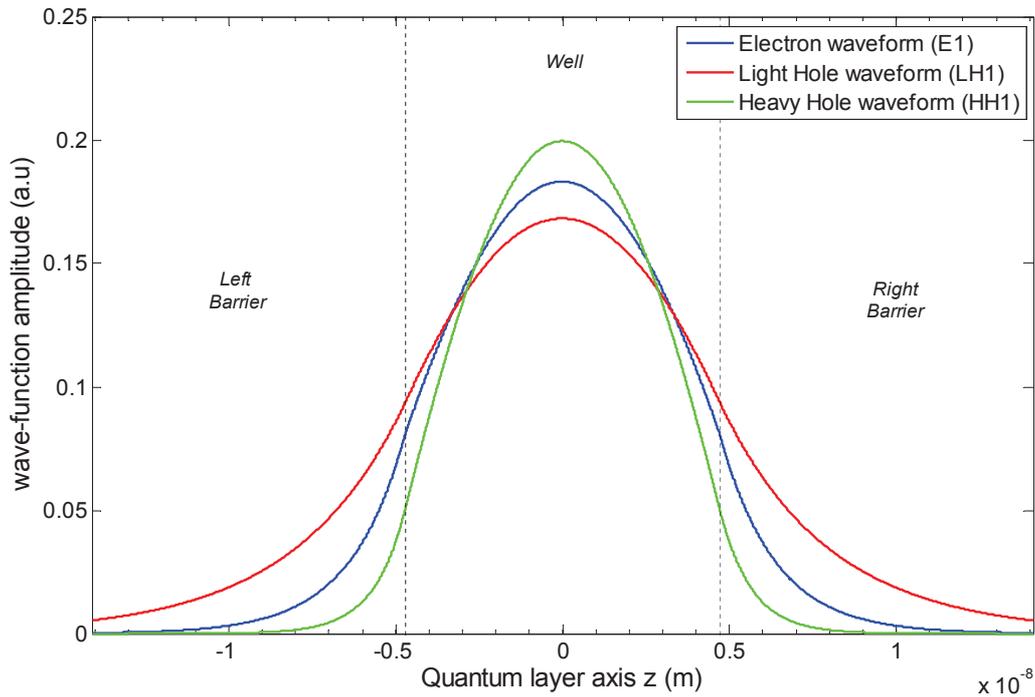
Figure A.2: Wave-functions of the QW-EAM for 1550 nm incident light under 0 V

At 0 V, wave-function of particles are confined within the well while evanescing waves at the barrier point out the low probability to find electrons and holes in that region (tunneling effect through the barrier is neglected). Only first energy level for each particle is illustrated in the figure.
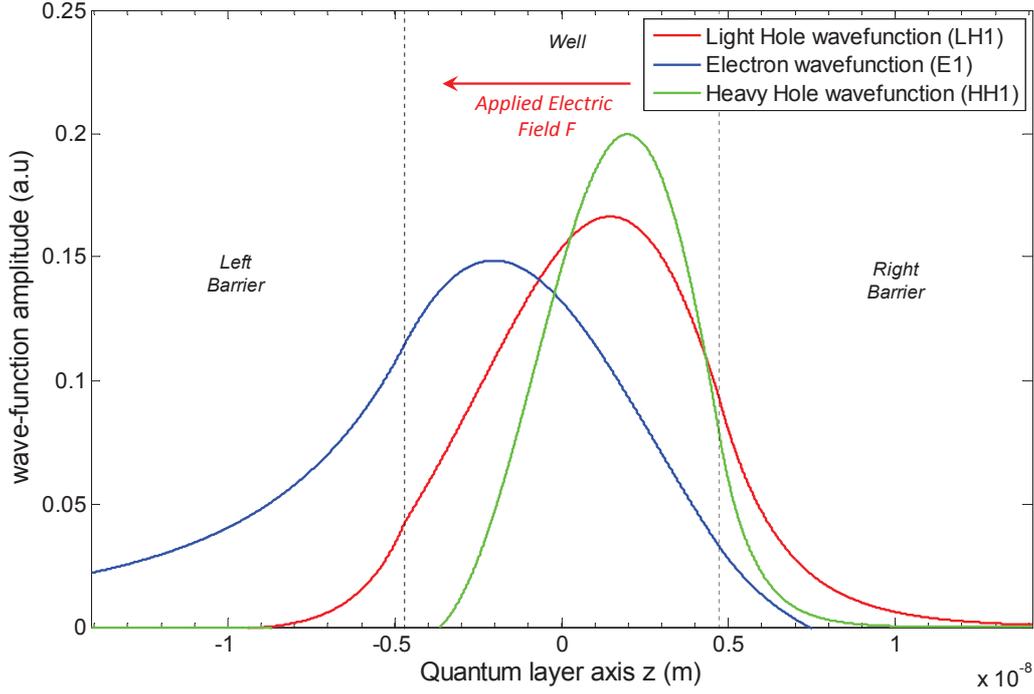
Figure A.3: Wave-functions for 1550 nm incident light under -3 V

Biasing the device creates a perpendicular electric field F that stretches the electron-hole pair. Wave-functions are pushed towards each side of the barrier. The field-induced electron-hole spatial separation is at the basis of the decrease of the luminescence of the EAM and a change of its absorption profile (*cf.* Figure A.4)

$$H_o(\Psi_x^F) = E_x^F \cdot \Psi_x^F = \frac{-\hbar^2}{2m_{x,b/w}^*} \cdot \frac{\mathrm{d}^2\Psi_x^F}{d^2 z} + (V_x(z) \pm q_e F z) \cdot \Psi_x^F(z) \tag{A.4}$$

Where: q_e the electron charge.

Solutions of Equation A.4 can be expressed in their vectorial form: $\Psi_x^F = \sum_{i=1}^{I_x} a_{x,i}^F \cdot \Psi_{x_i}^o$ given the normalization condition: $\sum_{i=1}^{I_x} |a_{x,i}|^2 = 1$.

By substituting the vectorial form of $\Psi_{x_i}^F$ into Equation A.4, the mathematical development leads to the linear system expressed by Equation A.5. Thus, E_x^F and $a_{x,i}^F$ are respectively the eigenvalues and the eigenvectors of the Hamiltonian matrix. Figure A.3 illustrates the particles wave-functions for 1550 nm incident light and under -3 V applied bias voltage.

$$\begin{pmatrix} E_{x_1}^o + \int_{-\infty}^{+\infty} \Psi_{x_1}^o(\pm q_e Fz)\Psi_{x_1}^o\mathrm{d}z & \cdots & E_{x_1}^o + \int_{-\infty}^{+\infty} \Psi_{x_1}^o(\pm q_e Fz)\Psi_{x_{I_x}}^o\mathrm{d}z \\ \vdots & \ddots & \vdots \\ E_{x_{I_x}}^o + \int_{-\infty}^{+\infty} \Psi_{x_{I_x}}^o(\pm q_e Fz)\Psi_{x_1}^o\mathrm{d}z & \cdots & E_{x_{I_x}}^o + \int_{-\infty}^{+\infty} \Psi_{x_{I_x}}^o(\pm q_e Fz)\Psi_{x_{I_x}}^o\mathrm{d}z \end{pmatrix} \bullet \begin{pmatrix} a_{x_1}^F \\ \vdots \\ a_{x_{I_x}}^F \end{pmatrix} = E_x^F \cdot \begin{pmatrix} a_{x_1}^F \\ \vdots \\ a_{x_{I_x}}^F \end{pmatrix} \tag{A.5}$$

Because two kinds of holes are considered in the model (light/heavy holes), the absorption process in the quantum well is driven by two coupled excitons called bi-exciton. We characterize numerically each exciton separately by computing their oscillator strength, their line-width enhancement and Stark-energy shift (exciton resonance wavelength λ_{ex}). The exciton resonance
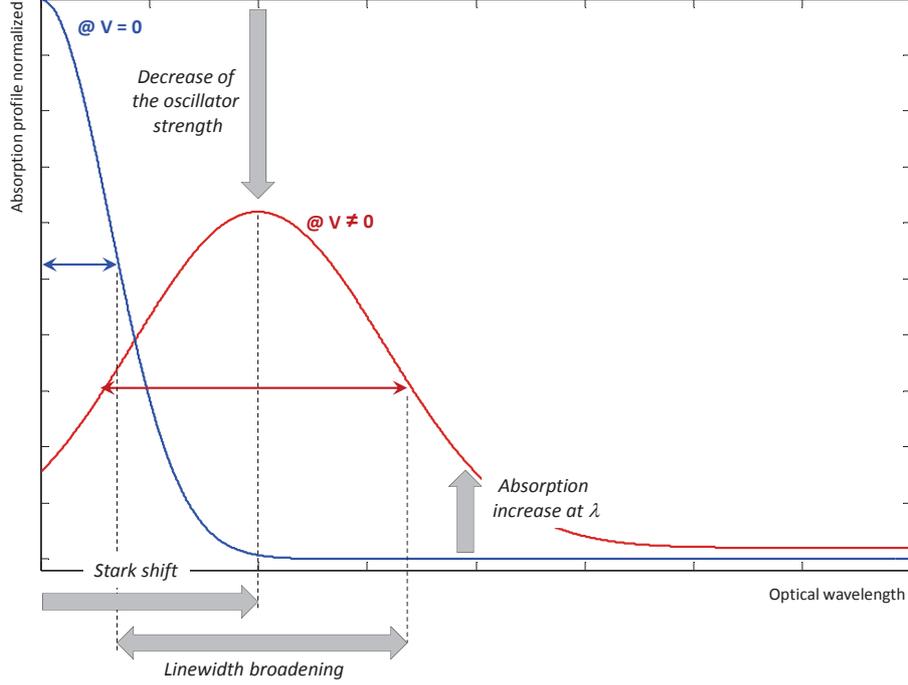
Figure A.4: Illustration of a single exciton Stark shift under an applied voltage.

Applying an external field causes a red shift of the absorption profile of the EAM. The exciton is "stretched" due to the spatial separation between electrons and holes. The Quantum Confined Stark shift Effect (QCSE) effect is characterized also by a decrease of the oscillator strength, a broadening of the linewidth and a slight increase of the absorption coefficient at a given optical wavelength. The optimal performance of the device (higher extinction ratio, higher RF gain) is achieved by adjusting the right bias.

wavelength is related to the QW gap energy E_g^w (computed as in [54]) and exciton biding energy $E_{b,ex}$ (assumed as in [49]) as: $hc/\lambda_{ex} = E_g^w + E_e^F + E_{lh/hh}^F - E_{b,ex}$. Following the suggestion of Miller *et al.* in [49], we describe the absorption profile of an exciton in a MQW by a Gaussian shape rather than a Lorentzian. With the approach of [27], the absorption coefficient under external field F at a given wavelength λ is expressed empirically through Equation A.6:

$$\alpha_{lh/hh}^F(\lambda) = A \cdot f_{lh/hh}^F \cdot G_{lh/hh}^F(\lambda) + \alpha_{bulk} \tag{A.6}$$

Where: A: a constant independent of the applied electric field F; α_{bulk}: background absorption approximated as the bulk material absorption; $f_{lh/hh}^F$: the oscillator strength of the exciton (e/lh,e/hh) par unit volume is proportional to overlapping integrals between electron and hole wave-functions as formulated in Equation A.7; $G_{lh/hh}^F$: The line-shape at an applied field F modeled at room temperature by a Gaussian function as in Equation A.8.

$$f_{lh/hh}^F = \frac{|U_{lh/hh}(0)| \cdot | \int_{-\infty}^{+\infty} \Psi_e^F \cdot \Psi_{lh/hh}^F \mathrm{d}z |^2}{\ell_w + \ell_b}. \tag{A.7}$$

Given: $U_{lh/hh}(0) = \sqrt{\frac{2}{\pi R_B^2}}$: the bi-exciton (e/lh, e/hh) envelope function evaluated at the origin relative coordinate and function of the Bohr radius of the exciton [19].

The absorption coefficient line-shape is given by Equation A.8:

$$G_{lh/hh}^F(\lambda) = \sqrt{\frac{\ln 2}{\pi}} \cdot \frac{1}{\Upsilon_{lh/hh}^F} \cdot \exp\left(-\ln 2 \cdot \left(\frac{hc\left(\frac{1}{\lambda_{ex}} - \frac{1}{\lambda}\right)}{\Upsilon_{lh/hh}^F}\right)^2\right) \tag{A.8}$$

Given: $\Upsilon_{lh/hh}^F$: The Half-Width Half-Maximum (HWHM) line-width of the (e/lh,e/hh) exciton when F is applied.

As illustrated by Figure A.4, the effect of an applied field F on the exciton resonance is to cause a red shift of the absorption curve (*i.e* shift of λ_{ex} to longer wavelengths) and a decrease in the oscillator strength. The line-width of the absorption curve, related to the lifetime of the excited state, is also broadened due to three mechanisms: on one hand, a homogenous broadening due to interaction (scattering) with optical phonons, on the other hand, an inhomogeneous broadening due to well width fluctuations and variations in the electric field from well to well. Although the homogenous broadening is assumed to be constant with the applied electric field (estimated to $\simeq 6.27\ meV$ according to [52]), the inhomogeneous broadening is modeled analytically as in [52], while the expression of the exciton energy is deduced from the approximation of energy shift of the ground state given by the variational calculations carried out by Bastard in [14]. Although a compressive strain has been applied to the MQW material to achieve optical polarization independence [95], only TE-mode incident light-waves are considered in the model. The absorption coefficient in TE-mode under an applied electric field F is expressed according to Equation A.9 as a weighted sum of the e/lh and e/hh absorption coefficients [75]:

$$\alpha_{TE}^F = \frac{\alpha_{hh}^F}{4} + \frac{3 \cdot \alpha_{lh}^F}{4} \tag{A.9}$$

Figure A.5 gives the set of absorption curves computed for TE-mode with an incident light wavelength from 1525 nm to 1600 nm under the application of a reverse bias voltage V_b.

To study the linearity of the modulator, we fit through Equation A.10 the absorption profile (with respect to V_b) at each optical channel with a double Gaussian fit function of the form:

$$\alpha(V_b, \lambda) = A_\lambda \cdot \exp\left(\frac{(V_b - F_\lambda)^2}{B_\lambda}\right) + C_\lambda \cdot \exp\left(\frac{(V_b - G_\lambda)^2}{D_\lambda}\right) + E_\lambda \tag{A.10}$$

Where: A_λ, B_λ, C_λ, D_λ, E_λ, F_λ and G_λ are λ-dependant fitting parameters

Figure A.6 shows as an example fitted absorption coefficient for 1530 nm and 1580 nm optical channels. The list of the different fitting parameters of 16 optical channels ranging from 1525 nm to 1600 nm is presented in Table A.2.

A.2 EAM chirp analytical modeling

The refractive index of the EAM is a complex number whose imaginary part stands for the absorption coefficient determined analytically in Section A.1. The real part of the refractive index
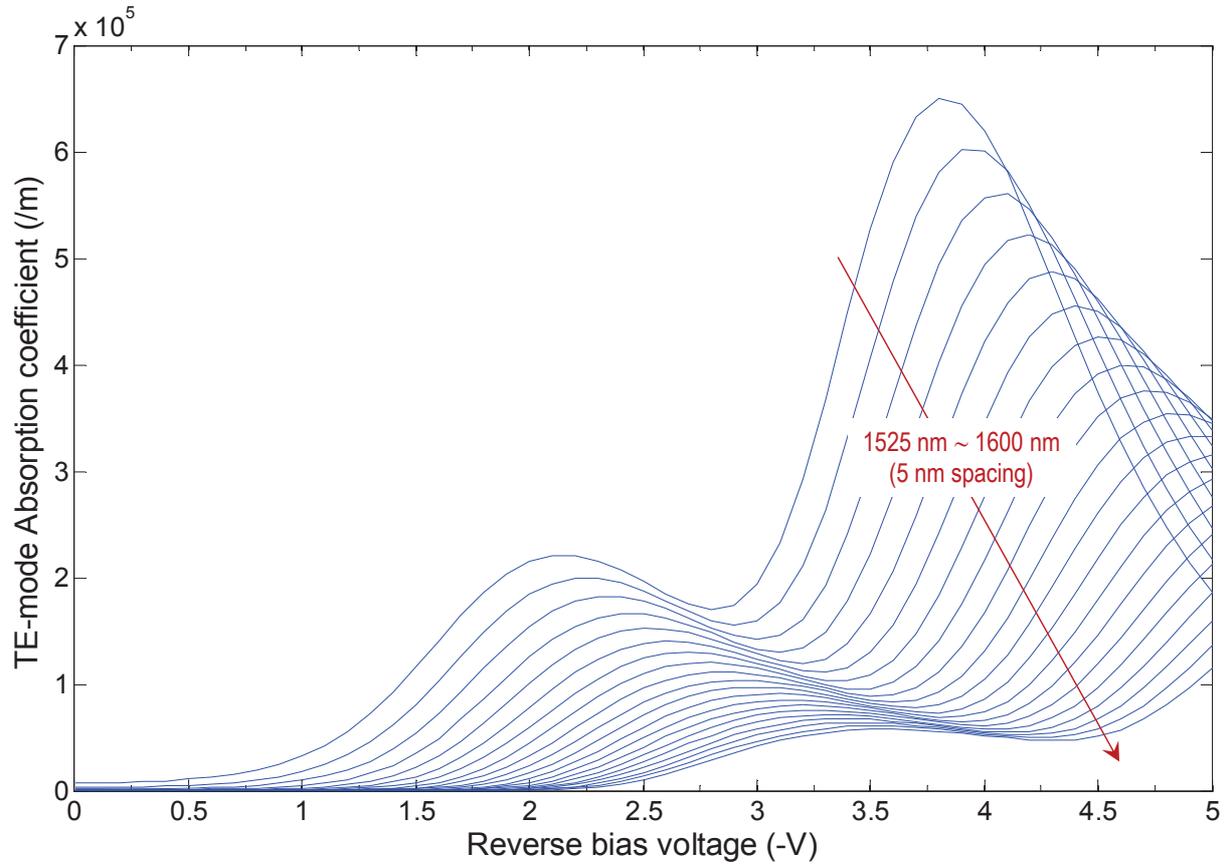
Figure A.5: MQW-EAM absorption coefficient profile from 1525 nm to 1600 nm.

The TE-mode absorption profile of the MQW-EAM is a weighted sum of both light hole and heavy hole exciton absorptions. The highest absorption is achieved at the resonance of the E-LH exciton.

Table A.2: MQW-EA modulator fitting parameters

λ nm	$A_\lambda(\times 10^5)$	$B_\lambda(\times 10^5)$	$C_\lambda(\times 10^5)$	$D_\lambda(\times 10^5)$	$E_\lambda(\times 10^5)$	$F_\lambda(\times 10^5)$	$G_\lambda(\times 10^5)$
1525	6.958	-0.4256	2.306	-0.5988	0.161	3.719	2.032
1530	6.48	-0.4143	2.157	-0.6172	0.07529	3.826	2.152
1535	6.006	-0.4063	1.999	-0.6259	0.02996	3.928	2.262
1540	5.544	-0.4065	1.845	-0.6266	0.007714	4030	2.364
1545	5.160	-0.4235	1.699	-0.6198	-0.002244	4.142	2.456
1550	5.004	-0.4797	1.563	-0.6043	-0.005739	4291	2.538
1555	5.808	-0.6681	1.431	-0.5764	-0.005866	4591	2.605
1560	4.880	-0.2055	1.277	-0.5348	-0.004531	6.332	2.649
1565	3.1380	-0.5787	1.164	-0.5366	-0.005158	11.13	2.722
1570	2.4122	-6.714	1.080	-0.5413	-0.005126	12.26	2.797
1575	1.9002	-8.816	0.9871	-0.5311	-0.004546	13.94	2.857
1580	1.647	-3.563	0.8967	-0.5100	-0.003261	7.196	2.904
1585	1.330	-1.749	0.7957	-0.4747	-0.001692	4.985	2.932
1590	07050	-1.129	0.6895	-0.4341	-0.0002721	4.266	2.947
1595	0.6064	-0.9146	0.5766	-0.3919	0.0007817	3.983	2.953
1600	0.5830	-0.7881	0.4934	-0.3615	0.001519	3.871	2.967
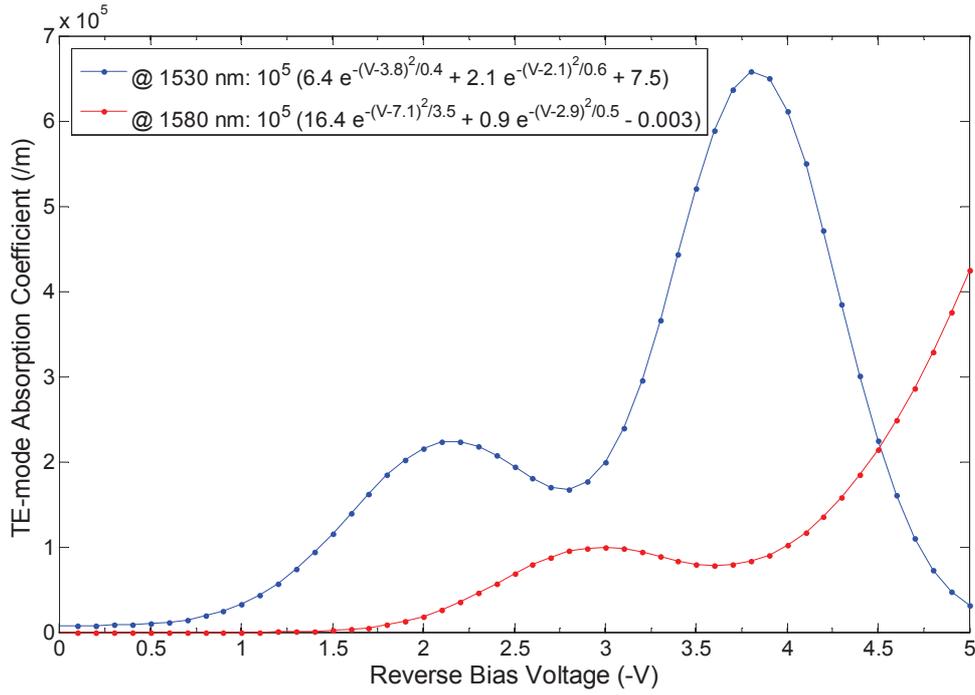
Figure A.6: Best fit expressions for EAM absorption profiles at 1530 and 1580 nm.

A least-square error double-Gaussian (one for each exciton) function is used to best-fit the absorption coefficient of the modulator [49]. Fitting parameters are accurately tuned to reproduce faithfully the shape of the absorption profile while ensuring a stable behavior of its derivatives.

of the modulator is computed by taking into account the composite nature of the absorption material layer of the device. To compute the effective (real part) of the EAM refractive index, we apply the method depicted in [86]. Including the optical confinement factor Γ^{eam} of the EAM (restricting the analysis only to TE-mode for simplicity), the effective refractive index of the absorption layer is computed according to Equation A.11:

$$n_{eff} = \sqrt{n_o^2 + \left((n_i^2 - n_o^2) \cdot \frac{\Gamma^{eam}}{2 - \Gamma^{eam}} \right)} \tag{A.11}$$

Given: n_o, n_i are respectively the refractive index of the cladding layer and the the absorption layer of the MQW-EAM waveguide.

Frequency chirping is commonly expressed by the line-width enhancement factor (*a.k.a* Henry factor α_H and chirp parameter) and the modulation waveform. The Henry factor, describing the sensitivity of the AM-FM conversion chirping phenomenon, is defined as the relative variation of the real part of the refractive index of the EAM with respect to its imaginary part [155]. Following the extensive analysis of Yamamoto *et al.* [152] and using results of energy levels of electrons and holes under an external field F (see Section A.1), we derive the values of the Henry factor at different optical channels. We should notice that because of the dependence of the chirp parameter with the bias voltage (the external electric field F), the values of α_H that will be assumed for the remaining of the model are those computed at optimal bias V_b^*.
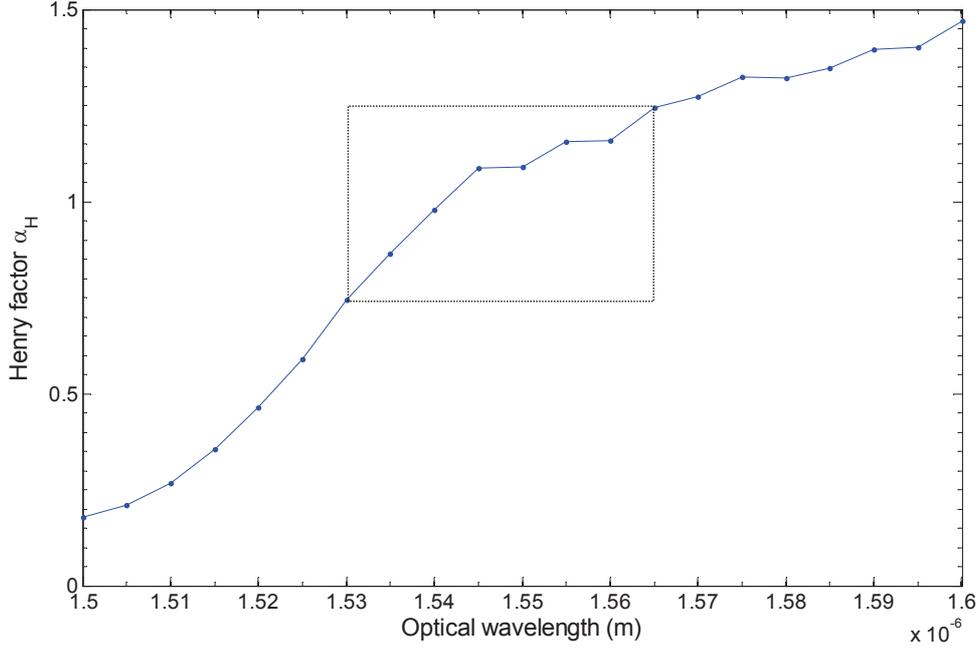
Figure A.7: EAM Henry factor (α_H) as function of photon wavelength.

Compared to semiconductor-based lasers and SOA modulators, EAMs show lower chirp factor (when it is appropriately biased, an EAM can feature a slightly negative chirp ideal for long haul optical transmission). At optimal bias voltage, the chirp parameter of our EAM varies within the range $0.7 \sim 1.2$ for the conventional C-band (*cf.* squared area in the figure).

Figure A.7 illustrates the evolution of α_H at V_b^* with optical wavelength.

According to [74], the chirping factor is related to the frequency excursion χ and the optical power at the output of the modulator P_{out} as in Equation A.12:

$$\chi = \frac{1}{2\pi} \cdot \frac{\mathrm{d}\Phi}{\mathrm{d}I} = \frac{\alpha_H}{4\pi P_{out}} \cdot \frac{\mathrm{d}P_{out}}{\mathrm{d}I} \tag{A.12}$$

Giving that: $P_{out} = \mathfrak{f}P_{in}$, where $\mathfrak{f}$ the EAM transfer function and $V = Z_m \cdot I$, where Z_m the modulator impedance; the expression of χ is further simplified leading to Equation A.13:

$$\chi = \frac{\alpha_H Z_m}{4\pi} \cdot \frac{\mathfrak{f}'(V_b)}{\mathfrak{f}(V_b)} \tag{A.13}$$

The optical field at the output of the modulator is expressed as: $v(t) = \sqrt{2\mathfrak{f}(V)P_{in}} \cos(w_o t + \Phi(t))$ given: $V = V_b(1 + x(t))$ the AC modulating voltage expressed with the RF signal $x(t)$; w_o the optical carrier angular frequency and $\Phi(t)$ the angular frequency excursion of the optical signal due to chirping. Supported by the analysis in [15] and the result of Equation A.13, Φ is expressed as: $\Phi(t) = \frac{V_b \alpha_H}{2} \frac{\mathfrak{f}'}{\mathfrak{f}} \int_t x(\xi)\mathrm{d}\xi$. Following the steps of the analysis carried out by Betti *et al.* in [15], the optical field $u(t)$ at the output of the fiber of impulse response h is given by:

$$u(t) = \sqrt{2P_{in}} \cdot \Re\left\{ e^{(\jmath(w_o t + \Phi(t)))} \cdot \int_{\mathbb{R}} h(\tau)\sqrt{\mathfrak{f}(V(t-\tau))} e^{(-\jmath(w_o \tau + \Phi(\tau) - \Phi(t-\tau)))}\mathrm{d}\tau \right\} \tag{A.14}$$

We expand both $\sqrt{\mathfrak{f}(V(t-\tau))}$ and $\sqrt{\alpha(t-\tau)}$ into polynomial series up to the third order (higher terms of the expansion are neglected because of the high bandwidth of the fiber medium). We introduce $H(\Omega) = 10^{\frac{-aL}{2}} e^{\left(-J\frac{\beta\Omega^2}{2\alpha_H V_b}\right)}$ the Fourier transform of $h(t)$ given the coefficient $\beta = \frac{-DL\lambda_o^2\alpha_H V_b}{c}$, the optical wavelength λ_o, the optical distance L, the fiber attenuation coefficient a and the fiber dispersion coefficient D. The expression of the output signal becomes:

$$u(t) = \sqrt{2P_{in}} \cdot \Re\left\{ e^{(J(w_o t + \Phi(\tau)))} \right.$$

$$\left. \cdot \left(g(t)H(\Omega) + g'(t)\frac{\mathrm{d}H}{\mathrm{d}(J\Omega)} + \frac{\mathrm{d}^2 H}{\mathrm{d}(J\Omega)^2}\frac{g''(t) + J\Phi''g}{2} + \frac{\mathrm{d}^3 H}{\mathrm{d}(J\Omega)^3} \right) \right\} \tag{A.15}$$

Where: $g = \sqrt{\mathfrak{f}}$ and g', g'' and g''' (respectively Φ', Φ'' and Φ''') first, second and third derivatives of g (respectively Φ).

Given the dependance of g on V, we derive the expression of the first three derivatives of g as function of the derivatives of V as the following:

$$g' = a_1 \cdot V' \tag{A.16}$$

$$g'' = a_1 \cdot V'' + a_2 \cdot V' \tag{A.17}$$

$$g''' = a_1 \cdot V''' + a_2 \cdot V'' + a_3 \cdot V' \tag{A.18}$$

While the coefficients a_1, a_2 and a_3 are computed at bias point as:

$$a_1 = \left.\frac{\mathfrak{f}'}{2g}\right|_{V_b} \tag{A.19}$$

$$a_2 = \left.\frac{\mathfrak{f}''\mathfrak{f} - \mathfrak{f}'}{2g^3}\right|_{V_b} \tag{A.20}$$

$$a_3 = \left.\frac{3\mathfrak{f}'^2 - 2\mathfrak{f}''\mathfrak{f} + 4\mathfrak{f}'''\mathfrak{f}^2 - 2\mathfrak{f}''\mathfrak{f}'\mathfrak{f}}{8g^5}\right|_{V_b} \tag{A.21}$$

Given that: $\frac{\mathrm{d}^n H}{\mathrm{d}(J\Omega)^n} = (-1)^n \int_{\mathbb{R}} h(\nu)\nu^n e^{-J\Omega\nu}\mathrm{d}\nu$ and considering the same assumptions as in [15] (*i.e.* $e^{-J\frac{\beta\Omega^2}{2\alpha_H V_b}} \approx 1$), we focus along the mathematical development only on the real part of $u(t)$ which leads to:

$$u(t) \simeq \sqrt{2P_{in}} \cdot 10^{\frac{-aL}{2}} \cdot \left(g - \beta g' x - \frac{g''\beta^2 x^2}{2} - \frac{\Phi'' g\beta}{4\pi\alpha_H V_b} \right.$$

$$\left. - \frac{g'''\beta^3 x^3}{6} + \frac{3\beta^2 x}{4} \cdot \frac{\Phi'' g' + \frac{\Phi''' g}{3}}{\alpha_H \pi V_b} \right) \cdot \cos(w_o t)\cos(\Phi) \tag{A.22}$$

To highlight IMD and HD components induced by chirping, we carry out a multi-tone analysis. The modulating signal $x(t)$ is expressed as a mix of 3 RF signals with angular frequencies

w_i and OMI m_i, thus: $x(t) = \sum_{i=1}^{3} m_i \cos(w_i t)$. Substituting the SCM formulation of x into Equation A.22, we get:

$$u(t) \simeq \sqrt{2P_{in}} \cdot 10^{\frac{-aL}{2}} \cos(\Phi) \cdot \left(DC + \left(\sum_i I_i \cos(w_i t) + Q_i \sin(w_i t) \right) \right.$$

$$+ \left(\sum_i I_{2i} \cos(2w_i t) + Q_{2i} \sin(2w_i t) \right) + \left(\sum_{i,j} I_{i \pm j} \cos(w_i \pm w_j t) + Q_{i \pm j} \sin(w_i \pm w_j t) \right)$$

$$+ \left(\sum_i I_{3i} \cos(3w_i t) + Q_{3i} \sin(3w_i t) \right) + \left(\sum_{i,j} I_{2i \pm j} \cos(2w_i \pm w_j t) + Q_{2i \pm j} \sin(2w_i \pm w_j t) \right)$$

$$\left. + \left(\sum_{i,j,k} I_{i \pm j \pm k} \cos(w_i \pm w_j \pm w_k t) + Q_{i \pm j \pm k} \sin(w_i \pm w_j \pm w_k t) \right) + \cdots \right)$$

$$(A.23)$$

Given: I_ℓ and Q_ℓ are the in-phase and quadrature phase amplitudes of the signal and its chirp-induced IMD/HDs falling at frequency component ℓ. Specifically, for the case of IMD3 noise we obtain:

- For IMD3 with 2 tones falling at $w_\ell = 2w_i - w_j$:

$$I_{2i-j} = a_1 \beta^2 V_b \cdot m_i^2 m_j \cdot (w_i^2 + \frac{w_j^2}{2}) + 3a_1 \beta^2 V_b \cdot m_i^2 m_j \cdot w_i (w_j - \frac{w_i}{2}) \qquad (A.24a)$$

$$Q_{2i-j} = a_2 \beta^2 V_b \cdot m_i^2 m_j w_i (w_i - \frac{w_j}{2}) \qquad (A.24b)$$

- For IMD3 with 3 tones falling at $w_\ell = w_i - w_j + w_k$:

$$I_{i-j+k} = a_1 \beta^2 V_b \cdot m_i m_j m_k \cdot (w_i^2 + w_j^2 + w_k^2) + 3a_1 \beta^2 V_b \cdot m_i m_j m_k \cdot (w_j w_i + w_j w_k - w_i w_k) \quad (A.25a)$$

$$Q_{i-j+k} = a_2 \beta^2 V_b \cdot m_i m_j m_k \cdot w_i (w_i + w_j + w_k) \qquad (A.25b)$$

The average chirp-induced IMD/HD optical noise power N_{opt} is computed as: $N_{opt} = \langle |u|^2 \rangle$, where $\langle \cdot \rangle$ the time average operator. Given that: $\langle \cos(\Phi)^2 \rangle \simeq 1$, the average optical noise power $N_{opt,\ell}$ of chirp-induced IMD/HD and falling at frequency component ℓ is given by: $N_{opt,\ell} \approx 2P_{in} \cdot 10^{-aL} \cdot (I_\ell^2 + Q_\ell^2)$.

A.3 RBS analytical modeling

According to [148], the Power Spectral Density (PSD) of the RBS noise is expressed as:

$$N_{rbs}(f) = \frac{10R_{rb}^2(2\alpha L + e^{-2aL} - 1)}{9} \cdot \mathfrak{F} \langle |R_{\varepsilon_{sig}}|^2 \rangle \qquad (A.26)$$

Given: $R_{\varepsilon_{sig}}$: The autocorrelation function of the signal electric field ε_{sig}; L: The fiber link length; a: Fiber attenuation coefficient; R_{rb}: RBS reflectance of the SMF ($R_{rb} = -27$ dB for single mode fiber [148]) and $\mathfrak{F}$: denotes the Fourier transformation operator.

We distinguish between two kinds of RBS noises. A first RBS noise (N_{rbs}^{in}) called input RBS is due to the interference of the back-reflected modulated signal with the optical signal at the input of the modulator. A second RBS noise (N_{rbs}^{out}) called output RBS is due to the interference of the back-reflected continuous-wave signal with the modulated signal at the output of the modulator.

A.3.1 Input RBS noise:

The PSD of the continuous wave signal ε_{sig} at the output of the DFB laser is approximated by a Lorentzian distribution with a spectral width $\Delta\nu$. The Fourier transform of the auto-correlation of ε_{sig} is also a Lorentzian distribution with a spectral width $2\Delta\nu$. Then, Equation A.26 is written as:

$$N_{rbs}^{in}(f) = \frac{10R_{rb}^2(2aL + e^{-2aL} - 1)}{9} \cdot \frac{2a\Delta\nu}{\pi(f^2 + 4\Delta\nu^2)} \tag{A.27}$$

RBS power falling at RF f_ℓ with a signal bandwidth B_ℓ is: $P_{rbs}^{in} = \int_{f_\ell \pm B_\ell/2} N_{rbs}^{in}(f)\mathrm{d}f$ [148].

A.3.2 Output RBS noise:

The electric field of the signal at the output of the EAM is expressed as function of the input optical power P_{in}, the transfer function of the EAM $\mathfrak{f}$ as:

$$\varepsilon_{sig} = \sqrt{2P_{in}\mathfrak{f}(V)} \cdot e^{j2\pi\int_0^t \gamma V_b x(\xi)\mathrm{d}\xi} \tag{A.28}$$

With: γ: the EAM chirping efficiency (frequency excursion) expressed in [Hz/V]; $x(t) = \sum_i m_i \cos(2\pi f_i)$ the modulating SCM RF signal.

Introducing $g = \sqrt{\mathfrak{f}}$, we exploit the Taylor development of g with respect to V (around the bias voltage V_b), thus the autocorrelation of ε_{sig} is given by:

$$R_{\varepsilon_{sig}} = \left[g_b + g_b'V(t) + g_b''\frac{V(t)^2}{2!} + \cdots\right] \cdot \left[g_b + g_b'V(t+\tau) + g_b''\frac{V(t+\tau)^2}{2!} + \cdots\right] \cdot e^{j2\pi\int_t^{t+\tau}\gamma V_b x(\xi)\mathrm{d}\xi} \tag{A.29}$$

Neglecting higher order terms in A.29, the Fourier transform of $R_{\varepsilon_{sig}}$ is expressed as:

$$\mathfrak{F}\langle|R_{\varepsilon_{sig}}|^2\rangle = \mathfrak{F}\left\langle[g_b^2 + g_b'^2V_b^2(1 + \sum_i \frac{m_i^2\cos(2\pi f_i\tau)}{2})]^2\right\rangle \otimes \mathfrak{F}\left\langle[\cos(2\pi\int_t^{t+\tau}\gamma V_b x(\xi)\mathrm{d}\xi)]^2\right\rangle \tag{A.30}$$

Where: $\otimes$ stands for the convolution product operator and $\langle\cdot\rangle$ the time average operator.

Given $\delta(f)$ the Dirac distribution function. The first term in Equation A.30 is worked out leading to:

$$\mathfrak{F}\left\langle \left[g_b^2 + g_b'^2 V_b^2 \left(1 + \sum_i \frac{m_i^2 \cos(2\pi f_i \tau)}{2} \right) \right]^2 \right\rangle = \left(g_b^4 + g_b'^4 V_b^4 + 2 g_b^2 g_b'^2 + V_b^2 + \frac{\sum_i m_i^4}{8} \right) \cdot \delta(f) \quad \text{(A.31)}$$

For high number of modulating RFs with small OMI, we assume x following a gaussian distribution, thus the second term of Equation A.30 is computed as:

$$\mathfrak{F}\left\langle \left[\cos(2\pi \int\limits_t^{t+\tau} \gamma V_b x(\xi) \mathrm{d}\xi) \right]^2 \right\rangle \simeq \frac{1}{\sigma_f \sqrt{\pi}} e^{\frac{-f^2}{4\sigma_f^2}} \quad \text{(A.32)}$$

given: $\sigma_f = V_b \gamma \sqrt{\dfrac{\sum_i m_i^2}{2}}$

Using results of Equations A.31 and A.32, and given that $\delta(f)$ is the identity element of the convolution product, the output RBS noise power falling at RF f_ℓ with a signal bandwidth B_ℓ is:

$$N_{rbs}^{out} = \frac{10 R_{rb}^2 (2aL + e^{-2aL} - 1)}{9} \cdot \left(g_b^4 + g_b'^4 V_b^4 + 2 g_b^2 g_b'^2 + V_b^2 + \frac{\sum_i m_i^4}{8} \right) \cdot \int\limits_{f_\ell - B_\ell/2}^{f_\ell + B_\ell/2} \frac{e^{\frac{-f^2}{4\sigma_f^2}}}{\sigma_f \sqrt{\pi}} \, \mathrm{d}f \quad \text{(A.33)}$$

A.4   OBI analytical modeling

According to the analysis of Desem [37], the PSD of the OBI noise produced by the beating between two modulated optical carriers i and j is given by the convolution of their respective PSDs as in Equation A.34:

$$N_{ij}(f) = 4\sqrt{P_{o,i} P_{o,j}} \cdot \sqrt{f(V_i) f(V_j)} \cdot |\cos(\Phi)| \cdot \left(S_i(f) \otimes S_j(f) \right) \cdot \langle \cos^2 \theta_{ij} \rangle \quad \text{(A.34)}$$

Given: $S_i(f)$ (respectively $S_j(f)$): The PSD of the electric field of OC modulated by RF i (respectively j). $P_{o,i}$ (respectively $P_{o,j}$): Received optical power of OC modulated by RF i (respectively j); θ_{ij}: the difference in polarization angle between fields i and j and Φ the phase difference between the two optical carriers.

The PSD of the continuous-wave signal at the output of the DFB laser is approximated with a Lorentz distribution showing a linewidth Δf. For simplicity, we assume that the optical signal at the output of the modulator keeps also the same distribution but with a broadened linewidth due to frequency chirping of the EAM. Thus, the power spectrum of OBI is approximately Lorentzian with a spectral width equal to the sum of the linewidths of the two beating optical signals [37]:

$$F(f) = \frac{4}{\pi(1 + \alpha_H^2)\Delta f} \cdot \left[1 + \left(\frac{f}{(1 + \alpha_H^2)\Delta f} \right)^2 \right]^{-1} \quad \text{(A.35)}$$

The term $(1 + \alpha_H^2)$ in Equation A.35 denotes the increase of the linewidth due to EAM chirping, α_H being the Henry factor of the modulator [37].

Considering: $g = \sqrt{f}$, we use the Taylor expansion of g around the bias voltage V_b (higher orders are neglected) to compute $\sqrt{f(V_i)f(V_j)}$ as the following:

$$g(V_i)g(V_j) \simeq g_b^2 + g_b g_b' \cdot (V_i + V_j) + \frac{g_b g_b''}{2!} \cdot \left(V_i^2 + V_j^2\right) + \frac{g_b' g_b''}{2!} \cdot \left(V_j V_i^2 + V_i V_j^2\right) + \left(\frac{g_b''}{2!} \cdot V_i V_j\right)^2 \quad \text{(A.36)}$$

To highlight IMD/HD components produced by the beating between subcarriers of optical carriers j and j, Equation A.36 is developed by expressing the modulating voltage V_i with OMI m_i and RF angular frequency w_i as: $V_i = V_b(1 + m_i \cos(w_i t))$. The mathematical development leads to the expression of the optical power of OBI-induced IMD3 noise falling on frequency $f_\ell = 2f_i - f_j$ with signal bandwidth B_ℓ as:

$$N_\ell^{obi} = \frac{g_b' g_b'' V_b^2}{4} \cdot \sqrt{P_{o,i} P_{o,j}} \cdot m_i^2 m_j \cdot |\cos(\Phi)| \cdot \int\limits_{f_\ell - B_\ell/2}^{f_\ell + B_\ell/2} F(f - f_\ell) \mathrm{d}f \quad \text{(A.37)}$$

Where: $\Phi = \frac{w_o \Delta L}{c}$ is expressed with the angular optical frequency w_o, light velocity in the vacuum c and ΔL the pathway difference between the two optical carriers.

Index

Bibliography

[1] O. Y. K. Alani A. de Grado Vivero and J. M. H. Elmirghani. Indoor airport radio-over-fiber network traffic model and performance analysis using load-balancing techniques. *OSA Journal of Optical Networking*, 8(3):272–284, Mar. 2009. (Cited on page 180.)

[2] A. Nirmalathas, P. A. Gamage, C. Lim, D. Novak and R. Waterhouse. Digitized radio-over-fiber technologies for converged optical wireless access network. 28(16):2366–2374, 2010. (Cited on pages 56 and 58.)

[3] A. Sharaiha. Harmonic and intermodulation distorsion analysis by perturbation and harmonic balance methods for in-line photodetection in a semiconductor optical amplifier. *IEEE/ Photonics Technology Letters*, 10(3):421–423, Mar. 1998. (Cited on page 88.)

[4] A. Stohr, K. Kitayama and D. Jager. Full-duplex fiber-optic RF subcarrier transmission using a dual-function modulator/photodetector. *IEEE/ Trans. on Microwave Theory and Techniques*, 47(7):1338–1342, July 1999. (Cited on page 86.)

[5] Agrawal G. P. *Fiber-optic communication systems*. Third Edition, Canada: Wiley-Interscience, 2002. (Cited on pages 97, 109, 110 and 114.)

[6] Alameh K. and Minasian R. A. Ultimate limits of subcarrier multiplexed lightwave transmission. *Electronic Letters*, 27:1260–1262, June 1991. (Cited on pages 100 and 113.)

[7] Analysys-Mason. The cost of deploying fiber-based next generation broadband infrastructure. Analysys-mason research report, Boradband Stakeholder Group, Cambridge UK, http://www.analysysmason.com, Jan. 2008. (Cited on page 182.)

[8] Arnold O. *et al.* Power consumption modeling of different base station types in heterogeneous cellular networks. *Future Network and Mobile Summit 2010 Conf. proc.*, (ISBN: 978-1-905824-16-8):1–8, Jan. 2010. (Cited on page 66.)

[9] B.-L. Dang and I. Niemegeers. Analysis of ieee 802.11 in radio over fiber home networks. *IEEE Conf. on Local Computer Networks*, pages 744–747, Nov. 2005. (Cited on page 59.)

[10] B.-L. Dang, V.-R. Prasad, and I. Niemegeers. On the mac protocols for radio over fiber indoor networks. *IEEE/ 1st Int. Conf. on Communications and Electronics, ICCE06*, pages 112–117, Oct. 2006. (Cited on page 60.)

[11] M. Pickavet B. Lannoo, D. Colle and P. Demeester. Radio-over-fiber-based solution to provide broadband internet access to train passengers. *IEEE/Communications Magazine*, 45(2):56–62, February 2007. (Cited on pages 11, 58 and 180.)

[12] B. Murmann. A/d converter trends: Power dissipation, scaling and digitally assisted architectures. *IEEE Custom Integrated Circuits Conference*, pages 105–112, January 2008. (Cited on page 66.)

[13] W.C. Babcock. intermodulation interference in radio systems. *Bell Systems Technical Journal*, 1:63–73, Jan. 1953. (Cited on pages 144 and 156.)

[14] Bastard G. *et al.* Variational calculations on a quantum well in a eletric field. *The American Physical Society/ Physical Review B*, 28(6):3241–3245, 1983. (Cited on page 215.)

[15] Betti S. *et al.* Non linear distortions due to the dispersive transmission of SCM optical signals in the presence of chirping effect: an accurate analysis. *IEEE/Photonic Technology Letters*, 10:1640–1643, Dec. 1997. (Cited on pages 218 and 219.)

[16] Mukherjee Biswanath. *Optical WDM Networks*. Davis: Springer, ISBN: 978-0387-29055-3, 2006. (Cited on page 102.)

[17] Kazmierski C. New colorless 10 gbps remote modulator for wavelength access. In *Proc. of SPIE 10.1117/2.1200802.1084*, 2008. (Cited on pages 90 and 91.)

[18] Minot C. Optical microwave interactions in photonic devices. *Annales des Telecommunications*, 58:1432–1458, 2003. (Cited on page 89.)

[19] Permarocchi C. *Exciton Dynamics in Semiconductor confined Systems.* Phd thesis manuscript, Lausanne, Suisse: Ecole Polytechnique Federale de Lausanne, 1998. (Cited on page 214.)

[20] C. Kazmierski, P. Chanclou, J. A. Lazaro. Advanced component technologies for colourless access networks. In *Proc. of SPIE 6728.I*, 2007. (Cited on page 86.)

[21] C. Lanzani. Open base station architecture: Can standardization enable true innovation. Technical presentation, Radiocomp. Aps, Oct. 2008. (Cited on page 69.)

[22] C. Lim *et al.* Fiber-wireless networks and subsystem technologies. *IEEE/Journal of Lightwave Technology*, 28(4):390–405, February 2010. (Cited on pages viii, 54 and 55.)

[23] C. M. Fonseca and P. J. Fleming. Genetic algorithm for multiobjective optimization: Formulation, discussion and generalization. In *Proc. of the fifth IEE Colloquium on Genetic Algorithms for Control Systems Engineering*, May 1993. (Cited on pages 23, 138 and 139.)

[24] C. Sui *et al.* Impact of electro-absorption modulator integrated laser on MB-OFDM ultra-wideband signals over fiber systems. *IEEE/Journal of Lightwave Technology*, 28(24):3548–3555, Dec. 2010. (Cited on pages 89 and 108.)

[25] Castleford *et al.* Impact of optical crosstalk in fibre-radio systems incoroporating WDM. In *Proc. of IEEE/ Int. Top. Meet. Micro. Photon.*, pages 51–54, 2000. (Cited on page 103.)

[26] Castleford *et al.* Optical crosstalk in fiber-radio WDM networks. *IEEE/ Trans. on Microwave Theory and Techniques*, 49(10):2030–2035, Oct. 2001. (Cited on page 104.)

[27] Chang William S. C. Chin M., Yu P. K. L. Optimization of multiple quantum well structures for waveguide electroabsorption modulators. *IEEE Journal of Quantum Electronics*, 27(3):696–701, March 1991. (Cited on pages 94 and 214.)

[28] M. J. Connelly. Wideband semiconductor optical amplifier steady-state numerical model. *IEEE Journal of Quantum Electronics*, 37(3):439–447, March 2001. (Cited on pages 95 and 210.)

[29] Cox III et *et al.* An analytic and experimental comparison of direct and external modulation in analog fiber-optic links. *IEEE/ Trans. on Microwave Theory and Techniques*, 38(5):501–509, May 1990. (Cited on page 94.)

[30] Cox III *et al.* Techniques and performance of intensity-modulation direct-detection analog optical links. *IEEE/Transactions on Microwave Theory and Techniques*, 45(8):1375–1383, Aug. 1997. (Cited on pages 84, 86, 87, 88, 92, 112 and 113.)

[31] Crisp M. *et al.* Wideband radio over fiber distributed antenna systems for energy efficient in-building wireless communications. *IEEE Conf. on Vehicular Technology*, pages 1–5, May 2010. (Cited on page 66.)

[32] D. Jager and A. Stohr. Optoelectronic components and integration devices: From concepts to applications. In *RTO SET Lecture Series on "Optics Microwave Interactions"*, pages 1–11, 2002. (Cited on page 91.)

[33] D. Jager, R. Heinzelmann and A. Stohr. Microwave optical interaction devices: From concept to applications. In *Proc. of IEEE/Microwave Conf.*, pages 1–4, 2000. (Cited on pages 85 and 86.)

[34] D. Wake, A. Nhansah and N.J. Gomes. Radio-over-fiber link design for next generation wireless systems. *IEEE/JLT*, 28(16):2456–2464, Aug. 2010. (Cited on pages 65, 70, 82, 87, 92 and 185.)

[35] D. Wake, D. Johansson and D.G. Moodie. Passive picocell: a new concept in wireless network infrastructure. In *Proc. of IEEE/ Elect. Lett.*, pages 404–406, 1997. (Cited on page 87.)

[36] S. Dahlfort and K. Laraqui. Exploring the antenna lambda connection. *OSA Proc. of OFC/NFOEC in Los Angeles, CA*, pages 1–3, Mar. 2012. (Cited on pages 180 and 181.)

[37] Can Desem. Optical interference in subcarrier multiplexed systems with multiple optical carriers. *IEEE/Journal on Selected Areas in Communications*, 8(7):1290–1295, September 1990. (Cited on pages 112, 222 and 223.)

[38] Patrick Donegan. Backhaul strategies for mobile carriers. Watch Service/Consultancy Report 4, Heavy Reading, http://www.heavyreading.com, March 2006. (Cited on pages 6, 33, 48, 51, 205 and 206.)

[39] Dupuis *et al.* 10 Gbit/s semi-insutlating buried heterostructure loss-less reflective amplified modulator for wavelength agnostic networks. In *Proc. of Optical Fiber Communication/ National Fiber Optic Engineers Conference*, pages 1–3, 2008. (Cited on pages 85 and 211.)

[40] E. Udvary and T. Broceli. Linearity and chirp investigations on SOA as an external modulator in SCM systems. In *Proc. of the European Microwave Association*, pages 217–222, 2007. (Cited on page 85.)

[41] El-Ghazali Talbi. *Metaheuristics: From Design to Implementation.* John Wiley & Sons., 2009. (Cited on pages 135, 136 and 140.)

[42] M. El-Sayed and P. Cagen. Mobile data explosion and planning of heterogeneous networks. In IEEE, editor, *Proc. of 15th Int. Telecommunications Network Strategy and Planning Symposium (Networks)*, Rome, Oct. 2012. (Cited on pages 5 and 47.)

[43] A. Hekkala *et al.* Analysis of and compensation for non-ideal rof links in das. *IEEE Wireless Communications*, 17(3):52–59, June 2010. (Cited on pages 76 and 122.)

[44] B. Jung *et al.* Centralized scheduling mechanism for enhanced end-to-end delay and qos support in integrated architecture of epon and wimax. *IEEE/ Journal of Lightwave Technology*, 28(16):2277–2288, Aug. 2010. (Cited on page 58.)

[45] B.T. Olsen *et al.* Techno-economic evaluation of the major telecommunication investment options for european players. *IEEE Network Journal*, pages 6–15, July 2006. (Cited on pages xi, 6, 48, 183 and 186.)

[46] M. A. Ali *et al.* On the vision of complete fixed-mobile convergence. *IEEE/ Journal of Lightwave Technology*, 28(16):2343–2357, Aug. 2010. (Cited on page 58.)

[47] M. Kantor *et al.* General framework for techno-economic analysis of next generation access networks. *IEEE Proc. of Int. Conf. on Transparent Optical Networks (ICTON)*, pages 1–4, July 2010. (Cited on page 182.)

[48] M.-T. Riaz *et al.* On radio over fiber for heterogeneous wireless networks. *IEEE/IFIP Conf. on Wireless and Optical Communications Networks*, pages 1–4, Apr. 2009. (Cited on page 60.)

[49] Miller D. A. B. *et al.* Electric field dependence of optical absorption near the band gap of quantum well structures. *The American Physical Society/Physical Review B*, 32(2):1043–1060, July 1985. (Cited on pages 209, 214 and 217.)

[50] S. Verbrugge *et al.* Operational expenditures for telecom operators. *Proc. of 9th Conf. on Optical Network Design and Modelling (ONDM05)*, pages 455–466, Feb. 2005. (Cited on pages xi and 187.)

[51] S. Verbrugge *et al.* Methodology and input availability parameters for calculating opex and capex costs for realistic network scenarios. *OSA Journal of Optical Networking*, 5(6):509–519, June 2006. (Cited on pages 182, 185, 186 and 187.)

[52] Stevens P. *et al.* Computer modeling of the electric field dependent absorption spectrum of multiple quantum well material. *IEEE/ Journal of Quantum Electronics*, 24(10):2007–2016, Oct. 1998. (Cited on pages 210 and 215.)

[53] Vurgaftman I. *et al.* Band parameters for iii-v compound semiconductor and their alloys. *American Institute of Physics/Journal of Applied Physics*, 89(11):5815–5875, June 2001. (Cited on page 211.)

[54] Williams C. K *et al.* Energy bandgap and lattice constant contours of iii-v quaternary alloys of the form ax by cz d or abx cy dz. *Journal of Electronic Materials*, 7(5):689–646, Jan. 1978. (Cited on pages 211 and 214.)

[55] Ericsson, Huawei, NEC, Nokia Siemens Networks, and Alcatel-Lucent. Common public radio interface (cpri) specification v4.0; interface specification. Technical specification, CPRI, http://www.cpri.info, Fab. 2008. (Cited on pages 67, 69 and 70.)

[56] GSMA Mobile for Development. Best practice procurement guide for green energy in india. White paper, GSMA in partnership with International Finance Corporation (IFC), http://www.gsma.com, March 2012. (Cited on page 202.)

[57] P. Chanclou F.Payoux and N. Genay. Wdm-pon with colorless onus. In OSA, editor, *OFC/NFOC*, number OTuG5, 2007. (Cited on page 86.)

[58] Frigo N. J. A model of intermodulation distortion in non-linear multicarrier systems. *IEEE Transactions on Communications*, 42:1216–1222, April 1994. (Cited on page 100.)

[59] Fujiwara *et al.* Impact of back-reflection on upstream transmission in WDM single-fiber loopback access networks. *IEEE/JLT*, 24(2):740–746, Feb. 2006. (Cited on pages 86 and 111.)

[60] R. Tucker G. Shen and C.-J. Chae. Fixed mobile convergence architectures for broadband access: Integration of EPON and WiMAX. *IEEE Communications Magazine*, 45(1):44–50, Aug. 2007. (Cited on page 60.)

[61] F. Xu G. Zhong and A.N. Willson Jr. A power-scalable reconfigurable fft/ifft ic based on a multi-processor ring. *IEEE Journal of Solid-State Circuits*, 41(2):483–495, feb. 2006. (Cited on page 66.)

[62] Gamage P. A. *et al.* Design and analysis of digitized rf-over-fiber links. *IEEE/ Journal of Lightwave Technology*, 27(12):2052–2061, June 2009. (Cited on page 63.)

[63] Girault G. *et al.* 10 gbit/s pon demonstration using a reamsoa in a bidirectional fiber configuration up to 25 km smf. *IEEE/ Proc. of ECOC*, 15:212–222, 2008. (Cited on page 111.)

[64] G.L. Li, C.K. Sun, S.A. Pappert, W.X. Chen and P.K.L. Yu. Ultrahigh-speed traveling-wave electroabsorption modulator- design and analysis. *IEEE/Trans. on Microwave Theory and Techniques*, 47(7):1177–1183, July 1999. (Cited on pages 92 and 93.)

[65] Godlewski *et al.* Analytical evaluation of various frequency reuse schemes in cellular OFDMA networks. In *Proc. of the 3rd Int. Conf. on Performance Evaluation Methodologies and Tools*, pages 32:1–32:10, 2008. (Cited on pages 123, 132 and 192.)

[66] Goebel B. *et al.* On the effect of fwm in coherent optical ofdm systems. *OSA/ Optical Fiber Communications*, pages 58–60, March 2008. (Cited on page 111.)

[67] Gyu-Woong Lee and Sang-Kook Han. Linear-dual electro-absorption modulator for analog optical transmission. *Microwave and Optical Technology Letters*, 22:369–373, 1999. (Cited on pages 98 and 99.)

[68] H. B. Kim and A. Wolisz. Performance evaluation of a mac protocol for radio over fiber wireless lan operating in the 60-ghz band. *IEEE Globecom Conf.*, pages 2659–2663, Dec. 2003. (Cited on page 60.)

[69] H. B. Kim and A. Wolisz. A radio over fiber based wireless access network architecture for rural areas. *IEEE Proc. of the 14th IST Mobile and Wireless Communications Summit*, pages 1–5, June 2005. (Cited on page 60.)

[70] Y. Bouslimani H. Chettat, L. M. Simohamed and H. Hamam. RoF networks: A comprehensive study. *IEEE/Proc. of. 3rd int. symp. on Wireless Pervasive Computing*, pages 495–498, May 2008. (Cited on page 55.)

[71] H. Kim and Y.C. Chung. Passive optical network for CDMA-based microcellular communication systems. *IEEE/JLT*, 19(3):301–311, Mar. 2001. (Cited on page 84.)

[72] Hamed Al-Raweshidy and Shozo Komaki. *Radio-over-Fiber Technologies for Mobile Communications Networks.* Artech House Inc., 2002. (Cited on pages 53, 92, 94, 99 and 113.)

[73] W. Van Heddeghem and F. Idzikowski. Equipment power consumption in optical multilayer networks Ű source data. Technical Report IBCN-12-001-01, IBBT Ghent University, http://powerlib.intec.ugent.be/, Jan. 2012. (Cited on pages 65 and 186.)

[74] Iwai *et al.* Reduction of dispersion-induced distortion in SCM transmission systems by using predistortion-linearized MQW-EA modulators. *IEEE/JLT*, 15(2):169–178, Feb. 1997. (Cited on pages 87, 101 and 218.)

[75] J. Piprek, Y.-J. Chiu and J. E. Bowers. Analysis of multi-quantum well electroabsorption modulators. In *Proc. of SPIE/Physics and simulation of optoelectronic devices*, 2002. (Cited on pages 88, 101 and 215.)

[76] J.C. Attard and J.E. Mitchell. Optical network architectures for dynamic reconfiguration of full duplex, multi-wavelength, radio-over-fiber. *OSA/Journal of Optical Networking*, 5(6):435–444, June 2006. (Cited on page 57.)

[77] K. Wakita and I. Kotaka. RF bandwidth capacity and SCM in RoF link employing optical frequency multiplication. In *Microwave Optic. Technol. Lett.*, pages 120–128, 1994. (Cited on page 84.)

[78] K.F. Man, K.S. Tang and S. Kwong. *Genetic Algorithms: Concepts and Designs.* Springer-Verlag, 2000. (Cited on pages 23, 138 and 139.)

[79] H. B. Kim and A. Wolisz. A radio over fiber based wireless access network architecture for rural areas. In IEEE, editor, *Proc. of the 14th IST Mobile and Wireless Communications Summit*, Dresden, Germany, June 2008. (Cited on page 76.)

[80] Koyama F. and Iga K. Frequency chirping in external modulators. *IEEE/Journal of Lightwave Technology*, 6:87–93, Jan. 1988. (Cited on page 101.)

[81] S.-J. Ku and C.-L. Wang. A new side-information free pts scheme for papr reduction in ofdm systems. In IEEE, editor, *Proc. of the 8th Int. Conf. on Wireless and Mobile*

Computing, Networking and Communications, Barcelona, Spain, Oct. 2012. (Cited on page 123.)

[82] Lam C. F. A simplified model for estimating the capacity limit of an optical link in transporting multichannel m-qam signals. *IEEE Photonics Technology Letters*, 12:1579–1581, Nov. 2000. (Cited on page 100.)

[83] K. Lee. Radio over fiber for beyond 3g. *IEEE Conf. on Microwave Photonics*, pages 9–10, Oct. 2005. (Cited on page 60.)

[84] Lengyel G. *et al.* A semi-empirical model for electro-absorption in GaAs/AlGaAs multiple quantum well modulator structures. *IEEE/Journal of Quantum Electronics*, 26:296–304, Feb. 1990. (Cited on page 209.)

[85] Asada M. and Suematsu Y. Density matrix theory of semiconductor lasers with relaxation broadening model gain and gain suppression in semiconductor lasers. *IEEE Journal of Quantum Electronics*, 21(5):434–442, May 1985. (Cited on page 96.)

[86] Saini M. and Sharma K. E. Equivalent refractive index of MQW waveguides. *IEEE Journal of Quantum Electronics*, 32(8):1383–1390, Aug. 1996. (Cited on page 217.)

[87] M. A. Ali and G. Metivier. Performance analysis of mutlichannel 16/64-QAM CATV distribution network using semiconductor optical amplifier as an external modulator. *IEEE/ Photonics Technology Letters*, 9(5):690–692, May 1997. (Cited on page 88.)

[88] *et al.* M. C. R. Medeiros. Radio over fiber access network architecture employing reflective semiconductor optical amplifiers. *IEEE/ Conf. proc. of ICTON-MW*, pages 1–5, Dec. 2007. (Cited on pages 11 and 57.)

[89] N. Ghazisaidi M. Maier and M. Reisslein. The audacity of fiber-wireless (fiwi) networks. *IEEE/3rd Int. Conf. on Access Networks, AccessNets 2008*, 6:16–35, Oct. 2009. (Cited on page 57.)

[90] M. Maier and M. Reisslein. AWG-based metro WDM networking. *Optical Communications Magazine*, 42(11):S19–S26, Nov. 2004. (Cited on page 71.)

[91] Jan Markandahl. *Mobile Network Operators and Cooperation.* Phd thesis, Kungliga Tekniska hogskolan (KTH)- Royal Institute of Technology, KTH Communication Systems-Stockholm, Sweden, Feb. 2011. (Cited on page 202.)

[92] MEF. Microwave technologies for carrier ethernet services. Technical document, Metro Ethernet Forum, http://metroethernetforum.org, Jan. 2011. (Cited on page 44.)

[93] Meslener G. J. Chromatic dispersion induced distortion of modulated monochromatic light employing direct detection. *IEEE/ Journal of Quantum Electronics*, QE-20:1208–1216, Aug. 1984. (Cited on page 108.)

[94] Muys W. and M. F. Mortier. Numerical simulations of clipping induced distortion in externally modulated lightwave am-scm systems. *IEEE Photonics Technology Letters*, 6(6):747–750, June 1994. (Cited on page 99.)

[95] Dupuis N. Integration par epitaxie selective d'un modulateur electro-absorbant et d'un amplificateur otpique a base de puits quantiques algainas. In *Metz, France: Universite de Metz, Ecole doctorale EMMA, PhD Thesis.*, 2009. (Cited on pages 91 and 215.)

[96] Nadir Dagli. Wide-bandwidth lasers and modulators for RF photonics. *IEEE/Transactions on Microwave Theory and Techniques*, 47(7):1151–1171, July 1999. (Cited on pages 82, 84, 85 and 86.)

[97] Technical Specification Group Radio Access Network. TR 36.814- further advancements for E-UTRA: Physical layer aspects (Release 9). Technical Report 36.814, 3rd generation partnership project, 2009. (Cited on page 66.)

[98] Anthony Ngoma. *Radio-over-Fibre Technology for Broadband Wireless Communication Systems.* Thesis manuscript, Eindhoven University of Technology, June 2005. (Cited on page 55.)

[99] Nguyen Q.-T. *et al.* Colorless components for wdm-based optical access networks. *IEEE/Proc. of Int. workshop on Photonics and Applications (IWPA)*, 6:11–14, Jan. 2008. (Cited on pages 85, 90 and 125.)

[100] Niiho *et al.* Transmission performance of multichannel wireless LAN system based on radio-over-fiber techniques. *IEEE/Trans. on Microwave Theory and Techniques*, 54(2):980–989, Feb. 2006. (Cited on pages 102 and 125.)

[101] O. K. Tonguz and H. Jung. Personal communications access networks using subcarrier multiplexed optical links. *IEEE/JLT*, 14(6):1400–1409, June 1996. (Cited on pages 18 and 102.)

[102] O. Tipmongkolsilp, S. Zaghloul and A. Jukan. The evolution of cellular backhaul technologies: Current issues and future trends. *IEEE Communications Surveys and Tutorials*, 13(1):97–113, 2011. (Cited on pages vii, 6, 43, 44, 46, 48 and 51.)

[103] OBSAI. Reference point 3 specification. Technical specification, OBSAI alliance, http://www.obsai.org, July 2008. (Cited on page 67.)

[104] OFC/NFOEC, editor. *Remote Amplified Modulators Key Components for 10Gbps WDM PON*, number 1-3. IEEE, Mar. 2010. (Cited on page 91.)

[105] Olshansky R. *et al.* Subcarrier multiplexed lightwave systems for broadband distribution. *IEEE/Journal of Lightwave Technology*, 7(9):1329–1342, Sept. 1989. (Cited on page 114.)

[106] N. L. S. da Fonseca P. H. Gomes and O. C. Branquinho. Optimization of the use of radio resource of radio-over-fiber access networks. In IEEE, editor, *Proc. of IEEE Globecom*, Miami, Dec. 2010. (Cited on page 76.)

[107] Monica Paolini. Crucial economics for mobile data backhaul. White paper, Senza Fili Consulting, http://www.senzafiliconsulting.com, Nov. 2011. (Cited on pages 6, 48 and 49.)

[108] Cisco White Paper. Ethernet power study of cisco and competitive products. Technical report, Cisco Systems Inc., 2008. (Cited on page 66.)

[109] J.P. Pareira and P. Ferreira. Infrastructure sharing as an opportunity to promote competition in local access networks. *Hindawi Pusblishing Corp. Journal of Computer Networks and Communications*, pages 1–11, Oct. 2012. (Cited on pages xi, 182, 185, 186 and 187.)

[110] Jennifer M. Pigg. Mobile backhaul evolution. Webinar, Yankee Group- Research and Consultancy, http://blogs.yankeegroup.com/2010/04/27/webinar-mobile-backhaul-evolution/, April 2010. (Cited on pages xi, 4, 43, 44, 45, 46, 48, 49, 182 and 187.)

[111] Prasanna A. Gamage *et al.* Design and analysis of digitized rf-over-fiber links. *IEEE/ Journal of Lightwave Technology*, 27(12):2052–2061, June 2009. (Cited on pages 60 and 66.)

[112] R. Berry et al. Spectrum markets: Motivation, challenges and implications. *IEEE Communications Magazine*, 48(11):146–155, Nov. 2010. (Cited on page 169.)

[113] A. D. Kavishwar R. G. Kaduskar. Mobile backhaul network. *IACSIT Press/Proc. of Int. Conf. on Information and Network Technology*, 4:211–216, Jan. 2011. (Cited on pages 42 and 49.)

[114] R. Hui *et al.* Subcarrier multiplexing for high speed optical transmission. *IEEE/Journal of Lightwave Technology*, 20(3):417–427, March 2002. (Cited on page 109.)

[115] R. Ngah, T. Prakoso and T. A. Rahman. Coverage range and cost comparison of remote antenna unit designs for in-building radio-over-fiber technology. *ITB J. ICT*, 2(1):24–41, Jan. 2008. (Cited on pages 65 and 185.)

[116] N. Scott R. Vaughan and D. White. The theory of bandpass sampling. *IEEE Transactions on Signal Processing*, 39:1973–1984, Sep. 1991. (Cited on page 61.)

[117] F. Mao B. Fu R. Zhang, S. Sun and J. Wang. A method to incentivize the third party devices to contribute in network and content service. In IEEE, editor, *Proc. of 15th Int. Telecommunications Network Strategy and Planning Symposium (Networks)*, Rome, Oct. 2012. (Cited on pages 5 and 47.)

[118] Tiana Ramahandry. Mobile bachaul: Trends and telcos' strategies. Innovation reports, IDATE Consulting and Research- IDATE Watch Services, http://idate-research.com, July 2011. (Cited on pages 6, 34, 48, 49, 51, 52 and 53.)

[119] Louise Van Rensburg. The uk energy retail market review: updated proposals for businesses. White paper (ref. 134/12), OFGEM: Office of the Gas and Electricity Markets, http://www.ofgem.gov.uk, Oct. 2012. (Cited on page 202.)

[120] R.G. Walker. High-speed III-V semiconductor intensity modulators. *IEEE/ Journal of Quantum Electronics*, 27(3):654–667, 1991. (Cited on page 85.)

[121] Robert J. Baxley *et al.* Power savings analysis of peak-to-average power ratio reduction in ofdm. *IEEE/ Transactions on Customer Electronics*, 50(3):792–798, Aug. 2004. (Cited on page 66.)

[122] Julius Robson. Small cells deployment strategies and best practice backhaul. White paper, Cambridge Broadband Networks, http://www.cbnl.com, Aug. 2012. (Cited on pages 6 and 48.)

[123] Rodney S. Tucker. Green optical communications- part i: Energy limitations in transport. *IEEE/ Journal of Selected Topics in Quantum Electronics*, 17(2):245–260, March 2011. (Cited on page 66.)

[124] Rodney S. Tucker. Scalability and energy consumption of optical and electronic packet switching. *IEEE/ Journal of Lightwave Technology*, 29(16):1–12, Aug. 2011. (Cited on page 66.)

[125] Roselli *et al.* Analog laser predistortion for multi-service radio-over-fiber systems. *IEEE/JLT*, 21(5):1211–1223, May 2003. (Cited on page 99.)

[126] Moray Rumney *et al. LTE and the Evolution to 4G Wireless: Design and Measurement Challenges.* Agilent Technologies, July 2009. (Cited on page 148.)

[127] Irmscher S. *Design, Fabrication and analysis of InP-InGaAsP Traveling-wave electroabsorption modulators.* Doctoral thesis, Stockholm: Royal Institute of Technology (KTH), 2003. (Cited on page 101.)

[128] M. Gasparroni S. Chia and P. Brick. The next generation for cellular networks: Backhaul. *IEEE Microwave Magazine*, 10(5):54–66, Aug. 2009. (Cited on pages 5, 45 and 47.)

[129] S. D. Dods and R. S. Tucker. A comparison of the homodyne crosstalk characteristics of optical add-drop multiplexers. *IEEE/Journal of Lightwave Technology*, 19(12):1829–1838, Dec. 2001. (Cited on pages 102, 103 and 104.)

[130] S. K. Narayankhedkar and R. K. Shevgaonkar. Interchannel crosstalk in fiber bragg grating based optical add drop multiplexer. *Elsevier/Information Sciences*, pages 53–59, May 2003. (Cited on page 106.)

[131] S. L. Woodward and M. R. Phillips. Optimizing subcarrier multiplexed WDM transmission links. *IEEE/Journal of Lightwave Technology*, 22(3):773–778, Mar. 2004. (Cited on page 109.)

[132] *et al.* S. Pato. On building a distributed antenna system with joint signal processing for next generation wireless access networks: The futon approach. *IEEE/7th Int. Conf. on Telecommunications, Santa Maria de Feira, Portugal.*, May. 2009. (Cited on pages 11 and 58.)

[133] S. Sesia, I. Toufik and M. Baker. *LTE: The UMTS long-term evolution from theory to practice.* John Wiley & Sons., 2009. (Cited on pages 27, 62, 63, 123, 149 and 192.)

[134] K. Wang A. Vastberg M. Forzati S. Tombaz, P. Monti and J. Zander. Impact of backhauling power consumption on the deployment of heterogeneous mobile networks. *IEEE/ Proc. of Global Telecommunications Conference (Globecom 2011)*, pages 1–5, Dec. 2011. (Cited on page 66.)

[135] J. Brown S. Vakeva, E. Liew and J. Blackney. Pricing for profit. White paper/brochure, Nokia Siemens Networks, http://nokiasiemensnetworks.com, Jan. 2009. (Cited on pages ix, 166 and 169.)

[136] G. Salami and R. Tafazolli. Inter-operator dynamic spectrum sharing (analysis, cost and implications). *Int. Journal of Computer Networks*, 2(1):47–61, Jan. 2010. (Cited on pages 170, 171 and 172.)

[137] Saleh A.A.M. Fundamental limit on number of channels in subcarrier multiplexed lightwave catv systems. *Electronic Letters*, 25:776–777, June 1989. (Cited on page 100.)

[138] Sauer *et al.* Radio-over-fiber for picocellular network architectures. *IEEE/JLT*, 25(11):3301–3320, Nov. 2007. (Cited on page 84.)

[139] Eitan Schwartz. Mobile backhaul: challenges and opportunities. White paper, RAD Data Communications Ltd., http://www.rad.com/21/Mobile-Backhaul, Jan. 2008. (Cited on page 206.)

[140] S.K. Narayankhedkar and R.K. Shevgaonkar. Nonuniform fiber gratings in optical networks. In *Proc. of the Pacific Rim Conference on Lasers and Electro-Optics*, pages 499–500, 1999. (Cited on page 106.)

[141] Timo Smura. *Techno-economic modelling of wireless network and industry architectures.* Phd dissertation, Aalto University, School of Electrical Engineering, Aalto, Finland, March 2012. (Cited on pages 48 and 182.)

[142] R. Struzak. On spectrum congestion and capacity of radio links. In *Annals of Operations Research*, volume 107, pages 339–347, Jan. 2001. (Cited on page 148.)

[143] Udvary *et al.* Semiconductor optical amplifier in analog optical links. In *Proc. of IEEE/ ICTON*, pages 201–206, 2003. (Cited on page 86.)

[144] Urban *et al.* Rayleigh backscattering-suppression in a WDM access network employing a reflective semiconductor optical amplifier. In *Proc. of IEEE/ LEOS*, pages 147–150, 2007. (Cited on pages 86 and 111.)

[145] Harish Vadada. Cloud ran, radio-over-fiber: Cloud paradigm for wireless networks. Analysis blog report, Telecom Cloud, http://www.telecom-cloud.net, Sept. 2011. (Cited on page 53.)

[146] *et al.* W. P. Lin. The modified star ring architecture for high-capacity subcarrier multiplexed passive optical networks. *Journal of Lightwave Technology*, 19(1):32–38, Jan. 2001. (Cited on pages 11 and 58.)

[147] W. Van Heddeghem *et al.* Power consumption modeling in optical multilayer networks. *Springer/ Photonic Network Communications*, (24):89–102, Jan. 2012. (Cited on pages 65 and 186.)

[148] Wan P. and Conradi J. . Impact of double rayleigh backscatter noise on digital and analog fiber systems. *IEEE/Journal of Lightwave Technology*, 14(3):288–297, March 1996. (Cited on pages 111, 220 and 221.)

[149] G. Kent Webb. A financial model of cable television with a simulation analysis of the 1993 rate regulations. *Springer Telecommunication Systems Journal*, 4(11):217–239, Feb. 1995. (Cited on page 182.)

[150] Welstand R. B. *et al.* Combined franz-keldysh and quantum confined stark effect waveguide modulator for analog signal transmission. *IEEE Journal of Lightwave Technology*, 17(11):497–502, March 1999. (Cited on page 91.)

[151] Won *et al.* 1.25-Gb/s wavelength-division-multiplexed single wavelength colorless radio-over-fiber systems using reflective semiconductor optical amplifier. *IEEE/JLT*, 25(11):3472–3478, Nov. 2007. (Cited on page 85.)

[152] Yamamoto *et al.* Theory of refractive index variation in quantum well structure and related intersectional optical switch. *IEEE/Journal of Lightwave Technology*, 6:1831–1840, Dec. 1988. (Cited on pages 209 and 217.)

[153] Yan Chen *et al.* Qos requirements of network applications on the internet. *IOS Press/ Information-Knowledge-Systems Management*, (4):55–76, Jan. 2004. (Cited on page 62.)

[154] Yang Y. *et al.* Multichannel digitized rf-over-fiber transmission based on bandpass sampling and fpga. *IEEE/ Transactions on Microwave Theory and Techniques*, 58(11):3181–3188, Nov. 2010. (Cited on pages 57, 61, 63 and 98.)

[155] Yasunori M. *et al.* Numerical simulations in the development process of ultrahigh-speed WDM electro-absorption modulators. *IEEE/LEOS Proc. of the third int. conf. on Numerical Simulation of Semiconductor Optoelectronic Devices*, 6:11–14, Jan. 2003. (Cited on page 217.)

[156] Yun *et al.* Analog performance of multiple-quantum-well electroabsorption modulator. *Springer/Optical and Quantum Electronics*, pages 1025–1031, July 2005. (Cited on pages 84, 86 and 91.)